國立交通大學

電子物理研究所

博士論文

腔內非線性光學之波長轉換與斑圖形成

Wavelength Conversion and Pattern Formation in Intracavity Nonlinear Optics

研究生：張雅婷

指導教授：陳永富　教授

蘇冠暐　教授

中華民國九十九年七月

腔內非線性光學之波長轉換與斑圖形成

Wavelength Conversion and Pattern Formation in Intracavity Nonlinear Optics

研 究 生：張雅婷　　Student：Ya-Ting Chang

指導教授：陳永富　　Advisor：Yung-Fu Chen

蘇冠暐　　Kuan-Wei Su

國 立 交 通 大 學

電 子 物 理 研 究 所

博 士 論 文

A Thesis

Submitted to Institute of Electrophysics

College of Science

National Chiao Tung University

in partial Fulfillment of the Requirements

for the Degree of

Doctor of Philosophy

in

Electrophysics

July 2010

Hsinchu, Taiwan, Republic of China

中華民國九十九年七月

腔內非線性光學之波長轉換與斑圖形成

學生：張雅婷　　指導教授：陳永富

蘇冠暐

國立交通大學電子物理研究所博士班

摘　　要

利用非線性晶體的受激拉曼散射特性，可以有效率地實現新波長固態雷射，然而在實驗過程中，我們發現拉曼雷射效能總是受限於晶體的熱透鏡效應，尤其是二極體雷射端面激發的固態腔內拉曼雷射。本論文分為兩個部分。第一部分致力於改善晶體的熱透鏡效應，用以得到高效率的腔內非線性波長轉換。首先，我們藉由量測三種結構 Nd:YVO_4 雷射晶體之等效熱透鏡焦距，比較其熱透鏡效應的強度，包括傳統晶體、單端複合晶體與雙端複合晶體。實驗結果證實:使用雙端接上 2.1 mm YVO_4 的複合晶體可以最有效地改善 1342 nm Nd:YVO_4 雷射之熱透鏡效應。之後，我們設計獨創性的雙端複合 Nd:YVO_4 晶體，並首次使用複合晶體當自發拉曼晶體，有效提升 Q-開關人眼安全拉曼雷射效能。我們又利用此雙端複合 Nd:YVO_4 自發拉曼晶體與 BBO 腔內混頻晶體，實現高效率 Q-開關黃綠光拉曼雷射。此外，我們首次使用釩酸鹽當拉曼晶體，將雷射晶體與拉曼晶體分開，提升了使用傳統晶體的 1176 nm Q-開關 Nd:YVO_4 自發拉曼雷射效能。

我們亦利用 Stokes 位移值小的 KTP 與 KTA 拉曼晶體，實現 Q-開關多階拉曼雷射，並觀察到受激拉曼散射與圓錐形二倍頻轉換分別形成的「交叉」與「圓環」遠場斑圖。本論文第二部分係利用非線性轉換機制，研究斑圖形成。我們利用有延伸性缺陷之非線性晶體，可從 Q-開關雷射加上腔內倍頻有效產生圓錐形二倍頻轉換。再利用光學技術量測近場模態，探討無序性波函數之空間分布結構，有趣的是，我們找到了波函數可以把混沌波與 Bessel 光束作連結。

Wavelength Conversion and Pattern Formation in Intracavity Nonlinear Optics

Student：Ya-Ting Chang　　Advisor： Yung-Fu Chen

Kuan-Wei Su

Institute of Electrophysics

National Chiao Tung University

ABSTRACT

Stimulated Raman scattering (SRS) has been regarded as an efficient and practical method of generating solid-state laser sources at new wavelengths. In our experiments, it is found that the thermal lensing effects are critical issues exacerbating the laser performance of diode-end-pumped solid-state intracavity Raman laser. The thesis is divided into two parts. The purpose of the first part is to improve the thermal effect and demonstrate high-efficiency intracavity nonlinear wavelength conversion. First the comparison of thermal lensing effects between conventional, single-end composite, and double-end composite Nd:YVO_4 crystals is investigated by measuring the effective focal lengths of thermal lens. The experimental results confirm that using a composite Nd:YVO_4 crystal with double 2.1-mm-long ends can efficiently improve the thermal lensing effect for 1342-nm transition. Then we design a original double-end composite Nd:YVO_4 crystal and first employ a composite crystal as a self-Raman medium to improve the laser performance of Q-switched eye-safe Raman laser. A high-efficiency Q-switched yellow-green Raman laser with self-Raman frequency conversion in the double-end composite Nd:YVO_4 crystal and intracavity sum-frequency generation in BBO crystal is also demonstrated. Moreover we use a new design of Q-switched Nd:YVO_4 Raman laser with an intracavity vanadate as a Raman crystal to improve the laser performance of 1176-nm self-Raman laser with a conventional Nd:YVO_4 crystal.

In addition, KTP and KTA crystals with low value of Stokes shifts permit generation of multi-frequency radiation with cascade SRS. The “cross” and “ring” far-field wave patterns of SRS and conical second harmonic generation (SHG) are observed in a cascade Raman laser respectively. The second part of this thesis is intended as an investigation of pattern formation in

a laser with nonlinear wavelength conversion. By using a nonlinear crystal with extended defects, the conical SHG is efficiently generated from a Q-switched laser with intracavity SHG. The near-field patterns of conical SHG can be used to explore the spatial structure of disordered wave functions. It is interesting that chaotic wave can be connected with Bessel beam by the wave functions.

誌 謝

在碩博班研究生涯的五年歲月，首先要感謝的是我的指導老師陳永富教授。感謝老師在專業的雷射領域中給予我最重要的指導與鼓勵，以及做人處事上的叮嚀。同時，也要感謝我的指導老師蘇冠暐教授的指導，老大總是能為我指點迷津，您對實驗的細心與耐心是我值得學習的榜樣。有兩位指導老師的幫助，並提供實驗室豐富的研究資源與環境，我才能完成此篇畢業論文，在此致上最誠摯的謝意。感謝口試委員祁甦教授、施宙聰教授、黃凱風教授、梁振民博士、賴暎杰教授在百忙中抽空前來，提供許多寶貴意見與指導。

此外，謝謝實驗室的成員蔡玲意、deer、小黃、黃哲彥、張漢龍、陳建誠、梁興弛、黃依萍、余彥廷、阿楨、林毓捷、莊威哲、陳毅帆、林昆毅、黃郁仁等在研究上的幫助與意見，以及生活上的陪伴。當然也要謝謝我的好朋友宗凰、凱慈、文萱、秉真、恩毓、穎書、瑜珊、孟姿、民樺、祐民等，在我需要你們的時候陪伴我，能一起分享喜怒哀樂是最幸福的事，有你們真好!

最後感謝我最親愛的家人，謝謝爸爸、媽媽、姐姐、弟弟在我求學過程中一路支持我，給予我最溫馨的關心與支持，讓我能專心於研究工作而無後顧之憂。

Contents

Guide to Figures

Chapter 6

Chapter 7

Guide to Tables

Chapter 1

Introduction

1.1 Motivation

Solid-state laser has been applied widely in medical treatment, biomedicine, remote-sensing, range-finder, industry, and defence. However, the spectra of solid-state lasers are confined to specific wavelengths due to the specific photoluminescence of laser gain medium. The rapid discovery of new Raman media has made Stimulated Raman scattering (SRS) regarded as an efficient and practical method of generating solid-state laser sources at new wavelengths [1-8]. Moreover, combining SRS and second harmonic generation (SHG) / sum frequency generation (SFG) can extend the output wavelengths to ultraviolet and visible spectral region with a number of useful applications.

Nd:YVO_4 and Nd:$GdVO_4$ crystals have been identified as useful materials for diode-pumped solid-state lasers. In 2001, Kaminskii et al. predicted that the tetragonal YVO_4 and $GdVO_4$ crystals with new $\chi^{(3)}$ nonlinear potential could serve as efficient Raman converters [9]. In 2004, the first demonstrations of actively Q-switched and passively Q-switched diode-pumped Nd:YVO_4 and Nd:$GdVO_4$ self-Raman laser were made by Chen [10-13]. However, the thermal effect has been regarded as a critical issue exacerbating the solid-state Raman laser performance including laser stability, critical pump power, output power, and conversion efficiency. An efficient intracavity nonlinear wavelength conversion could be accomplished by overcoming the thermal effect, particularly for a diode-end-pumped solid-state self-Raman laser. The first emphasis of the thesis is placed on improvement of thermal effect in Nd-doped

intracavity Raman lasers with vanadates as Raman media.

The second emphasis of the thesis is placed on investigation of pattern formation. In our experiments, it is found that pattern formation can be observed in a laser with nonlinear wavelength conversion. By using a nonlinear crystal of KTP or KTA in a Q-switched laser, we observe interesting transverse wave patterns of SRS and conical SHG. However, the pattern formation of SRS has not been reported to date. In 2006, Chen et al. experimentally demonstrated that the near-field wave patterns of conical SHG of a laser in random domain structures can be used to explore the spatial structure of two-dimensional disordered wave functions with weak localization [14]. It was also verified that using conical SHG can serve as a diagnostic tool for topographical characterization of crystals [14]. We also use a frequency-doubled laser to study the pattern formation of conical SHG at the beginning. In addition to the chaotic wave pattern, we observe quasi-Bessel beam and symmetry-breaking Bessel beam patterns. More interestingly, we find a mathematical function which can connect Bessel beam with chaotic wave. Further investigations of pattern formation of Raman emission will be carried out.

1.2 Overview of the Thesis

After introducing the motivation, the thesis starts with a review of the basic concepts of solid-state Raman lasers including Raman scattering principle, Raman media, solid-state intracavity Raman laser configuration, modeling investigation of Q-switched intracavity Raman laser, and spectral coverage of solid-state Raman laser in the Chapter 2.

In recent years, employing a composite crystal with nonabsorbing undoped end has been regarded as a promising method for reducing thermal lensing effect. In the Chapter 3, we introduce thermal lensing effect and first study the comparison of thermal lensing effects between conventional, single-end composite, and double-end composite Nd:YVO_4 crystals for 1064- and 1342-nm transitions by measuring the effective focal lengths of thermal lens. The efficient improvement of thermal lensing effect in a composite Nd:YVO_4 crystal with double 2.1-mm-long ends for 1342-nm transition is confirmed.

The improvement of thermal effects in gain medium is critically important for developing self-Raman solid-state lasers because the Raman gain coefficient decreases substantially with increasing temperature above room temperature. In the Chapter 4, we design a original double-end composite Nd:YVO_4 crystal and first use composite crystal as a self-Raman medium to demonstrate a compact efficient actively Q-switched eye-safe laser at 1525 nm. Moreover, an efficient Q-switched dual-wavelength laser at 1176 and 559 nm with self-Raman frequency conversion in

the double-end composite Nd:YVO_4 crystal and intracavity sum-frequency generation in BBO is demonstrated.

However, the optimization of self-Raman laser is restricted because the laser gain medium simultaneously serves as a Raman medium. In the Chapter 5, we first use a new design of actively Q-switched 1176-nm Nd:YVO_4 laser with an intracavity YVO_4 crystal as a Raman medium for improving the laser performance of 1176-nm self-Raman laser with a conventional Nd:YVO_4. In next section, by using a similar laser cavity with another laser gain medium Nd:YAG with better thermal property and longer fluorescence lifetime, the laser performance is further improved. The comparison of 1176-nm Raman laser performance between Nd:YVO_4 self-Raman laser, Nd:YVO_4/YVO_4 Raman laser, and Nd:YAG/YVO_4 Raman laser with conventional crystal is discussed.

In the Chapter 6, KTP and KTA crystals with low Raman shifts at 270 and 235 cm^{-1} are employed to product multi-frequency radiation with cascade SRS, respectively. In addition, we observe interesting transverse wave patterns of SRS and conical SHG in cascade Raman lasers with intracavity SHG.

Although the conversion efficiency of noncollinear conical SHG is substantially lower than collinear axial SHG, there are interesting research topics about noncollinear conical SHG. The Chapter 7 starts with introducing the generation of conical SHG. In the next section, we show the interesting near- and far-field patterns of conical SHG in a frequency-doubled Nd:YVO_4 self-Raman laser with intracavity SHG in a KTP crystal. Moreover, we use a GdCOB crystal with extended defects in a

Q-switched Nd:YAG laser to efficiently generate conical SHG. The near-field wave patterns include chaotic wave, quasi-Bessel beam, and symmetry-breaking Bessel beam patterns. The transverse disordered wave patterns are associated with a superposition of a number of monochromatic plane waves with different directions and phases. Furthermore, the near- and far-field patterns of frequency-doubled Q-switched Nd:YAG laser with intracavity BBO as SHG crystal are shown. Finally, the proceeding work and future work are discussed in the Chapter 8.

Chapter 2

Stimulated Raman Scattering

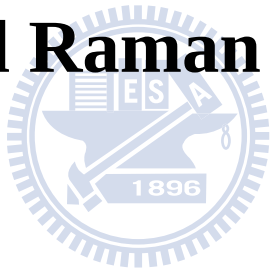

2.1 Raman Scattering

Spontaneous Raman scattering effect was first discovered by C. V. Raman in 1928 [1]. As illustrated in Fig. 2-1, an incident light illuminated a medium sample which can be a solid, liquid, or gas, and the scattered light is observed spectroscopically. A difference in frequency between incident and scattered monochromatic light was observed and it is dependent of the properties of molecular, not incident light. Raman and Krishnan had observed scattered light with smaller frequency in sixty kinds of liquids and vapors [2]. They confirm that the scattered light is a secondary form of scattering, not fluorescent, due to its relatively high intensity and polarization.

Raman scattering is a $\chi^{(3)}$, nonlinear inelastic light scattering process in which an incident photon interacts with a molecule of Raman medium. An incident photon is absorbed by a molecule of Raman medium and then emits a photon called Stokes photon with a lower energy as shown in Fig. 2-1(a). The Stokes shift leaves Raman medium in excited state. If the material is already in an excited state, then the scattered photon can be higher in energy called anti-Stokes photon as shown in Fig. 2-1(b). The anti-Stokes shift leaves Raman medium in ground state. The energy and momentum conversion are applied:

$$\hbar\omega_S = \hbar\omega_p \pm \hbar\omega_R \tag{2-1}$$

$$k_S = k_p \pm k_R \tag{2-2}$$

in which $\hbar$, ω, and k are the Planck's constant, angular frequency, and wavevector, and the subscripts S, p, R refer to the scattered photon, incident pump photon, and the phonon created or annihilated in the scattering process, respectively. The energy difference ($\hbar\omega_R$) between the incident photon and the scattered photon matches the rotation/vibration energy of a molecule in gas or liquid, or the phonon energy of a solid Raman medium. The wavelength of Stokes component is shifted to a longer wavelength than incident wavelength. One the other hand, the wavelength of anti-Stokes component is shifted to a shorter wavelength.

$(a)\ \omega_S = \omega_p - \omega_R$ => Stokes shift $(b)\ \omega_S = \omega_p + \omega_R \Rightarrow$ anti-Stokes shift

$\omega_S = \omega_p - \omega_R$ $\omega_S = \omega_p + \omega_R$

Fig. 2-1. Spontaneous Raman scattering with (a) Stokes photon generation ($\omega_S < \omega_p$) and (b) anti-Stokes photon generation ($\omega_S > \omega_p$)

The number of anti-Stokes photon is typically much smaller than the Stokes photon resulted from the smaller population of the excited state compared to ground state in the thermal equilibrium by the Boltzmann factor exp(-($\hbar\omega/k_B$T)), where k_B is

the Boltzmann constant and T is the temperature.

Stimulated Raman scattering (SRS) occurs when the intensity of the incident light is increased and then the scattered Raman field is enhanced. SRS was discovered by Woodbury and Ng in 1962 [3]. A near-infrared component at 766 nm was detected in the laser output of 694-nm Q-switched ruby laser with a nitrobenzene Kerr cell. The frequency shift coincides with the vibration frequency of the strongest Raman shift of nitrobenzene. Woodbury and Ng confirmed that the near-infrared component is resulted from SRS. As shown in Fig. 2-2, with both pump laser and Stokes photons illuminating on Raman medium, the medium experiences a transition from ground state E_i to virtual level and is left in the excited state E_f. As in spontaneous Raman scattering, the energy difference ($\hbar\omega_R$) coincide the properties of Raman medium expressed by:

$$\hbar\omega_R = E_f - E_i = \hbar(\omega_p - \omega_S) \tag{2-3}$$

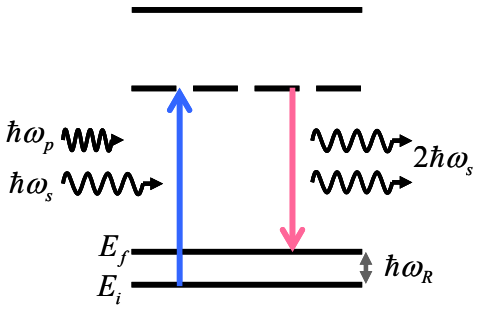

Fig. 2-2. Energy level diagram for Stimulated Raman scattering

SRS results in a stimulation of an additional Stokes photon coherent with the incident Stokes photons. Therefore SRS can generate more intense coherent radiation at new frequency. Stimulated Raman scattering (SRS) is an efficient and practical method of frequency conversion based on a third-order nonlinear optical process. If the intensity of incident light is sufficiently high, then the nonlinear optical phenomena occur. The induced polarization per unit volume P in a medium depends on the amplitude of the electric field of incident light E and can be expanded in a series of power of E:

$$P = \varepsilon_O \chi^{(1)} \cdot E + \varepsilon_O \chi^{(2)} \cdot |E|^2 + \varepsilon_O \chi^{(3)} \cdot |E|^3 + \cdots \tag{2-4}$$

where ε_0 is the dielectric constant, $\chi^{(1)}$ is the linear optical susceptibility and $\chi^{(2)}$, $\chi^{(3)}$ are the second-, third-order nonlinear optical susceptibility of the medium. The nonlinear polarization terms become more and more significant with increasing the amplitude of the electric field. The term containing $\chi^{(2)}$ is responsible for second-order nonlinear optical effect including second harmonic generation (SHG), sum frequency generation (SFG), difference frequency generation (DFG), and optical parametric amplification (OPO). The term containing $\chi^{(3)}$ is responsible for third-order nonlinear optical effect including SRS, stimulated Rayleigh scattering, stimulated Brillouin scattering, self-focusing, self-mode-locking. The phenomenon of competition between SRS and self-focusing usually occurs in a high-power intracavity Raman laser. Therefore the optimum mode size in the self-Raman medium is subject to a compromise between lowering the SRS threshold and avoiding optical damage induced by self-focusing [4]

If the intensity of first-Stokes photon is sufficiently high, then it can act as a pump source for the second-Stokes photon. Therefore the second-Stokes component will be generated and possibly higher order as shown in Fig. 2-3. The energy conversion for n[th]-order Stokes emission is applied:

$$\hbar\omega_{s(n)} = \hbar\omega_p - n\hbar\omega_R \tag{2-5}$$

The n[th]-order Stokes wavelength $\lambda_{s(n)}$ is expressed by:

$$\frac{1}{\lambda_{s(n)}} = \frac{1}{\lambda_p} - n \times \nu_R \tag{2-6}$$

where λ_p is the incident pump wavelength, $\nu_R=\omega_R/c$ is the Raman shift of Raman medium, and c is the light speed in Raman medium. With a suitable output coupler whose coating is designed to suit the Stokes wavelengths, the qusi-continuous tunable Raman laser could be achieved by using a Raman medium with a low Raman shift.

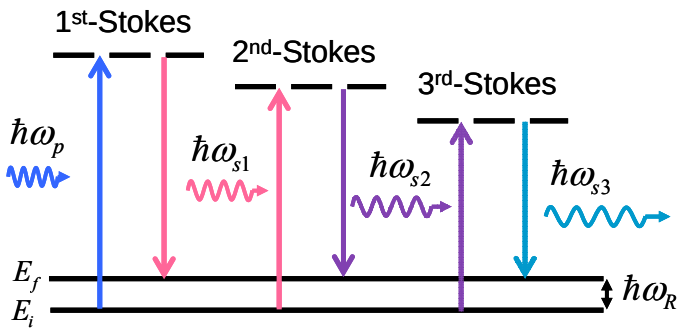

Fig. 2-3. Energy level diagram for high-order Raman emission

2.2 Raman Media

Spontaneous Raman scattering was discovered by Raman in 1928 and was widely applied in spectroscopy. In 1962, the first observation of SRS was made after the discovery of laser which can provide the high peak powers required for SRS. Raman media include liquids, gases, and solids. In 1963, the crystalline Raman media including diamond (C), calcite (CaCO3) and α-sulfur (S) were used for frequency conversion and the properties are summarized in table 2-1 [5]. Although SRS in crystalline media has been proposed for over 40 years, there has been a resurgence of interest in solid-state Raman lasers due to the discovery and development of new Raman crystals. In particular, the high conversion efficiency up to 77% was demonstrated by use of $LiIO_3$ Raman crystal in arclamp pumped Nd:YALO laser in 1977 [6]. Currently, the crystals commonly used for SRS are $LiIO_3$, $Ba(NO_3)_2$, $BaWO_4$, $KGd(WO_4)_2$, and $PbWO_4$ listed in table 2-2 [7-11].

Material	Raman shift (cm^{-1})	Raman linewidth (cm^{-1})	Cross section (a.u.)
diamond	1333	2.7	100
calcite	1086	1.2	6
α-sulfur	216		

Table 2-1. Spectroscopic characteristics of Raman-active materials diamond, calcite, and α-sulfur [5].

Raman crystals with good thermal and mechanical properties, high Raman gain, high optical damage threshold, high transmission at the pump and Stokes wavelengths have considerable potential for frequency conversion of SRS. The thermal properties are important because the heat generated through inelastic SRS process is accumulated in a Raman crystal. In high-power operation, the thermal effects become critical issues for the SRS process and the property of high damage threshold is helpful for practical purposes. Higher Raman gain corresponds with a lower SRS threshold. The higher transmission at the pump and Stokes wavelengths results in less cavity loss.

Material	Raman shift (cm^{-1})	Raman linewidth (cm^{-1})	Cross section (arb. units)	Raman gain (cm/GW)	Damage threshold (GW/cm^2)
$LiIO_3$	822	5	54	4.8(1064 nm)	~ 0.1
$Ba(NO_3)_2$	1047	0.4	21	47 (532 nm) 11 (1064 nm)	~ 0.4
$BaWO_4$	924	1.6	52	8.5 (1064 nm) 40 (532 nm)	~ 5
$KGd(WO_4)_2$	768 901	6.7 5.7	59 54	4.4 (1064 nm) 11.8 (532 nm) 3.3 (1064 nm)	~ 10
$PbWO_4$	904	4.7		3.1 (1064 nm) 8.4 (532 nm)	~ 1

Table 2-2. Spectroscopic characteristics of the Raman-active materials $LiIO_3$, $Ba(NO_3)_2$, $BaWO_4$, $KGd(WO_4)_2$, and $PbWO_4$ [7-11].

Recently, potassium titanyl phosphate (KTP), rubidium titanyl phosphate (RTP), and potassium titanyle arsenate (KTA) which are widely recognized as prominent

nonlinear optical crystals involving nonlinear optical susceptibility $\chi^{(2)}$ have been experimentally confirmed to be practical SRS converter devices [12-16]. It has been demonstrated that the low value of the KTP-related Stokes shift (270 cm^{-1}) [17] and KTA-related Stokes shift (234 and 671 cm^{-1}) [18] permit generation of multi-frequency radiation with cascade SRS [12, 19-20]. The Raman spectrum of RTP measured by Carvajal shows the dominant RTP Stokes shift at 260 cm^{-1} [21]. Our own measured spontaneous Raman spectra of KTP, RTP, and KTA crystals are shown in Fig 2.4 and their Raman shift (Stokes shift) and Raman linwidth are summarized in table 2-4. Our measured results are consistent with Raman spectra reported in Ref. [17, 18, and 21].

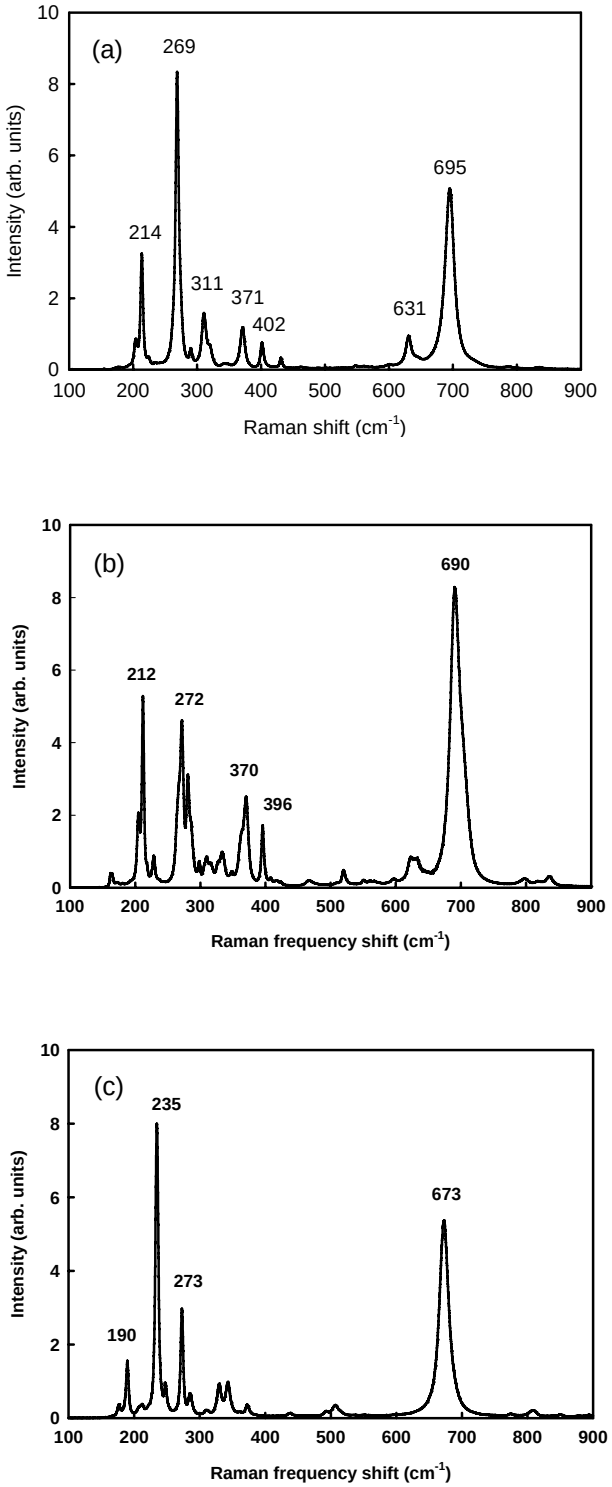

Fig. 2-4. Spontaneous Raman spectrum of (a) KTP (b) RTP and (c) KTA

Material	Raman shift (cm^{-1})	Raman linewidth (cm^{-1})
KTP	214	4.8
	269	6.2
	311	9.6
	371	8.8
	402	6.22
	631	12.2
	695	16.9
RTP	212	4
	272	10.1
	370	13.4
	396	4.7
	690	20.9
KTA	190	4.7
	235	5.4
	273	4.7
	673	16.8

Table 2-3. Measured characteristics of the Raman-active materials KTP, RTP and KTA.

Nd-doped YVO_4 and $GdVO_4$ crystals have been identified as useful materials for diode-pumped solid-state lasers due to its high absorption coefficient and large thermal conductively [22-25]. In 2001, it was predicted that the new Raman crystals yttrium othovanadate (YVO_4) and gadolinium othovanadate ($GdVO_4$) would be promising Raman media [26]. Therefore, YVO_4 and $GdVO_4$ crystals become highly attractive self-Raman laser media based on combinations of their stimulated-emission and SRS properties. The Raman gain coefficients of YVO_4 and $GdVO_4$ crystals at the most intense peaks 890 and 882 cm^{-1}, respectively, were found to be greater than 4.5 cm/GW with a linewidth around 3 cm^{-1} summarized in table 2-4 [26]. In addition, our

own measured spontaneous Raman spectra of YVO_4 and $GdVO_4$ crystals are shown in Fig 2.5 and their Raman shift and Raman linwidth are summarized in table 2-5. Our measured results agree with that reported in Ref. [26].

Material	Raman shift (cm^{-1})	Raman linewidth (cm^{-1})	Cross section (arb. units)	Raman gain (cm/GW)	Damage threshold (GW/cm^2)
YVO_4	890	2.6	92	> 4.5 (1064 nm)	~ 1
$GdVO_4$	882	3	92	> 4.5 (1064 nm)	~ 1

Table 2-4. Summary characteristics of the Raman-active materials YVO_4, and $GdVO_4$ [26].

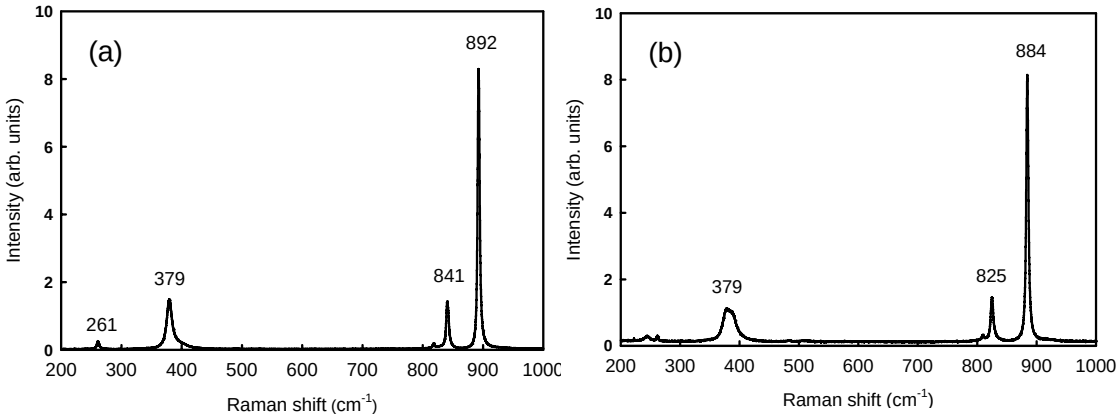

Fig. 2-5. Spontaneous Raman spectrum of (a) YVO_4, and (b) $GdVO_4$.

Material	Raman shift (cm^{-1})	Raman linewidth (cm^{-1})
YVO_4	261 379 841 892	4.8 10.5 5 4
$GdVO_4$	379 825 884	26 5.7 4.4

Table 2-5. Measured characteristics of the Raman-active materials YVO_4, and $GdVO_4$.

2.2.1 Raman Gain Coefficient

Raman gain of crystal Raman medium is proportional to the exponential of Raman crystal length and Raman gain coefficient. For a single-pass Raman generator, the pump laser is spontaneously scattered to be amplified scattered Stokes light after passing through a Raman medium. The Stokes intensity grows as [27]

$$I_S(l) = I_S(0)\exp(g_s I_p l) \tag{2-7}$$

where l is the Raman crystal length, $I_s(0)$ is the Stokes intensity at the crystal surface, I_p is the pump intensity, and g_S is the Raman gain coefficient which is given by

$$\frac{g_s}{I_p} = \frac{\lambda_p \lambda_S^{\,2} N}{\hbar c \pi n_S^{\,2}} \left(\frac{d\sigma / d\Omega}{\Delta v_R} \right) \tag{2-8}$$

where λ_p and λ_S is the pump and Stokes wavelength, respectively, N is the number density of molecules, $d\sigma/d\Omega$ is the Raman scattering cross section, Δv_R is the half-maximum Raman linewidth, $\hbar$ is the Planck's constant, c is the velocity of light

in vacuum, n_S is the refractive index of Raman medium at λ_S. Raman gain coefficient is proportional to the Raman scattering cross section and is inversely proportional to the Raman linewidth. In addition, Raman gain coefficient decreases substantially with increasing temperature above room temperature [28]. For example, the Raman spectra of silicon crystal for various temperatures are shown as Fig. 2-6 [29].

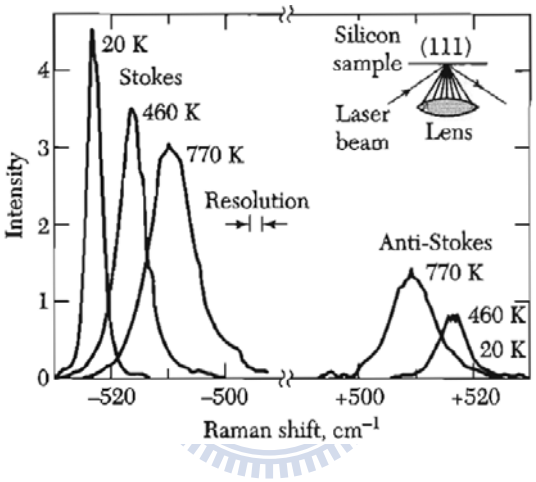

Fig. 2-6. Raman spectra of silicon crystal [29]

2.3 Solid-State Raman Laser Configuration

Solid-state Raman lasers have been realized in Raman generation, extracavity, intracavity, and coupled cavity configurations [30-33]. In our experiments, we use diode-end-pumped intracavity configuration in which the pump laser and Raman crystal are placed in the same cavity as shown in Fig. 2-7. The configuration of diode-pumped solid-state intracavity Raman laser has advantages on compactness, low SRS threshold, and high efficiency. If the laser crystal can simultaneously serve as a Raman crystal, the intravavity self-Raman laser without an additional Raman crystal is more compact. The Q-switch device (acousto-optic or electro-optic) is used to generate high peak power pulse to reach the SRS threshold. The front mirror has high-reflection coating at the fundamental and Stokes wavelengths and high-transmission coating at the diode wavelength. The output coupler is designed to suit the lasing Stokes wavelengths with high-reflection coating (high-Q) at fundamental wavelength and partial-reflection coating at lasing Stokes wavelength.

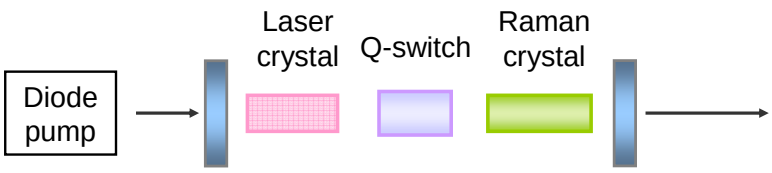

Fig. 2-7. Schematic diagram of a diode-pumped solid-state intracavity Raman laser.

Combining SRS with SHG or SFG can generate the solid-state laser source at new wavelengths in the spectral range of visible and UV light [33]. The diode-end-pumped solid-state laser with intracavity SRS and SHG/SFG we used in our experiments is shown as Fig. 2-8. The front mirror has high-reflection coating at the fundamental, Stokes, and SHG/SFG wavelengths and high-transmission coating at the diode wavelength. The output coupler is designed to suit the SHG/SFG wavelengths with high-reflection coating (high-Q) at fundamental and Stokes wavelengths and partial-reflection coating at SHG/SFG wavelength.

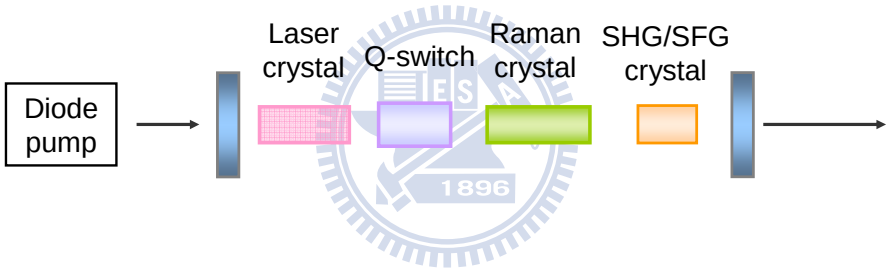

Fig. 2-8. Schematic diagram of a diode-pumped solid-state laser with intracavity SRS and SHG or SFG.

The mode size of laser beam is designed to lower the SRS threshold, maximize the conversion efficiency, and avoid optical damage induced by self-focusing. However, for self-Raman laser, the optimum mode size in the self-Raman medium is subject to a compromise between maximizing the conversion efficiency and avoiding optical damage induced by self-focusing [34].

2.4 Modeling Investigation of Q-Switched Intracavity Raman Laser

In Q-switched operation, the rate equations for intracavity Raman laser at first-Stokes wavelength can be expressed by [35, 36]

$$\frac{\mathrm{d}n}{\mathrm{d}t} = -\gamma\sigma c\varphi_{\mathrm{L}} n \tag{2.4.1}$$

$$\frac{\mathrm{d}\varphi_{\mathrm{L}}}{\mathrm{d}t} = \frac{2\varphi_{\mathrm{L}}}{t_{\mathrm{RT}}}[\sigma n l_{\mathrm{L}} - gh\nu_{\mathrm{R1}} c\varphi_{\mathrm{R1}} l_{\mathrm{R}}] - \frac{\varphi_{\mathrm{L}}}{t_{\mathrm{L}}} \tag{2.4.2}$$

$$\frac{\mathrm{d}\varphi_{\mathrm{R1}}}{\mathrm{d}t} = \frac{2\varphi_{\mathrm{R1}}}{t_{\mathrm{RT}}} hcl_{\mathrm{R}}[g_{\mathrm{R1}}\nu_{\mathrm{R1}}\varphi_{\mathrm{L}} - g_{\mathrm{R2}}\nu_{\mathrm{R2}}\varphi_{\mathrm{R2}}] - \frac{\varphi_{\mathrm{R1}}}{t_{\mathrm{R1}}} \tag{2.4.3}$$

$$\frac{\mathrm{d}\varphi_{\mathrm{R2}}}{\mathrm{d}t} = \frac{2\varphi_{\mathrm{R2}}}{t_{\mathrm{RT}}} hcl_{\mathrm{R}}[g_{\mathrm{R2}}\nu_{\mathrm{R2}}\varphi_{\mathrm{R1}} - g_{\mathrm{R3}}\nu_{\mathrm{R3}}\varphi_{\mathrm{R3}}] - \frac{\varphi_{\mathrm{R2}}}{t_{\mathrm{R2}}} \tag{2.4.4}$$

, where n is the population inversion density of laser medium and σ is the stimulated emission cross section of the laser medium. φ_{L} and φ_{Rn} are the intracavity photon density of fundamental and n$^{\mathrm{th}}$-Stokes photons inside the laser cavity, respectively. $t_{\mathrm{RT}}=2l_C/c$ is the round-trip transit time in the cavity of optical length lc, c is the light speed in vacuum, γ is the inversion-reduction factor, $t_{\mathrm{L}}=t_{\mathrm{RT}}/(L_{\mathrm{L}}-\ln(R_{\mathrm{L}}))$ and $t_{\mathrm{Rn}}=t_{\mathrm{RT}}/(L_{\mathrm{Rn}}-\ln(R_{\mathrm{Rn}}))$ are intracavity lifetimes of the fundamental and n$^{\mathrm{th}}$-Stokes photons, respectively. R_{L}, R_{Rn} and L_{L}, L_{Rn} are the reflectivities of output coupler and loss inside the cavity at fundamental and n$^{\mathrm{th}}$-Stokes wavelengths, respectively. l_{L} and l_{R} are the lengths of laser and Raman medium, respectively. g_{Rn} is the Raman gain

coefficient of n^{th}-Stokes component , h is the Plank constant, and v_{Rn} is the frequency of n^{th}-Stokes photon. When pump energy is sufficient to reach Raman gain, it is rapidly converted to the first-Stokes pulse. Stokes pulse with is often much shorter than the fundamental pulse. The second-Stokes pulse can be produced as the intensity of first-Stokes pulse is sufficient to pump it, and possibly higher-order.

The energy of Raman laser can be obtain by integrating the output power over time as follows [36]

$$E_{Rn} = \int_0^{t_{Rn}} P_{out} dt = \frac{S c h v_{Rn}}{2} \ln(\frac{1}{R_{Rn}}) \int_0^{t_{Rn}} \varphi_{Rn} dt \qquad (2.4.5)$$

where t_{Rn} is the Raman pulse duration and S is the cross section of Raman beam in the cavity. The Raman pulse with is the same as the width of Stokes photon density φ_{Rn}.

2.5 The Most Common Spectral Coverage of Solid-State Raman Laser

2.5.1 Infrared Raman laser

The output wavelength of Raman laser is determined by the wavelength of the fundamental pump laser and the Raman spectrum of the Raman medium. Most solid-state Raman lasers have been pumped by Nd lasers operating at fundamental wavelength near 1.06 or 1.32 μm. For Nd-doped Raman laser with commonly used Raman crystal (Raman shift: 800-900 cm^{-1}) such as $Ba(NO_3)_2$ [37], $Ba(WO_4)_2$ [38], $KGd(WO_4)_2$ [39] and so on, the spectral coverage from 1.1 to 1.3 μm and from 1.4 to 1.55 μm can be achieved with the fundamental wavelength near 1.06 and 1.32 μm, respectively. Since water absorption in eye tissue and the intraocular fluid prevents light in the spectral range of 1.4-1.8 μm from reaching the retina as shown in Fig. 2-9(d), there is a considerable interest in compact laser source with wavelengths in this eye-safe regime. The applications of eye-safe lasers include remote-sensing, atmospheric science, and laser range-finder, etc..

The radiation with wavelengths shorter than 315 nm and greater than 1.9 μm is completely absorbed by the cornea of the eye as shown in Fig. 2-9(a). The radiation between 315 and 400 nm is absorbed at the lens as shown in Fig. 2-9(b). The radiation between 400 to 700 nm is focused on the retina and represents the greatest hazard.

The radiation between 700 to 1400 nm is partially absorbed before it reaches the retina as shown in Fig. 2-9(c). As shown in Fig. 2-9(d), the radiation between 1.4-1.8 μm is absorbed by the cornea and aqueous humor and it can not reach the retina.

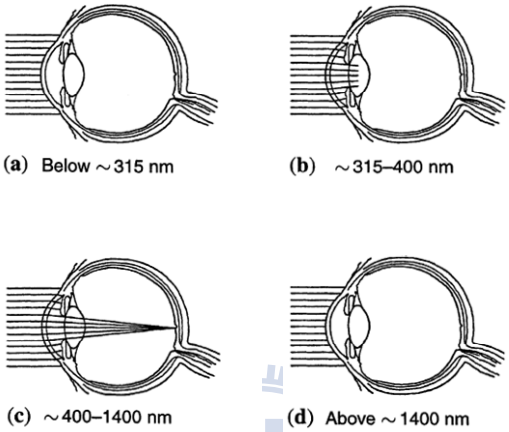

Fig. 2-9. Spectral transmission characteristics of a human eye exposed to laser radiation with wavelength (a) below 345 nm (b) between 315 to 400 nm (c) between 400 to 1400 nm and (d) above 1400 nm [40]

2.5.2 Visible/Ultraviolet Raman Laser

Combining SRS with SHG or SFG, the new laser sources in the spectral region of visible and UV light have been successfully generated as shown in Fig. 2.10 [33]. More interestingly and importantly, yellow lights are useful for biomedicine, ophthalmology, dermatology, and laser guide stars. The applications of visible and ultraviolet lasers include laser bathymetry, underwater detection, and biological detection.

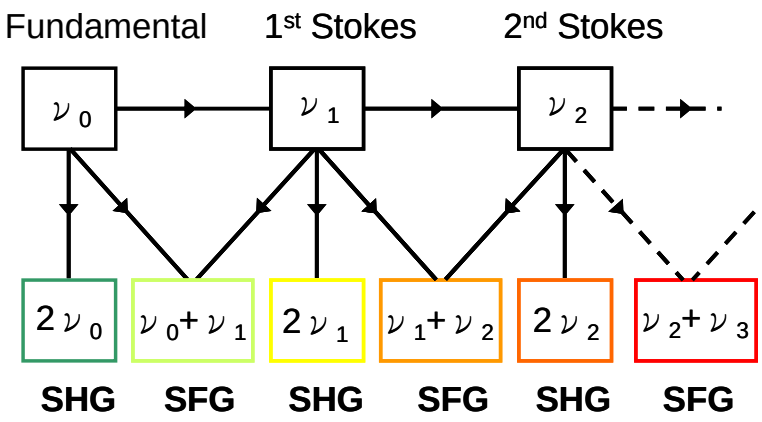

Fig. 2-10. Diagram showing the selectable frequency of a laser combining cascaded SRS emission and SHG/SFG with a fundamental laser of frequency ν_0.

Chapter 3

The Influence of Thermal Lensing Effect

3.1 Thermal Lensing Effect

Diode-pumped solid-state laser has been adopted widely due to its compactness, high efficiency, and reliability [1]. Comparing with a diode-side-pumped configuration, the smaller laser beam waist, higher density of pump power, and inhomogeneous heating make thermal lensing effect become a serious problem in a diode-end-pumped configuration. The localized absorption of pump power in a laser crystal leads heat converted from pump power to accumulate near the pumped facet of laser crystal. The nonuniform temperature distribution of laser crystal is represented by a parabolic-logarithmic function [2]. The temperature-dependent variation of refractive index and the end bulging effect make laser crystal act as a thermal lens [3]. Owing to the nonuniform temperature distribution the temperature gradients accrue stress that could bring thermal fracture under high pump power operation [3]. There exists a fracture-limited pump power for laser crystal that makes scaling to a higher average power be restricted [4]. For a diode-end-pumped solid-state laser, the laser performance including laser stability, maximum achievable average power, efficiency, and degradation of laser beam quality is significantly influenced by thermal lensing effect [5-7]. Therefore, promotion of laser performance can be accomplished by efficient reduction of thermal lensing effect.

According to the theoretical thermal modeling of CW end-pumped solid-state laser presented by Innocenzi *et al*., the effective focal length can be approximately expressed by [8]

$$f_{th} = \frac{\pi K \omega_p^{\,2}}{\xi\, P_{in}(dn/dT)}\left[\frac{1}{1-\exp(-\alpha\, l_a)}\right] = \frac{C\omega_p^{\,2}}{P_{in}} \tag{3-1}$$

where K is the thermal conductivity, ω_p is the pump-beam radius in the active medium in the unit of mm, ξ is the fractional thermal loading, P_{in} is the pump power in the unit of watt (W), (dn/dT) is the thermal-optical coefficient of n, α is the absorption coefficient, l_a is the length of the active medium, C is a proportional constant in the unit of W/mm. End-pumped solid state laser cavity can be designed to optimize the laser performance by determining the focal length of thermal lens. Several methods for determining the focal length of thermal lens in diode-end-pumped laser crystal have been presented [9-14].

In the past few years, employing a composite crystal with nonabsorbing undoped end has been regarded as a promising method for cooling the laser crystal to improve the laser performance of diode-pumped solid state laser [15-23]. With the reduction of temperature and stress, a more uniform longitudinal temperature distribution can be generated to bring out a higher fracture-limited pump power and a higher average power.

3.2 Comparison of Thermal Lensing Effects between Single-End and Double-End Diffusion-Bonded Nd:YVO_4 Crystals for $^4F_{3/2}\rightarrow{}^4I_{11/2}$ and $^4F_{3/2}\rightarrow{}^4I_{13/2}$ Transitions

Nd:YVO_4 crystal has been seen as an excellent laser material for diode-pumped solid-state laser due to its broad absorption bandwidth and large laser emission cross section at the $^4F_{3/2}\rightarrow{}^4I_{11/2}$ (1064 nm) and $^4F_{3/2}\rightarrow{}^4I_{13/2}$ (1342 nm) transitions. In this work, we measure the focal lengths of thermal lens of one conventional and two types of composite Nd:YVO_4 crystal for the 1064- and 1342-nm transitions. One composite Nd:YVO_4 crystal is bounded with an undoped end at its pumped facet, and the other composite crystal is bounded with undoped ends at its two facets. The composite crystals are fabricated by the method of diffusion-bonding with high quality on the interface. The simple setup of continuous-wave (CW) laser is utilized to measure the focal length of thermal lens under easy operation. While the cavity length is increased to the critical cavity length, the thermal lensing effect leads the laser cavity to become unstable. By finding the critical cavity length, the effective focal length of thermal lens can be worked out. We observe that the stronger thermal lensing effect in Nd:YVO_4 crystal for the 1342-nm transition than that for the 1064-nm transition due to the higher thermal loading accompanying the lower conversion efficiency. The power performance, focal lengths of thermal lens and thermal lensing effects for the three types of Nd:YVO_4 crystal for the 1064 and 1342 nm transitions will be discussed in this work.

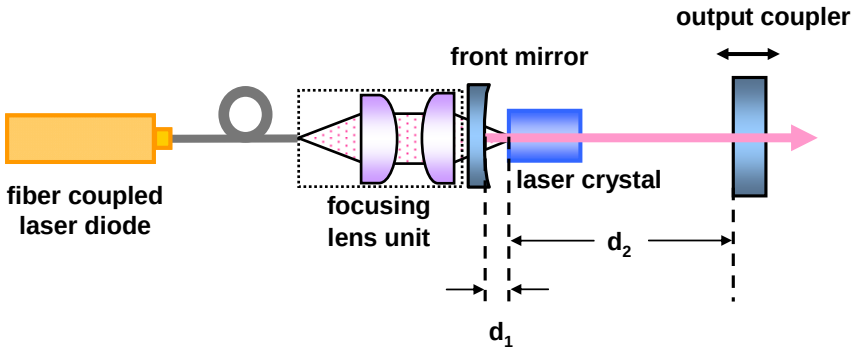

Fig. 3-1. Experimental setup of a diode-end-pumped Nd:YVO_4 CW laser for measuring the effective focal length of thermal lens in the laser crystal.

3.2.1 Experimental Setup

The experimental setup shown in Fig. 3-1 for measuring effective focal lengths of thermal lens in a diode-end-pumped laser crystal is the setup of normal CW Nd:YVO_4 laser. The output coupler connected with a stepper motor can be moved in the longitudinal direction to change the cavity length. The cavity length can be changed from 2.5 to 50 cm by controlling the stepper motor. The laser crystal is pumped by an 808-nm fiber-coupled laser diode with a core diameter of 0.8 mm, a numerical aperture of 0.16, and the maximum output power was 22 W. The pump beam is reimaged into the laser crystal and the radius was about 0.4 mm. The laser crystal is wrapped in indium foil and mounted on water-cooled copper blocks. The water temperature is maintained at 17^{o}C. The entrance face of the 500-mm radius-of-curvature concave front mirror is coated for antireflection at the pump wavelength of 808nm (R<0.2%) and the other face is coated for high-transmission at 808 nm (T>90%) as well as high-reflection (R>99.8%) at the lasing wavelength. In

this work, we consider the thermal lensing effect for the diode-end-pumped CW Nd:YVO_4 lasers operated at 1064 and 1342 nm. The individual coatings of front mirrors and output couplers are required for achievement of different lasing wavelengths. The two flat output couplers have the reflectance of 88% at 1064 and 92% at 1342 nm used for CW 1064 and 1342 nm lasers, respectively.

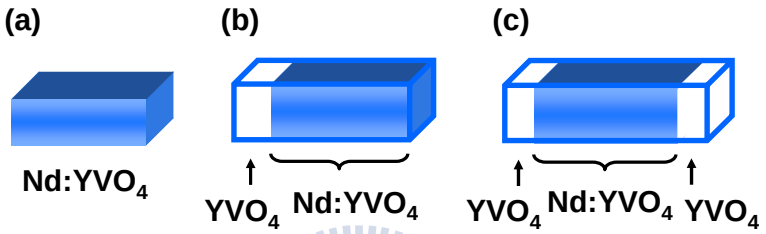

Fig. 3-2. The three types of laser crystal with different structures. (a) Conventional Nd:YVO_4 crystal. (b) Diffusion-bonded Nd:YVO_4 crystal with single end at its pumped facet (YVO_4-Nd:YVO_4). (c) Diffusion-bonded Nd:YVO_4 crystal with double end (YVO_4-Nd:YVO_4-YVO_4).

Figure 3-2 shows the three types of a-cut Nd:YVO_4 laser crystal employed in this work. Fig. 3-2(a) shows a 3 mm × 3 mm × 9 mm, 0.27-at.% Nd:YVO_4 crystal. Fig. 3-2(b) shows a 4 mm × 4 mm × 12 mm diffusion-bonded crystal called YVO_4-Nd:YVO_4 with single 2.7-mm-long undoped end at the pumped facet of 0.3-at.% active Nd:YVO_4 crystal. Fig. 3-2(c) shows a 4 mm × 4 mm × 14 mm diffusion-bonded crystal called YVO_4-Nd:YVO_4-YVO_4 with double 2.1-mm-long undoped ends bonded to the both facets of 0.3-at.% active Nd:YVO_4 crystal. The Nd concentration is measured by the company supplying the crystals. Both sides of the three crystals are coated for antireflection at 1064 and 1342 nm (R<0.2%).

3.2.2 Experimental Results and Discussions

The laser performance of diode-end-pumped solid-state laser is strongly affected by thermal lensing effect. Figure 3-3 and Fig. 3-4 depict experimentally measured average CW power of 1064 and 1342 nm with respect to the cavity length for the three types of Nd:YVO_4 crystal under individual pump power, respectively. The sign of P_{in} in the Fig. 3-3 and Fig. 3-4 means the input pump power. The average CW power is optimized at the cavity length of 2.5 cm with pump power of 8.32 and 7.61 W for 1064 and 1342 nm, respectively. In order to make sure that the transverse mode is the TEM_{00} mode without high-order mode, the optimization is done near the pump threshold. Note that while the cavity length is increased and the power is decreased rapidly, optimizing average power is not allowed. It is because the extraordinary high-order mode may compensate the power decay from thermal lensing effect.

While the cavity length is increased to a critical cavity length, the strong thermal lensing effect causes the laser cavity to become unstable. The relationships between average CW output power and cavity length are shown as Fig. 3-3 and Fig. 3-4. The maximum power at short cavity of the conventional crystal is much lower than that of the other two composite crystals mainly due to the difference in dopant concentration. The critical cavity length is determined based on unified criterion that the output power is dropped to the 70% of maximum power at the stable (short) cavity. The corresponding focal length of thermal lens f_{th} is expressed by [24]

$$\frac{1}{f_{th}} = \frac{1}{d_2 + l\left(\frac{1}{n} - 1\right)} - \frac{1}{r - d_1} \tag{3-2}$$

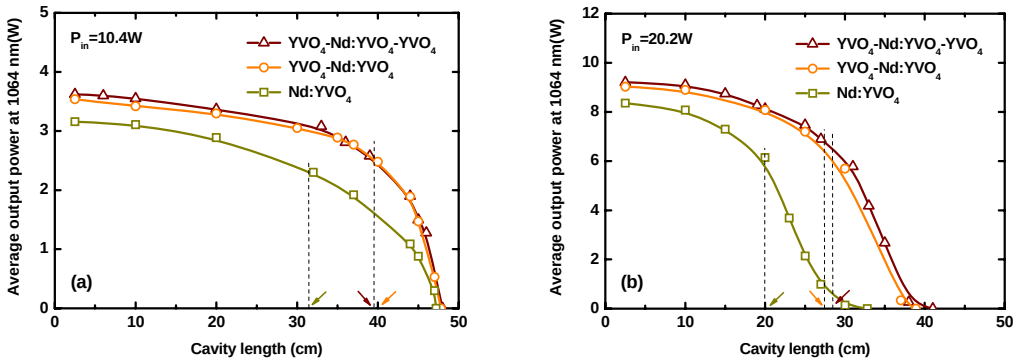

Fig. 3-3. Experimentally measured average CW output power of 1064 nm with respect to the cavity length for the three types of Nd:YVO_4 laser crystal with an input pump power (a) Pin=10.4 W (b) Pin=20.2 W. The arrows indicate the locations of critical cavity length.

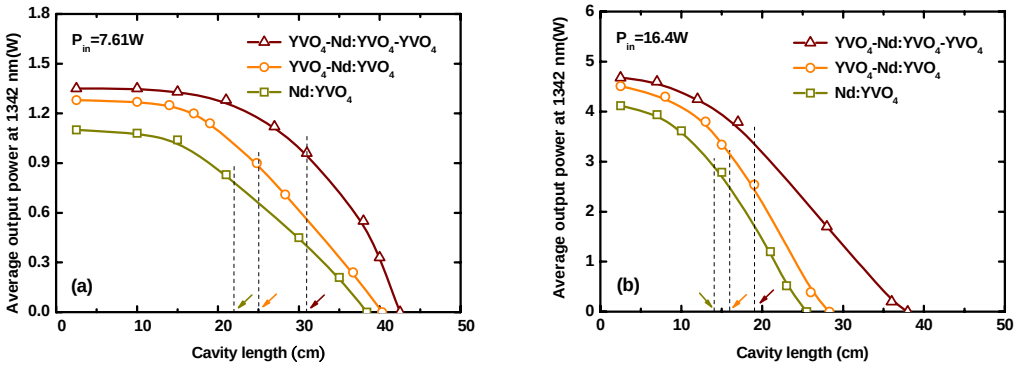

Fig. 3-4. Experimentally measured average CW output power of 1342 nm with respect to the cavity length for the three types of Nd:YVO_4 laser crystal with an input pump power (a) Pin=7.61 W (b) Pin=16.4 W. The arrows indicate the locations of critical cavity length.

where d_1 and d_2 are the distances from the pumped facet of laser crystal to the front mirror and output coupler, respectively, l is the length of the laser crystal, n is the refractive index of the laser crystal, r is the radius of curvature of the front mirror. d_1 is around 2.4, 1.1, and 1.6 mm for conventional Nd:YVO_4, composite YVO_4-Nd:YVO_4, and YVO_4-Nd:YVO_4-YVO_4, respectively, and is fixed during the experiments. We substitute the critical cavity lengths in terms of d_1 and d_2 into the Eq. (3-2) to get the effective focal lengths of thermal lens f_{th}. Even though this easy experimental method can not give an absolutely accurate f_{th}, the relative precision is sufficient to make comparison of thermal properties.

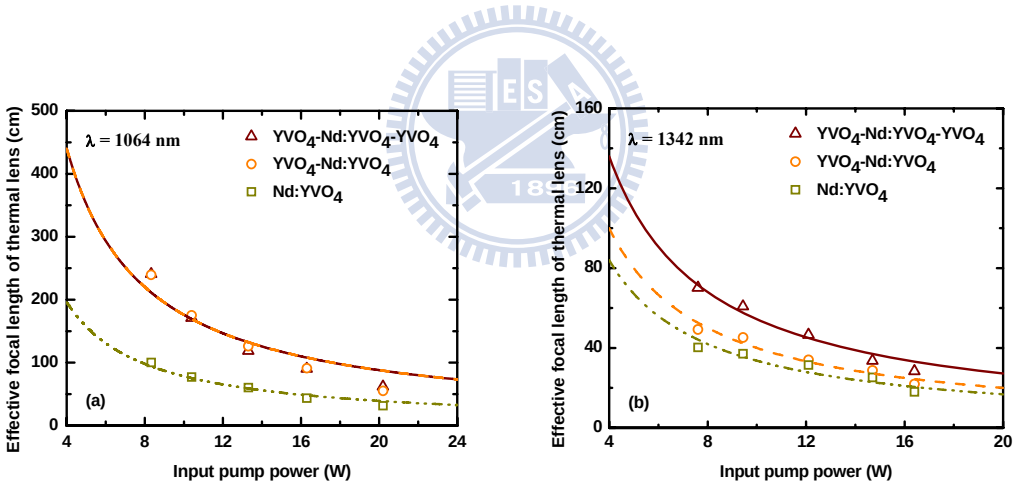

Fig. 3-5. The relationship between the effective focal length of thermal lens and the input pump power for three types of Nd:YVO_4 crystal operated at (a) 1064 and (b) 1342 nm. The symbols represent experimental data and the curves are theoretical fitted results.

The experimentally obtained f_{th} are plotted as symbols in Fig. 3-5. Because the thermal conductivity of YVO_4 in the b- and c-axis of 5.1 and 5.23 W/(mK) are very close, respectively, it can be seen as a radial symmetry thermal model [4]. The

Innocenzi model for rod-type crystal is available here. The Eq. (3-1) is used to fit the experimental data and the theoretical fitted curves with the approximate corresponding constants *C* are depicted in Fig. 3-5. The constants *C* of the conventional Nd:YVO_4, composite YVO_4-Nd:YVO_4, and YVO_4-Nd:YVO_4-YVO_4 for the 1064-nm transition are 4.9×10^4, 11×10^4, and 11×10^4 W/mm, respectively. The constants *C* of the conventional Nd:YVO_4, composite YVO_4-Nd:YVO_4, and YVO_4-Nd:YVO_4-YVO_4 for the 1342-nm transition are 2.1×10^4, 2.5×10^4, and 3.4×10^4 W/mm, respectively. The bigger constant *C* which represents the longer focal length of thermal lens means the weaker thermal lensing effect. The increase of the pump power enhances the thermal lensing effect. With the equal pump power, the focal length of thermal lens for CW 1342-nm laser is shorter than that for CW 1064-nm laser due to the higher thermal loading. The higher thermal loading accompanying the lower conversion efficiency is mainly attributed to the higher quantum defect for the longer laser wavelength.

According to the above-mentioned constants *C*, it is proven that both the focal lengths of thermal lens in the YVO_4-Nd:YVO_4 and YVO_4-Nd:YVO_4-YVO_4 are increased by nearly 2.2-times that in the conventional Nd:YVO_4 for the 1064-nm transition. The focal lengths of thermal lens in the YVO_4-Nd:YVO_4 and YVO_4-Nd:YVO_4-YVO_4 are increased by nearly 1.2 and 1.6-times that in the conventional Nd:YVO_4 for the 1342-nm transition, respectively. Even though the ability of thermal diffusivity in a laser crystal with bigger cross section is inferior [17, 25], the focal lengths of thermal lens in the two composite Nd:YVO_4 crystals are longer than that in the conventional Nd:YVO_4 crystal. In addition, we discuss the

influence of different dopant concentration and the length of active medium on the thermal lens. The absorption coefficient α for a typical laser diode with the center wavelength of 808 nm is expressed by [4]

$$\alpha = 2 \cdot N_d \ (\text{mm}^{-1}) \tag{3-3}$$

where N_d is the Nd dopant concentration in the unit of %. The values of αl are 4.86, 5.58, and 5.88 for the conventional Nd:YVO_4, the composite YVO_4-Nd:YVO_4, and YVO_4-Nd:YVO_4-YVO_4, respectively. According to the Eq. (3-1), the bigger value of αl represents the shorter focal length of thermal lens. But the differences in the value of $(1-\exp(-\alpha l))^{-1}$ between the three crystals is below 0.5 % and could be ignored. Further, the influence of different cross section on the thermal diffusivity is small for edge cooling system. Even we consider the influence, the conventional crystal with small cross section would have better thermal diffusivity and the conclusion does not be changed. Therefore, it is seen that the improvement of thermal lensing effect contributed by employing the two diffusion-bonded Nd:YVO_4 crystals greatly overcomes the disadvantage of the bigger cross section.

The experimental results reveal that the thermal lensing effect in the YVO_4-Nd:YVO_4 is nearly equal to that in the YVO_4-Nd:YVO_4-YVO_4 for the highest efficient 1064-nm transition. Therefore only single 2.7-mm-long undoped end at the pumped facet of laser crystal is sufficient for improving the thermal lensing effect to increase the effective focal length of thermal lens to nearly 2.2 times that of the conventional Nd:YVO_4 crystal for CW 1064-nm laser. However, the improvement in thermal lensing effect of the YVO_4-Nd:YVO_4-YVO_4 with double 2.1-mm-long

undoped ends noticeably outperforms that of the YVO_4-Nd:YVO_4 with single 2.7-mm-long undoped end for the 1342-nm transition. As a result of the stronger thermal lensing effect for the 1342-nm transition, the double undoped ends bonded to the both facets of active medium are essential for assisting thermal diffusing to increase the effective focal length of thermal lens to nearly 1.6 times that of the conventional Nd:YVO_4 crystal.

3.3 Conclusion

The comparison of thermal lensing effects between diffusion-bonded YVO_4-Nd:YVO_4 and YVO_4-Nd:YVO_4-YVO_4 crystals with single- and double-end, respectively, is demonstrated by measuring the effective focal lengths of thermal lens. The both types of diffusion-bonded crystal can improve the thermal lensing effects of conventional Nd:YVO_4 crystal. The YVO_4-Nd:YVO_4 with single 2.7-mm-long undoped end is capable of accomplishing the improvement in thermal lensing effect of YVO_4-Nd:YVO_4-YVO_4 with double 2.1-mm-long undoped ends for the 1064-nm transition. However, the improvement of YVO_4-Nd:YVO_4-YVO_4 with double 2.1-mm-long undoped ends remarkably tower over that of YVO_4-Nd:YVO_4 with single 2.7-mm-long undoped end for the 1342-nm transition with higher thermal loading. Therefore YVO_4-Nd:YVO_4 and YVO_4-Nd:YVO_4-YVO_4 crystals can serve as promising substitutes for a conventional Nd:YVO_4 crystal to reduce thermal lensing effect and scale to a higher average power of diode-end-pumped CW Nd:YVO_4 lasers operated at 1064 and 1342 nm, respectively.

Chapter 4

Compact Efficient Intracavity Raman Laser with a Diffusion-Bonded Crystal

4.1 Introduction

In our experiments, it has been found that Raman laser performance is hindered by the thermal loading because the Raman gain coefficient decreases substantially with increasing temperature above room temperature [1]. In high-power operation, the laser crystal acts as a thermal lens because heat converted from pump power accumulates at the pumped end of laser crystal. In addition, the thermal loading generated through inelastic SRS process in Raman crystal resulted in second thermal lens. Therefore, thermal lensing effect is a significant issue for developing high-efficiency Raman lasers. The thermal lensing effects in $LiIO_3$, $BaNO_3$, and Nd:$GdVO_4$ Raman crystals have been investigated [2-5]. In chapter 3, it is experimentally verified that double-end diffusion-bonded Nd:YVO_4 crystal can serve as a promising substitutes for a conventional Nd:YVO_4 crystal to reduce the thermal lensing effect and improve the laser performance of diode-end-pumped CW lasers operated 1342 nm. In this chapter, a compact efficient Q-switched eye-safe Nd:YVO_4 Raman laser at 1525 nm and a high-efficiency Q-switched dual-wavelength Nd:YVO_4/BBO laser at 1176 and 559 nm are demonstrated with a double-end diffusion-bonded Nd:YVO_4 crystal employed as a self-Raman medium.

4.2 Compact Efficient Q-Switched Eye-Safe Laser at 1525 nm with a Double-End Diffusion-Bonded Nd:YVO_4 Crystal as a Self-Raman Medium

Since water absorption in eye tissue and the intraocular fluid prevents light in the spectral range of 1.4-1.8 μm from reaching the retina, there is a considerable interest in compact laser sources with wavelengths in this eye-safe regime. The methods of generating eye-safe laser include optical parametric oscillators [6-9], Er^{3+}, Cr^{4+}, and Yb^{3+} doped solid-state laser [10-12], and stimulated Raman scattering (SRS) [13-20]. SRS has been convinced to be a promising method for wavelength conversion in solid-state lasers [21-23]. The discovery of new Raman materials gives birth to the laser sources at new wavelengths. In the recent years, eye-safe lasers from SRS frequency conversion have been successfully demonstrated in several Raman materials such as $Ba(NO_3)_2$, Nd:YVO_4, Nd:$GdVO_4$, Nd:$SrWO_4$, Nd:$KGWO_4$, $BaWO_4$, and $PbWO_4$ [13-20]. The laser crystal simultaneously serving as a Raman crystal can provide the advantage of compactness and simplicity for an intracavity SRS laser [24]. The laser emission at wavelengths of 1176 and 1525 nm based on self-SRS action in 1064- and 1342-nm actively Q-switched Nd:YVO_4 laser have been reported, respectively [1, 14, 25]. However, the overall performance is hindered by the thermal effects because the Raman gain coefficient decreases substantially with increasing temperature above room temperature [1]. Therefore, to improve the thermal effects in

the gain medium is critically important for developing self-Raman solid-state lasers.

In the past few years, the thermal effects have been verified to be efficiently improved by using the so-called composite crystal as a gain medium [26-34]. The composite crystal is fabricated by the diffusion bonding of a doped crystal to an undoped crystal with the same cross section. To the best of our knowledge, the composite crystal has not been applied to the self-Raman laser systems. In this work, we employ a double-end diffusion-bonded Nd:YVO_4 crystal to investigate the output performance of the self-Raman laser at 1525 nm.

4.2.1 Experimental Setup

The experimental setup of a diode-pumped actively Q-switched eye-safe Raman laser employing a composite Nd:YVO_4 crystal is shown in Fig. 4-1. The laser crystal is an *a*-cut 4 mm × 4 mm × 20 mm double-end diffusion-bonded Nd:YVO_4 crystal bounded with one 2-mm-long undoped YVO_4 end at the pumped facet of 0.3-at.% Nd^{3+}-doped Nd:YVO_4 crystal and one 8-mm-long undoped YVO_4 end at the other facet. The laser crystal is supplied by Witcore Co., Ltd. With the 1342-nm fundamental pump wavelength, the wavelength of the first-Stokes component for the YVO_4 Stokes shift at 890-cm^{-1} can be calculated to be around 1525 nm. The front and output coupler are designed for the first-Stokes generation. Both sides of the laser crystal are coated for antireflection at 1330-1530 nm (R<0.2%). In addition, the laser crystal is wrapped with indium foil and mounted in a water-cooled copper block. The

water temperature is maintained at 22°C. The front mirror is a 500-mm radius-of-curvature concave mirror with antireflection coating at 808 nm on the entrance face (R<0.2%), high-transmission (HT) coating at 808 nm (T>90%), and high-reflection (HR) coating at 1342 and 1525 nm on the other face (R>99.8%). The output coupler is a flat mirror with high-reflection coating at 1342 nm and partial-reflection (PR) coating at 1525 nm (R=65%). The pump source is an 808-nm fiber-coupled laser diode with a core diameter of 600 μm, a numerical aperture of 0.16, and a maximum power of 17.2 W. The pump beam is reimaged at the laser active medium and the waist radius is nearly 250 μm. The 30-mm-long acousto-optic Q-switcher (NEOS Technologies) has antireflectance coatings at 1342 nm on both faces and is driven at a 27.12-MHz center frequency with 15.0 W of rf power. The overall laser cavity length is 75 mm.

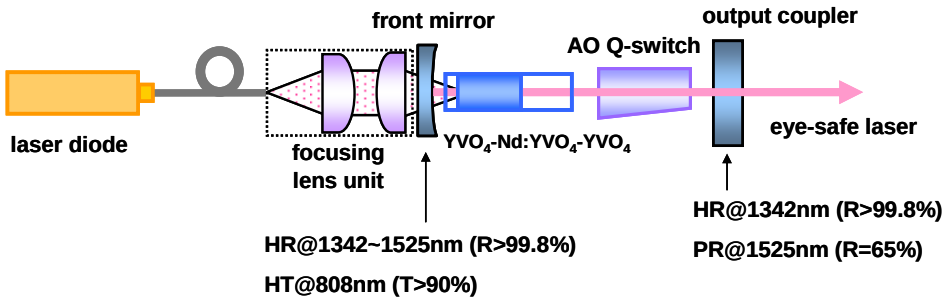

Fig. 4-1. Experimental setup of a diode-end-pumped actively Q-switched Nd:YVO_4 Raman laser.

4.2.2 Experimental Results and Discussions

We firstly use a simple laser setup for CW operation at 1342 nm to investigate the improvement of the thermal lensing effect in a double-end diffusion-bonded

Nd:YVO_4 crystal [35]. For this investigation an output coupler with partial reflection at 1342 nm is used instead of the above-mentioned Raman cavity output coupler. The optimum reflectivity of the output coupler is found to be approximately 92–94%. The effective focal lengths of the thermal lens are estimated based on the fact that the laser system will start unstable for a cavity length longer than the critical length related to the thermal lensing. Even though the absolute accuracy is not easily achieved, this method is confirmed to provide the high relative accuracy for the effective focal lengths of the thermal lens [35]. Figure 4-2 shows the experimental data and fitted lines of thermal lensing power in a conventional crystal and a double-end diffusion-bonded crystal with the same dopant concentration. It can be seen that the effective focal length in a double-end diffusion-bonded crystal is nearly 1.6 times that in a conventional Nd:YVO_4 crystal. As a result, the thermal effects can be substantiated to be significantly reduced in a double-end diffusion-bonded crystal.

When the Raman cavity output coupler is used in the laser cavity, the pumping threshold for the Raman laser output is found to be 2–3 W for the pulse repetition rates within 20-40 kHz. The beam quality factor is found to be better than 1.5 over the entire operating region. The spectrum of laser output is measured by an optical spectrum analyzer (Advantest Q8381A) employing a diffraction lattice monochromator with a resolution of 0.1 nm. As shown in Fig. 4-3, the optical spectrum for the actively Q-switched self-Raman output displayed that the fundamental laser emission is at 1342 nm and the Stokes component is at 1525 nm. The frequency shift between Stokes and laser lines is in good agreement with the optical vibration modes of tetrahedral VO_4^{-3} ionic groups (890 cm^{-1}) [36].

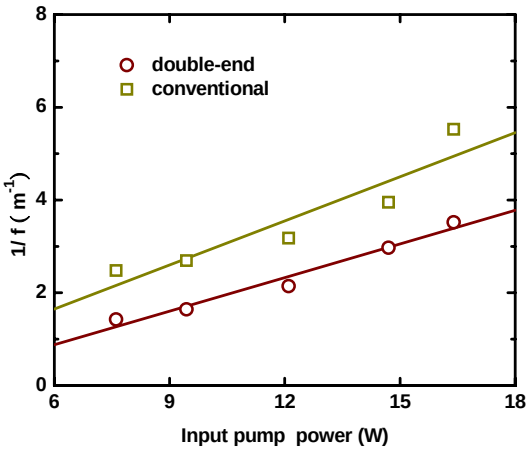

Fig. 4-2. Dependences of thermal lensing power on input pump power for conventional and double-end diffusion-bonded Nd:YVO_4 CW laser at 1342 nm.

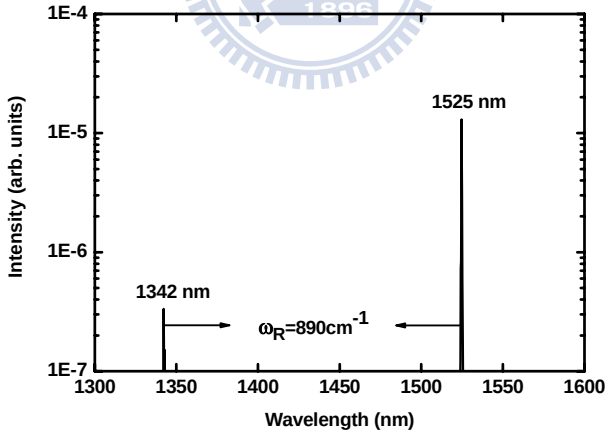

Fig. 4-3. Optical spectrum of the diode-pumped actively Q-switch Nd:YVO_4 self-Raman laser.

Figure 4-4 shows the experimental results of the average output power at 1525 nm with respect to the input pump power for the present self-Raman laser at pulse repetition rates of 20 and 40 kHz. For comparison, the previous results obtained by

Chen [14] with a conventional 0.2%-doped Nd:YVO_4 crystal at a repetition rate of 20 kHz is also depicted in the same figure. Note that there were no experimental data for a conventional 0.2%-doped Nd:YVO_4 crystal at a pulse repetition rate of 40 kHz because of the high lasing threshold. It can be seen that the Raman lasing threshold for a double-end diffusion-bonded Nd:YVO_4 crystal is approximately 2.0 W that is substantially lower than the lasing threshold of 8.5 W for a conventional Nd:YVO_4 crystal at the repetition rate of 20 kHz. Moreover, the lasing threshold at a pulse repetition rate of 40 kHz for present self-Raman laser is below 3.0 W. A rather low lasing threshold for high pulse repetition rates comes from the fact that the undoped part of the composite crystal increases the interaction length and then enhances the Raman gain.

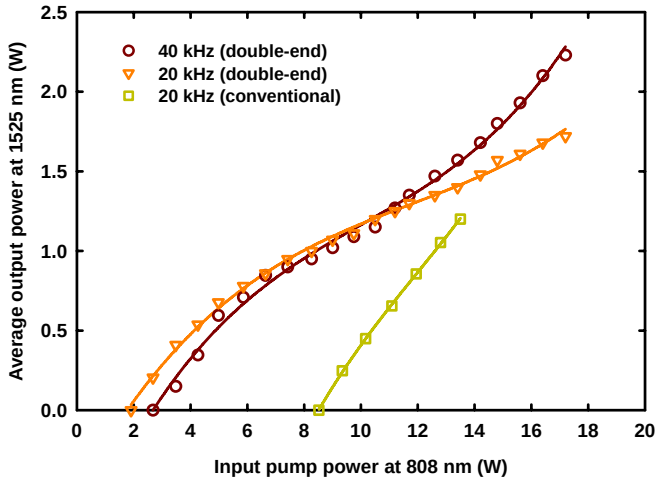

Fig. 4-4. The average output power at 1525 nm with respect to the input pump power at pulse repetition rates of 20 and 40 kHz shown as the down-triangle and circle symbols respectively for the double-end diffusion-bonded Nd:YVO_4 crystal and that at 20 kHz shown as the square symbol for a conventional Nd:YVO_4 crystal reported by Chen [14].

It has been experimentally evidenced that the maximum output power for a conventional self-Raman laser is limited by the critical pump power that induces a large temperature gradient in the gain medium to lead to the Raman gain lower than the cavity losses [1]. Consequently, the output power begins to saturate when the pump power exceeds the critical pump power. As shown in Fig. 4-4, the critical pump power for the self-Raman laser with a double-end diffusion-bonded Nd:YVO_4 crystal can exceed 17.2 W that is limited by the available pump power and is considerably greater than the critical pump power of 13.5 W with a conventional Nd:YVO_4 crystal. As a result, at the pulse repetition rate of 20 kHz, the self-Raman laser with a double-end diffusion-bonded Nd:YVO_4 crystal can generate the maximum average output power up to 1.72 W that is approximately 43% higher than the result with a conventional 0.2 %-doped Nd:YVO_4 crystal [14]. At a repetition rate of 40 kHz, the maximum power at 1525 nm is even up to 2.23 W with an input pump power of 17.2 W, corresponding to a conversion efficiency of 13%. To the best of our knowledge, this is the highest average power for diode-pumped eye-safe self-Raman laser.

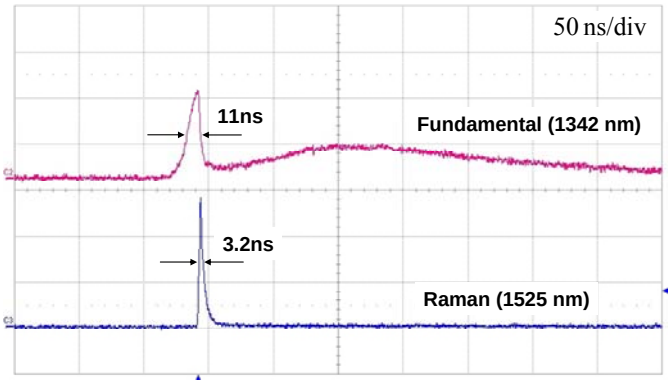

Fig. 4-5. Temporal characteristics of the fundamental and Raman pulses at a pulse repetition rate of 40 kHz with a pump power of 17.2 W.

The temporal traces for the fundamental and Raman pulses are recorded by a LeCroy digital oscilloscope (Wavepro 7100, 10 Gsamples/s, 1-GHz bandwidth) with two fast p-i-n photodiodes. At a repetition rate of 40 kHz the pulse energy is up to 56 μJ with an input pump power of 17.2 W and the pulse width is measured to be approximately 3.2 ns, as shown in Fig. 4-5. The corresponding peak power is higher than 17 kW. At the pulse repetition rate of 20 kHz, the maximum pulse energy is up to 86 μJ. Figure 4-6 shows the pulse width at a pulse repetition rate of 20 kHz with a pump power of 17.2 W. It can be seen that although a second tiny Raman pulse usually follows the main first peak, its contribution is rather limited. Consequently the peak power can be generally higher than 22 kW. Since the fundamental energy is remained after first Raman pulse, the sub-pulse of fundamental wave is formed shown as Fig. 4-5 and Fig. 4-6. At a pulse repetition rate of 20 kHz, the remaining energy is sufficient to reach Raman gain and a second tiny Raman pulse is produced shown as Fig. 4-6. The sub-pulse would not be generated if the reflectivity of output coupler was lowered.

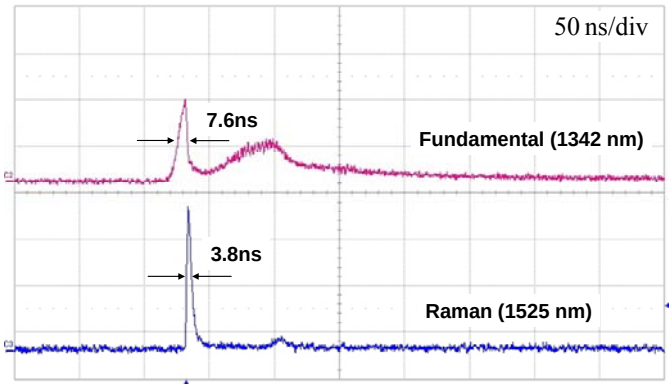

Fig. 4-6. Temporal characteristics of the fundamental and Raman pulses at a pulse repetition rate of 20 kHz with a pump power of 17.2 W.

4.3 High-Efficiency Q-Switched Dual-Wavelength Emission at 1176 and 559 nm with Intracavity Raman and SFG

In the recent years, new laser sources in the spectral range of visible and UV light have been successfully generated by combining SRS with second Harmonic generation (SHG) or sum frequency generation (SFG) [37]. More interestingly and importantly, yellow lights are useful for biomedicine, ophthalmology and dermatology. To date, the highest yellow average power of 3.14 W at 590 nm for a pulse repetition rate of 10 kHz was obtained by doubling diode-side-pumped Nd:YAG/$BaWO_4$ Raman laser [38]. In continuous-wave (CW) operation, the highest yellow average power of 2.51 W at 586.5 W was generated from intracavity frequency-doubling of a diode-end-pumped Nd:$GdVO_4$ self-Raman laser [39]. Recently, the yellow-green laser near 560 nm has been shown to give excellent excitation of phycoerythrins and low molecular weight fluorochromes [40]. The methods of generating yellow-green solid-state laser sources include external-cavity Raman laser pumped by frequency-doubled Nd^{3+} lasers, SHG in low-gain Nd^{3+} lasers, frequency-doubled optically pumped semiconductor laser, and SFG or SHG in infrared Raman lasers. Firstly, He et al. reported on a 532 nm-pumped multi-wavelength lasers comprising 25-mJ yellow-green emission at 563 nm based on cascade Raman generation in a $Ba(NO_3)_2$ crystal [41]. Kaminskii et al. reported on a greater than 1-mJ $PbWO_4$ Raman laser at 559 nm pumped by Q-switched frequency-doubled Nd:YAG laser at 532 nm [42]. Then, Jia et al. reported on a 1.67-W CW laser at 556 nm generated by

frequency-doubling 1112-nm diode-pumped Nd:YAG laser [43]. Räikkönen et al. reported on a 55-mW yellow-green emission at 561 nm from frequency-doubling of a 1123-nm diode-pumped passively Q-switched Nd:YAG laser [44]. Hilbich et al. reported on diode-pumped frequency-doubled optically pumped semiconductor lasers comprising two higher than 100-mW CW yellow-green emissions at 554 and 565 nm [45]. In addition, selectable-wavelength Q-switched Nd:YAG/KGW Raman laser with intracavity SFG and SHG in angle-tuned BBO (β-BaB_2O_4) generated average power of 0.77 W at 559 nm presented by Pask et al.. [46].

Recently, Nd:YVO_4 and Nd:$GdVO_4$ crystals have been identified as excellent laser gain media as well as SRS gain media for diode-pumped all-solid-state lasers [47, 48]. Quite recently, the $\chi^{(3)}$-nonlinear generation effects in tetragonal $LuVO_4$ vanadates has been discovered [47, 48]. The realization of Nd:YVO_4, Nd:$GdVO_4$, and Nd:$LuVO_4$ self-Raman lasers have been demonstrated [1, 14, 25, 36, 49-50]. In this work we employ a self-Raman Nd:YVO_4 laser to develop an efficient yellow-green laser at 559 nm based on intracavity sum-frequency-mixing of the 1064-nm fundamental wave and the 1176-nm first-Stokes component. With an input pump power of 17.5 W, the maximum average power at 559 nm is 1.67 W and the residual average power at 1176 nm is 0.53 W at a pulse repetition rate of 100 kHz, corresponding to conversion efficiency of 9.5% and 3%, respectively. To the best of our knowledge, it is the highest power at 559 nm obtained with intracavity SFG in a self-Raman laser.

4.3.1 Experimental Setup

The experimental setup of a diode-end-pumped actively Q-switched Nd:YVO_4 self-Raman laser with intracavity SFG is shown in Fig. 4-7. The pump source is an 808-nm fiber-coupler laser diode with a core diameter of 600 μm, a numerical aperture of 0.16 and a maximum power of 18 W. The pump beam is focused at the active medium, and the waist radius is approximately 250 μm. An *a*-cut 20-mm-long composite 0.3-at.% Nd^{3+}-doped Nd:YVO_4 crystal bounded with a 2-mm-long and an 8-mm-long undoped YVO_4 ends at its pumped facet and the other facet, respectively, is simultaneously used as a laser crystal and a self-Raman medium. With a fundamental pump wavelength of 1064 nm, the wavelength of the first-Stokes emission in accordance with the YVO_4 Stokes shift at 890 cm^{-1} is calculated to be around 1176 nm [23]. Both sides of the laser crystal is coated for antireflection at 1000-1200 nm (R<0.2%). The laser cavity is designed for the sum-frequency mixing of the fundamental wave and the first-Stokes laser. The 10-mm-long type-Ⅰ BBO crystal with a phase-matching cutting angle (θ=22.1° and ϕ=0°) is used as a sum-frequency mixer. Besides, the composite Nd:YVO_4 and BBO crystals are both wrapped with indium foil and mounted in water-cooled copper blocks. The water temperature is maintained at 20°C. The front mirror M1 is a 500-mm radius-of-curvature concave mirror with antireflection coating at 808 nm on the entrance face (R<0.2%), high-transmission coating at 808 nm (T>90%), and high-reflection coating at 1000-1200 nm on the other face (R>99.8%). The 30-mm-long acousto-optic Q-switcher (NEOS Technologies) has antireflectance

coatings at 1064 nm on both faces and is driven at a 27.12-MHz center frequency with 15.0 W of rf power. The flat intracavity mirror M2 has high-transmission coating at 1064 nm and 1176 nm (T>95%) as well as high-reflection coating at 559 nm (R>99.7%). The output coupler M3 is a flat mirror with high-reflection coating at 1064 nm (R>99.8%), partial-reflection coating at 1176 nm (R=98.1%), and high-transmission coating at 559 nm (T>85%). The overall laser cavity length is around 113 mm.

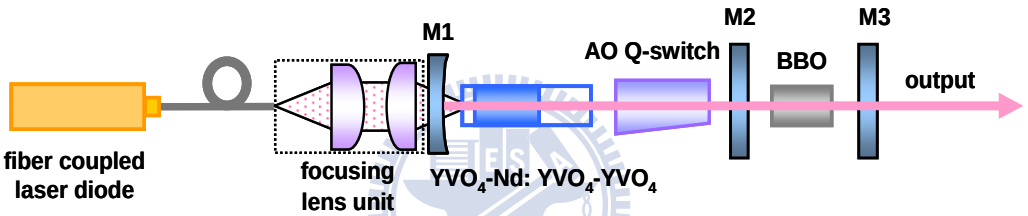

Fig. 4-7. Experimental setup of a diode-end-pumped actively Q-switched Nd:YVO_4/BBO laser with intracavity self-Raman frequency conversion and sum-frequency generation.

4.3.2 Experimental Results and Discussions

Since it has been verified that the enhancement of Raman gain is attributed from the significant reduced thermal effects and the increase of the Raman interaction length in a double-end diffusion-bonded Nd:YVO_4 crystal [51], we use a double-end diffusion-bonded Nd:YVO_4 crystal as a self-Raman gain medium in this work. The two two-mirror cavities are set up. The first two-mirror cavity with a output coupler having partial-reflection coating at 1064 nm (R=85%) is used to set up a Q-switched

Nd:YVO_4 laser at 1064 nm. With an input pump power of 17.5 W, average power of 8.7 W at 1064 nm is obtained at a pulse repetition rate of 100 kHz. The second two-mirror cavity with a output coupler having high-reflection coating at the 1064 nm and partial reflection coating at the first-Stokes component of 1176 nm (R=56%) is used for the Q-switched Nd:YVO_4 self-Raman laser at 1176 nm. The laser cavity length is 7 cm and the pumping threshold for the Raman laser is 2.7 W to 3.5 W at the pulse repetition rates of 80 kHz to 120 kHz. With an input pump power of 12.1 W, the average output power of 3 W and the peak power of 7.6 kW at 1176 nm are achieved at a pulse repetition rate of 100 kHz, corresponding to a high conversion efficiency of 24.8%. The average power at 1176 nm and conversion efficiency are 2 times and 1.8 times that of the Nd:YVO_4 self-Raman laser with a conventional Nd:YVO_4 crystal without undoped endcaps, respectively [1].

After confirming the performance of the Q-switched Raman laser at 1176 nm, the laser cavity is designed for sum-frequency mixing of the fundamental wave and the first-Stokes component. The BBO crystal, the intracavity mirror M2, and the output coupler M3 are inserted in the laser cavity. The cavity alignment and the tilt of BBO crystal must be regulated to optimize the laser performance. As a result of the high-reflection coating at SFG wavelength on mirror M2, the present linear three-mirror-cavity takes the advantages of reduced loss of SFG emission transmitting through the front mirror M1 as well as reduced absorption of SFG emission in the Nd:YVO_4 which lowers the thermal load in the Nd:YVO_4 compared to the linear two-mirror-cavity [39]. Additionally, the present laser configuration is more compact than the three-mirror folded cavity. Note that the present output coupler M3 is

non-optimal for SFG emission. Therefore, a higher output power at SFG wavelength can be obtained with the optimum output coupler having high-reflection coating at 1176 nm. The spectrum of laser output is measured by an optical spectrum analyzer (Advantest Q8381A) employing a diffraction lattice monochromator with a resolution of 0.1 nm. The experimental optical spectrum of the laser output is shown in Fig. 4-8, and it can be seen that the main laser output is the yellow-green laser at 559 nm from sum-frequency-mixing of 1176 and 1064 nm. The pumping threshold for oscillation at 559 nm is around 4.3 W to 6 W for the pulse repetition rates of 80 kHz to 120 kHz. The residual laser output is the first-Stokes laser at 1176 nm. The intensity of the fundamental wave at 1064 nm is weak and hard to measure due to the high-reflection coating at 1064 nm on the output coupler.

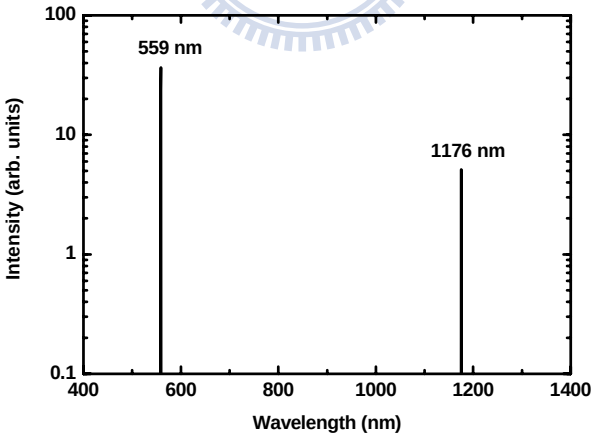

Fig. 4-8. Optical spectrum of the diode-end-pumped actively Q-switched Nd:YVO_4/BBO laser.

Figure 4-9 shows the total average power as well as individual average power at Stokes wavelength of 1176 nm and SFG wavelength of 559 nm with respect to the

input pump power at a pulse repetition rate of 100 kHz. The M^2 beam quality factor is found to be less than 2.0 for all pump powers. The average power at 1176 nm is saturated at around 0.55 W with an input pump power above 12 W. With an input pump power of 12.9 W, the average power of 0.56 W at 1176 nm is obtained, corresponding to a conversion efficiency of 4.3%. However, increasing input pump power to higher than 12 W is beneficial for enhancing SFG average power. While the input pump power is increased to 17.5 W, the average power at 559 nm is up to 1.67 W corresponding to a conversion efficiency of 9.5%. The higher average output at 559 nm and the lower average output power at 1176 nm would be obtained if an output coupler with high-reflection coating at both 1064 and 1176 nm (R>99.8%) was used.

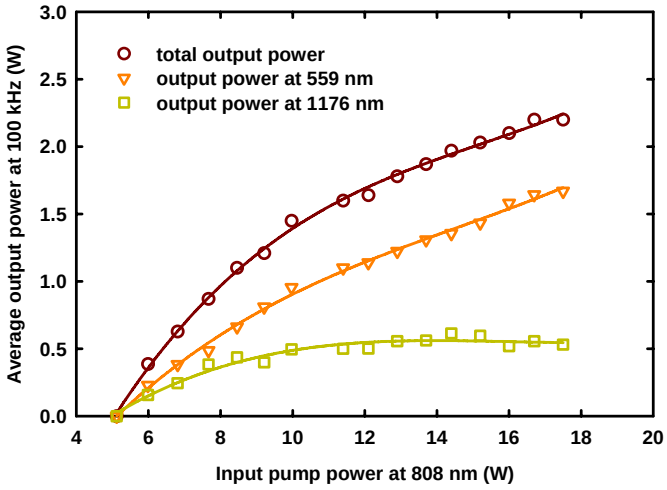

Fig. 4-9. The total average output power as well as individual average output power at 559 and 1176 nm with respect to the input pump power at a pulse repetition rate of 100 kHz.

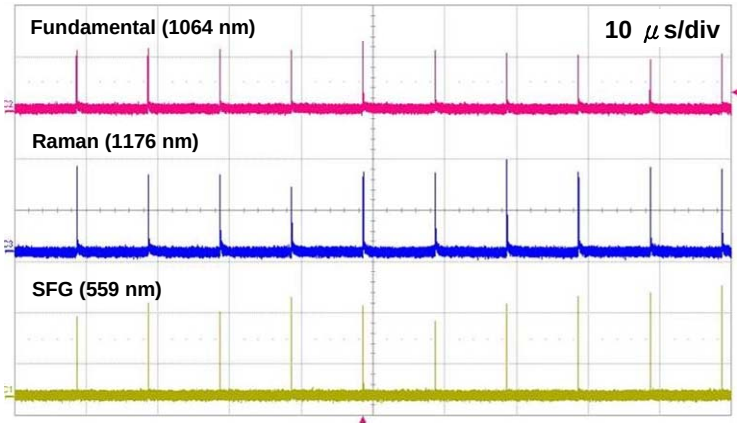

Fig. 4-10. Typical oscilloscope traces of pulse trains at 1064, 1176, and 559 nm.

The temporal traces for the laser emission comprising the fundamental, Raman, and SFG pulses are recorded by a LeCroy digital oscilloscope (Wavepro 7100, 10 Gsamples/s, 1-GHz bandwidth) with two fast p-i-n photodiodes. The oscilloscope trace of output pulse trains is shown in Fig. 4-10. It can be seen that the pulse-to-pulse amplitude fluctuation is within ±15%. Note that the vertical scales for the pulses at 1064, 1176, and 559 nm are separate arbitrary units. The pulse widths of 1176 and 559 nm are measured to be shorter than 55 and 10 ns over the entire operation, respectively. As shown in Fig. 4-11, the pulse widths of 1176 and 559 nm pulses are approximately 32 and 5.4 ns with an input pump power of 17.5 W at a pulse repetition rate of 100 kHz, respectively. As shown in Fig. 4-11, the Raman pulse is generated after SFG pulse. It is because that when the intracavity power density of the fundamental pulse reaches the SRS threshold, the Raman and fundamental pulses are simultaneously rapidly converted to SFG pulse. Therefore, there exists a longer time shift of fundamental and Raman pulses than Raman laser without SFG. In summary,

an efficient dual-wavelength Q-switched laser at 559 and 1176 nm based on self-Raman and intracavity SFG is demonstrated by using a double-end diffusion-bonded Nd:YVO_4 crystal and a BBO crystal. At a pulse repetition rate of 100 kHz, the main average output power of 1.67 W at 559 nm and the residual average output power of 0.53 W at 1176 nm is generated with an input pump power of 17.5 W, corresponding to conversion efficiency of 9.5% and 3% and peak power of 3.1 and 0.17 kW, respectively. The total conversion efficiency of SRS and SFG is 12.5%.

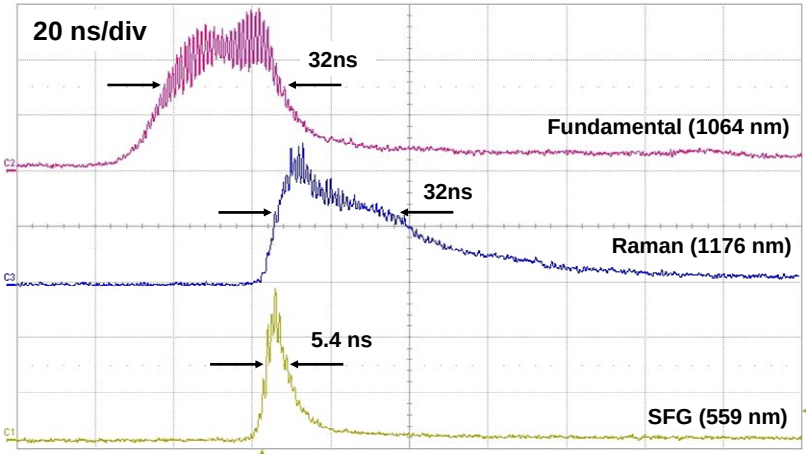

Fig. 4-11. Typical oscilloscope traces for output pulses at 1064, 1176, and 559 nm.

4.4 Conclusion

A compact efficient high-power diode-pumped actively Q-switched self-Raman laser at 1525 nm is demonstrated by employing a double-end diffusion-bonded Nd:YVO_4 crystal. Experimental results reveal that the double-end composite crystal can reduce the thermal effects to reach a higher critical pump power. More importantly, the undoped part plays a critical role in lowering the lasing threshold at high pulse repletion rates because of the increase of the Raman interaction length. At the pulse repetition rate of 20 kHz, the maximum average output power with the composite crystal is found to be nearly 40% higher than that with a conventional Nd:YVO_4 crystal. The maximum average output power of 2.23 W at first-Stokes wavelength of 1525 nm is generated at a pulse repetition rate of 40 kHz, and the pulse width of Raman pulse is about 3.2 ns with an input pump power of 17.2 W. The corresponding conversion efficiency and peak power are approximately 13% and 17.4 kW, respectively.

In addition, an efficient yellow-green laser at 559 nm with intracavity SFG in a diode-pumped Q-switched Nd:YVO_4 self-Raman laser is demonstrated. We utilize a double-bonded diffusion-bonded Nd:YVO_4 crystal as a self-Raman gain medium to improve thermal lensing effect and enhance the Raman gain. With input pump power of 17.5 W, the maximum average power at 559 nm is 1.67 W and the average power at 1176 nm is 0.53 W at a pulse repetition rate of 100 kHz, corresponding to

conversion efficiency of 9.5% and 3%, respectively. The peak power of 559 nm pulse amounts to 3.1 kW.

Chapter 5

Intracavity Raman Laser with a Vanadate Crystal

5.1 Power Scale-Up of the Diode-Pumped Actively Q-Switched Nd:YVO_4 Raman Laser with a YVO_4 Crystal as a Raman Shifter

In the past few years, self-Raman lasers have been successfully demonstrated in several Raman materials such as Nd:$SrWO_4$ [1], Nd:$KG(WO_4)_2$ [2], Yb:$KGd(WO_4)_2$ [3], Nd:$PbWO_4$ [4], Nd:YVO_4 [5], Nd:$GdVO_4$ [6], and Nd:$Gd_xY_{1-x}VO_4$ [7]. The laser crystal simultaneously serving as a Raman crystal can provide the advantage of compactness and simplicity for an intracavity SRS laser [8]. In 2004, Nd:YVO_4 crystal is firstly used to demonstrate the laser emission at wavelengths of 1176 and 1525 nm based on self-SRS action in 1064- and 1342-nm actively Q-switched Nd:YVO_4 laser, respectively [5, 9]. The issue of the field-induced crystal damage usually restricted the output powers in self-Raman Q-switched lasers. In addition, the optimization is hindered because the laser crystal simultaneously serves as a Raman material. The optimum mode size in the self-Raman medium is subject to a compromise between lowering the SRS threshold and avoiding optical damage induced by self-focusing [6]. In this work, to our knowledge, we report a new design of a diode-pumped actively Q-switched 1176-nm Nd:YVO_4 Raman laser to increase the average power, repetition rate, peak power, and damage threshold comprehensively. An YVO_4 crystal is used as a Raman shifter in an actively Q-switched laser.

5.1.1 Experimental Setup

Figure 5-1 shows the experimental configuration for actively Q-switched Nd:YVO_4 1176-nm Raman laser which differs from self-Raman laser. The pump source is an 808-nm fiber-coupled laser diode with the core diameter of 800 μm, the numerical aperture of 0.16, and the maximum output power of 25 W. A focusing lens unit with a 85% coupling efficiency is used to reimage the pump beam into the gain medium with a pump spot radius of 400μm. The gain medium, a 9-mm-long a-cut Nd:YVO_4 crystal with low concentrations, 0.25 at. %, is used to reduce thermally induced fracture [5]. Both sides of this laser crystal ie coated for antireflection (AR) at 1.06 μm (R<0.2%). The Raman crystal is a 9.6-mm-long a-cut YVO_4 crystal. These two crystals are both wrapped with indium foil and mounted in water-cooled copper blocks individually. The 30-mm-long acousto-optic (AO) Q switch (NEOS Technologies) has AR coating at 1064 nm on both faces and is driven at a 27.12-MHz center frequency by 15 W of RF power. The resonator is a plano-concave configuration. Front mirror, a 500-mm radius-of-curvature concave mirror, is coated with AR coating at 808 nm (R<0.2%) on the entrance face, and with high-reflection (HR) coating at 1064 nm (R>99.8%) and high-transmission (HT) coating at 808 nm (T>90%) on the other face. The coating of front mirror at 1176 nm is also high-reflection. The output coupler (OC) is a flat mirror with HR coating at 1064 nm (R>99.8%) and partial-reflection (PR) coating at 1176 nm (R=51%). The cavity length is around 115 mm and depends on pumping power. The spectrum of laser output is monitored by an optical spectrum analyzer (Advantest Q8381A, including a

diffraction lattice monochromator) with a resolution of 0.1 nm. The temporal behaviors for fundamental and Raman pulses are recorded by a LeCroy digital oscilloscope (Wavepro 7100, 10 Gs/s, 1-GHz bandwidth) with two fast p-i-n photodiode and an interference filter allowing transmission only at 1064 nm.

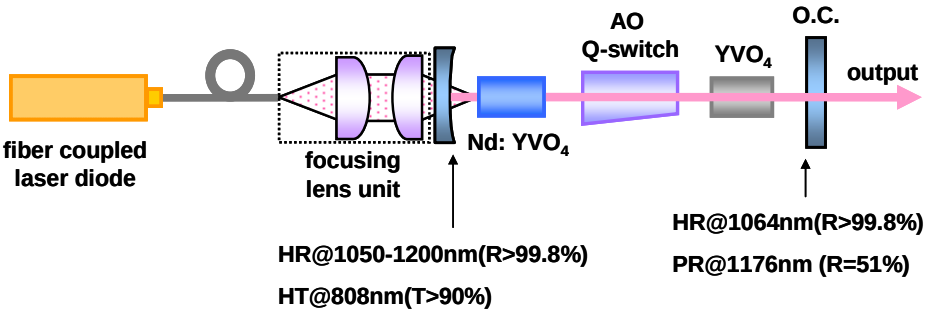

Fig. 5-1. Experimental setup of a diode-pumped actively Q-switched Nd:YVO_4 Raman laser at 1176 nm with an YVO_4 crystal as a Raman shifter.

5.1.2 Experimental Results and Discussions

As a stimulated Raman material, taking the place of Nd:YVO_4 by YVO_4 has advantages on robustness and output properties. Figure 5-2 displays the experimental result for optical spectrum of the laser output and Raman scattering spectrum of the YVO_4. The first Stokes wavelength near 1176 nm is converted from the fundamental wavelength near 1064 nm by Raman peak at 890 cm^{-1}. The Raman shift of Nd:YVO_4 and YVO_4 are almost the same, came from the same periodic YVO_4 lattice. But crystals without dopant has more perfect lattice, which bring on higher damage threshold and more stable frequency conversion. So, we can use the pure YVO_4 as a Raman crystal in the position where the intensity is highest in the cavity, and still

increase the pumping power. Further, the reflectance of OC can be lower (from 93% to 51%) to scale up average output power due to lower lasing threshold at Raman wavelength. By using lower reflection coating we can narrow the pulse width. At the same time, when we over drive pump current during the experiment, the damage never happened in Nd:YVO_4, but in Raman crystal. That means that the SRS is generated mainly in pure YVO_4, a more reliable and replaceable component in practical laser.

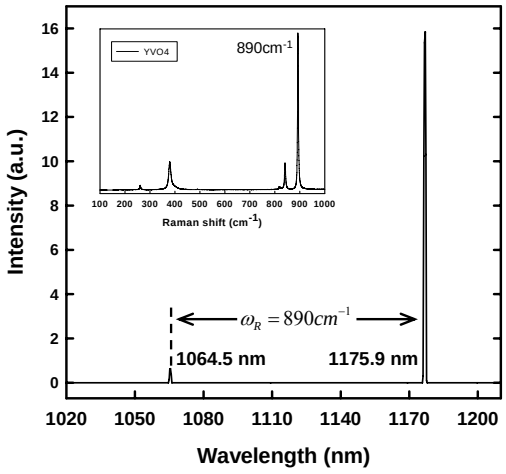

Fig. 5-2. Optical spectrum of the actively Q-switched Raman output. The Raman scattering spectrum of an YVO_4 crystal showed in inset, which is almost the same as it of Nd:YVO_4 crystal.

Figure 5-3 and Fig. 5-4 illustrate the output performance of actively Q-switched 1176-nm Nd:YVO_4 Raman laser. The average output power at the Stokes wavelength of 1176 nm with respect to the incident pump power for various pulse repetition rate of 20, 40, 60, and 80 kHz shown in Figure 5-3. Because the thermal loading of the end-pumped Q-switched Nd-doped laser increases with decreasing repetition rate [10, 11], it can be seen that although the pumping threshold is higher, increasing the pulse

repetition rate can efficiently increase the maximum average output power at 1176 nm and its maximum pump power ($P_{p,max}$). And for a certain repetition rate, to pump over $P_{p,max}$ will get the unstable Raman conversion and fall the output power. The average output power is up to 2.61 W with an incident pump power of 18.7 W at a repetition rate of 80 kHz, corresponding to the conversion efficiency of 14% and slope efficiency of 40%. Comparing to results of 1176-nm self-Raman laser using Nd:YVO_4 with lower dopant concentration of 0.2 at.% [5], this Raman laser still has the increase of ratio in average power of 74% and in conversion efficiency of 0.7%. It could be better if we were able to use 0.2 at.% Nd:YVO_4 and correctly AR-coated c-cut [12] YVO_4 in this Raman laser. On the other hand, the maximum pulse energy is generally greater then 40 μJ at repetition rate from 20 to 60 kHz, and up to 43.5 μJ at 40 kHz with an incident pump power of 12.7 W. The maximum pulse energy at repetition rate of 80 kHz is 32.6 μJ.

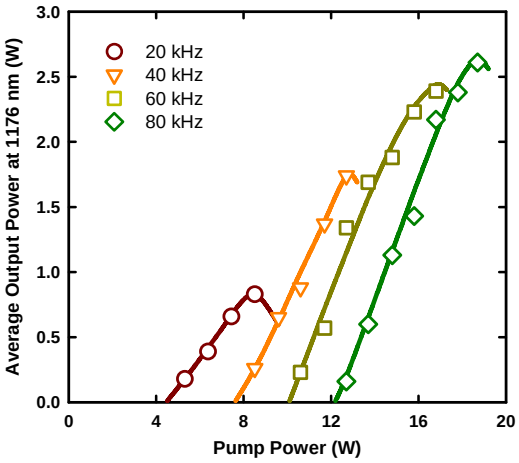

Fig. 5-3. The average output power at the Stokes wavelength of 1176 nm with respect to the incident pump power at different pulse repetition rate from 20 kHz to 80 kHz.

The typical time traces for fundamental and Raman pulses are shown in Figure 5-4. The pulse width is always shorter then 5 ns, but the effective pulse width is much shorter due to mode-locked shape. With the pulse energy of 43.5 μJ, the pulse width of the pulse envelop in Figure 5-4 is 4.5 ns, and the peak power of the pulse seen as a Gaussian shape should be 9.7 kW. However, after curve fitting for the mode-locked shape, the peak power is enhanced to 14 kW, 1.45 times the 9.7 kW. In other words, the effective pulse width is around 3.1 ns which is much shorter than 18 ns of self-Raman laser [5]. Comparing to 1176-nm actively Q-switched Nd:YVO_4 self-Raman laser of 4.2 kW [5], the output peak power is enhanced to be more than two times. The present peak-power level is close to the results of the passively Q-switched Nd:$GdVO_4$ self-Raman lasers in which the average power, pulse width and peak power are found to be 83 mW, 500 ps, and 9.2 kW at 1174 nm [13], or 140 mW, 750 ps, and 8.4 kW at 1176 nm [14].

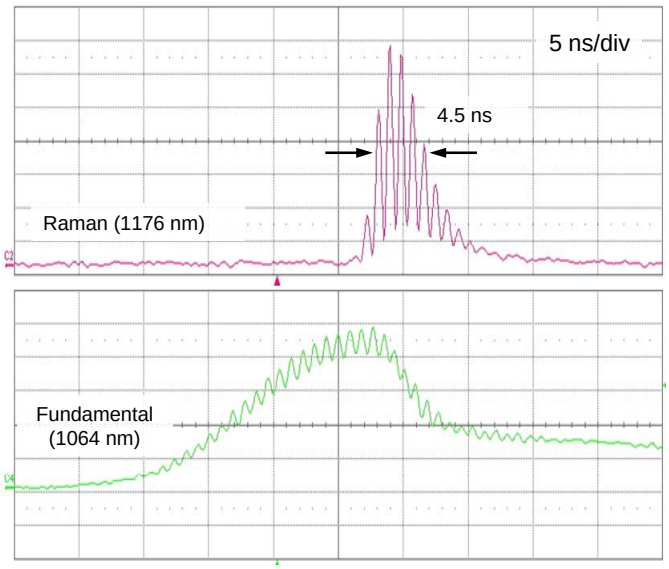

Fig. 5-4. An oscilloscope trace with mode-locking effect for fundamental and Raman pulses.

5.2 Efficient High-Peak-Power Diode-Pumped Actively Q-Switched Nd:YAG/YVO_4 Intracavity Raman Laser

Neodymium-doped yttrium aluminum garnet and yttrium othovanadate (Nd:YAG and Nd:YVO_4) are the most widely used materials of solid-state laser gain medium [10, 15]. The Nd:YVO_4 crystal has a strong broadband absorption and an effective stimulated emission cross section which is five times larger than Nd:YAG [16]. These properties imply that a Nd:YVO_4 laser usually has the higher efficiency and broader operating temperature than a Nd:YAG laser. However, the Nd:YAG crystal has other advantages such as better thermal property and much longer fluorescence lifetime. In particular, the long lifetime can raise the output pulse energy of a fundamental actively Q-switched laser and should be able to raise the output pulse energy of an actively Q-switched Raman laser at the Stokes wavelength. This means that the conversion efficiency of the intracavity SRS might be increased in a actively Q-switched Nd:YAG solid-state laser.

In the section of 5.1, we have exhibited the actively Q-switched Nd:YVO_4 Raman laser with a YVO_4 crystal. In this work, we report the high-pulse-energy and high-peak-power intracavity YVO_4 SRS generation in a compact diode-pumped actively Q-switched Nd:YAG laser.

5.2.1 Experimental Setup

Figure 5-5 depicts the experimental configuration for the diode-pumped actively Q-switched Nd:YAG/YVO_4 Raman laser. The cavity mirrors which have special dichroic coating for efficient conversion at the first-Stokes wavelength form a plano-concave configuration. The input mirror is a 500-mm radius-of-curvature concave mirror with antireflection coating at 808 nm on the entrance face (R<0.2%), high-reflection coating at 1050~1200 nm (R>99.8%) and high-transmission coating at 808 nm on the other surface (T>90%). The output coupler is a flat mirror with high-reflection coating at 1064 nm (R>99.8%) and partial-reflection coating at 1176 nm (R=51%). Note that the output coupler reflectivity is not optimized and it is limited in availability.

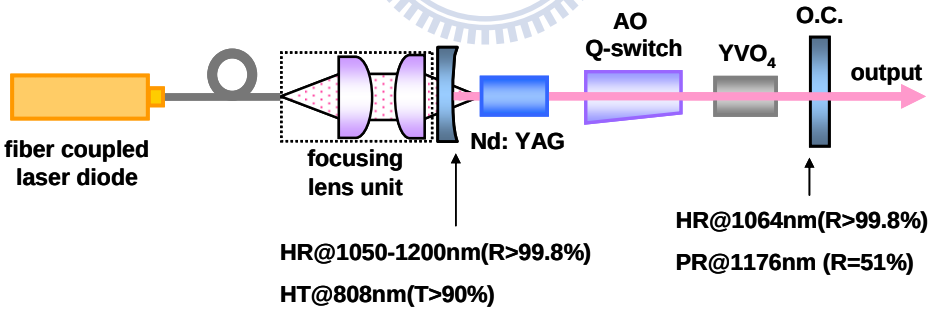

Fig. 5-5. Experimental setup of a diode-pumped actively Q-switched Nd:YAG/YVO_4 Raman laser at 1176 nm.

The pump source is an 808-nm fiber-coupled laser diode with a core diameter of 800 μm, a numerical aperture of 0.16 and a maximum output power of 25 W. A focusing lens system with an 85% coupling efficiency is used to re-image the pump

beam into the laser crystal. The waist radius of the pump beam is approximately 400 μm. The laser medium is a 0.8-at.% Nd^{3+}:YAG crystal with a length of 10 mm. Both sides of this laser crystal are coated for antireflection (AR) at 1.06 μm (R<0.2%). The Raman crystal is an a-cut YVO_4 crystal with a length of 9.6 mm. These two crystals are both wrapped with indium foil and mounted in water-cooled copper blocks individually. The water temperature is maintained at 20 ^{o}C. The 30-mm-long acousto-optic Q-switch (NEOS Technologies) has antireflection coatings at 1064 nm on both faces and is driven at a 27.12 MHz center frequency with 15 W of RF power. The overall laser cavity length is around 9 cm. The thermal detector (Coherent LM-10 HTD) is used to measure the average power of fundamental and Stokes output.

5.2.2 Experimental Results and Discussions

The actively Q-switched Nd:YAG laser performance at 1064 nm is firstly studied for evaluating the conversion efficiency of the intracavity SRS. For this investigation, an output coupler with partial reflection at 1064 nm is used instead of the above-mentioned Raman cavity output coupler. The optimum reflectivity of the output coupler is found to be approximately 80%. The pump threshold for 1064-nm oscillation is below 2.5 W and insensitive to the pulse repetition rate. With an incident pump power of 16.2 W, the average output powers at 1064 nm are 5.8-6.3 W for pulse repetition rates in the range of 20-50 kHz.

In addition, the partially polarized laser beam with a polarization ratio of 3:1 should be excited by the acousto-optic Q-switch and nonlinear Raman crystal.

However, when the intracavity Raman laser is used, the relatively random polarization may benefit the robustness of the Raman crystal compared to Nd:YVO_4/YVO_4 Raman laser reported in the section 3-2 [17]. Therefore, our experimental results reveal that the same Raman crystals can sustain higher peak power per unit area in Nd:YAG laser. In other words, the maximum operating pump power becomes higher. The experimental result for optical spectrum of the Raman laser is monitored by an optical spectrum analyzer (Advantest Q8381A, including a diffraction grating monochromator) with a resolution of 0.1 nm. The first Stokes wavelength of 1176 nm is converted from the fundamental wavelength at 1064 nm by Raman shift at 890 cm^{-1} from an YVO_4 crystal [9]. There is no second Stokes wavelength observed for all pumping power.

Figure 5.6 illustrates the average output power at 1176 nm with respect to the incident pump power for pulse repetition rates of 20, 30, and 50 kHz. For the Raman operation with a fixed pulse repetition rate and a fixed cavity length, a critical pump power or a maximum operating pump power exists. The thermal lensing effect will cause the cavity to be unstable beyond the critical pump power. Reducing the pulse repetition rate leads to a lower threshold for stimulated Raman output, but it leads to a smaller critical pump power and a smaller maximum output power because of the increased thermal loading of the end-pumped Q-switched Nd-doped laser [18]. However, the meaning behind the critical pump power may not be all the same as normal actively Q-switched Nd-doped lasers. Compared with the fundamental operation at 1064 nm, the much lower optical-to-optical conversion efficiency for Raman operation may cause much higher thermal loading on the gain medium. The

additional thermal lensing effect from SRS on a Raman crystal should also be considered. Then, the SRS conversion efficiency could be sensitive to the cavity stability, which will induce the drop in critical pump power. Moreover, the self-focusing-induced damage on the YVO_4 crystal never occurs at low pulse repetition rate while the pump power is overdriven.

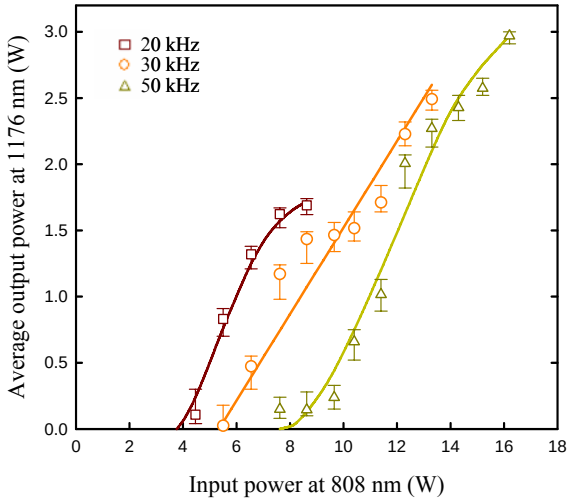

Fig. 5-6. Average output power at the Stokes wavelength of 1176 nm with respect to the incident pump power at various pulse repetition rates of 20, 30, and 50 kHz.

Nevertheless, the efficient average output powers at 1176 nm are 1.6, 2.5, and 3.0 W at pulse repetition rates of 20, 30, and 50 kHz with the incident pump power of 7.6, 13.3, and 16.2 W, respectively. As a consequence, the maximum SRS conversion efficiency of 62-47% with respect to the output power that is available from the fundamental laser of 1064 nm is demonstrated at the pulse repetition rate of 20~50 kHz. Then, the maximum optical-to-optical conversion efficiency from 808-nm pump are as high as 21.3~18.3% at the pulse repetition rate of 20~50 kHz. The overall

conversion efficiency is the second-highest one for Raman lasers until now to our knowledge [19, 20]. The efficiency could be improved if we can use a c-cut YVO_4 crystal [12] with properly antireflection coating and an optimized output coupler. From the average output power and the pulse repetition rate, the pulse energy E_p at 1176 nm with respect to the incident pump power is depicted in Fig. 5-7. The maximum pulse energies E_{max} at pulse repetition rates of 20 and 30 kHz are both higher than 83 μJ. The E_{max} of this Nd:YAG/YVO_4 Raman laser is almost two times the E_{max} of the Nd:YVO_4/YVO_4 Raman laser in almost the same actively Q-switched scheme reported in the section of 3-2 [17].

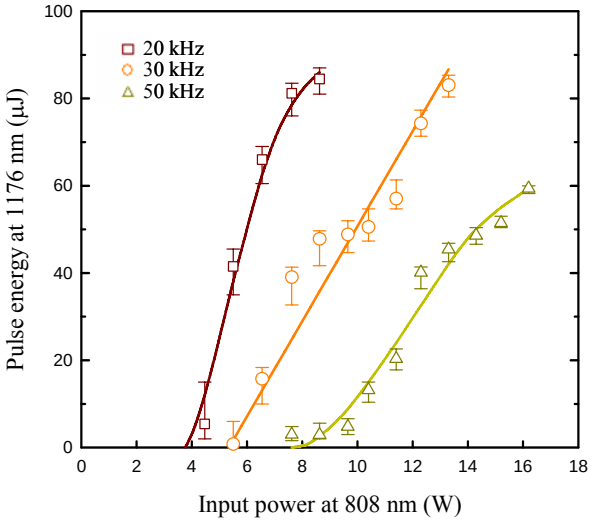

Fig. 5-7. Pulse energy at 1176 nm with respect to the incident pump power at various pulse repetition rates of 20, 30, and 50 kHz.

The temporal behaviors were recorded by a LeCroy digital oscilloscope (Wavepro 7100, 10 GS/s, 1-GHz bandwidth) with two fast InGaAs p-i-n photodiodes. An interference filter allowing transmission only at 1064 nm is used for extracting weak

fundamental signal. Figures 5-8 shows the pulse shape for the fundamental and Raman components. With a pulse energy of 81.2 μJ at 1176 nm, the pulse width of the pulse envelope in Fig. 5-8 is 2.2 ns, and the peak power of the pulse seen as a Gaussian shape without oscillation should be 36.9 kW. However, the observed mode-locked phenomenon causes the Raman pulse to assume a deeply modulated shape, and peak power P_{peak} cannot be approximated as the E_p divided by the envelope width same as Nd:YVO_4/YVO_4 Raman laser [17]. We have to employ the temporal shape of a single pulse in arbitrary unit, $\psi(t)$, to determine the correct P_{peak}. Note that the screen shots and numerical data of $\psi(t)$ are simultaneously recorded in the oscilloscope so that we could use the numerical data for calculation, which can be expressed as $P_{peak} = C \cdot \psi_{\max}(t)$, where the $\psi_{\max}(t)$ indicates the peak value of $\psi(t)$. Factor C is determined by the fact that $E_p = C \cdot \int_T \psi(t)dt$, where T indicates the temporal range of the single pulse. Consequently, the peak power of the Raman pulse in Fig. 5-8 is 43.5 kW.

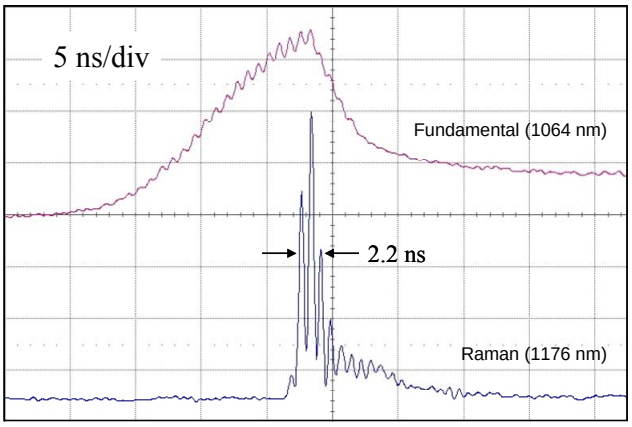

Fig. 5-8. Oscilloscope trace with mode-locking effect for fundamental and Raman pulses. The figure is recorded with an incident pump power of 7.6 W at a pulse repetition rate of 20 kHz.

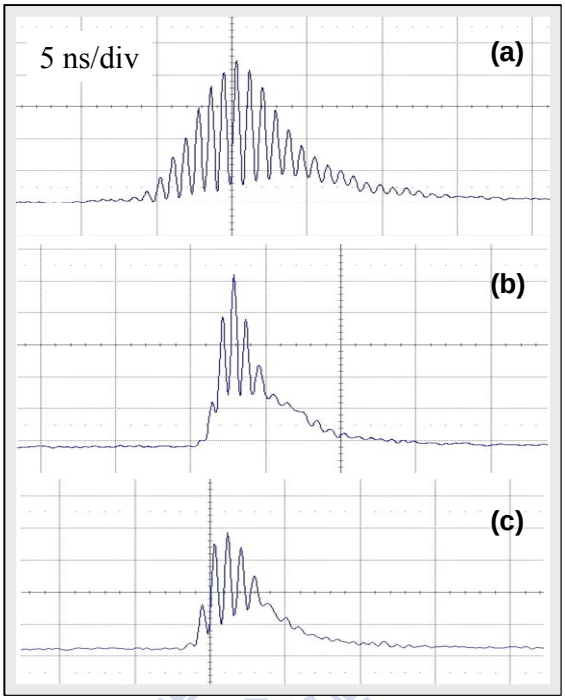

Fig. 5-9. Evolvement of pulse shapes dependent on pump power at a pulse repetition rate of 50 kHz. With incident pump power of 8.6 W, 12.3 W, and 14.8 W, the peak power is (a) 560 W, (b) 13.1 kW, and (c) 15.5 kW.

It can also be observed that the pulse shape and modulated oscillation depth are varied with increased pump power. For example, Fig. 5-9 depicts the typical evolvement of pulse shapes that are dependent on pump power at 50 kHz. Note that the vertical axes of the pulses are separate arbitrary units. With a pump power of 8.6 W, which is near the threshold of SRS, the envelope width of 7.1 ns and deep mode-locked oscillation are showed in Fig. 5-9 (a). Although the pump power is increased to 12.3 W, the envelope width is narrowed to a minimum of 3.1 ns with a P_{peak} of 13.1 kW as shown in Fig. 5-9 (b). Meanwhile, the mode-locked oscillation depth decreased when the pump power is increased from the threshold to the 12.3 W.

Then the pulse envelope broadened slightly after the pump power of 12.3W, but the mode-locking effect is enhanced. With a pump power of 14.8 W, the pulse is observed with an almost saturated P_{peak} of 15.5 kW as showed in Fig. 5-9 (c). Finally, the pulse-to-pulse amplitude fluctuation of the Raman output is monitored to be approximately less than ±10%.

The temporal behavior and real P_{peak} appear to be available. In fact, with further observation, the FWHM of each mode-locked pulse inside the envelope is 500~600 ps. Narrow mode-locked pulses might be restricted by the 1-GHz bandwidth of the oscilloscope and photo detectors. The restriction is easy to be overlook during the experiment. In other words, the P_{peak} could be much higher than what we calculated in our research and in Ref. [17]. However, a conventional autocorrelator for short-pulse measurement of a stable cw mode-locked laser can not provide reliable measurement results for Q-switched mode-locked laser. We estimate that the real-time oscilloscope and photodetectors with an 8~10-GHz bandwidth are required for sure tracing on the time domain. Nevertheless, the high-speed optoelectronic equipment is still being fine tuned and is not yet available for general use. It will be interesting to study the mechanism and behavior of the compact mode-locked actively Q-switched intracavity Raman lasers by use of YVO_4 crystals.

Compared with the results from the Nd:YVO_4/YVO_4 Raman laser in almost the same actively Q-switched scheme, the Nd:YAG/YVO_4 Raman laser raises the maximum output pulse energy from 43 to 83 μJ and the peak power from 14 kW to 43.5 kW [17].

5.3 Conclusion

In conclusion, with a YVO_4 crystal as a stimulated Raman crystal in a 1064-nm actively Q-switched Nd:YVO_4 laser, the maximum operating pump power, repetition rate, average output power, pulse width, and the peak power at the Stokes wavelength of 1176 nm are substantially improved as listed in table 3-1. With an incident pump power of 18.7 W, the average power is 2.61 W at 80 kHz corresponding to the conversion efficiency of 13.9%. The output pulses noticeably display mode-locking phenomena that lead to the maximum peak power to be higher than 10.5 kW at 1176 nm operated at the pulse repetition rate from 20 to 80 kHz. With an incident pump power of 12.7 W, the pulse energy and peak power is higher than 43.5 μJ and 14 kW at 40 kHz.

In addition, it is experimentally demonstrated that the maximum operating pump power and conversion efficiency can be further improved simultaneously by use of a similar Raman laser cavity with another gain medium, Nd:YAG, as listed in table 3-1. 3-W average output power of the efficient diode-pumped actively Q-switched Nd:YAG/YVO_4 intracavity Raman laser at 1176 nm is generated at a pulse repetition rate of 50 kHz. The maximum conversion efficiency is up to 21.3-18.3% at a pulse repetition rate of 20-50 kHz. The maximum pulse energy is higher than 83 μJ at both 20 kHz and 30 kHz. The output pulses display mode-locking phenomena that result in a maximum peak power of 43.5 kW.

	Pulse repetition rate (kHz)	Input pump power (W)	Average output power (W)	Conversion efficiency (%)	Pulse energy (μJ)	Pulse width (ns)	Peak power (kW)
Nd:YVO_4 self-Raman laser	20	10.8	1.5	13.9	75	18	4.2
Nd:YVO_4 /YVO_4 Raman laser	80	18.7	2.6	13.9	32.5	5	9
	40	12.7	1.7	13.7	43.5	4.5	14
Nd:YAG/YVO_4 Raman laser	50	16.2	3	18.5	60	3.5	17.1
	30	13.3	2.5	18.8	83.3	3	27.8
	20	7.6	1.6	21.3	81	2.2	43.5

Table. 5-1. Comparison of laser performance between Nd:YVO_4 self-Raman laser, Nd:YVO_4/YVO_4, and Nd:YAG/YVO_4 Raman lasers at 1176 nm.

Chapter 6

Intracavity Cascade Raman Laser with a KTP or KTA Crystal

6.1. Introduction

Raman lasers which are based on intracavity stimulated Raman scattering (SRS) in Raman active crystals have a very promising potential for various applications such as pollution detection, remote sensing, and medical system [1-3]. Recently, potassium titanyl phosphate (KTP) and rubidium titanyl phosphate (RTP) which are widely recognized as prominent nonlinear optical crystals involving nonlinear optical susceptibility $\chi^{(2)}$ have been experimentally confirmed to be practical SRS converter devices [4-6]. The low value of the KTP-related Stokes shift (270 cm^{-1}) [7] permits generation of multi-frequency radiation with cascade SRS. Nowadays, simultaneous multi-frequency lasing lines with high peak powers in the room temperature is of practical importance for the terahertz (THz) generation with the nonlinear optical difference frequency method [8-10].

Neodymium-doped single vanadate crystals including Nd:YVO_4 and Nd:$GdVO_4$ have been identified as excellent laser materials for diode-pumped solid-state lasers because of their large absorption and large emission cross sections [11-18]. In the Q-switching operation, however, the large emission cross sections usually limit their energy storage capacities. To overcome this hindrance, mixed Nd:$Y_xGd_{1-x}VO_4$ crystals were recently developed with Y ions replacing some of the Gd ions in Nd:$GdVO_4$ single crystal [19-22]. It has been experimentally confirmed that such mixed crystals are substantially superior to single crystals for Q-switching and mode-locking performance because of their broader fluorescence linewidth [22-24].

6.2 Diode-Pumped Multi-Frequency Q-Switched Laser with Intracavity Cascade Raman Emission in KTP Crystal

In this work, we present the first demonstration of a diode-pumped actively Q-switched mixed Nd:$Y_{0.3}Gd_{0.7}VO_4$ laser with an intracavity KTP crystal to produce cascade SRS emission up to the fourth order. With an incident pump power of 14 W, the actively Q-switched intracavity Raman laser, operating at 50 kHz, produces an average output power up to 0.92 W with a pulse energy of 18.4 J. The maximum peak power is generally higher than 2 kW.

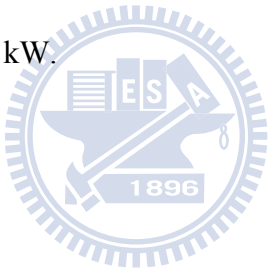

6.2.1 Experimental Setup

The schematic diagram for the experimental setup of a diode-pumped actively Q-switched Nd:$Y_xGd_{1-x}VO_4$ laser with a KTP crystal as an intracavity SRS medium is illustrated in Fig. 6-1. Spontaneous Raman spectral data on KTP crystal reveal that the strongest Raman scattering was observed near 270 cm^{-1} [7]. With a fundamental pump wavelength of 1064 nm, the first four Stokes lines for the most intense Raman peak can be calculated to be 1096, 1129, 1166, and 1204 nm, respectively. The flat front mirror has antireflection coating (R<0.2%) at the diode wavelength on the entrance face, high-reflection coating (R>99.5%) at the lasing and SRS wavelengths, and high-transmission coating (T>90%) at the diode wavelength on the other surface. The

flat output coupler has the reflectivities R=99.6% at 1064 nm, R=99.1% at 1096 nm, R=86.3% at 1129 nm, R=48.0% at 1166 nm, and R=27.5% at 1204 nm. Note that the present output coupler is selected, but not optimized, from the available mirrors in our laboratory. Nevertheless, experimental results reveal that cascade SRS operation including the first four Stokes components can be obtained.

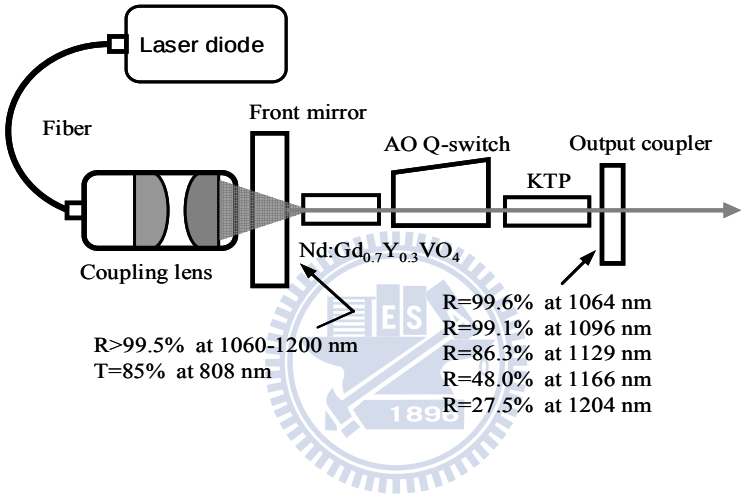

Fig. 6-1. Experimental setup of a diode-pumped actively Q-switched Nd:$Y_{0.3}Gd_{0.7}VO_4$ laser with a KTP crystal as an intracavity SRS medium.

The pump source is an 808-nm fiber-coupled laser diode (Coherent Inc.) with a core diameter of 0.8 mm, a numerical aperture of 0.16, and a maximum output power of 16 W. A focusing lens with a 12.5-mm focal length and 85% coupling efficiency is used to reimage the pump beam into the laser crystal. The average radius of the pump beam is near 0.35 mm. The active laser medium is a 0.2-at.% Nd:$Y_{0.3}Gd_{0.7}VO_4$ crystal with a length of 10 mm. The Raman medium is a 20-mm-long KTP crystal with a cutting angle along the *x* axis ($\theta=90^o$ and $\phi=0^o$). Both sides of the Nd:$Y_{0.3}Gd_{0.7}VO_4$

and KTP crystals are coated for antireflection at 1000–1200 nm (R<0.2%). In addition, they are wrapped with indium foil and mounted in a water-cooled copper block. The water temperature is maintained at 20 ^{o}C. The 30-mm-long acousto-optic Q-switch device (NEOS Model 33027-15-2-1) had antireflection coating at 1064 nm on both faces and is driven at a 27.12-MHz center frequency with 15.0 W of rf power.

The present cavity is a flat–flat resonator that is stabilized by the thermally induced lens in the laser crystal. This concept was found nearly simultaneously by Zayhowski and Mooradian [25] and by Dixon *et al* [26]. A linear flat–flat cavity is an attractive design because it reduces complexity and makes the system compact and rugged. However, the end-pump-induced thermal lens is not a perfect lens, but is rather a lens with aberration. It has been found that the thermally induced diffraction loss is a rapidly increasing function of the mode-to-pump ratio at a given pump power. When the incident pump power is greater than 5 W, the optimum mode-to-pump ratio is found to be in the range of 0.8-1.0 [27]. Since the laser rod is very close to the front mirror, the laser mode size in the gain medium can be given by [28]

$$\omega_l = \sqrt{\frac{\lambda}{\pi}} \frac{\left(L\ f_{th}\right)^{1/4}}{\left(1 - L/f_{th}\right)^{1/4}} \tag{6-1}$$

where f_{th} is the effective focal length of the thermal lens,

$$L = L_{cav} + l\,(1/n - 1) + l_{\mathrm{KTP}}\,(1/n_{\mathrm{KTP}} - 1) + l_{\mathrm{Q}}\,(1/n_{\mathrm{Q}} - 1) \tag{6-2}$$

is the effective cavity length, L_{cav} is the cavity length, l is the length of the gain medium, n is the refractive index of the gain medium, l_{KTP} is the length of the KTP

crystal, n_{KTP} is the KTP refractive index for the output laser beam, l_Q is the length of the Q-switched crystal, and n_Q is the refractive index of the Q-switched crystal for the output laser beam. The effective focal length for an end-pumped laser rod can be approximately expressed as

$$f_{th} = C\,\omega_p^2 / P_{in} \tag{6-3}$$

where ω_p is the pump size in the unit of mm, P_{in} is the incident pump power in the unit of watt (W), and C is a proportional constant in the unit of W/mm. The effective focal length at a given pump power can be experimentally estimated from the longest cavity length with which a flat-flat cavity can sustain stable. Therefore, we perform the laser experiments to obtain the critical cavity lengths for different pump powers at a fixed pump size. We use Eq. (6-3) to fit the experimental results and find the constant C to be approximately 1.7×10^4 W/mm.

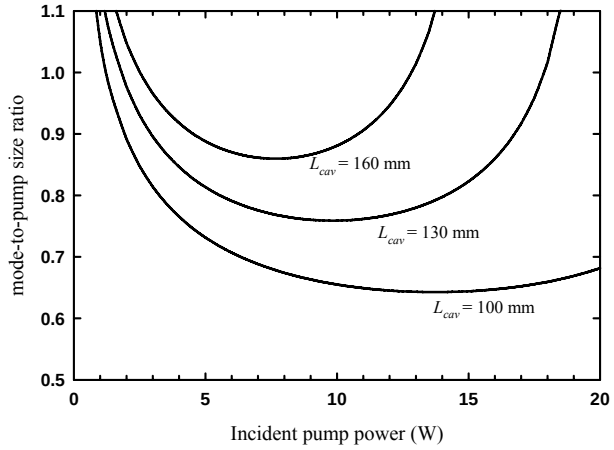

Fig. 6-2. Dependence of the mode-to-pump size ratio on the incident pump power for several cavity lengths .

The dependence of the mode-to-pump size ratio on the pump power for the present cavity is calculated by using Eqs. (6-1)-(6-3) and the following parameters: C=1.7×10^4 W/mm, ω_p =0.35 mm, l_Q=30 mm, n_Q=1.5, l=10 mm, n=2.16, n_{KTP}=1.75, and l_{KTP}=20 mm. The calculated results for several cavity lengths are shown in Fig. 6-2. It is clear that the mode-to-pump size ratio is around 0.8 at L_{cav}=130 mm for the pump powers in the range of 5~15 W, leading to a good compromise between overlapping efficiency and thermal effect. As a consequence, we arrange the cavity length to be 130 mm.

6.2.2 Experimental Results and Discussions

Figure 6-3 depicts the average output powers with respect to the incident pump power at the 50-kHz Q-switching operation for the setup shown in Fig. 6-1. The threshold powers for the first Stokes mode is 4.5 W. The first Stokes output at 1096 nm increases with the pump power until the second Stokes threshold of 6.2 W is reached, and it is then clamped at a level of 50 mW. When the pump power is increased to approximately 8.2 W, the third Stokes radiation at 1166 nm start to be emitted and the second Stokes emission is almost saturated at a power of 0.6 W. The slope efficiency of the second Stokes at 1129 nm with respect to the pump power from 6.2 W to 8.2 W is approximately 30%. At pump power higher than the fourth Stokes threshold of 10.5 W, the total output power is nearly clamped at 0.92 W. The maximum output powers at 1096 nm, 1129 nm, 1166 nm, and 1204 nm are approximately 0.05 W, 0.61 W, 0.25 W, and 0.11 W, respectively. Note that the present output coupler is not optimized for the overall conversion efficiency.

Therefore, it is possible to obtain a higher output power with the optimum output coupler. On the other hand, the optimum conversion efficiency for the specific Stokes component can be obtained by optimizing the output coupler with high reflection for the lower order Stokes modes and high transmission for the next order Stokes mode. Furthermore, no damage to the KTP crystal is observed over several hours of operation, and the laser performance is reproducible on a day-to-day basis.

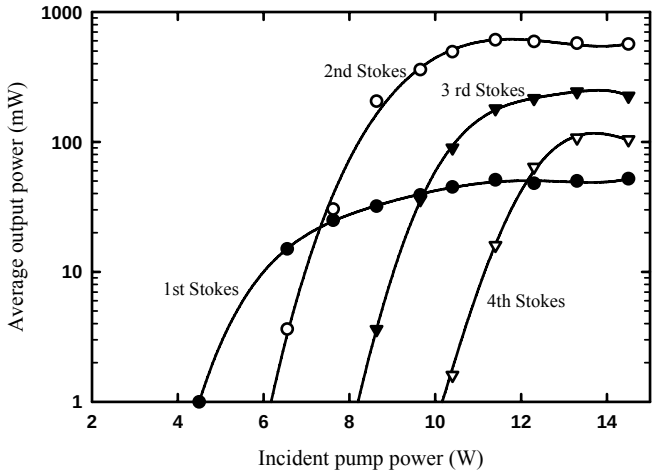

Fig. 6-3. Dependence of the average output power on the incident pump power for Q-switching operation at 50 kHz.

An optical spectrum analyzer (Advantest Q8381A) is used to measure the spectral information of the laser output. The present spectrum analyzer employing a diffraction lattice monochromator can be used for high-speed measurement of pulse light with a resolution of 0.1 nm. Figure 6-4 shows the emission spectrum measured at the output of the Raman laser for the pump power of 14.0 W. It can be seen that the optical spectra include the main output of the different order Stokes lines as well as

the residual outputs of the fundamental wave at 1064 nm. The frequency shift between the Stokes and the laser lines is in good agreement with the asymmetric bending mode of a distorted TiO_6 octahedron 270 cm^{-1} [7].

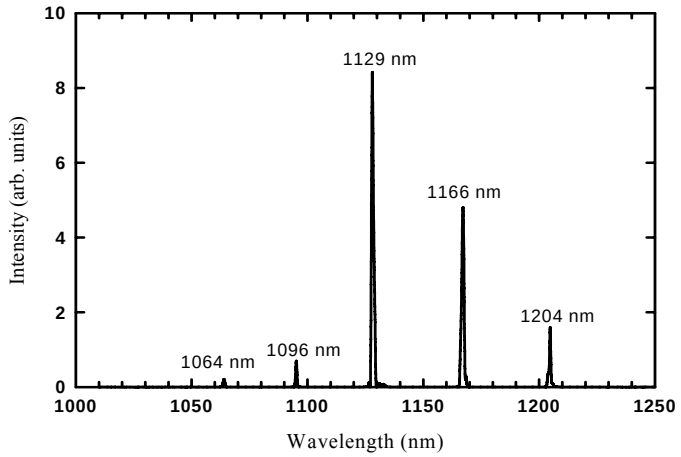

Fig. 6-4. Emission spectrum measured at the output of the Raman laser for the pump power of 14 W.

The temporal behavior of the output pulse is recorded by a LeCroy digital oscilloscope (Wavepro 7100, 1-GHz bandwidth, 10 G samples/sec) with two InGaAs p-i-n photodiodes for measuring the output pulses at fundamental and SRS emissions, respectively. The temporal characteristics of the fundamental pulse and Raman pulses are depicted in Figs. 6-5(a)-(d) for four different pump powers of 5.0 W, 7.0 W, 9.0 W and 11.0 W. It can be seen that when the intracavity power density at the fundamental wavelength reaches the SRS threshold, the fundamental pulse is rapidly converted the Stokes output. Although the channel numbers of the oscilloscope are

not sufficient to separate the temporal profiles of each Stokes orders, the experimental results in Figs. 6-5(a)-(d) apparently reveal that various order Stokes pulses are generated step by step with increasing the pump power. Furthermore, the Q-switched pulse envelope displays clear modulated pulses. The separation of the modulated pulses was found to be 0.86 ns, which matched exactly with the cavity roundtrip time. Therefore, the modulated pulses can be confirmed to come from the longitudinal-mode beating. The estimated energy of the highest pulse inside envelope was found to be close to 18.4 μJ and the maximum peak power was greater than 2 kW.

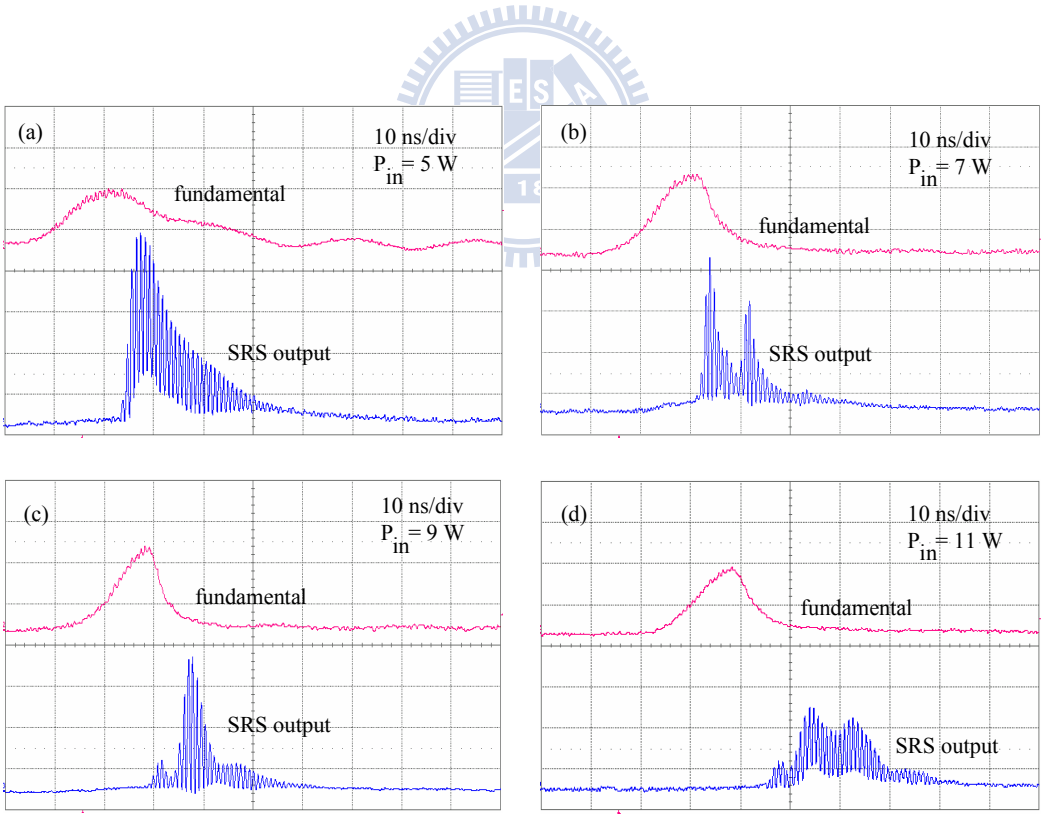

Fig. 6-5. Temporal characteristics of the fundamental pulse and Raman pulses (a) 5 W, (b) 7 W, (c) 9 W, (d) 14 W

6.3 Pattern Formation of Diode-Pumped Multi-Frequency Q-Switched Laser with Intracavity Cascade Raman Emission in KTA Crystal [Future Work]

We find patterns like “cross” in diode-pumped actively Q-switched cascade Nd:YAG/KTA Raman laser with a KTA crystal which simultaneously serves as Raman, SHG, and three-wave mixing crystal. The experimental setup is similar to Fig.6-1 with different laser and Raman media. The present laser medium is a 0.8-at.% Nd:YAG crystal with a length of 10 mm. The Raman medium is a 20-mm-long KTA crystal with a cutting angle along the *x* axis ($\theta=90^o$ and $\phi=0^o$). Spontaneous Raman spectral data on KTA crystal reveal that the strong Raman scattering is observed near 235 and 273cm^{-1} as shown in Fig.2-4(C) with linewidths around 5.4 amd 4.7 cm^{-1} summarized in table 2-4, respectively. With a fundamental pump wavelength of 1064 nm, the first two Stokes lines for the most intense Raman peak at 235 cm^{-1} can be calculated to be 1091 and 1120 nm and the second Stokes lines for the Raman peak at 273 cm^{-1} can be calculated to be 1130 nm. With a pump wave of 1130 nm, the first two Stokes lines can be calculated to be 1160 and 1192 nm for the most intense Raman peak at 235 cm^{-1}. The flat output coupler has the reflectivities R=99.6% at 1064 nm, R=99.3% at 1091 nm, R=96.5% at 1120 nm, R=83.6% at 1130 nm, R=50% at 1160 nm, and R=4.9% at 1192 nm. The multi-wavelength emission spectra in the near-infrared and visible regions are shown in Fig. 6-6 and Fig.6-7. The wavelengths of visible emission converted through SHG and SFG are summarized in table 6-1.

Moreover, the interesting “cross” far-field patterns of green Raman emission are observed as shown in Fig.6-8. The investigation of the pattern formation will be carried out in the future work.

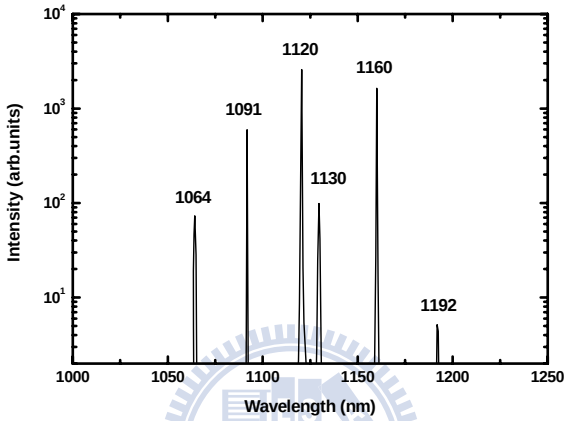

Fig. 6-6. Optical spectrum of the multi-wavelength diode-pumped actively Q-switched cascade Nd:YAG/KTA Raman laser in the near-infrared region with a fundamental wavelength of 1064 nm.

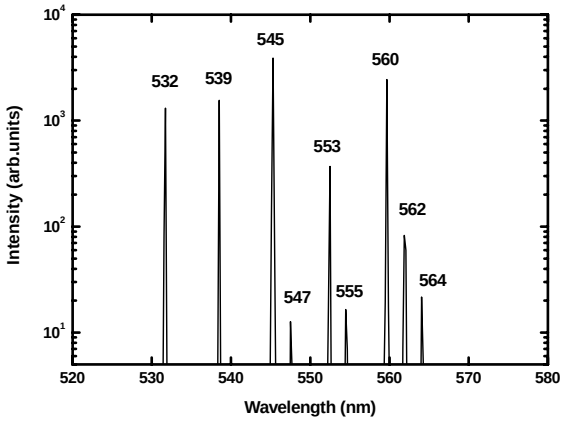

Fig. 6-7. Optical spectrum of the multi-wavelength diode-pumped actively Q-switched cascade Nd:YAG/KTA Raman laser in the visible region with a fundamental wavelength of 1064 nm.

Infrared λ (nm)	SHG (nm)
1064	532
1091	545
1095	547
1120	560
1130	564

Infrared λ_1, λ_2 (nm)	SFG (nm)
1064, 1091	539
1091, 1120	553
1091, 1130	555
1120, 1130	562

Table. 6-1. The green-emission generation of diode-pumped actively Q-switched cascade Nd:YAG/KTA Raman laser with a fundamental wavelength of 1064 nm.

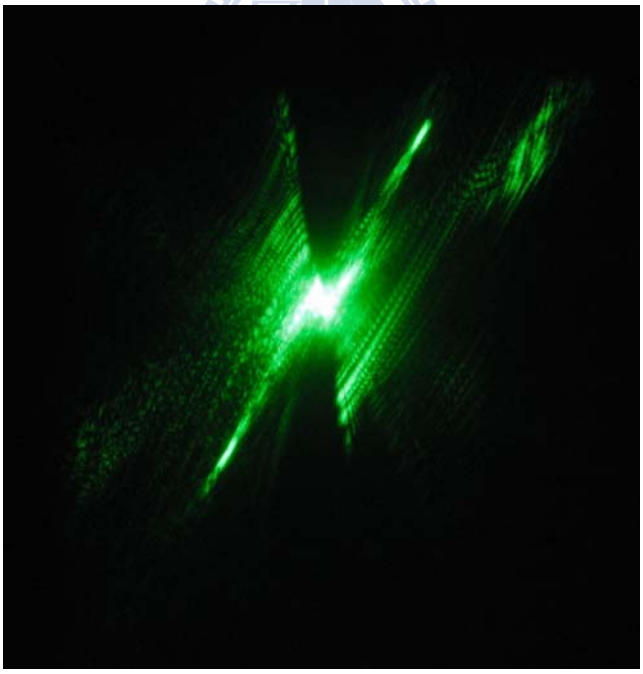

Fig. 6-8. The far-field pattern of the diode-pumped actively Q-switched cascade Nd:YAG/KTA Raman green emission with a fundamental wavelength of 1064 nm.

In addition, the experimental setup is design for the fundamental laser at 1.3 μm. For the most intense Raman peak at 235 cm^{-1}, the first three Stokes lines can be calculated to be 1362, 1406, and 1454 nm with a fundamental wave of 1319 nm, and the first three Stokes lines can be calculated to be 1382, 1429, and 1479 nm with a fundamental wave of 1338 nm. The flat output coupler has the reflectivities R=99.6% at 1319 nm, R=99.2% at 1338 nm, R=99.2% at 1362 nm, R=99.1% at 1382 nm, R=98.7% at 1406 nm, R=97.3% at 1428 nm, R=71.2% at 1454 nm, R=51.3% at 1478 nm, and R=73.8% at 1505 nm. The multi-wavelength emission spectra in the near-infrared, red, and blue emission are shown in Fig. 6-9, Fig.6-10 and Fig.6-11. The wavelengths of red emission converted through SHG and SFG are summarized in table 6-2. The blue emission spectrum converted through three-wave mixing is summarized in table 6-3. Moreover, the interesting “cross” far-field patterns of red and blue Raman emission are shown in Fig.6-12 and Fig.6-13, respectively. The patterns of conical SHG and three-wave mixing are also observed and will be discussed in section 7.1. The investigation of the pattern formation should also be carried out in the future work.

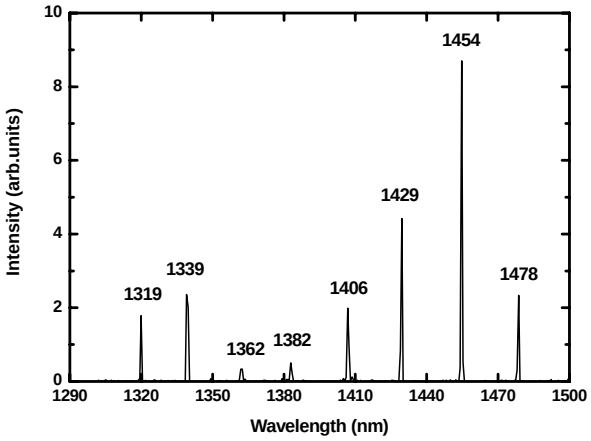

Fig. 6-9. Optical spectrum of the multi-wavelength diode-pumped actively Q-switched cascade Nd:YAG/KTA Raman laser in the near-infrared region with fundamental wavelengths of 1319 and 1338 nm.

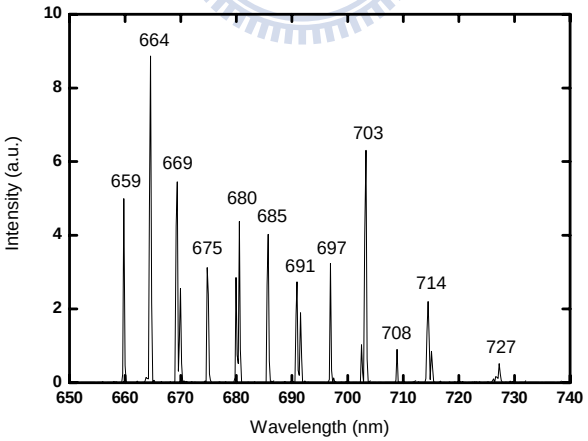

Fig. 6-10. Optical spectrum of the multi-wavelength diode-pumped actively Q-switched cascade Nd:YAG/KTA Raman laser at red wavelength with fundamental wavelengths of 1319 and 1338 nm.

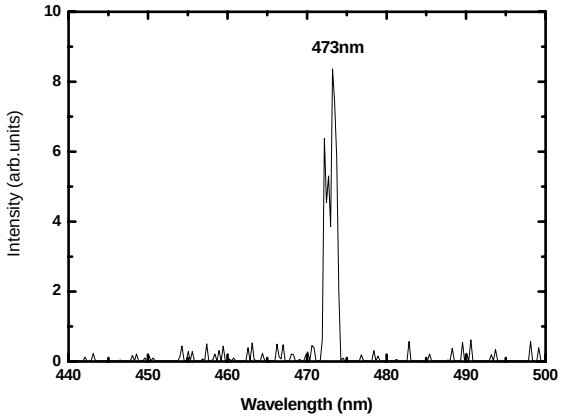

Fig. 6-11. Optical spectrum of the multi-wavelength diode-pumped actively Q-switched cascade Nd:YAG/KTA Raman laser at the blue wavelength with fundamental wavelengths of 1319 and 1338 nm.

Infrared λ (nm)	SHG (nm)
1319	659
1338	669
1362	680
1382	691
1406	703
1429	714
1454	727

Infrared λ_1, λ_2 (nm)	SFG (nm)
1319, 1338	664
1338, 1362	675
1362, 1382	685
1382, 1406	697
1406, 1429	708

Table. 6-2. The red-emission generation of diode-pumped actively Q-switched cascade Nd:YAG/KTA Raman laser with fundamental wavelengths of 1319 and 1338 nm.

Infrared λ_1, λ_2, and λ_3 (nm)
1319, 1478, 1478
1338, 1454, 1478
1362, 1429, 1478
1362, 1454, 1454
1406, 1382, 1478
1454, 1382, 1429
1406, 1429, 1429
1406, 1406, 1454

Table. 6-3. The 473-nm blue-emission generation of diode-pumped actively Q-switched cascade Nd:YAG/KTA Raman laser with fundamental wavelengths of 1319 and 1338 nm.

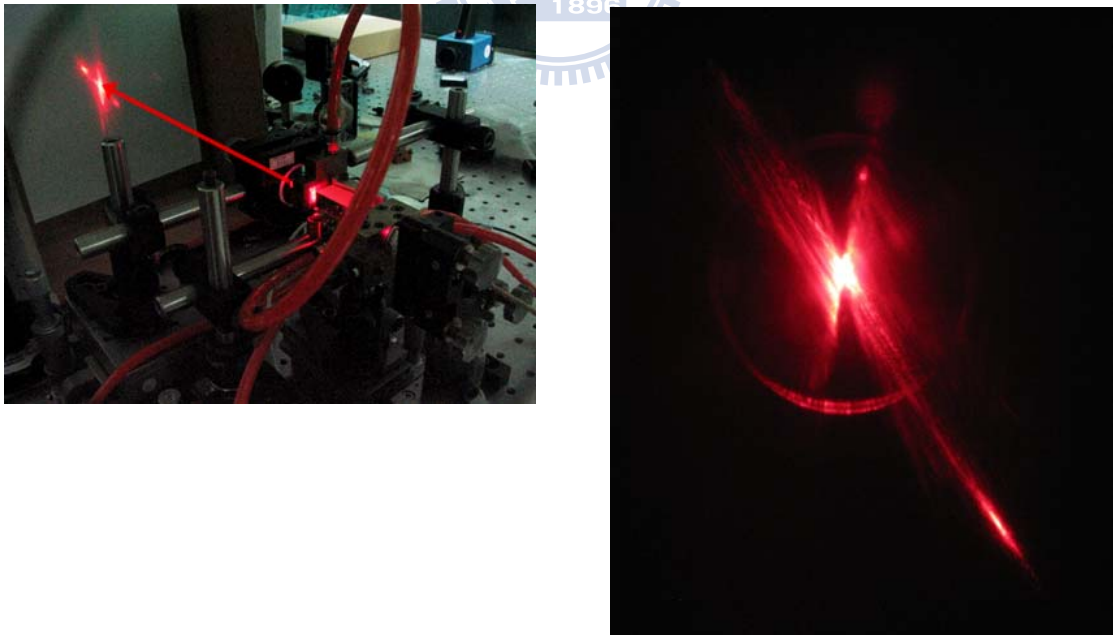

Fig. 6-12. The far-field patterns of the diode-pumped actively Q-switched cascade Nd:YAG/KTA Raman red emission with fundamental wavelengths of 1319 and 1338 nm.

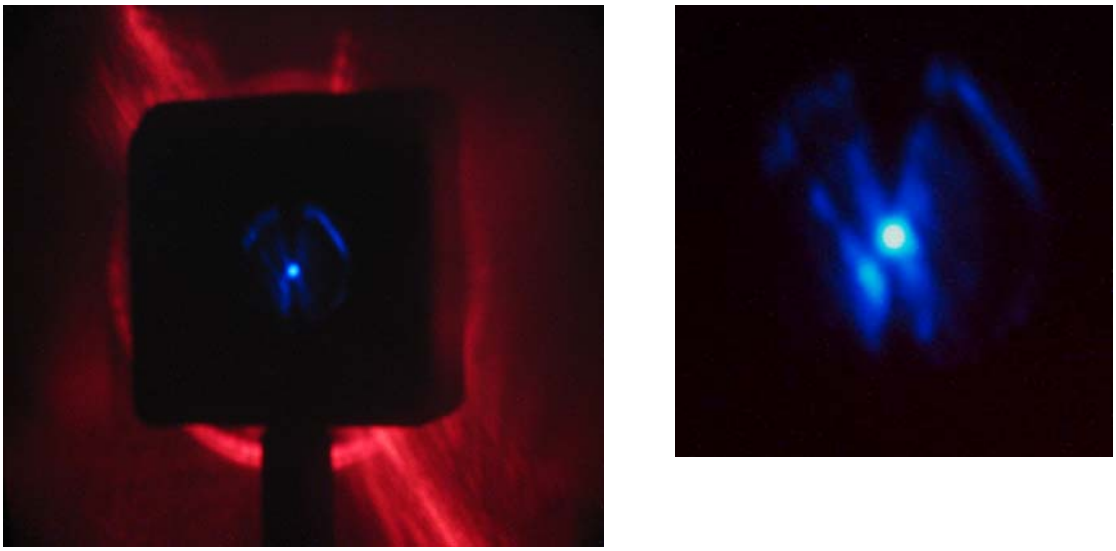

Fig. 6-13. The far-field patterns of the diode-pumped actively Q-switched cascade Nd:YAG/KTA Raman blue emission with fundamental wavelengths of 1319 and 1338 nm.

6.4 Conclusion

We have developed a diode-pumped actively Q-switched mixed Nd:$Y_{0.3}Gd_{0.7}VO_4$ laser with an intracavity KTP crystal to produce cascade SRS emission up to the fourth order. With an incident pump power of 14 W and a repetition rate of 50 kHz, the average output powers at 1096 nm, 1129 nm, 1166 nm, and 1204 nm are approximately 0.05 W, 0.61 W, 0.25 W, and 0.11 W, respectively. The maximum peak power is found to be higher than 2 kW. Moreover, there are interesting “cross” transverse patterns of Raman emission with KTP or KTA as Raman crystal.

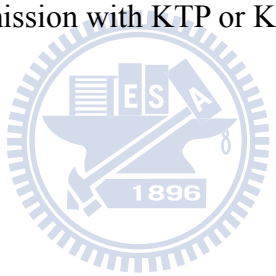

Chapter 7

Pattern Formation of Conical Second Harmonic Generation

7.1 Conical Second Harmonic Generation

Second harmonic generation (SHG) is a widely used method of wavelength conversion based on second-order nonlinear optics. In additional to developing efficient frequency-doubled lasers with collinear SHG, there are interesting research topics about noncollinear conical SHG [1-4]. It has been verified that the formation of conical SHG is resulted from the random scattering and phase matching condition [4]. The coherent waves are randomly scattered while passing through a nonlinear crystal with extended defects shown as Fig. 7-1. The phase-matching condition for the conical SHG in a nonlinear crystal with disordered structure is generally written as

$$\vec{k}_1 + \vec{k}_1' = \vec{k}_2 \tag{7-1}$$

As shown in Fig. 7-2(a), where $\vec{k}_1$ is the axial fundamental wave, $\vec{k}_1'$ is the scattered off-axis fundamental wave, and $\vec{k}_2$ is the phase-matched off-axis SHG wave. The cone angles φ is determined by the effective refractive indices of nonlinear crystal. The far-field pattern comprises the phase-matched off-axis SHG waves with cone angles φ as shown in Fig. 7-2(b).

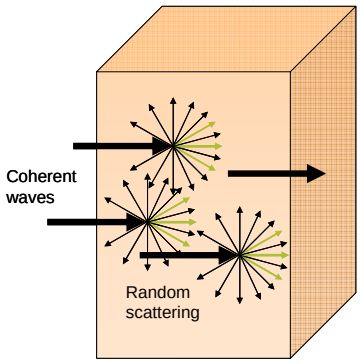

Fig. 7-1. The coherent waves are randomly scattered when passing through a nonlinear crystal with extended defects.

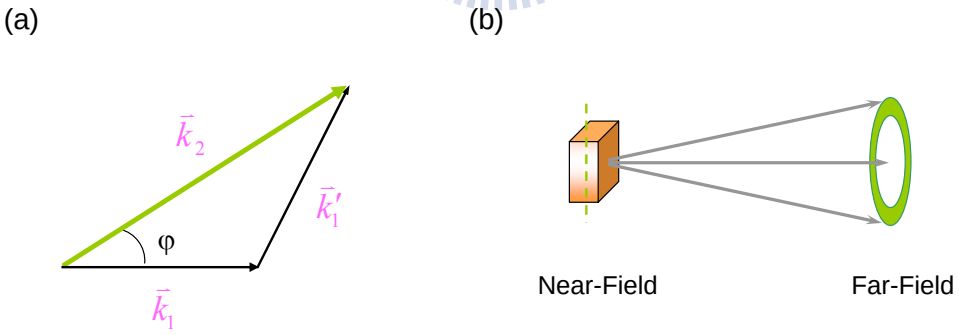

Fig. 7-2. (a) Phase-matching diagram for conical SHG process in which $\vec{k}_1$ is the axial fundamental beam, $\vec{k}_1'$ is the scattered off-axis fundamental beam, and $\vec{k}_2$ is the phase-matched off-axis SHG beam. (b) The formation of typical far-field pattern of conical SHG.

7.2 Frequency-Doubled Q-Switched Nd:YVO_4 Self-Raman Laser with Intracavity KTP as SHG Crystal [Future work]

The far-field patterns of conical SHG are observed in a diode-pumped actively Q-switched Nd:YVO_4 self-Raman laser with intracavity SHG in a KTP crystal. The experimental setup is shown in Fig.7-3. With a fundamental pump wavelength of 1064 nm, the first Stokes line for the most intense Raman peak at 890 cm^{-1} can be calculated to be 1176 nm. The flat output coupler has the high-reflection coating at 1064 nm (R>99.8%) and 1176 nm (R=98%), and partial-transmission coating at 588 nm (T=66.7%). Note that the present output coupler is selected but not optimized. The present self-Raman laser medium is a 0.1-at.% Nd:YVO_4 crystal with a length of 12 mm. The SHG medium is a 10-mm-long KTA crystal with a cutting angle ($\theta=70.2^o$ and $\phi=0^o$) to satisfy the type Ⅱ SHG phase matching condition of the first Stokes line at 1176 nm. The experimental optical spectra of laser output in the near-infrared and visible regions are shown in Fig. 7-4 and Fig.7-5, respectively. The yellow-green light at 559 nm is converted from sum-frequency-mixing of 1064 and 1176 nm. The yellow-orange light at 588 nm is converted from frequency-doubling of 1176 nm.

The experimental visible far-field wave pattern of conical SHG is observed as shown in Fig.7-6. The investigation of the pattern formation will be carried out in the future.

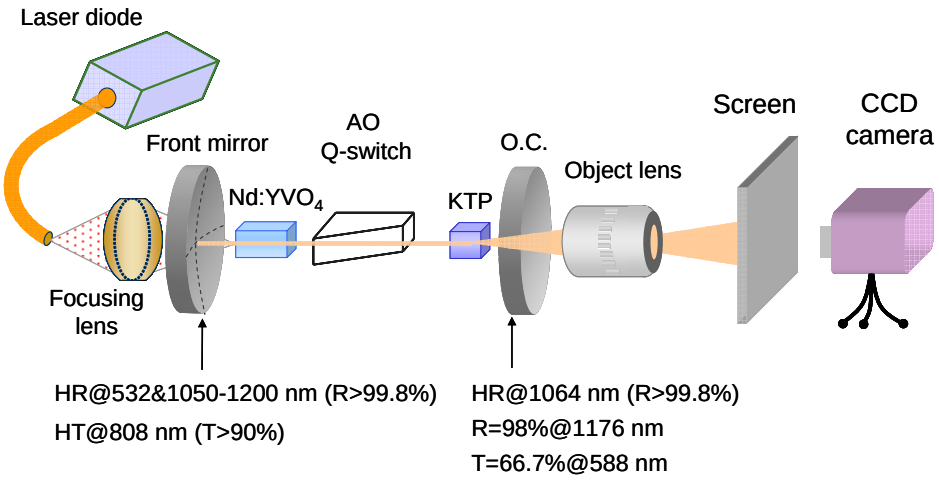

Fig. 7-3. Experimental setup of a diode-end-pumped actively Q-switched Nd:YVO_4 self-Raman laser with intracavity SHG in the KTP crystal.

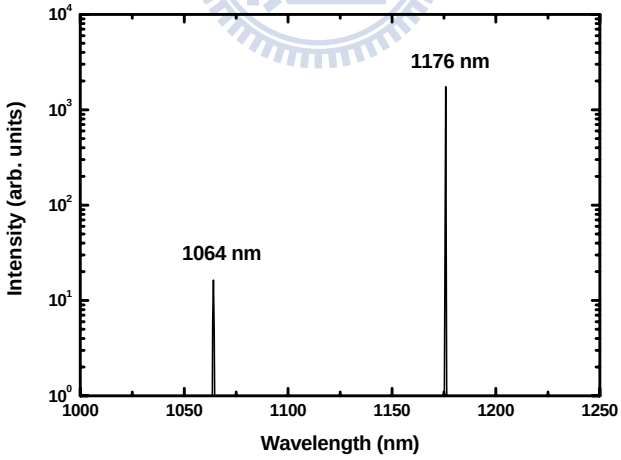

Fig. 7-4. Optical spectrum of the diode-pumped actively Q-switched frequency-doubled Nd:YVO_4/KTP self-Raman laser in the near-infrared region.

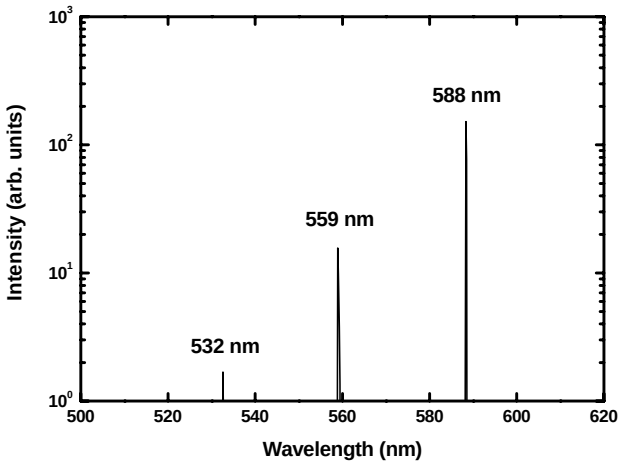

Fig. 7-5. Optical spectrum of the diode-pumped actively Q-switched frequency-doubled Nd:YVO_4/KTP self-Raman laser in the visible region.

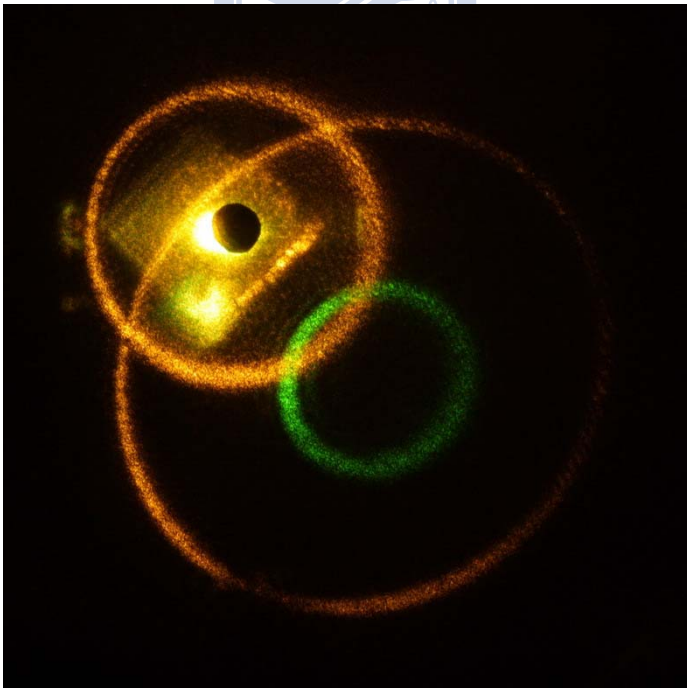

Fig. 7-6. The experimental visible far-field wave pattern of the diode-pumped actively Q-switched frequency-doubled Nd:YVO_4/KTP self-Raman laser.

7.3 Frequency-Doubled Q-Switched Nd:YAG Laser with Intracavity GdCOB as SHG Crystal

In 2006, Chen et al. originally develop an intracavity conical SHG scheme to investigate the spatial structure of transverse two-dimentional (2D) disordered wave functions with weak localization [4]. With a nonlinear crystal with extended defects as a SHG medium in Q-switched laser, the conical SHG is efficiently generated. By measuring near-field patterns of conical SHG, the disordered wave functions can be explored. It has been confirmed that using conical SHG can serve as a diagnostic tool for topographical characterization of crystals.

7.3.1 Experimental Setup

The experimental setup of a diode-pumped actively Q-switched Nd:YAG laser with intracavity SHG in a GdCOB crystal is shown in Fig. 7-7. The laser crystal is a 10-mm-long 0.8-at.% Nd^{3+}:YAG crystal. The GdCOB crystal is cut for type I frequency doubling in the *XY* planes ($\theta=90^o$, $\phi=46^o$) with a length of 6 mm and a cross section of 3 mm × 3 mm. Both sides of the Nd:YAG and GdCOB crystals are coated for antireflection at 1064 nm (R<0.2%). In addition, both of the Nd:YAG and GdCOB crystal are wrapped with indium foil and mounted in a water-cooled copper block. The water temperature is maintained at 20°C. The pump source is an 808-nm fiber-coupled laser diode with a core diameter of 1 mm and a maximum power of 10 W. The 30-mm-long acousto-optic Q-switch (NEOS Technologies) has

antireflectance coatings at 1064 nm on both faces and is driven at a 27.12-MHz center frequency with 15.0 W of rf power. The front mirror is a 500-mm radius-of-curvature concave mirror with antireflection coating at 808 nm on the entrance face (R<0.2%), high-transmission (HT) coating at 808 nm (T>90%), and high-reflection (HR) coating at 1064 nm (R>99.8%) and 532 nm (R>99%) on the other face. The output coupler is a flat mirror with high-reflection coating at 1064 nm (R>99.8%) and high-transmission coating at 532 nm (T>85%).

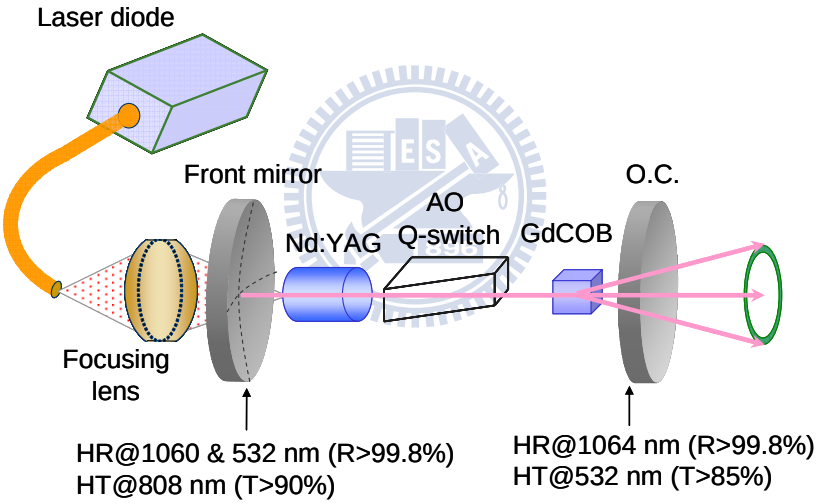

Fig. 7-7. Experimental setup of a diode-end-pumped actively Q-switched Nd:YAG laser with intracavity SHG in the GdCOB crystal.

7.3.2 Experimental Results and Discussions

The pulse repetition rate for the Q-switched pulses is fixed at 30 kHz. The lasing thresholds for the axial and conical SHG beams are nearly the same and approximately 2 W. The output powers of both axial and conical SHG are on the

order of 1 mW with a pump power of 7 W. The experimental results reveal that the cone angles of the far-field patterns are almost the same for all the transverse positions of the GdCOB crystal as shown in Figs. 7-8. However, the near-field patterns are found to be profoundly related to the topographical characterization of the nonlinear crystal. Figures 7-9(a)-(c) show the three corresponding examples of the experimental near-field wave patterns of conical SHG measured at different transverse positions of the GdCOB crystal. Note that the paraxial propagation and the phase matching condition lead the present conical SHG to be a kind of 2D random scattering process. It can be seen that the experimental near-field pattern of Fig. 7-9(a) represents 2D disordered wave function with weak localization, that is, 2D chaotic wave. Berry conjectured that the eigenstates of chaotic systems can be described by a superposition of numerous plane waves with random amplitudes *a*, directions and relative phases ϕ, but constant wave number *k* [5]:

$$\psi(\vec{r}) = \sum_n a_n \cdot \exp[i(\vec{k}_n \cdot \vec{r} + \phi_n)] \tag{7-2}$$

The experimental near-field pattern of Fig. 7-9(c) represents zero-order quasi-Bessel beam. The integral representation of Bessel function is expressed as

$$J_n(kr) = \frac{1}{2\pi}\int_0^{2\pi} e^{i(kr\sin\theta - n\theta)} d\theta \tag{7-3}$$

Now we consider zero-order Bessel function (n=0) and θ is substituted for $\frac{\pi}{2} - \alpha + \theta$. The zero-order Bessel function can be expressed by

$$J_0(kr) = \frac{1}{2\pi}\int_0^{2\pi} e^{ikr\sin\theta} d\theta = \frac{1}{2\pi}\int_0^{2\pi} e^{ikr\cos(\alpha-\theta)} d\theta \tag{7-4}$$

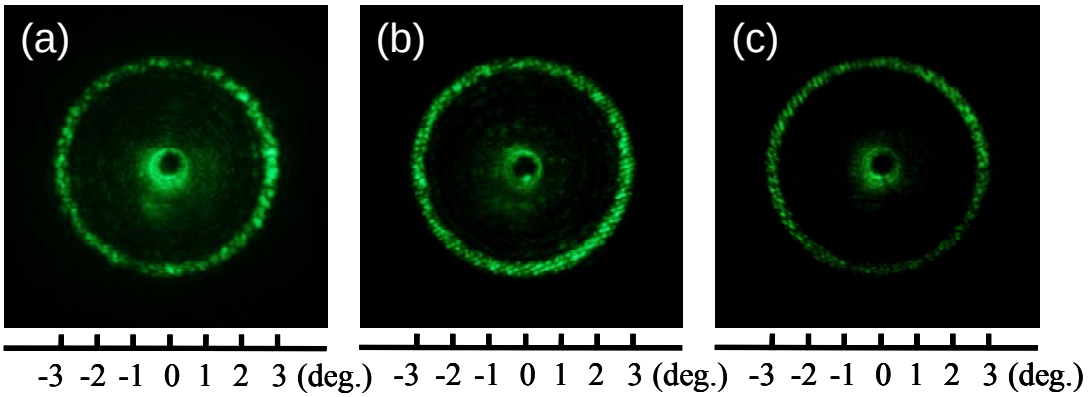

Fig. 7-8. Three examples of the experimental far-field wave patterns measured at different transverse positions of the GdCOB crystal.

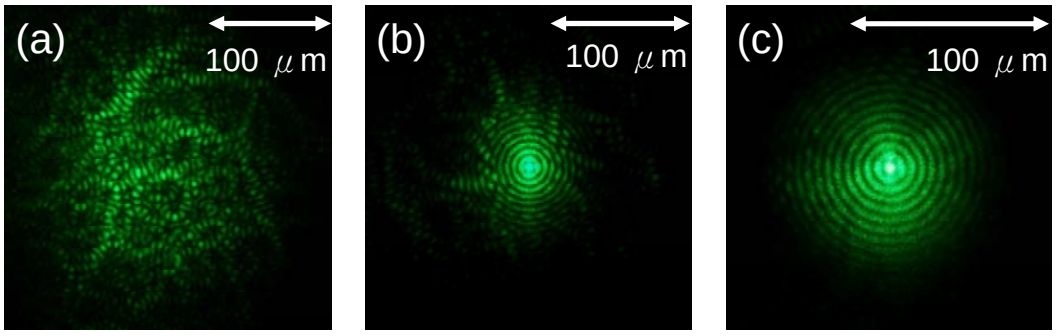

Fig. 7-9. Three examples of the experimental near-field wave patterns corresponding to the far-field wave patterns shown in Figs. 7-8(a)-(c), respectively.

As the k, r -space diagram shown in Fig. 7-10, $kr\cos(\alpha-\theta)$ can be expressed by

$$\begin{aligned} kr\cos(\alpha-\theta) &= kr(\cos\alpha\cos\theta+\sin\alpha\sin\theta) \\ &= k_x x + k_y y = \vec{k}\cdot\vec{r} \end{aligned} \tag{7-5}$$

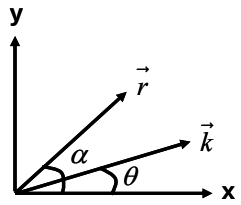

Fig. 7-10. The k, r -space diagram of plane wave

Therefore zero-order Bessel beam can be obtained from a superposition of numerous plane waves with constant amplitude, phases, and wave number *k*, but different directions.

$$J_0(kr) = \frac{1}{2\pi}\int_0^{2\pi} e^{i\vec{k}\cdot\vec{r}}d\theta = \frac{1}{2\pi}\sum_{s=0}^{\infty} e^{i\vec{k}_s\cdot\vec{r}} \tag{7-6}$$

From Eqs. (7-2) and (7-6), it can be found that both chaotic and Bessel beams are resulted from a superposition of numerous plane waves. The differences between chaotic and Bessel beams are amplitudes and phases of superposed plane waves.

For paraxial approximation, the longitudinal wave number k_z becomes much greater than k_x and k_z.

$$k_z >> k_x, k_y \tag{7-7}$$

For a single k_z, the transverse wave number k_t can be approximately expressed by

$$k_t = \sqrt{k^2 - k_z^{\,2}} = \sqrt{k_x^{\,2} + k_y^{\,2}} \tag{7-8}$$

With the cone angle of the far-field patterns, the present near-field patterns are associated with a superposition of plane waves with random directions and relative phases ϕ, but constant transverse wave number $k_t=k_2 \sin\varphi$.

$$\begin{aligned}\Psi(\vec{r}') &= \sum_k a_k \cdot e^{i\vec{k}\cdot\vec{r}'} = \sum_{k_x,k_y,k_z} a_k \cdot e^{i(k_x x'+k_y y'+k_z z')} \\ &= e^{ik_z z'} \sum_{k_x,k_y} a_k \cdot e^{i\phi(k_x,k_y)} \cdot e^{i(k_x x'+k_y y')} \\ &= e^{ik_z z'} \int_0^{2\pi} a(\theta) \cdot e^{i\phi(\theta)} e^{ik_t[(\cos\theta)x'+(\sin\theta)y']} d\theta \\ &= e^{ik_z z'} \sum_i^N a_i \cdot e^{i\phi_i} e^{ik_t[(\cos\theta_i)x'+(\sin\theta_i)y']} = e^{ik_z z'} \cdot \Psi(x,y)\end{aligned} \tag{7-9}$$

First we suppose that the amplitudes of plane waves are constant. The numerical near-fields $|\Psi(x,y)|^2$ calculated with Eq. (7-9) are associated with a superposition of monochromatic plane waves with random directions and random relative phases of (0 to 2π), (0 to 1.5π), (0 to 1.2π), (0 to 1π), (0 to 0.5π), and without relative phase shown in Figs. 7-11 (a)-(f), respectively. With random relative phases between 0 to 2π, the numerical near-field exhibits a network of quasilinear ridge structures like 2D chaotic waves as shown in Fig. 7-11(a). With the same phases, the numerical near-field exhibits zero-order Bessel beam as shown in Fig. 7-11(f). The numerical near-fields with a range of random phases smaller than 2π exhibit symmetry-breaking Bessel beam as shown in Figs. 7-11(b)-(e).

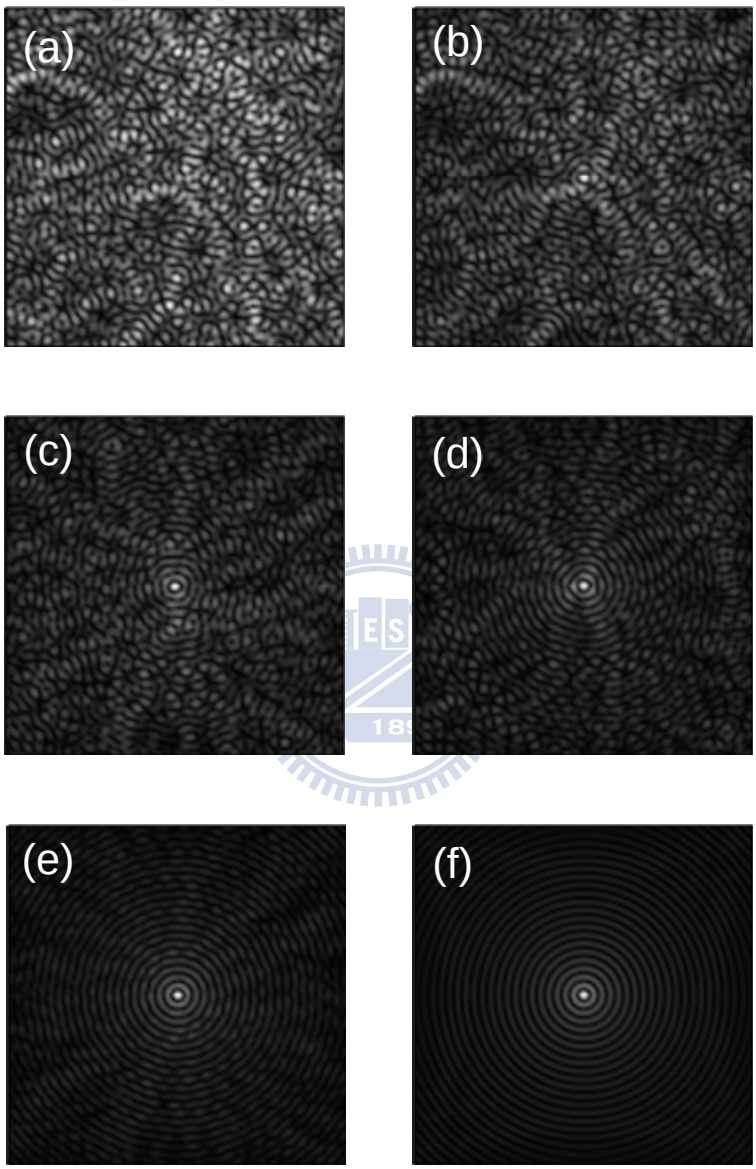

Fig. 7-11. Numerical near-field patterns with random directions and random relative phases between (a) 0 to 2 π, (b) 0 to 1.5 π, (c) 0 to 1.2 π, (d) 0 to 1 π, (e) 0 to 0.5 π, and (f) without relative phase.

In order to coincide with the experimental wave patterns, the wave function of Eq. (7-9) is enveloped with Gaussian distribution. The modified wave function of near-field is expressed as

$$\Psi'(x,y) = e^{\frac{-[(x-b)^2+(y-d)^2]}{2\sigma^2}} \Psi(x,y) \tag{7-10}$$

where the parameters b, d, and σ are constants. The numerical near-fields $\left|\Psi'(x,y)\right|^2$ calculated with Eq. (7-10) correspond to the experimental near-field patterns in Figs. 7-9(a)-(c) and are shown in Figs. 7-12(a)-(c), respetively.

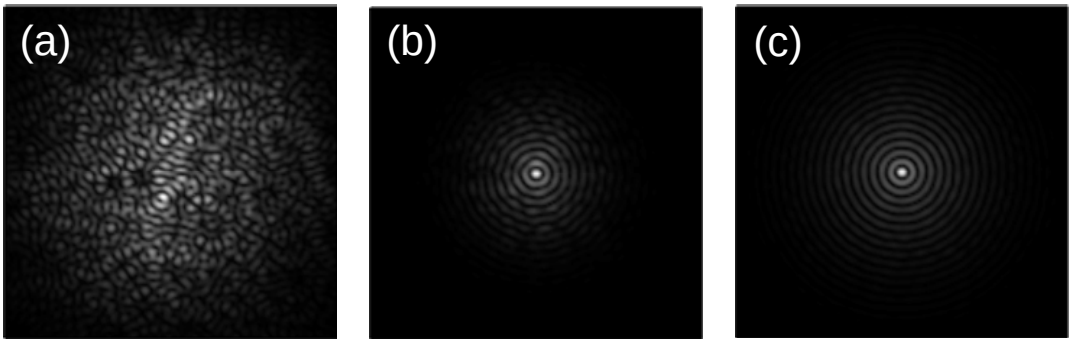

Fig. 7-12. Numerical near-field patterns corresponding to the experimental near-field wave patterns shown in Figs. 7-9 (a)-(c), respectively. The numerical patterns with random directions and random relative phases between (a) 0 to 2 π, (b) 0 to 0.9 π, and (c) 0 to 0.3 π

The numerical far-field wave functions can be obtained by "Fresnel Integrals"

$$\begin{aligned}\Psi(x,y,t) &= \int\int\int e^{\frac{i\pi u^2}{2}} e^{\frac{i\pi v^2}{2}} \Psi'(x,y,0)e^{-i\omega t}\, d\phi\, du\, dv \\ &= \int\int\int e^{\frac{i\pi u^2}{2}} e^{\frac{i\pi v^2}{2}} a\cdot e^{i\phi} e^{i(k_x x + k_y y - \omega t)}\, d\phi\, du\, dv\end{aligned} \tag{7-11}$$

The numerical far-fields patterns calculated with Eq. (7-11) correspond to the numerical near-field patterns in Figs. 7-12(a)-(c) and are shown in Figs. 7-13(a)-(c), respetively.

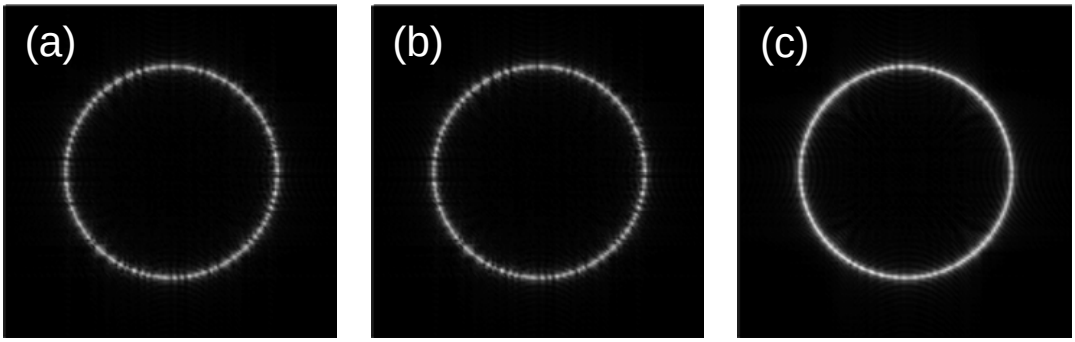

Fig. 7-13. Numerical far-field patterns corresponding to the experimental far-field wave patterns shown in Figs. 7-8(a)-(c), respectively. The numerical patterns with random directions and random relative phases between (a) 0 to 2 π, (b) 0 to 0.9 π, and (c) 0 to 0.3 π.

In addition, the interference patterns of multi-quasi-Bessel beam are observed and shown in Fig. 7-14. The corresponding numerical near-fields of multi-Bessel beam are calculated with a superposition of multiple wave functions expressed as Eq. (7-10) and are shown in Fig. 7-15.

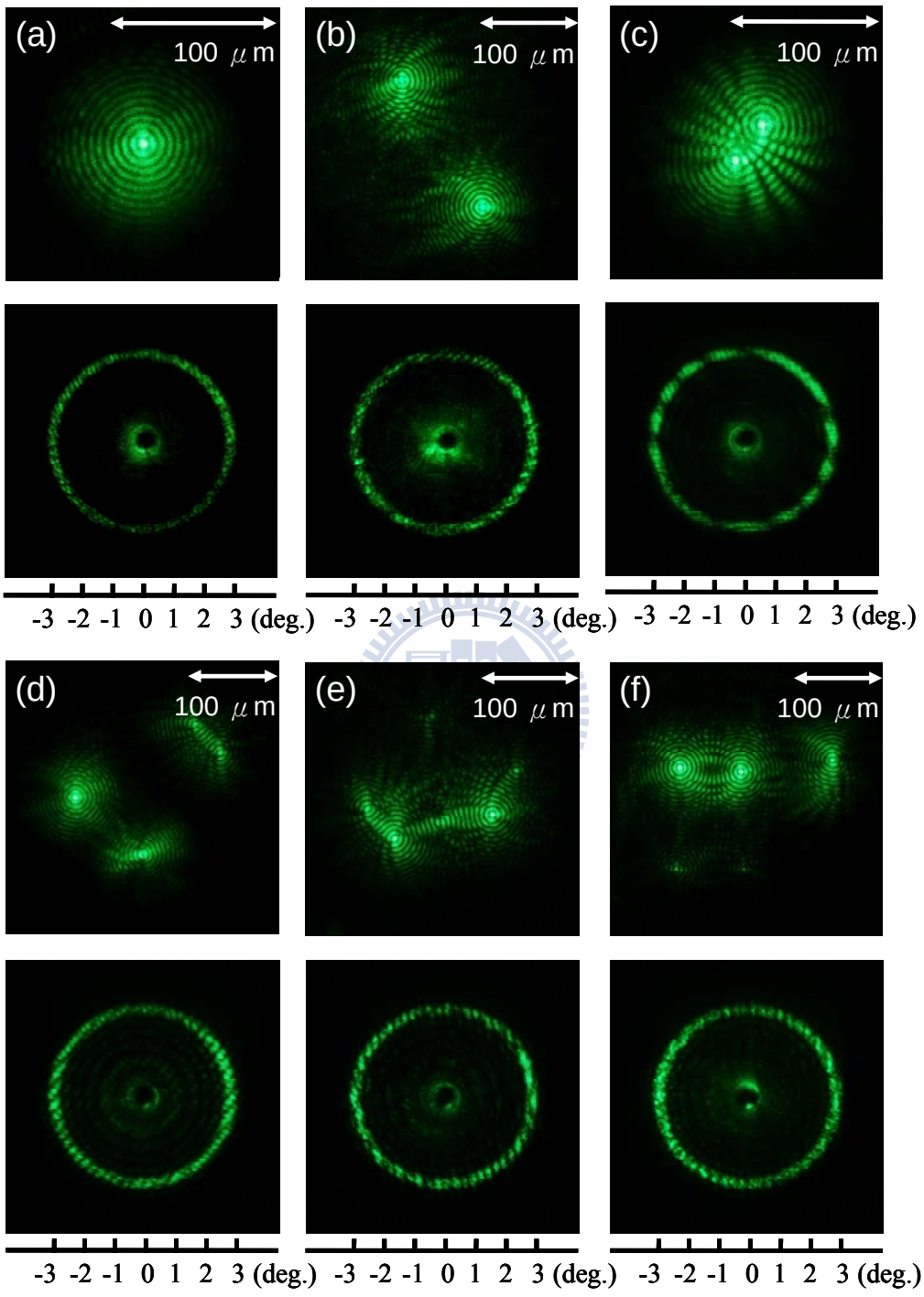

Fig. 7-14. Experimental near-field and far-field interference patterns of multi-quasi-Bessel beams.

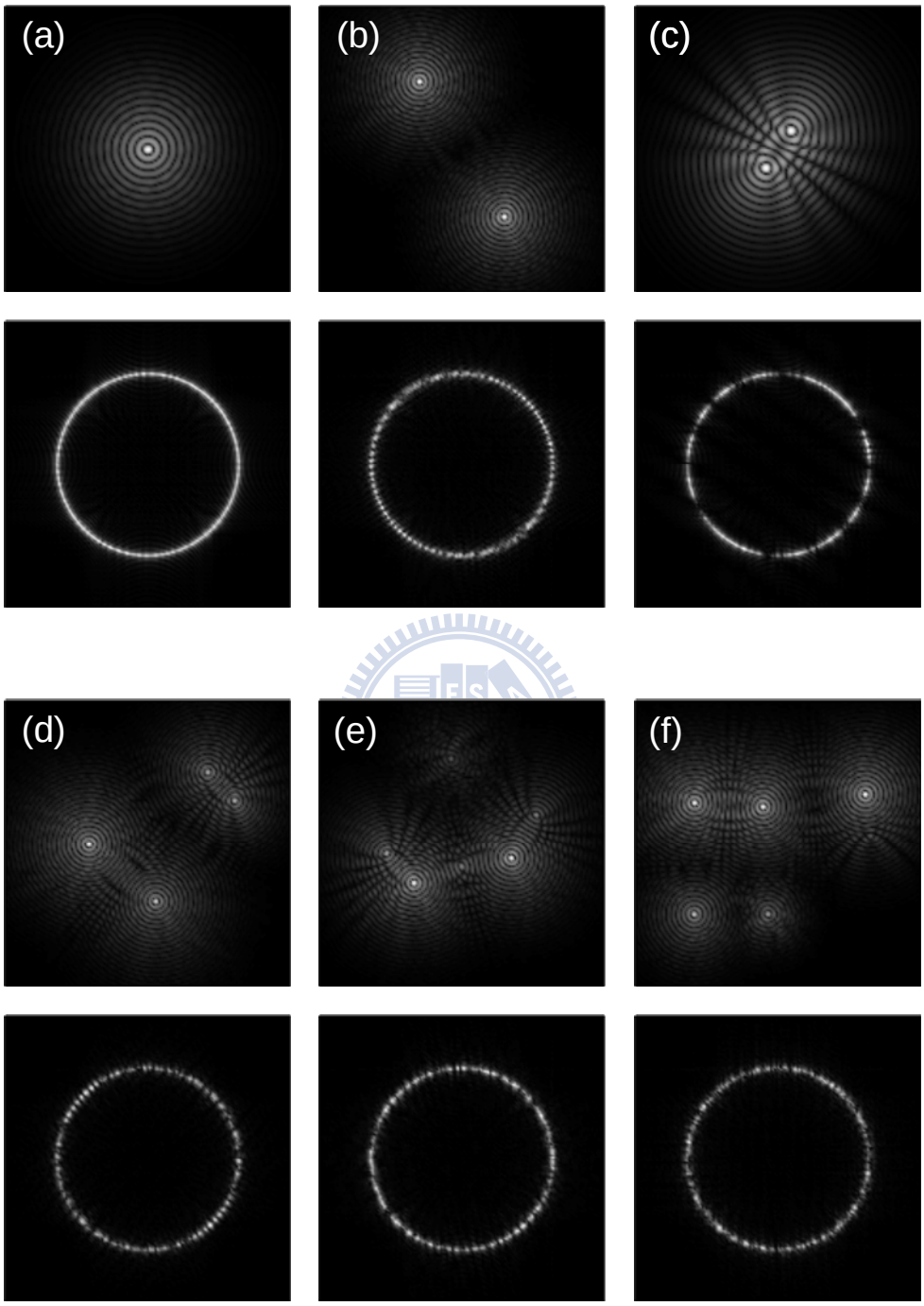

Fig. 7-15. Numerical near-field and far-field interference patterns of multi-Bessel beams corresponding to the experimental patterns shown in Figs. 7-14(a)-(f), respectively.

7.4 Frequency-Doubled Q-Switched Nd:YAG Laser with Intracavity BBO as SHG Crystal [Future work]

We use the similar experimental setup of diode-pumped actively Q-switched frequency-doubled Nd:YAG laser as shown in Fig. 7-7 with another intracavity SHG crystal to explore the wave functions of conical SHG. The SHG crystal is an a-cut BBO crystal with a length of 2 mm and a cross section of 3 mm × 3 mm. Figure 7-16(a)-(c) show the experimental near-field wave patterns measured at different transverse positions of the BBO crystal. The corresponding experimental far-field wave patterns are shown in Fig. 7-17. The investigations of the pattern formation will be carried out.

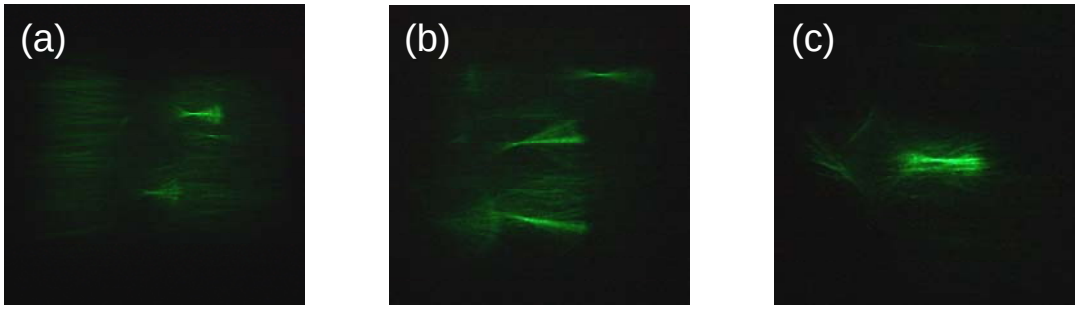

Fig. 7-16. Experimental near-field patterns measured at different transverse positions of the BBO crystal.

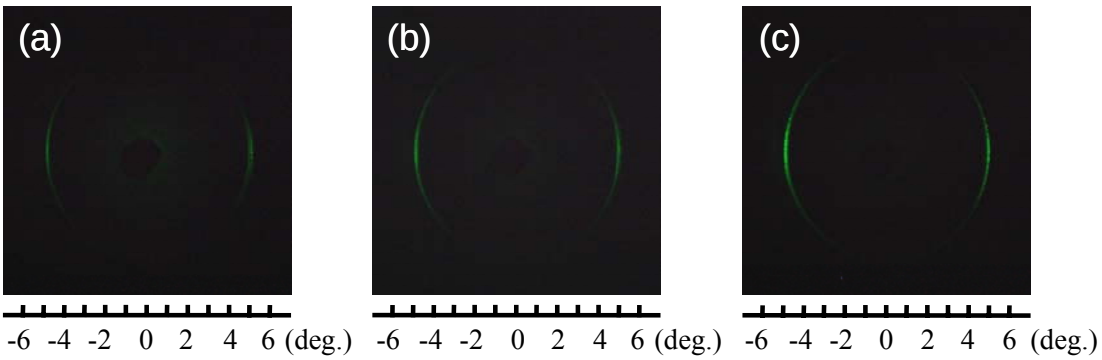

Fig. 7-17. Experimental far-field patterns corresponding to the experimental near-field patterns shown in Figs. 7-16(a)-(c), respectively.

7.5 Conclusion

The near-field patterns of conical SHG of a laser in random domain structures can be used to explore the spatial structure of 2D disordered wave functions. First we use a GdCOB crystal with extended defects as a SHG crystal in Q-switched Nd:YAG laser. The disordered wave functions of GdCOB crystal include chaotic waves, qusi-Bessel beam, and symmetry-breaking quasi-Bessel beam. The numerical wave functions are resulted from a superposition of a number of monochromatic plane waves with different directions and relative phases. The numerical near-field and far-field wave patterns agree well with the experimental wave patterns. In addition, the pattern formations of both frequency-doubled Q-switched Nd:YAG/BBO laser and frequency-doubled Q-switched Nd:YVO_4/KTP self-Raman laser will be investigated.

Chapter 8

Summary and Future work

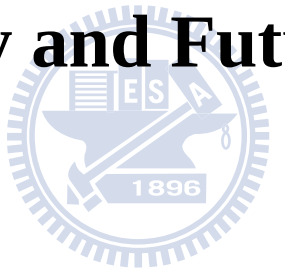

8.1 Summary

We have demonstrated wavelength-versatile diode-pumped solid-state intracavity Raman lasers based on third-order nonlinear effect over a wide spectral range including near-infrared and eye-safe wavelengths. By combining stimulated Raman scattering (SRS) and second Harmonic generation (SHG) / sum-frequency generation, the spectral coverage of solid-state Raman lasers can be extended to visible wavelengths useful for a number of applications.

In our experiments, it is found that thermal lensing effect is a critical issue exacerbating the performance of diode-pumped solid-state intracavity Raman laser. We first study the comparison of thermal lensing effects between single-end and doubled-end composite crystals by measuring the effective focal lengths of thermal lens. It is verified that the thermal lensing effect in a composite Nd:YVO_4 crystal with single 2.7-mm-long end can be sufficiently improved for the $^4F_{3/2}\rightarrow{}^4I_{11/2}$ transition. However, using a composite Nd:YVO_4 crystal with double 2.1-mm-long ends is a great improvement over a composite Nd:YVO_4 crystal with single 2.7-mm-long end for the $^4F_{3/2}\rightarrow{}^4I_{13/2}$ transition with higher quantum defect. After confirming the efficient improvement of thermal lensing effect in a double-end composite crystal, we design an original doubled-end composite crystal as a self-Raman gain medium to improve thermal effect and enhance Raman gain. We first report on an efficient Q-switched eye-safe self-Raman laser at 1525 nm with a double-end diffusion-bonded Nd:YVO_4 crystal. With an input pump power of 17.2 W, average power of 2.23 W at

the first-Stokes wavelength of 1525 nm is generated at a pulse repetition rate of 40 kHz, corresponding to a conversion efficiency of 13%. Therefore a diode-end-pumped Raman laser with a double-end composite crystal as a self-Raman medium has advantages of robustness, enhanced Raman gain, and high conversion efficiency. Moreover, an efficient Q-switched dual-wavelength laser with self-frequency Raman conversion in the original double-end composite Nd:YVO_4 and intracavity sum-frequency generation in BBO is reported. With an input pump power of 17.5 W, average power of 0.53 W at the first-Stokes 1176 nm and average power of 1.67 W at the sum-frequency mixed 559 nm are simultaneously generated at a pulse repetition rate of 100 kHz, corresponding to a total conversion efficiency of 12.5%.

However, the optimization of self-Raman laser is limited because the laser crystal simultaneously serves as a Raman shifter. A YVO_4 crystal is employed to achieve efficient stimulated Raman scattering conversion in a diode-pumped actively Q-switched Nd:YVO_4 laser. The output performance of actively Q-switched 1176-nm Nd:YVO_4 Raman laser including reliability, average output power, pulse repetition rate, pulse width, and peak power are substantially improved. With an incident pump power of 18.7 W, the average power is greater than 2.6 W at 80 kHz. The pulse width of the pulse envelop is shorter then 5 ns with mode-locked modulation. With an incident pump power of 12.7 W, the pulse energy and peak power is higher than 43 μJ and 14 kW at 40 kHz. Moreover by using a similar laser cavity with another laser crystal Nd:YAG with better thermal property and longer fluorescence lifetime, the laser performance including critical pump power, average output power, conversion efficiency, pulse energy, pulse width and peak power is improved. With an incident

pump power of 16.2 W, an 1176-nm first-Stokes average output power of 3.0 W is generated at a pulse repetition rate of 50 kHz, corresponding to a conversion efficiency of 18.3%. The maximum conversion efficiency of 21.3% is found at 20kHz. The maximum pulse energy is higher than 83 μJ at both 20 and 30 kHz. With an incident pump power of 7.6 W, the underestimated peak power of 43.5 kW is demonstrated at 20 kHz with mode locked modulation.

In addition, KTP and KTA crystals with low value of Stokes shift permit generation of multi-frequency radiation with cascade SRS. A diode-pumped actively Q-switched mixed Nd:$Y_{0.3}Gd_{0.7}VO_4$ laser with an intracavity KTP crystal is developed to produce cascade SRS emission up to the fourth order. Besides, there are "cross" patterns of the cascade SRS emission observed accidentally. With an incident pump power of 14 W and a repetition rate of 50 kHz, the average output powers at the first-, second-, third-, and fourth-Stokes modes are approximately 0.05 W, 0.61 W, 0.25 W, and 0.11 W, respectively. The maximum peak power is greater than 2 kW. Moreover by using an intracavity KTA crystal in a diode-pumped actively Q-switched Nd:YAG laser, both the cascade Raman emission and conical SHG are efficiently generated. The "cross" far-field patterns of cascade SRS emission and "ring" far-field patterns of conical SHG are observed. The pattern formation can be observed in a laser with nonlinear wavelength conversion.

Furthermore, a diode-pumped actively Q-switched Nd:YAG laser with a nonlinear crystal of GdCOB with extended defects is developed to efficiently generate conical SHG that are a kind of two-dimension random scattering process. The experimental near-field patterns in GdCOB exhibit chaotic waves, quasi-Bessel beams,

and multi-quasi-Bessel beams. It is found that the numerical near-field wave functions are resulted from a superposition of a number of monochromatic plane waves with random directions and phases. It is interesting that chaotic waves can be connected with Bessel beams by the numerical near-field wave functions. The experimental near- and far-field wave patterns agree well with the numerical near- and far-field wave patterns.

8.2 Future Work

The investigation of pattern formation above-mentioned in the section 6.3, 7.2 and 7.4 will be carried out in the future. Moreover the spatial structure of wave patterns in nonlinear crystal including GdCOB, KTP, KTA, and BBO crystals with various cutting angles will be investigated by using an intracavity conical SHG scheme. Moreover, the near-field and far-field wave pattern formations of Raman emission will also be investigated.

For diode-end-pumped Raman laser, the self-focusing effect which would induce optical damage is a critical issue for scaling up the power of intracavity Raman laser. In our experiment, it is found that the average output power can be enhanced with increasing the pulse repetition rate, but the Raman threshold will be increased. Therefore side-pump diode laser with bigger laser beam waist can be used to increase the average power of Raman laser.

References

Chapter 1

[1] H. M. Pask, "The design and operation of solid-state Raman lasers," Prog. Quantum Electron. **27**, 3 (2003).

[2] P. Černý, H. Jelínková, P. G. Zverev, and T. T. Basiev "Solid state laser with raman frequency conversion," Progress Quantum Electronics **28**, 113 (2004).

[3] J. A. Piper and H. M. Pask, "Crysatalline Raman Lasers," IEEE J. Sel. Top. Quantum Electron. **13**, 692 (2007).

[4] H. M. Pask, P. Dekker, R. P. Mildren, D. J. Spence, and J. A. Piper, "Wavelength-versatile visible and UV sources based on crystalline Raman lasers," Prog. Quantum Electron. **32**, 121 (2008).

[5] E. O. Ammann, C. D. Decker, "0.9-W Raman oscillator," J. Appl. Phys. **48**, 1973 (1977).

[6] A.S. Eremenko, S.N. Karpukhin, and A.I. Stepanov, "Stimulated Raman scattering of the second harmonic of a neodymium laser in nitrate crystals," Sov. J. Quantum Electron. **10**, 113 (1980).

[7] P. Cerný, P.G. Zverev, H. Jelínková, T.T. Basiev, "Efficient Raman shifting of picosecond pulses using $BaWO_4$ crystal," Opt. Commun. **177**, 397 (2000).

[8] J. Findeisen, H.J. Eichler, and P. Peuser, "Self-stimulating, transversally diode pumped Nd^{3+}: $KGd(WO_4)_2$ Raman laser," Opt. Commun. **181**, 129 (2000).

[9] A. A. Kaminskii, K. Ueda, H.J. Eichler, Y. Kuwano, H. Kouta, S.N. Bagaev, T.H. Chyba, J.C. Barnes, G.M. A. Gad, T. Murai, and J. Lu, "Tetragonal vanadates YVO_4 and $GdVO_4$ – new efficient $\chi^{(3)}$-materials for Raman lasers," Opt. Commun. **194**, 201 (2001).

[10] Y. F. Chen, "Efficient subnanosecond diode-pumped passively Q-switched Nd:YVO_4 self-stimulated Raman laser," Opt. Lett. **29**, 1251 (2004).

[11] Y. F. Chen, “High-power diode-pumped actively Q-switched Nd:YVO_4 self-Raman laser: influence of dopant concentration,” Opt. Lett. **29**, 1915 (2004).

[12] Y. F. Chen, “Compact efficient self-frequency Raman conversion in diode-pumped passively Q-switched Nd:$GdVO_4$ laser,” Appl. Phys. B **78**, 685 (2004).

[13] Y. F. Chen, “Efficient 1521-nm Nd:$GdVO_4$ Raman laser”, Opt. Lett. **29**, 2632 (2004).

[14] Y. F. Chen, K. W. Su, T. H. Lu, and K. F. Huang, “Manifestation of weak localization and long-range correlation in disordered wave functions from conical second harmonic generation,” Phys. Rev. Lett. **96**, 033905 (2006).

Chapter 2

[1] C. V. Raman, “A new radiation,” Indian Journal of Physics, **2**, 387 (1928).

[2] C. V. Raman and K. S. Krishnan, “A new type of secondary radiation,” Nature, **121**, 501 (1928).

[3] E. J. Woodbury, W. K. Ng, “Ruby laser operation in the near IR,” Proceedings of the IRE **50**, 2367 (1962).

[4] Y. F. Chen, “Efficient 1521-nm Nd:$GdVO_4$ Raman laser”, Opt. Lett. **29**, 2632 (2004).

[5] G. Eckhardt, D. P. Bortfeld, and M. Geller, “Stimulated emission of Stokes and anti-Stokes Raman lines from diamond, calcite, and α–sulfur single crystals,” Appl. Phys. Lett. **3**, 137 (1963).

[6] E. O. Ammann, C. D. Decker, “0.9-W Raman oscillator,“ J. Appl. Phys. **48**, 1973 (1977).

[7] J. Falk, R. Moshrefzadeh, “Oblique Raman and polariton scattering in lithium iodate,” IEEE J. Quantum Electron. **21**, 110 (1985).

[8] S. N. Karpukhin, A. I. Stepanov, “Generation of radiation in a resonator under conditions of stimulated Raman scattering in $Ba(NO_3)_2$, $NaNO_3$, and $CaCO_3$

crystals," Sov. J. Quantum Electron. **16**, 1027 (1986).

[9] T. T. Basiev, V. N. Voitsekhovskii, P. G. Zverev, F. V. Karpushko, A. V. Lyubimov, S. B. Mirov, V. P. Morozov, I. V. Mochalov, A. A. Pavlyuk, G. V. Sinitsyn, V. E. Yakobson, "Conversion of tunable radiation from a laser utilizing an LiF crystal containing F-2 color centers by stimulated Raman scattering in $Ba(NO_3)_2$ and $KGd(WO_4)_2$. Soviet J. Quantum Electron. **17**, 1560 (1987).

[10] P. Cerny, H. Jelinkova, T. T. Basiev, P. G. Zverev, "Properties of transient and steady-state stimulated Raman scattering in $KGd(WO_4)_2$ and $BaWO_4$ tungstate crystals," Proc. of the SPIE: Growth, Fabrication, Devices, and Applications of laser and Nonlinear Materials, SPIE, Bellingham, **4268**, 101 (2001).

[11] A. A. Kaminskii, C. L. McCray, H. R. Lee, S. W. Lee, D. A. Temple, T. H. Chyba, W. D. Marsh, J.C. Barnes, A. N. Annanenkov, V. D. Legun, H. J. Eichler, G. M. A. Gad, K. Ueda "High efficiency nanosecond Raman lasers based on tetragonal $PbWO_4$ crystals," Opt. Commun. **183**, 277 (2000).

[12] Y. F. Chen, "Stimulated Raman scattering in a potassium titanyl phosphate crystal: simultaneous self-sum frequency mixing and self-frequency doubling," Opt. Lett. **30**, 400 (2005).

[13] S. Pearce, C. L. M. Ireland, and P. E. Dyer, "Solid-state Raman laser generating <1ns, multi-kilohertz pulses at 1096 nm," Opt. Commun. **260**, 680 (2006).

[14] V. Pasiskevicius, C. Canalias, and F. Laurell, "Highly efficient stimulated Raman scattering of picosecond pulses in $KTiOPO_4$," Appl. Phys. Lett. **88**, 041110 (2006).

[15] Z. Liu, Q. Wang, X. Zhang, Z. Liu, J. Chang, H. Wang, S. Zhang, S. Fan, W. Sun, G. Jin, X. Tao, S. Zhang, and H. Zhang, "A $KTiOAsO_4$ Raman laser," Appl. Phys. B **94**, 585 (2009).

[16] S. Pearce, C. L. M. Ireland, P. E. Dyer, "Solid-state Raman laser generating <1ns, multi-kilohertz pulses at 1096 nm," Opt. Commun. **260**, 680 (2006).

[17] G. A. Massey, T. M. Loehr, L. J. Willis, and J. C. Johnson, "Raman and Electro-optic Properties of Potassium Titanate Phosphate," Appl. Opt. **19**, 4136 (1980).

[18] Chi-Shun Tu, A. R. Guo, Ruiwu Tao, R. S. Katiyar, Ruyan Guo, and A. S. Bhalla, "Temperature dependent Raman scattering in $KTiOPO_4$ and $KTiOAsO_4$ single crystals," J. Appl. Phys. **79**, 3235 (1996).

[19] Y. T. Chang, Y. P. Huang, K. W. Su, and Y. F. Chen, "Diode-pumped multi-frequency Q-switched laser with intracevity cascade Raman emission," Opt. Express **16**, 8286 (2008).

[20] K. Zhong, J. S. Li, D. G. Xu, X. Ding, R. Zhou, W. Q. Wen, Z. Y. Li, X. Y. Xu, P. Wang, and J. Q. Yao, "Multi-wavelength generation based on cascaded Raman scattering and self-frequency-doubling in KTA," Laser Phys. **20**, 750 (2010).

[21] J. J. Carvajal, Growth and Characterisation of $RbTiOPO_4$: (Nb, Ln), A New Self-frequency Doubling Crystal, Chapter 6, Ph. D. Theses, Universitat Rovira i Virgili, Tarragona, Spain.

[22] T. Jensen, V. G. Ostroumov, J. P. Meyn, G. Huber, A. I. Zagumennyi, and I. A. Shcherbakov, "Spectroscopic characterization and laser performance of diode-laser-pumped Nd:$GdVO_4$," Appl. Phys. B **58**, 373 (1994).

[23] V. Lupei, N. Pavel, Y. Sato, and T. Taira, "Highly efficient 1063-nm continuous-wave laser emission in Nd:$GdVO_4$," Opt. Lett. **28**, 2366 (2003).

[24] T. Ogawa, Y. Urata, S. Wada, K. Onodera, H. Machida, H. Sagae, M. Higuchi, and K. Kodaira, "Efficient laser performance of Nd:$GdVO_4$ crystals grown by the floating zone method," Opt. Lett. **28**, 2333 (2003).

[25] C. P. Wyss, W. Luthy, H. P. Weber, V. I. Vlasov, Y. D. Zavartsev, P. A. Studenikin, A. I. Zagumennyi, and I. A. Shcherbakov, "Performance of a diode-pumped 5W Nd^{3+}:$GdVO_4$ microchip laser at 1.06 μm," Appl. Phys. B **68**, 659 (1999).

[26] A. A. Kaminskii, K. Ueda, H.J. Eichler, Y. Kuwano, H. Kouta, S.N. Bagaev, T.H. Chyba, J.C. Barnes, G.M. A. Gad, T. Murai, and J. Lu, "Tetragonal vanadates YVO_4 and $GdVO_4$ – new efficient $\chi^{(3)}$-materials for Raman lasers," Opt.

Commun. **194**, 201 (2001).

[27] H. M. Pask, "The design and operation of solid-state Raman lasers," Prog. Quantum Electron. **27**, 3 (2003).

[28] Y. F. Chen, "High-power diode-pumped actively Q-switched Nd:YVO_4 self-Raman laser: influence of dopant concentration," Opt. Lett. **29**, 1915 (2004).

[29] C. Kittel, "Introduction to Solid State Physics," 7th ed. Wiley, (1996).

[30] H. M. Pask, "The design and operation of solid-state Raman lasers," Prog. Quantum Electron. **27**, 3 (2003).

[31] P. Černý, H. Jelínková, P. G. Zverev, and T. T. Basiev "Solid state laser with raman frequency conversion," Progress Quantum Electronics **28**, 113 (2004).

[32] J. A. Piper and H. M. Pask, "Crysatalline Raman Lasers," IEEE J. Sel. Top. Quantum Electron. **13**, 692 (2007).

[33] H. M. Pask, P. Dekker, R. P. Mildren, D. J. Spence, and J. A. Piper, "Wavelength-versatile visible and UV sources based on crystalline Raman lasers," Prog. Quantum Electron. **32**, 121 (2008).

[34] Y. F. Chen, "Efficient 1521-nm Nd:$GdVO_4$ Raman laser", Opt. Lett. **29**, 2632 (2004).

[35] S. H. Ding, X. Y. Zhang, Q. P. Wang, F. F. Su, P. Jia, S. T. Li, S. Z. Fan, J. Chang, S. S. Zhang, and Z. J. Liu, "Theoretical and experimental study on the self-Raman laser with Nd:YVO_4 crystal," IEEE J. Quantum Electron. **42**, 927 (2006).

[36] F. F. Su, X. Y. Zhang, Q. P. Wang, S. H. Ding, P. Jia, S. T. Li, S. Z. Fan, C. Zhang, and B. Liu "Diode pumped actively Q-switched Nd:YVO4 self-Raman laser," J. Phys. D: Appl. Phys. **39**, 2090 (2006).

[37] N. Takei, S. Suzuki, and F. Kannari, "20-Hz operation of an eye-safe cascade Raman laser with a $Ba(NO_3)_2$ crystal," Appl. Phys. B **74**, 521 (2002).

[38] Z. P. Wang, D. W. Hu, X. Fang, H. J. Zhang, X. G. Xu, J. Y. Wang, and Z. H. Shao, "Eye-safe Raman laser at 1.5 μm based on $BaWO_4$ crystal," Chin. Phys. Lett. **25**, 122 (2008).

[39] J. H. Huang, J. P. Lin, R. B. Su, J. H. Li, H. Zheng, C. H. Xu, F. Shi, Z. Z. Lin, J. Zhuang, W. R. Zeng, and W. X. Lin, "Short pulse eye-safe laser with a stimulated Raman scattering self-conversion based on a Nd:KGW crystal," Opt. Lett. **32**, 1096 (2007).

[40] W. Koechner, *Solid-State Laser Engineering*, 6th ed. (Springer, New York, 2006).

Chapter 3

[1] T. Y. Fan and R. L. Byer, "Diode laser-pumped solid-state lasers," IEEE J. Quantum Electron. **24**, 895 (1988).

[2] A. K. Cousins, "Temperature and thermal stress scaling in finite-length end-pumped laser rods," IEEE J. Quantum Electron. **28**, 1057 (1992).

[3] W. Koechner, chapter 7 in *Solid-State Laser Engineering*, 6th ed. (Springer, New York, 2006).

[4] Y. F. Chen, "Design criteria for concentration optimization in scaling diode end-pumped lasers to high powers: influence of thermal fracture," IEEE J. Quantum Electron. **35**, 234 (1999).

[5] Y. F. Chen, T. M. Huang, C. F. Kao, C. L. Wang, and S. C. Wang, "Optimization in scaling fiber-coupled laser-diode end-pumped lasers to higher power: influence of thermal effect," IEEE J. Quantum Electron. **33**, 1424 (1997).

[6] Y. F. Chen, C. F. Kao, T. M. Huang, C. L. Wang, and S. C. Wang, "Influence of thermal effect on output power optimization in fiber-coupled laser-diode end-pumped lasers," IEEE J. Sel. Top. Quantum Electron. **3**, 29 (1997).

[7] W. A. Clarkson, "Thermal effects and their mitigation in end-pumped solid-state lasers," J. Phys. D **34**, 2381 (2001).

[8] M. E. Innocenzi, H. T. Yura, C. L. Fincher, and R. A. Fields, "Thermal modeling of continuous-wave end-pumped solid-state lasers," Appl. Phys. Lett. **56**, 1831 (1990).

[9] S. C. Tidwell, J. F. Seamans, M. S. Bowers, and A. K. Cousins, "Scaling CW diode-end-pumped Nd:YAG lasers to high average powers," IEEE J. Quantum Electron. **28**, 997 (1992).

[10] B. Neuenschwander, R. Weber, and H. P. Weber, "Determination of the thermal lens in solid-state lasers with stable cavities," IEEE J. Quantum Electron. **31**, 1082 (1995).

[11] B. Ozygus, and Q. Zhang, "Thermal lens determination of end-pumped solid-state lasers using primary degeneration modes," Appl. Phys. Lett. **71**, 2590 (1997).

[12] F. Song, C. Zhang, X. Ding, J. J. Xu, and G. Y. Zhang, "Determination of thermal focal length and pumping radius in gain medium in laser-diode-pumped Nd:YVO_4 lasers," Appl. Phys. Lett. **81**, 2145 (2002).

[13] S. Chénais, S. Forget, F. Druon, F. Balembois, and P. Georges, "Direct and absolute temperature mapping and heat transfer measurements in diode-end-pumped Yb:YAG," Appl. Phys. B **79**, 221 (2004).

[14] S. Z. Fan, X. Y. Zhang, Q. P. Wang, S. T. Li, S. H. Ding, and F. F. Su, "More precise determination of thermal lens focal length for end-pumped solid-state lasers," Opt. Commun. **266**, 620 (2006).

[15] F. Hanson, "Improved laser performance at 946 and 473 nm from a composite Nd:$Y_3Al_5O_{12}$ rod," Appl. Phys. Lett. **66**, 3549 (1995).

[16] R. Weber, B. Neuenschwander, M. M. Donald, M. B. Roos, and H. P. Weber, "Cooling schemes for longitudinally diode laser-pumped Nd:YAG rods," IEEE J. Quantum Electron. **34**, 1046 (1998).

[17] M. Tsunekane, N. Taguchi, T. Kasamatsu, and H. Inaba, "Analytical and experimental studies on the characteristics of composite solid-state laser rods in diode-end-pumped geometry," IEEE J. Sel. Top. Quantum Electron. **3**, 9 (1997).

[18] M. Tsunekane, N. Taguchi, and H. Inaba, "Efficient 946-nm laser operation of a composite Nd:YAG rod with undoped ends," Appl. Opt. **37**, 5713 (1998).

[19] M. Tsunekane, N. Taguchi, and H. Inaba, “Improvement of thermal effects in a diode-end-pumped, composite Tm:YAG rod with undoped ends,” Appl. Opt. **38**, 1788 (1999).

[20] M. P. MacDonald, Th. Graf, J. E. Balmer, and H. P. Weber, “Reducing thermal lensing in diode-pumped laser rods,” Opt. Commun. **178**, 383 (2000).

[21] J. Šulc, H. Jelínková, V. Kubeček, K. Nejezchleb, and K. Blažek, “Comparison of different composite Nd:YAG rods thermal properties under diode pumping,” Proc. SPIE **4630**, 128 (2002).

[22] D. Kracht, R. Wilhelm, M. Frede, K. Dupré, and L. Ackermann, “407 W end-pumped multi-segmented Nd:YAG laser,” Opt. Express **13**, 10140 (2005).

[23] Z. Zhuo, T. Li, X Li, and H. Yang, “Investigation of Nd:YVO_4/YVO_4 composite crystal and its laser performance pumped by a fiber coupled diode laser,” Opt. Commun. **274**, 176 (2007).

[24] Y. F. Chen, “Pump-to-mode size ratio dependence of thermal loading in diode-end-pumped solid-state lasers,” J. Opt. Soc. Am. B **17**, 1835 (2000).

[25] W. Koechner, “Thermal lensing in a Nd:YAG laser rod,” Appl. Opt. **9**, 2548 (1970).

Chapter 4

[1] Y. F. Chen, “High-power diode-pumped actively Q-switched Nd:YVO_4 self-Raman laser: influence of dopant concentration,” Opt. Lett. **29**, 1915 (2004).

[2] M. Revermann, H. M. Pask, J. L. Blows, and T. Omatsu “Thermal lensing measurements in an intracavity $LiIO_3$ Raman laser,” Advanced Solid State Lasers, OSA Technical Digest Series, Optical Society of America, ME13 (2000).

[3] H. M. Pask, J. L. Blows and J. A. Piper, M. Revermann, and T. Omatsu, “Thermal lensing in a Barium nitrate Raman laser,” Advanced Solid-State Lasers, C. Marshall, ed., OSA Trends in Optics and Photonics, Optical Society of America, Vol. 50, TuB15 (2001).

[4] H. M. Pask, “The design and operation of solid-state Raman lasers,” Prog. Quantum Electron. **27**, 3 (2003).

[5] Zhichao Wang, Chenlin Du, Shuangchen Ruan, and Li Zhang, “Thermal lens measurements in a Nd:GdVO4 self-Raman laser,” Optics & Laser Technology **42**, 873 (2010).

[6] L. R. Marshall and A. Kaz, “Eye-safe output from noncritically phase-matched parametric oscillators,” J. Opt. Soc. Am. B, **10**, 1730 (1993).

[7] G. H. Xiao, M. Bass, and M. Acharekar, “Passively Q-switched solid-state lasers with intracavity optical parametric oscillators,” IEEE J. Quantum Electron. **34**, 2241 (1998).

[8] Y. F. Chen, S. W. Chen, S. W. Tsai, and Y. P. Lan, “High-repetition-rate eye-safe optical parametric oscillator intracavity pumped by a diode-pumped Q-switched Nd:YVO_4 laser, Appl. Phys. B **76**, 263 (2003).

[9] Y. F. Chen, Y. C. Chen, S. W. Chen and Y. P. Lan, “High-power efficient diode-pumped passively Q-switched Nd:YVO_4/KTP/Cr^{4+}:YAG eye-safe laser,” Opt. Commun. **234**, 337 (2004).

[10] R. Fluck, R. Häring, R. Paschotta, E. Gini, H. Melchior, and U. Keller, “Eyesafe pulsed microchip laser using semiconductor saturable absorber mirrors,” Appl. Phys. Lett. **72**, 3273 (1998)

[11] I. Sokolska, E. Heumann, S. Kuck, T. Łukasiewicz, “Laser oscillation of Er^{3+}:YVO_4 and Er^{3+}, Yb^{3+}:YVO_4 crystals in the spectral range around 1.6 μm,” Appl. Phys. B **71**, 893 (2000).

[12] A. Sennaroglu, “Broadly tunable Cr^{4+}-doped solid-state lasers,” Prog. Quantum Electron. **26**, 287 (2002).

[13] N. Takei, S. Suzuki, and F. Kannari, “20-Hz operation of an eye-safe cascade Raman laser with a $Ba(NO_3)_2$ crystal,” Appl. Phys. B **74**, 521 (2002).

[14] Y. F. Chen, “Efficient 1521-nm Nd:$GdVO_4$ Raman laser,” Opt. Lett. **29**, 2632 (2004).

[15] A. Brenier, G. Jia, and C. Tu, "Raman lasers at 1.171 and 1.517 μm with self-frequency conversion in $SrWO_4:Nd^+$ crystal," J. Phys.: Condens. Matter **16**, 9103 (2004).

[16] J. H. Huang, J. P. Lin, R. B. Su, J. H. Li, H. Zheng, C. H. Xu, F. Shi, Z. Z. Lin, J. Zhuang, W. R. Zeng, and W. X. Lin, "Short pulse eye-safe laser with a stimulated Raman scattering self-conversion based on a Nd:KGW crystal," Opt. Lett. **32**, 1096 (2007).

[17] Y. X. Fan, Y. Liu, Y. H. Duan, Q. Wang, L. Fan, H. T. Wang, G. H. Jia, and C. Y. Tu, "High-efficiency eye-safe intracavity Raman laser at 1531 nm with $SrWO_4$ crystal," Appl. Phys. B **93**, 327 (2008).

[18] Z. P. Wang, D. W. Hu, X. Fang, H. J. Zhang, X. G. Xu, J. Y. Wang, and Z. H. Shao, "Eye-safe Raman laser at 1.5 μm based on $BaWO_4$ crystal," Chin. Phys. Lett. **25**, 122 (2008).

[19] G. M. A. Gad, H. J. Eichler, and A. A. Kaminskii, "Highly efficient 1.3-μm second-Stokes $PbWO_4$ Raman laser," Opt. Lett. **28**, 426 (2003).

[20] H. M. Pask, "The design and operation of solid-state Raman lasers," Prog. Quantum Electron. **27**, 3 (2003).

[21] P. Černý, H. Jelínková, P. G. Zverev, and T. T. Basiev "Solid state laser with raman frequency conversion," Prog. Quantum Electron. **28**, 113 (2004).

[22] J. A. Piper and H. M. Pask, "Crysatalline Raman Lasers," IEEE J. Sel. Top. Quantum Electron. **13**, 692 (2007).

[23] A. A. Kaminskii, K. Ueda, H. J. Eichler, Y. Kuwano, H. Kouta, S. N. Bagaev, T. H. Chyba, J. C. Barnes, G. M. A. Gad, T. Murai, J. Lu, "Tetragonal vanadates YVO_4 and $GdVO_4$ – new efficient $\chi^{(3)}$-materials for Raman lasers," Opt. Commun. **194**, 201 (2001).

[24] S. H. Ding, X. Y. Zhang, Q. P. Wang, F. F. Su, P. Jia, S. T. Li, S. Z. Fan, J. Chang, S. S. Zhang, and Z. J. Liu, "Theoretical and experimental study on the self-Raman laser with $Nd:YVO_4$ crystal," IEEE J. Quantum Electron. **42**, 927 (2006).

[25] F. F. Su, X. Y. Zhang, Q. P. Wang, S. H. Ding, P. Jia, S. T. Li, S. Z. Fan, C. Zhang, and B. Liu "Diode pumped actively Q-switched Nd:YVO4 self-Raman laser," J. Phys. D: Appl. Phys. **39**, 2090 (2006).

[26] F. Hanson, "Improved laser performance at 946 and 473 nm from a composite Nd:$Y_3Al_5O_{12}$ rod," Appl. Phys. Lett. **66**, 3549 (1995).

[27] R. Weber, B. Neuenschwander, M. M. Donald, M. B. Roos, and H. P. Weber, "Cooling schemes for longitudinally diode laser-pumped Nd:YAG rods," IEEE J. Quantum Electron. **34**, 1046 (1998).

[28] M. Tsunekane, N. Taguchi, T. Kasamatsu, and H. Inaba, "Analytical and experimental studies on the characteristics of composite solid-state laser rods in diode-end-pumped geometry," IEEE J. Sel. Top. Quantum Electron. **3**, 9 (1997).

[29] M. Tsunekane, N. Taguchi, and H. Inaba, "Efficient 946-nm laser operation of a composite Nd:YAG rod with undoped ends," Appl. Opt. **37**, 5713 (1998).

[30] M. Tsunekane, N. Taguchi, and H. Inaba, "Improvement of thermal effects in a diode-end-pumped, composite Tm:YAG rod with undoped ends," Appl. Opt. **38**, 1788 (1999).

[31] M. P. MacDonald, Th. Graf, J. E. Balmer, and H. P. Weber, "Reducing thermal lensing in diode-pumped laser rods," Opt. Commun. **178**, 383 (2000).

[32] J. Šulc, H. Jelínková, V. Kubeček, K. Nejezchleb, and K. Blažek, "Comparison of different composite Nd:YAG rods thermal properties under diode pumping," Proc. SPIE **4630**, 128 (2002).

[33] D. Kracht, R. Wilhelm, M. Frede, K. Dupré, and L. Ackermann, "407 W end-pumped multi-segmented Nd:YAG laser," Opt. Express **13**, 10140 (2005).

[34] Z. Zhuo, T. Li, X Li, and H. Yang, "Investigation of Nd:YVO_4/YVO_4 composite crystal and its laser performance pumped by a fiber coupled diode laser," Opt. Commun. **274**, 176 (2007).

[35] Y. T. Chang, Y. P. Huang, K. W. Su, and Y. F. Chen, "Comparison of thermal lensing effects between single-end and double-end diffusion-bonded NdYVO4

crystals for $^4F_{3/2}\rightarrow{}^4I_{11/2}$ and $^4F_{3/2}\rightarrow{}^4I_{13/2}$ transitions," Opt. Express, **16**, 21155 (2008).

[36] Y. F. Chen, "Compact efficient all-solid-state eye-safe laser with self-frequency Raman conversion in a Nd:YVO_4 crystal," Opt. Lett. **29**, 2172 (2004).

[37] H. M. Pask, P. Dekker, R. P. Mildren, D. J. Spence, and J. A. Piper, "Wavelength-versatile visible and UV sources based on crystalline Raman lasers," Prog. Quantum Electron. **32**, 121 (2008).

[38] S. T. Li, X. Y. Zhang, Q. P. Wang, X. L. Zhang, Z. H. Cong, H. J. Zhang, and J. Y. Wang, "Diode-side-pumped intracavity frequency-doubled Nd:YAG/$BaWO_4$ Raman laser generating average output power of 3.14 W at 590 nm," Opt. Lett. **32**, 2951 (2007).

[39] A. J. Lee, H. M. Pask, P. Dekker, and J. A. Piper, "High efficiency, multi-Watt CW yellow emission from an intracavity-doubled self-Raman laser using Nd:$GdVO_4$," Opt. Express **16**, 21958 (2008).

[40] W. Telford, M. Murga, T. Hawley, R. Hawley, B. Packard, A. Komoriya, F. Haas, and C. Hubert, "DPSS yellow-green 561-nm lasers for improved fluorochrome detection by flow cytometry," Cytometry Part A **68A**, 36 (2005).

[41] C. He, and T. H. Chyba, "Solid-state barium nitrate Raman laser in the visible region," Opt. Commun. **135**, 273 (1997).

[42] A. A. Kaminskii, C. L. McCray, H. R. Lee, S. W. Lee, D. A. Temple, T. H. Chyba, W. D. Marsh, J. C. Barnes, A. N. Annanenkov, V. D. Legun, H. J. Eichler, G. M. A. Gad and K. Ueda, "High efficiency nanosecond Raman lasers based on tetragonal $PbWO_4$ crystals," Opt. Commun. **183**, 277 (2000).

[43] F. Q. Jia, Q. Zheng, Q. H. Xue, Y. K. Bu, and L. S. Qian, "Yellow light generation by frequency doubling of a diode-pumped Nd:YAG laser," Opt. Commun. **259**, 212 (2006).

[44] E. Räikkönen, O. Kimmelma, M. Kaivola, and S. C. Buchter, "Passively Q-switched Nd:YAG/KTA laser at 561 nm," Opt. Commun. **281**, 4088 (2008).

[45] S. Hilbich, W. Seelert, V. Ostroumov, C. Kannengiesser, R. v. Elm, J. Mueller, E. Weiss, H. Zhou, and J. Chilla, “New wavelengths in the yellow orange range between 545 nm to 580 nm generated by an intracavity frequency-doubled optically pumped semiconductor laser," Proc. SPIE **6451**, 64510C (2007).

[46] H. M. Pask, R. P. Mildren, and J. A. Piper, “Optical field dynamics in a wavelength-versatile, all-solid-state intracavity cascaded pulsed Raman laser,” Appl. Phys. B **93**, 507 (2008).

[47] A. A. Kaminskii, “Laser crystals and ceramics: recent advances,” Laser & Photon. Rev. **1**, 93 (2007).

[48] A. A. Kaminskii, S. N. Bagayev, H. J. Eichler, H. Rhee, K. Ueda, K. Takaichi, K. Oka, H. Shibata, Y. Hatanaka, and Y. Matsumoto, “Steady-state picosecond stimulated Raman scattering in two host-crystals for Ln^{3+} and Ln^{2+} lasants,” Laser Phys. Lett. **3**, 385 (2006).

[49] Y. F. Chen, “Compact efficient self-frequency Raman conversion in diode-pumped passively Q-switched Nd:$GdVO_4$ laser,” Appl. Phys. B **78**, 685 (2004).

[50] A. A. Kaminskii, M. Bettinelli, J. Dong, D. Jaque, and K. Ueda, “Nanosecond Nd^{3+}:$LuVO_4$ self-Raman laser,” Laser Phys. Lett. **6**, 374 (2009).

[51] Y. T. Chang, K. W. Su, H. L. Chang, and Y. F. Chen, “Compact efficient Q-switched eye-safe laser at 1525 nm with a double-end diffusion-bonded Nd:YVO_4 crystal as a self-Raman medium,” Opt. Express **17**, 4330 (2009).

Chapter 5

[1] A. Brenier, G. Jia, and C. Tu, “Raman lasers at 1.171 and 1.517 μm with self-frequency conversion in $SrWO_4$:Nd^{3+} crystal,” J. Phys.: Condens. Matter **16**, 9103 (2004).

[2] J. Findeisen, H. J. Eichler, and P. Peuser, “Self-stimulating, transversally diode pumped Nd^{3+}:$KGd(WO_4)_2$ Raman laser,” Opt. Commun. **181**, 129 (2000).

[3] A. A. Lagatsky, A. Abdolvand, and N. V. Kuleshov, "Passive Q switching and self-frequency Raman conversion in a diode-pumped Yb:$KGd(WO_4)_2$ laser", Opt. Lett. **25**, 616 (2000).

[4] W. Chen, Y. Inagawa, T. Omatsu, M. Tateda, N. Takeuchi, and Y. Usuki, "Diode-pumped, self-stimulating, passively Q-switched Nd^{3+}:$PbWO_4$ Raman laser", Opt. Commun. **194**, 401 (2001).

[5] Y. F. Chen, "High-power diode-pumped actively Q-switched Nd:YVO_4 self-Raman laser: influence of dopant concentration," Opt. Lett. **29**, 1915 (2004).

[6] Y. F. Chen, "Efficient 1521-nm Nd:$GdVO_4$ Raman laser", Opt. Lett. **29**, 2632 (2004).

[7] Y. F. Chen, M. L. Ku, L. Y. Tsai, and Y. C. Chen, "Diode-pumped passively Q-switched picosecond Nd:$GD_xY_{1-x}VO_4$ self-stimulated Raman laser", Opt. Lett. **29**, 2279 (2004).

[8] S. H. Ding, X. Y. Zhang, Q. P. Wang, F. F. Su, P. Jia, S. T. Li, S. Z. Fan, J. Chang, S. S. Zhang, and Z. J. Liu, "Theoretical and experimental study on the self-Raman laser with Nd:YVO_4 crystal," IEEE J. Quantum Electron. **42**, 927 (2006).

[9] Y. F. Chen, "Compact efficient all-solid-state eye-safe laser with self-frequency Raman conversion in a Nd:YVO_4 crystal," **29**, 2172 (2004).

[10] K. Andryunas, Y. Vishakas, V. Kabelka, I. V. Mochalov, A. A. Pavlyuk, G. T. Petrovskii, V. Syrus, "Stimulated-Raman self-conversion of Nd^{3+} laser-light in double tungstenate crystls," JETP Lett. **42**, 410 (1985).

[11] K. Andryunas, Y. Vishakas, V. Kabelka, I. V. Mochalov, A. A. Pavlyuk, G. T. Petrovskii, V. Syrus, "Method of picosecond pulse generation at a Raman frequency," Patent of USSR 1227074 (1984).

[12] P. G. Zverev, A. Y. Karasik, A. A. Sobol, D. S. Chunaev, T. T. Basiev, A. I. Zagumennyi, Y. D. Zavartsev, S. A. Kutovoi, V. V. Osiko, I. A. Shcherbakov, "Stimulated Raman scattering of picosecond pulses in $GdVO_4$ and YVO_4 crystals," Advanced Solid-State Photonics, OSA Technical Digest, paper TuB10, 25 (2004).

[13] T. T. Basiev, S. V. Vassiliev , V. A. Konjushkin, V. V. Osiko, A. I. Zagumennyi, Y. D. Zavartsev, S. A. Kutovoi, I. A. Shcherbakov, "Diode pumped 500-picosecond Nd:$GdVO_4$ Raman laser," Laser Phys. Lett. **1**, 237 (2004).

[14] Y. F. Chen, "Compact efficient self-frequency Raman conversion in diode-pumped passively Q-switched Nd:$GdVO_4$ laser," Appl. Phys. B **78**, 685 (2004).

[15] B. K. Zhou, T. J. Kane, G. J. Dixon, and R. L. Byer, "Efficient, frequency-stable laser-diode-pumped Nd:YAG laser," **10**, 62 (1985).

[16] W. Kochner and M. Bass, chapter 2 in *Solid-State Lasers*, (Springer-Verlag, 2003)

[17] K. W. Su, Y. T. Chang, and Y. F. Chen, "Power scale-up of the diode-pumped actively Q-switched Nd:YVO_4 Raman laser with an undoped YVO_4 crystal as a Raman shifter," Appl. Phys. B **88**, 47 (2007).

[18] Y. P. Lan, Y. F. Chen, and S. C. Wang, "Repetition-rate dependence of thermal loading in diode-end-pumped Q-switched lasers: influence of energy-transfer upconversion", Appl. Phys. B **71**, 27 (2000).

[19] J. A. Piper and H. M. Pask, "Crysatalline Raman Lasers," IEEE J. Sel. Top. Quantum Electron. **13**, 692 (2007).

[20] X. H. Chen, X. Y. Zhang, Q. P. Wang, P. Li, S. T. Li, Z. H. Cong, G. H. Jia, and C. Y. Tu, "Highly efficient diode-pumped actively Q-switched Nd:YAG-$SrWO_4$ intracavity Raman laser," Opt. Lett. **33**, 705 (2008).

Chapter 6

[1] A. A. Kaminskii, "Modern developments in the physics of crystalline laser materials," Phys. Sts. Sol. (a) **200**, 215 (2003).

[2] T. T. Basiev and R. C. Powell, "Special issue on solid state Raman lasers-Introduction," Opt. Mater. **11**, 301 (1999).

[3] H. M. Pask, “The design and operation of solid-state Raman lasers,” Prog. in Quantum Electron. **27**, 3 (2003).

[4] Y. F. Chen, “Stimulated Raman scattering in a potassium titanyl phosphate crystal: simultaneous self-sum frequency mixing and self-frequency doubling,” Opt. Lett. **30**, 400 (2005).

[5] S. Pearce, C. L. M. Ireland, and P. E. Dyer, “Solid-state Raman laser generating <1ns, multi-kilohertz pulses at 1096 nm,” Opt. Commun. **260**, 680 (2006).

[6] V. Pasiskevicius, C. Canalias, and F. Laurell, “Highly efficient stimulated Raman scattering of picosecond pulses in $KTiOPO_4$,” Appl. Phys. Lett. **88**, 041110 (2006).

[7] G. A. Massey, T. M. Loehr, L. J. Willis, and J. C. Johnson, “"Raman and Electro-optic Properties of Potassium Titanate Phosphate,”Appl. Opt. **19**, 4136 (1980).

[8] K. Kawase, M. Mizuno, S. Sohma, H. Takahashi, T. Taniuchi, Y. Urata, S. Wada, H. Tashiro, and H. Ito, “Difference-frequency terahertz-wave generation from 4-dimethylamino-N-methyl-4-stilbazolium-tosylate by use of an electronically tuned Ti:sapphire laser,” Opt. Lett. **24**, 1065 (1999).

[9] K. Kawase, T. Hatanaka, H. Takahashi, K. Nakamura, T. Taniuchi, and H. Ito, “Tunable terahertz-wave generation from DAST crystal by dual signal-wave parametric oscillation of periodically poled lithium niobate,” Opt. Lett. **25**, 1714 (2000).

[10] K. Suizu, K. Miyamoto, T. Yamashita, and H. Ito, “High-power terahertz-wave generation using DAST crystal and detection using mid-infrared powermeter,” Opt. Lett. **32**, 2885 (2007).

[11] R. A. Fields, M. Birnbaum, and C. L. Fincher, “Highly efficient Nd:YVO_4 diode-laser end-pumped laser, ” Appl. Phys. Lett. **51**, 1885 (1987).

[12] A. Sennaroglu, “ Efficient continuous-wave operation of a diode-pumped Nd:YVO_4 laser at 1342 nm, ” Opt. Commun. **164**, 191 (1999).

[13] Y. F. Chen, "Design criteria for concentration optimization in scaling diode end-pumped lasers to high powers: influence of thermal fracture," IEEE J. Quantum Electron. **35**, 234 (1999).

[14] A. Y. Yao, W. Hou, Y. P. Kong, L. Guo, L. A. Wu, R. N. Li, D. F. Cui, Z. Y. Xu, Y. Bi, and Y. Zhou, " Double-end-pumped 11-W Nd:YVO_4 cw laser at 1342 nm," J. Opt. Soc. Am. B **22**, 2129 (2005).

[15] T. Jensen, V. G. Ostroumov, J. P. Meyn, G. Huber, A. I. Zagumennyi, and I. A. Shcherbarkov, "Spectroscopic characterization and laser performance of diode-laser-pumped Nd:$GdVO_4$," Appl. Phys. B **58**, 373 (1994).

[16] H. J. Zhang, X. L. Meng, L. Zhu, H. Z. Zhang, P. Wang, J. Dawes, C. Q. Wang, and Y. T. Chow, "Investigation on the growth and laser properties of Nd:$GdVO_4$ single crystal," Cryst. Res. Technol. **33**, 801 (1998).

[17] T. Ogawa, Y. Urata, S. Wada, K. Onodera, H. Machida, H. Sagae, M. Higuchi, and K. Kodaira, "Efficient laser performance of Nd:$GdVO_4$ crystals grown by the floating zone method," Opt. Lett. **28**, 2333 (2003).

[18] V. Lupei, N. Pavel, Y. Sato, and T. Taira, "Highly efficient 1063-nm continuous-wave laser emission in Nd:$GdVO_4$," Opt. Lett. **28**, 2366 (2003).

[19] L. J. Qin, X. L. Meng, L. Zhu, J. H. Liu, B. C. Xu, H. Z. Xu, F. Y. Jiang, C. L. Du, X. Q. Wang, and Z. S. Shao, "Influence of the different Gd/Y ratio on the properties of Nd:$Y_xGd_{1-x}VO_4$ mixed crystals," Chem. Phys. Lett. **380**, 273 (2003).

[20] J. Liu, X. Meng, Z. Shao, M. Jiang, B. Ozygus, A. Ding, and H. Weber, "Pulse energy enhancement in passive Q-switching operation with a class of Nd:$Gd_xY_{1-x}VO_4$ crystals," Appl. Phys. Lett. **83**, 1289 (2003).

[21] Y. F. Chen, M. L. Ku, L. Y. Tsai, and Y. C. Chen, "Diode-pumped passively Q-switched picosecond Nd:$Gd_xY_{1-x}VO_4$ self-stimulated Raman laser," Opt. Lett. **29**, 2279 (2004).

[22] J. L He, Y. X. Fan, J. Du, Y. G. Wang, S. Liu, H. T. Wang, L. H. Zhang, and Y. Hang, "4-ps passively mode-locked Nd:$Gd_{0.5}Y_{0.5}VO_4$ laser with a semiconductor saturable-absorber mirror," Opt. Lett. **29**, 2803 (2004).

[23] S. P. Ng, D. Y. Tang, A. Q. Liu, L. J. Qin, and X. L. Meng, "Short pulse passively Q-switched $NdGdYVO_4$ laser using a GaAs mirror, " Opt. Coomun. **259**, 256 (2006).

[24] H. H. Yu, H. J. Zhang, Z. P. Wang, J. Y. Wang, Y. G. Yu, Z. S. Shao, M. H. Jiang, and X. Y. Zhang, "Continuous wave and passively Q-switched laser performance of Nd-doped mixed crystal Nd:$Lu_{0.5}Gd_{0.5}VO_4$," Appl. Phys. Lett. **90**, 231110 (2007).

[25] J. J. Zayhowski and A. Mooradian, "Single-frequency microchip Nd lasers," Opt. Lett. **14**, 24 (1989).

[26] G. J. Dixon, L. S. Lingvay, and R. H. Jarman, "Properties of close coupled monolithic, lithium neodymium, tetraphosphate lasers," Proc. SPIE **1104**, 107 (1989).

[27] Y. F. Chen, T. M. Huang, C. F. Kao, C. L. Wang, and S. C. Huang, "Optimization in scaling fiber-coupled laser-diode end-pumped lasers to higher power: influence of thermal effect," IEEE J. Quantum Electron. **33**, 1424 (1997).

[28] Y. F. Chen, "High-power diode-pumped Q-switched intracavity frequency-doubled Nd:YVO_4 laser with a sandwich-type resonator," Opt. Lett. **24**, 1032 (1999).

Chapter 7

[1] G. J. Zhang, S. Horinouchi, T. Kinoshita, and K. Sasaki, Theoretical analysis of the spatial phase-matching loci for second-harmonic generation and multiwave-mixing interactions," Appl. Opt. 34, 5301 (1995).

[2] Arthur R. Tunyagi, Michael Ulex, and Klaus Betzler, "Noncollinear optical frequency doubling in strontium barium niobate," Phys. Rev. Lett. **90**, 243901 (2003).

[3] P. Xu, S. H. Ji, S. N. Zhu, X. Q. Yu, J. Sun, H. T. Wang, J. L. He, Y. Y. Zhu, and N. B. Ming, "Conical Second Harmonic Generation in a Two-Dimensional $\chi^{(2)}$ Photonic Crystal: A Hexagonally Poled $LiTaO_3$ Crystal," Phys. Rev. Lett. 93, 133904 (2004).

[4] Y. F. Chen, K. W. Su, T. H. Lu, and K. F. Huang, "Manifestation of weak localization and long-range correlation in disordered wave functions from conical second harmonic generation," Phys. Rev. Lett. 96, 033905 (2006).

[5] M. V. Berry, "Regular and Irregular Semiclassical Wave Functions," J. Phys. A: Math. Gen. **10**, 2083 (1977).

Publication List

A. Journal Papers

[1] Y. F. Chen, K. W. Su, Y. T. Chang, and W. C. Yen, "Compact efficient eye-safe intracavity optical parametric oscillator with a shared cavity configuration," Appl. Opt. **46**, 3597-3601 (2007).

[2] K. W. Su, Y. T. Chang, and Y. F. Chen, "Power scale-up of the diode-pumped actively Q-switched Nd:YVO_4 Raman laser with an undoped YVO_4 crystal as a Raman shifter," Appl. Phys. B **88**, 47-50 (2007).

[3] Y. T. Chang, Y. P. Huang, K. W. Su, and Y. F. Chen, "Diode-pumped multi-frequency Q-switched laser with intracavity cascade Raman emission," Opt. Express **16**, 8286-8291 (2008).

[4] Y. P. Huang, Y. T. Chang, K. W. Su, Y. F. Chen, and K. F. Huang, "AlGaInAs intracavity selective absorber for an efficient high-power Nd:YAG laser operation at 1.44 μm," Opt. Lett. **33**, 1452-1454 (2008).

[5] K. W. Su, Y. T. Chang, and Y. F. Chen, "Efficient high-peak-power diode-pumped actively Q-switched Nd:YAG/YVO_4 intracavity Raman laser," Appl. Opt. **47**, 6675-6679 (2008).

[6] Y. T. Chang, Y. P. Huang, K. W. Su, and Y. F. Chen, "Comparison of thermal lensing effects between single-end and double-end diffusion-bonded Nd:YVO_4 crystals for $^4F_{3/2}\rightarrow{}^4I_{11/2}$ and $^4F_{3/2}\rightarrow{}^4I_{13/2}$ transitions," Opt. Express **16**, 21155-21160 (2008).

[7] Y. P. Huang, H. L. Chang, Y. J. Huang, Y. T. Chang, K. W. Su, W. C. Yen, and Y.

F. Chen, “Subnanosecond mJ eye-safe laser with an intracavity optical parametric oscillator in a shared resonator,” Opt. Express. **17**, 1551-1556 (2009).

[8] Y. T. Chang, H. L. Chang, K. W. Su, and Y. F. Chen, “Compact efficient Q-switched eye-safe laser at 1525 nm with a double-end diffusion-bonded Nd:YVO_4 crystal as a self-Raman medium,” Opt. Express **17**, 4330-4335 (2009).

[9] Y. T. Chang, H. L. Chang, K. W. Su, and Y. F. Chen, “High-efficiency Q-switched dual-wavelength emission at 1176 and 559 nm with intracavity Raman and sum-frequency generation,” Opt. Express **17**, 11892-11897 (2009).

B. Conference Papers

K.W. Su, Y.T. Chang, and Y.F. Chen, “High-peak-power diode-pumped actively Q-switched Nd:YAG intracavity Raman laser with an undoped YVO_4 crystal”, Solid State Lasers XVII, PW2008, Proceedings of SPIE 6871, San Jose, USA (Jan 2008)

Compact efficient eye-safe intracavity optical parametric oscillator with a shared cavity configuration

Y. F. Chen,[1,*] K. W. Su,[1] Y. T. Chang,[1] and W. C. Yen[2]

[1]Department of Electrophysics, National Chiao Tung University, Hsinchu, Taiwan
[2]Chung-Shan Institute of Science and Technology, Lung-Tan, Tao-Yuan, Taiwan

*Corresponding author: yfchen@cc.nctu.edu.tw

Received 12 October 2006; revised 3 December 2006; accepted 7 December 2006;
posted 11 December 2006 (Doc. ID 76051); published 18 May 2007

We present a compact efficient eye-safe intracavity optical parametric oscillator pumped by a passively Q-switched Nd:YAG laser in a shared cavity configuration. A signal pulse of 3.3 mJ energy at a 1573 nm wavelength with a peak power of 150 kW was achieved. The effective conversion efficiency with respective to the optimized 1064 nm Q-switched pulse energy was as high as 51%. © 2007 Optical Society of America

OCIS codes: 140.3580, 140.5560.

1. Introduction

Compact nanosecond pulsed lasers operating with emission at the eye-safe wavelength region (1.5–1.6 μm) are of great interest for many applications such as laser radar, active imaging, and remote sensing [1,2]. The methods for generating eye-safe lasers include the solid-state lasers with Er^{3+}-doped or Cr^{4+}-doped media [3–6] and the Raman lasers pumped by Nd-doped lasers [7–10]. Another promising approach for high-peak-power eye-safe laser sources is based on intracavity optical parametric oscillators (OPO) [11–16]. The advent of high damage threshold nonlinear crystals and diode-pumped Nd-doped lasers leads to a renaissance of interest in intracavity OPOs. Recently we demonstrated a compact efficient eye-safe OPO pumped by a diode-pumped passively Q-switched Nd:GVO_4 laser to produce peak powers at 1573 nm higher than 10 kW [17]. However, the applications for long-distance laser rangefinders require pulse energies in the millijoule range and peak powers greater than 100 kW [2].

The conventional configurations for intracavity OPO pumped by Q-switched Nd-doped lasers [11–17] are based on the coupled cavity configuration in which there are separate resonators for the signal and fundamental optical fields. However, the amplitude stability of the signal outputs for the coupled cavity configuration is severely dependent on the cavity alignment because the resonator lengths and the longitudinal-mode spacing are different for the pump and signal beams. Recently it was confirmed [18] that the shared cavity configuration in which the pump and signal beams share the same resonator provides a substantially superior amplitude stability in comparison with the coupled cavity configuration. Therefore it is of practical interest to develop the eye-safe intracavity OPO in the millijoule range with the shared cavity configuration.

In this work we use a shared resonator configuration to construct a compact intracavity OPO in the millijoule range. A lens duct is designed to be an efficient coupling lens for the diode-pumped passively Q-switched Nd:YAG/Cr^{4+}:YAG laser. With the passively Q-switched laser to pump the intracavity OPO, 3.3 mJ pulses with 150 kW peak power at 1573 nm are generated. The effective conversion efficiency with respective to the optimized pulse energy form the passively Q-switched 1064 nm laser is up to 51%.

2. Experimental Setup of Intracavity Optical Parametric Oscillator

The pump source is a quasi-cw high-power diode stack (Coherent G-stack package, Santa Clara, Calif.,

0003-6935/07/173597-05$15.00/0

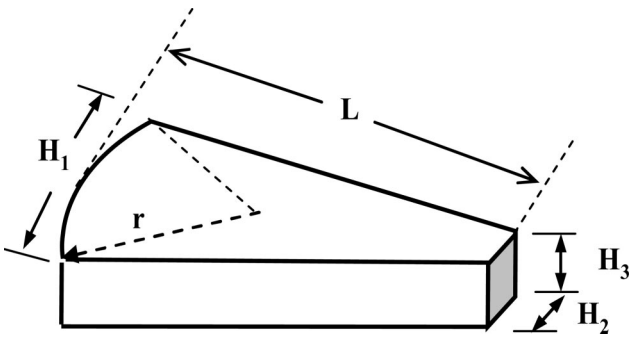

Fig. 1. Schematic of a lens duct in which r is the radius of the input surface, L is the length of the duct, H_1 is the width of the input surface, H_2 is the width of the output surface, and H_3 is the thickness of the duct.

USA) that consists of six 10 mm long diode bars generating 80 W per bar, for a total of 480 W at the central wavelength of 808 nm. The diode stack is designed with 0.4 mm spacing between the diode bars so the overall area of emission is approximately 10 mm (slow axis) × 2.4 mm (fast axis). The full divergence angles in the fast and slow axes are approximately 35° and 10°, respectively. A lens duct was designed to efficiently couple the pump radiation from the diode stack into the laser crystal. As shown in Fig. 1, there are five geometric parameters, r, L, H_1, H_2, and H_3, for a lens duct, where r is the radius of the input surface, L is the length of the duct, H_1 is the width of the input surface, H_2 is the width of the output surface, and H_3 is the thickness of the duct [19,20]. With the ray-tracing analysis [20], the coupling efficiency was found to be up to 87% for a lens duct with the parameters of r = 10 mm, L = 32 mm, H_1 = 12 mm, H_2 = 2.7 mm, and H_3 = 3 mm. Based on the theoretical result, a lens duct was manufactured and used in the experiment.

Figure 2(a) shows the experimental setup of the intracavity OPO pumped by a diode-pumped passively Q-switched Nd:YAG/Cr^{4+}:YAG laser in a shared cavity configuration. The fundamental laser cavity was formed by a coated Nd:YAG crystal and an output coupler. The OPO cavity entirely overlapped with the fundamental laser cavity. The Nd:YAG crystal had a 1.0 at. % Nd^{3+} doping concentration, a diameter of 5 mm, and a length of 10 mm. To set up the shared cavity, the incident side of the laser crystal was coated to be highly reflective at 1064 and 1573 nm (R > 99.8%) and highly transmitted at the pump wavelength of 808 nm (T > 90%). The other side of the laser crystal was coated to be antireflective at 1064 and 1573 nm (R < 0.2%). A KTP crystal was used to be the nonlinear crystal of the OPO. The KTP crystal, 4 mm × 4 mm × 20 mm, was employed in a type II noncritical phase-matching configuration along the x axis ($\theta = 90°$, and $\phi = 0°$) to have both a maximum effective nonlinear coefficient and no walk off between the pump, signal, and idler beams. On the other hand, a Cr^{4+}:YAG crystal was used to serve as a saturable absorber for passive Q-switching. The Cr^{4+}:YAG crystal had a thickness of 3 mm with 60% initial transmission at 1064 nm. Both sides of the KTP and Cr^{4+}:YAG crystals were coated for antireflection at 1573 and 1064 nm. The output coupler had a dichroic coating that was highly reflective at 1064

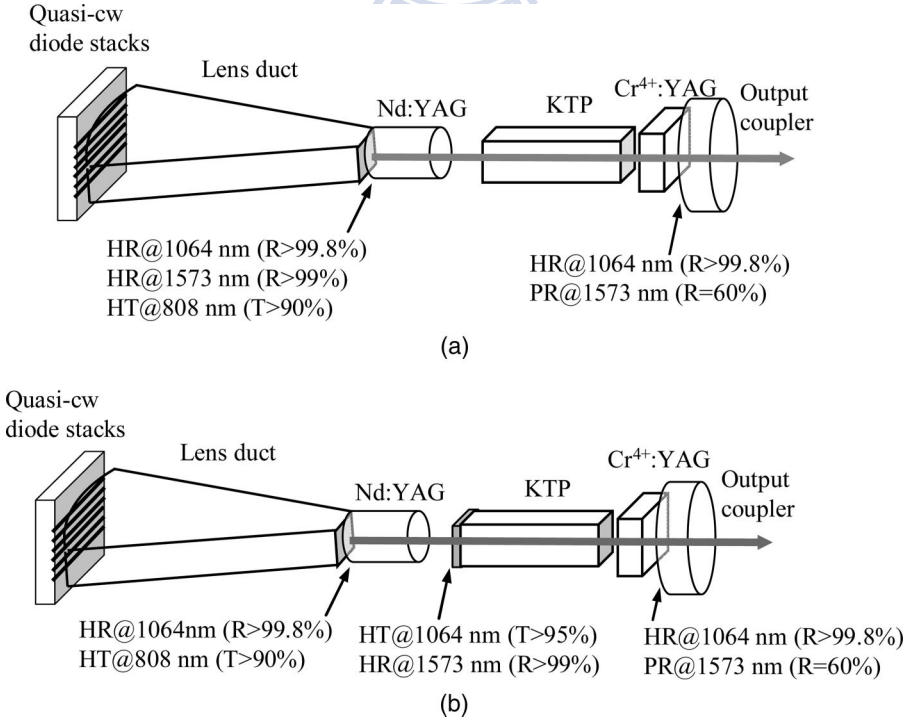

Fig. 2. Schematic of the intracavity OPO pumped by a diode-pumped passively Q-switched Nd:YAG/Cr^{4+}:YAG laser. (a) Shared cavity, (b) coupled cavity.

nm (R > 99.8%) and partially reflective at 1573 nm (R = 60%). All crystals were wrapped with indium foil and mounted in conductively cooled copper blocks. The total cavity length was approximately 50 mm.

For comparison, the conventional coupled cavity configuration is depicted in Fig. 2(b). It can be seen that the OPO cavity in the coupled resonator configuration was formed by a coated KTP crystal and an output coupler and the OPO cavity length was approximately 25 mm. One side of the KTP crystal was coated to have high reflection at the signal wavelength of 1573 nm (R > 99.8%) and high transmission at the pump wavelength of 10643 nm (T > 95%). The other side of the KTP crystal was coated for antireflection at 1573 and 1063 nm.

The pulse temporal behavior at 1063 and 1571 nm was recorded by a LeCroy digital oscilloscope (Wavepro 7100; 10 G samples/s, 1 GHz bandwidth) with a fast InGaAs photodiode. The spectral information of the laser was monitored by an optical spectrum analyzer (Advantest Q8381A, Tokyo, Japan). The spectrum analyzer employing diffraction grating monochromator can be used for high-speed measurement of pulse light with the resolution of 0.1 nm.

3. Experimental Results

First, the quasi-cw free-running operation without KTP and Cr^{4+}:YAG crystals was performed to confirm the pumping efficiency of the lens duct and the quality of the laser crystal. For this investigation the diode stack was derived to emit optical pulses 200 μs long, at a repetition rate of 100 Hz with a maximum duty cycle of 2%. Furthermore an output coupler with 96% reflectivity at 1064 nm was used instead of the above-mentioned OPO output coupler. Figure 3 plots the experimental results of the free-running operation for the output average power as a function of the diode pump power. It can be seen that the output power of 160 W was achieved at an incident pump power of 360 W. The overall slope efficiency was found to be as high as 45%. The fairly good efficiency affirms the pump scheme to be practical.

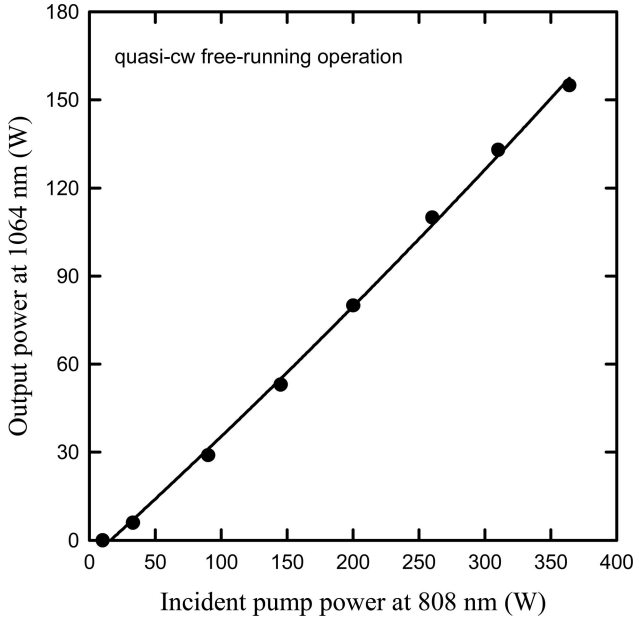

Fig. 3. Output power at 1064 nm with respect to the incident pump power at 808 nm for quasi-cw free-running operation.

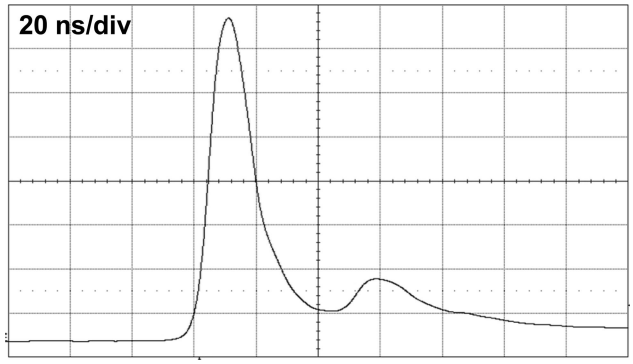

Fig. 4. Temporal shape for the passively Q-switched Nd:YAG/Cr^{4+}:YAG laser at 1064 nm.

We estimated the performance of the passively Q-switched Nd:YAG/Cr^{4+}:YAG laser before the intracavity OPO experiment. For this investigation an output coupler with partial reflection at 1064 nm was used, and the diode stack was derived to emit optical pulses 250 μs long at a repetition rate of 10 Hz. The optimum Q-switched performance at 1064 nm provides the baseline for evaluating the conversion efficiency of the intracavity OPO. The optimum reflectivity of the output coupler was found to be approximately 60%. The threshold of the Q-switched laser operation was found to be approximately 102 mJ, and the output pulse energy at 1064 nm was measured to be 6.5 mJ. As shown in Fig. 4, the effective pulse width was found to be approximately 19 ns; consequently, the peak power was up to 330 kW.

With an OPO output coupler, the intracavity OPO experiment was performed. The threshold of the intracavity OPO was found to be nearly the same as that of the passively Q-switched laser. The output

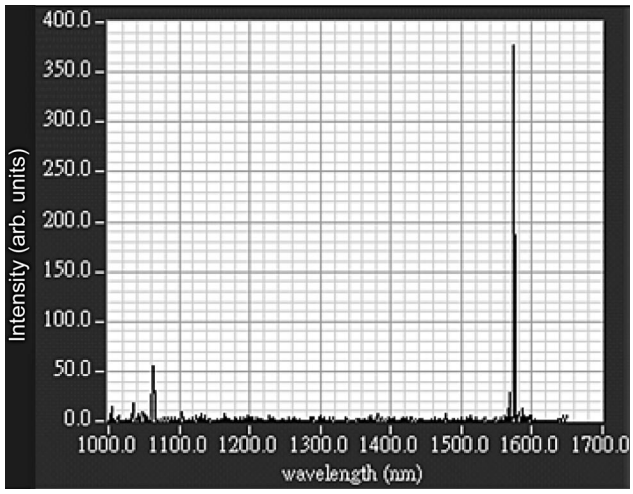

Fig. 5. Optical spectrum measurement for the intracavity OPO.

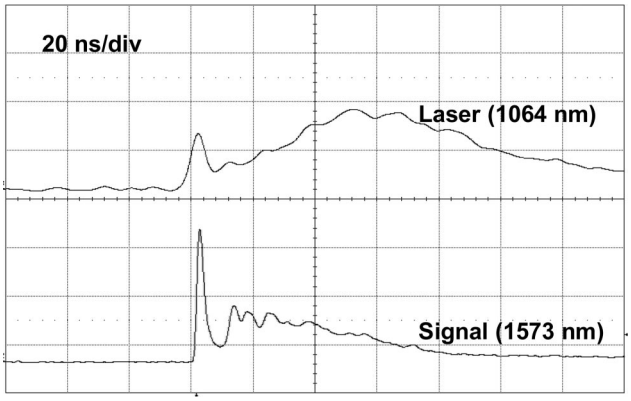

Fig. 6. Typical temporal shapes for the laser and signal pulses.

pulse energy of the signal wave at 1573 nm was measured to be 3.3 mJ. The effective conversion efficiency with respect to the optimized pulse energy from the passively Q-switched laser is up to 51%. For the coupled cavity [12], the conversion efficiency was found to be approximately 26%. In other words, the conversion efficiency of the shared cavity configuration is significantly superior to that of the coupled cavity configuration. The OPO performance of the shared cavity basically depends on the total laser power of all longitudinal modes not on the explicit distribution of the laser power among the longitudinal modes. The small perturbations in the stable resonators usually lead to considerable variations in the power distribution among the longitudinal modes and do not significantly affect the total laser power. On the other hand, in the coupled cavity configuration the OPO and laser resonators have different longitudinal mode spacings; mostly only one longitudinal laser mode is utilized to pump the OPO, and only one signal longitudinal mode builds up. Therefore the overall conversion efficiency of the shared cavity configuration is substantially superior to that of the coupled cavity configuration.

The typical result for the optical spectrum measurement is depicted in Fig. 5. Figure 6 shows the temporal shapes of the laser and signal pulses. It can be seen that the signal output consisted of a short intensive leading peak accompanied by a long weak ripple. The long weak ripple may come from the interaction between different longitudinal modes; thus far, the mechanism of its appearance is still unknown and needs further investigation. With the numerical integration, the signal peak power was calculated and found to be approximately 150 kW. The signal peak power is expected to be enhanced by the use of an output coupler with a lower reflectivity at the signal wavelength. The spatial distribution of the signal output was recorded with an infrared CCD and displayed in Fig. 7. The beam quality M^2 factor was estimated to be approximately 1.5.

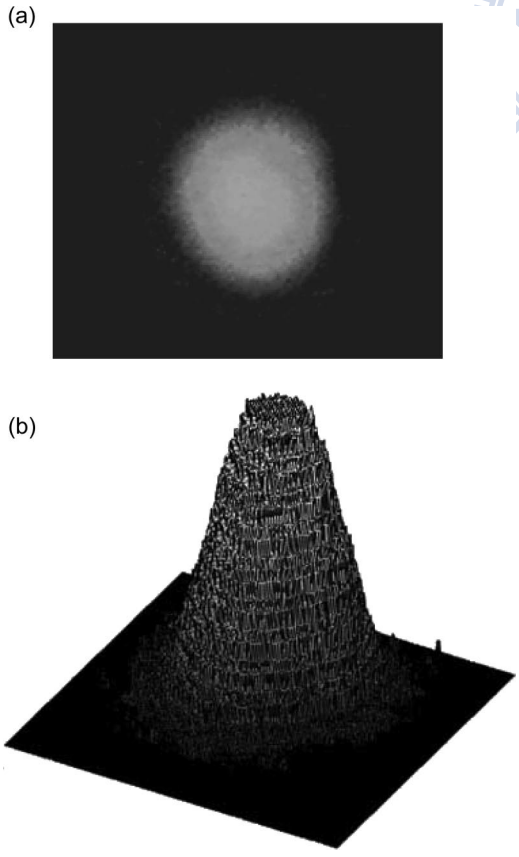

Fig. 7. Experimental far-field pattern of the signal output pulse. (a) 2D image, (b) 3D representation.

4. Conclusions

We have employed a diode-pumped passively Q-switched Nd:YAG laser to pump an intracavity OPO in a shared cavity configuration. A lens duct has been designed to efficiently couple the pump radiation from the diode stack into the laser crystal. A slope efficiency of 45% has been obtained for the quasi-cw free-running operation in the fundamental mode lasing. For the Q-switching operation at 1064 nm, the cavity produced 6.5 mJ pulses with 330 kW peak power. With the Q-switched laser to pump the OPO at 1573 nm, 3.3 mJ pulses with 150 kW peak power have been achieved, corresponding to an effective conversion efficiency of 51% with respect to the optimized pulse energy at 1064 nm.

References

1. E. Gregor, D. E. Nieuwsma, and R. D. Stultz, "20 Hz eye-safe laser rangefinder for air defense," in Proc. SPIE **1207,** 124–134 (1990).
2. J. E. Nettleton, B. W. Schilling, D. N. Barr, and J. S. Lei, "Monoblock laser for a low-cost, eyesafe, microlaser range finder," Appl. Opt. **39,** 2428–2432 (2000).
3. S. Kück, K. Petermann, U. Pohlmann, U. Schönhoff, and G. Huber, "Tunable room-temperature laser action of Cr^{4+}-doped $Y_3Sc_xAl_{5-x}O_{12}$," Appl. Phys. B **58,** 153–156 (1994).
4. N. V. Kuleshov, A. A. Lagatsky, A. V. Podlipensky, V. P. Mikhailov, A. A. Kornienko, E. B. Dunina, S. Hartung, and G. Huber, "Fluorescence dynamics, excited-state absorption and stimulated emission of Er^{3+} in $KY(WO_4)_2$," J. Opt. Soc. Am. B **15,** 1205–1212 (1998).
5. I. Sokólska, E. Heumann S. Kück, and T. Łukasiewicz, "Laser oscillation of Er^{3+}:YVO_4 and Er^{3+}, Yb^{3+}:YVO_4 crystals in the

spectral range around 1.6 μm," Appl. Phys. B **71,** 893–896 (2000).
6. A. Sennaroglu, "Broadly tunable Cr^{4+}-doped solid-state lasers in the near infrared and visible," Prog. Quantum Electron. **26,** 287–352 (2002).
7. P. Černý, H. Jelínkova, P. Zverev, and T. T. Basiev, "Solid-state lasers with Raman frequency conversion," Prog. Quantum Electron. **28,** 113–143 (2004).
8. Y. F. Chen, "Compact efficient all-solid-state eye-safe laser with self-frequency Raman conversion in a Nd:YVO4 crystal," Opt. Lett. **29,** 2172–2174 (2004).
9. Y. F. Chen, "Efficient 1521 nm Nd:$GdVO_4$ Raman laser," Opt. Lett. **29,** 2632–2634 (2004).
10. J. T. Murray, R. C. Powell, D. Smith, W. Austin, and R. A. Stolzenberger, "Generation of 1.5 μm radiation through intracavity solid-state Raman shifting in $Ba(NO_3)_2$ nonlinear crystals," Opt. Lett. **20,** 1017–1019 (1995).
11. Y. Yashkir and H. M. van Driel, "Passively *Q*-switched 1.57 μm intracavity optical parametric oscillator," Appl. Opt. **38,** 2554–2559 (1999).
12. A. Agnesi, S. Dell'Acqua, and G. Reali, "Diode-pumped quasi-cw intracavity optical parametric oscillator at 1.57 μm with efficient pulse shortening," Appl. Phys. B **70,** 751–753 (2000).
13. R. Dabu, C. Fenic, and A. Stratan, "Intracavity pumped nanosecond optical parametric oscillator emitting in the eye-safe range," Appl. Opt. **40,** 4334–4340 (2001).
14. W. Zendzian, J. K. Jabczyński, and J. Kwiatkowski, "Intracavity optical parametric oscillator at 1572 nm wavelength pumped by passively *Q*-switched diode-pumped Nd:YAG laser," Appl. Phys. B **76,** 355–358 (2003).
15. Y. F. Chen, S. W. Chen, Y. C. Chen, Y. P. Lan, and S. W. Tsai, "Compact efficient intracavity optical parametric oscillator with a passively *Q*-switched Nd:YVO_4/Cr^{4+}:YAG laser in a hemispherical cavity," Appl. Phys. B **77,** 493–495 (2003).
16. B. W. Schilling, S. R. Chinn, A. D. Hays, L. Goldberg, and C. W. Trussell, "End-pumped 1.5 μm monoblock laser for broad temperature operation," Appl. Opt. **45,** 6607–6615 (2006).
17. Y. F. Chen, S. W. Chen, L. Y. Tsai, Y. C. Chen, and C. H. Chien, "Efficient subnanosecond intracavity optical parametric oscillator pumped with a passively *Q*-switched Nd:$GdVO_4$ laser," Appl. Phys. B **79,** 823–825 (2004).
18. Y. F. Chen and L. Y. Tsai, "Comparison between shared and coupled resonators for passively *Q*-switched Nd:GdVO4 intracavity optical parametric oscillators," Appl. Phys. B **82,** 403–406 (2006).
19. R. J. Beach, "Theory and optimization of lens ducts," Appl. Opt. **35,** 2005–2015 (1996).
20. R. Fu, G. Wang, Z. Wang, E. Ba, G. Mu, and X. Hu, "Design of efficient lens ducts," Appl. Opt. **37,** 4000–4003 (1998).

Appl. Phys. B 88, 47–50 (2007)
DOI: 10.1007/s00340-007-2648-0

Applied Physics B
Lasers and Optics

K.W. SU✉
Y.T. CHANG
Y.F. CHEN

Power scale-up of the diode-pumped actively Q-switched Nd:YVO_4 Raman laser with an undoped YVO_4 crystal as a Raman shifter

Department of Electrophysics, National Chiao Tung University, F353, Engineering Building VI, No 1001, Ta Hsueh Rd, Hsinchu 300, Taiwan

Received: 18 December 2006 /
Revised version: 9 February 2007
Published online: 15 May 2007 •

ABSTRACT With an undoped YVO_4 crystal as a Raman shifter, we substantially improved the reliability and the output performance of an actively Q-switched 1176-nm Nd:YVO_4 Raman laser. With an incident pump power of 18.7 W, the average power is greater than 2.6 W at 80 kHz. The pulse width of the pulse envelope is shorter then 5 ns with mode-locked modulation. With an incident pump power of 12.7 W, the pulse energy and peak power is higher than 43 μJ and 14 kW at 40 kHz.

PACS 42.55.Ye; 42.55.Xi; 42.60.Gd

1 Introduction

Since the development of new Raman crystals in the last decade [1–12], the stimulated Raman scattering (SRS) in crystal [13] has provided solid-state lasers with an important way of operating in different wavelengths. The most commonly known materials for SRS are $Ba(NO_3)_2$ [14], $LiIO_3$ [15], $KGd(WO_4)_2$ [16], $PbWO_4$ [17], and $BaWO_4$ [5, 6, 18–22]. Moreover, for self-Raman lasers, the materials such as Yb:$KGd(WO_4)_2$ [23], Nd:$KGd(WO_4)_2$ [24–31], Nd:$PbWO_4$ [32], Nd:$Gd_xY_{1-x}VO_4$ [33, 34], Nd:$PbMoO_4$ and Nd:$SrMoO_4$ [11, 12] have been reported. A combination of their laser-emission and SRS properties made these crystals appealing self-Raman media. Nevertheless, the Raman scattering was generated by host material. Lasers could offer a number of advantages if the SRS could be transferred from self-Raman media to additional undoped crystals.

Nd-doped YVO_4 and $GdVO_4$ crystals, the acknowledged useful gain media, were used in passively Q-switched (PQS) and actively Q-switched (AQS) self-Raman lasers [34–39]. For instance, an AQS Nd:YVO_4 self-Raman laser demonstrated the average power, pulse width and peak power of 1.5 W, 18 ns and 4.2 kW for the Stokes wavelength of 1176 nm [36]. However, the issue of the filed-induced crystal damage usually restricted the output powers in self-Raman Q-switched lasers [39].

✉ Fax: +886-35 725230, E-mail: yfchen@cc.nctu.edu.tw

In this work, to our knowledge, we report a new design of a diode-pumped AQS 1176-nm Nd:YVO_4 Raman laser to increase the average power, repetition rate, peak power, and damage threshold comprehensively. An undoped YVO_4 crystal is employed to be an intracavity Raman shifter in a Nd:YVO_4 AQS laser. At an incident pump power of 18.7 W, the AQS Raman laser produces an average power greater than 2.6 W with a pulse repetition rate of 80 kHz. The output pulses noticeably display a mode-locking phenomenon that leads to the maximum peak power to be higher than 14 kW.

2 Experimental setup

Figure 1 shows the experiment configuration for AQS Nd:YVO_4 1176-nm Raman laser which differs from self-Raman laser. The pump source was an 808-nm fiber-coupled laser diode with the core diameter of 800 μm, the numerical aperture of 0.16, and the maximum output power of 25 W. A focusing lens unit with a 85% coupling efficiency was used to reimage the pump beam into the gain medium with a pump spot radius of 400 μm. The gain medium, a 9-mm-long a-cut Nd:YVO_4 crystal with low concentrations, 0.25 at. %, was used to reduce thermally induced fracture [36]. Both sides of this laser crystal were coated for antireflection (AR) at 1.06 μm ($R < 0.2\%$). The Raman crystal was a 9.6-mm-long a-cut undoped YVO_4 crystal. These two crystals were both wrapped with indium foil and mounted in water-cooled copper blocks individually. The 30-mm-long acousto-optic (AO) Q switch (NEOS Technologies) had AR coating at 1064 nm on both faces and was driven at a 27.12-MHz center frequency by 15 W of RF power. The resonator was a plano-concave configuration. Front mirror, a 500-mm radius-of-curvature concave mirror, was coated with AR coating at 808 nm ($R < 0.2\%$) on the entrance face, and with high-reflection (HR) coating at 1064 nm ($R > 99.8\%$) and high-transmission (HT) coating at 808 nm ($T > 90\%$) on the other face. The coating of front mirror at 1176 nm was high-reflection, too. The output coupler (OC) was a flat mirror with HR coating at 1064 nm ($R > 99.8\%$) and partial-reflection (PR) coating at 1176 nm ($R = 51\%$). The cavity length was around 115 mm and depended on pumping power. The spectrum of laser output was monitored by an optical spectrum analyzer (Advantest Q8381A, includ-

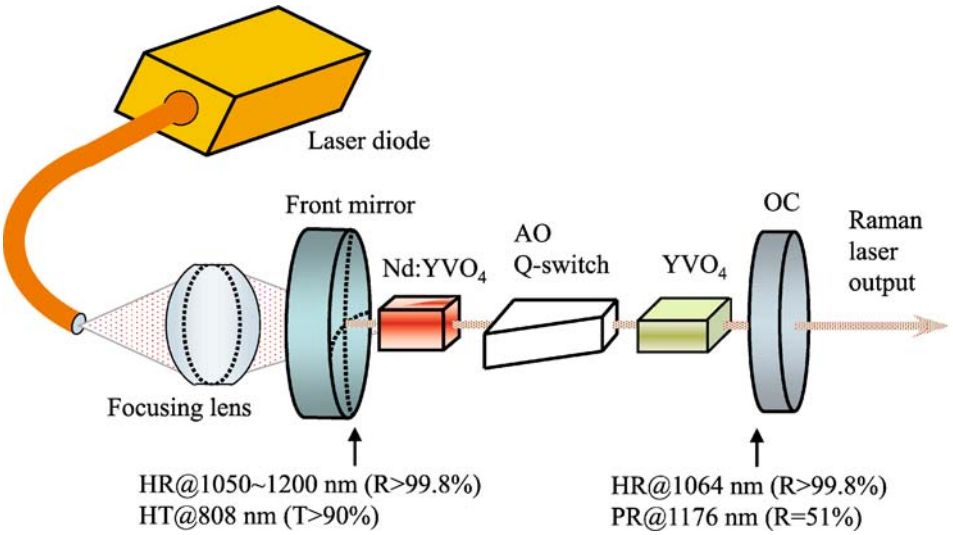

FIGURE 1 Schematic of a diode-pumped actively Q-switched Nd:YVO_4 Raman laser at 1176 nm

ing a diffraction lattice monochromator) with a resolution of 0.1 nm. The temporal behaviors for fundamental and Raman pulses were recorded by a LeCroy digital oscilloscope (Wavepro 7100, 10 Gs/s, 1-GHz bandwidth) with two fast p-i-n photodiode and an interference filter allowing transmission only at 1064 nm.

3 Experimental results and discussion

As a stimulated Raman material, taking the place of Nd:YVO_4 by undoped YVO_4 has advantages on robustness and output properties. Figure 2 displays the experimental result for optical spectrum of the laser output and Raman scattering spectrum of the YVO_4. The first Stokes wavelength near 1176 nm was conversed from the fundamental wavelength near 1064 nm by Raman peak at 890 cm^{-1}. The Raman shift of Nd:YVO_4 and undoped YVO_4 were almost the same, came from the same periodic YVO_4 lattice. But crystals without dopant had more perfect lattice, which brought on higher damage threshold and more stable frequency conversion. So, we can put the pure YVO_4 as a Raman crystal in the position where the intensity is highest in the cavity, and still increase the pumping power. Further, the reflectance of OC can be lower (from 93% to 51%) to scale up average output power due to lower lasing threshold at Raman wavelength. By using lower reflection coating, we can narrow the pulse width. At the same time, when we over drove current during the experiment, the damage never happened in Nd:YVO_4, but in Raman crystal. That means the SRS was generated mainly in pure YVO_4, a more reliable and replaceable component in practical laser.

Figures 3 and 4 illustrate the output performance of AQS 1176-nm Nd:YVO_4 Raman laser. The average output power at the Stokes wavelength of 1176 nm with respect to the inci-

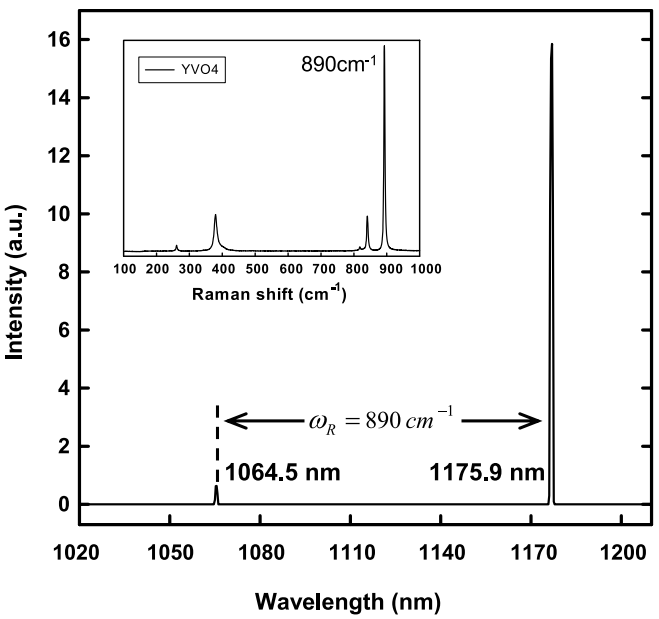

FIGURE 2 Optical spectrum of the actively Q-switched Raman output. The Raman scattering spectrum of an YVO_4 crystal showed in *inset*, which is almost the same as it of Nd:YVO_4 crystal

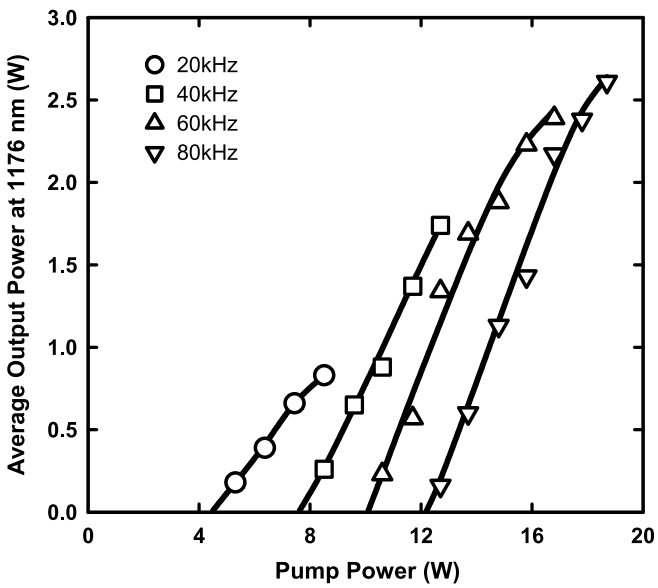

FIGURE 3 The average output power at the Stokes wavelength of 1176 nm with respect to the incident pump power at different pulse repetition rate from 20 kHz to 80 kHz

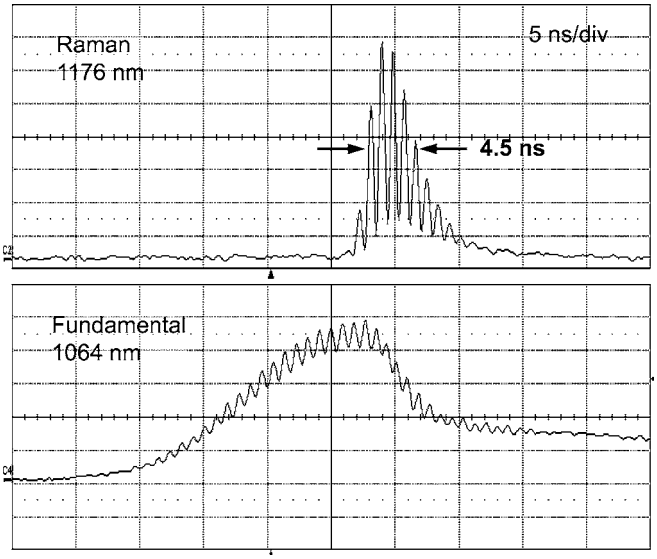

FIGURE 4 An oscilloscope trace with mode-locking effect for fundamental and Raman pulses

dent pump power for different pulse repetition rate of 20, 40, 60, and 80 kHz shown in Fig. 3. Because the thermal loading of the end-pumped Q-switched Nd-doped laser increases with decreasing repetition rate [24, 25], it can be seen that although the pumping threshold is higher, increasing the pulse repetition rate can efficiently increase the maximum average output power at 1176 nm and its maximum pump power ($P_{p,max}$). And for a certain repetition rate, to pump over $P_{p,max}$ will get the unstable Raman conversion and fall the output power. The average output power is up to 2.61 W with an incident pump power of 18.7 W at a repetition rate of 80 kHz, corresponding to the conversion efficiency of 14% and slope efficiency of 40%. Comparing to results of 1176-nm self-Raman laser by use of Nd:YVO_4 with lower dopant concentration of 0.2 at. % [36], this Raman laser still has the increase of ratio in average power of 74% and in conversion efficiency of 0.7%. It could be better if we were able to use 0.2 at. % Nd:YVO_4 and correctly AR-coated c-cut [41] YVO_4 in this Raman laser. On the other hand, the maximum pulse energy is generally greater then 40 μJ at repetition rate from 20 to 60 kHz, and up to 43.5 μJ at 40 kHz with an incident pump power of 12.7 W. The maximum pulse energy at repetition rate of 80 kHz is 32.6 μJ.

The typical time traces for fundamental and Raman pulses are shown in Fig. 4. The pulse width is always shorter then 5 ns, but the effective pulse width is much shorter due to mode-locked shape. With the pulse energy of 43.5 μJ, the pulse width of the pulse envelop in Fig. 4 is 4.5 ns, and the peak power of the pulse seen as a Gaussian shape should be 9.7 kW. However, after curve fitting for the mode-locked shape, the peak power is enhanced to 14 kW, 1.45 times the 9.7 kW. In other words, the effective pulse width is around 3.1 ns which is much shorter than 18 ns of self-Raman laser [36]. Comparing to 1176-nm Nd:YVO_4 AQS self-Raman laser of 4.2 kW [36], the output peak power was enhanced to be more than two times. The present peak-power level was close to the results of the PQS Nd:$GdVO_4$ self-Raman lasers in which the average power, pulse width and peak power were found to be 83 mW, 500 ps, and 9.2 kW at 1174 nm in [37], or 140 mW, 750 ps, and 8.4 kW at 1176 nm in [38].

4 Conclusions

In conclusion, with an undoped YVO_4 as a stimulated Raman crystal, we substantially improve the damage threshold, repetition rate, average output power, pulse width, and the peak power of AQS Nd:YVO_4 Raman lasers at 1176 nm. With an incident pump power of 18.7 W, the average power is 2.6 W at 80 kHz correspond to the optical-to-optical conversion efficiency of 14%. Coming with the mode-locked pulse shape, the effective cavity dump of intracavity SRS leads to peak power at 1176 nm that is generally greater than 10.5 kW at repetition rate from 20 to 80 kHz. With an incident pump power of 12.7 W, the pulse energy and peak power is higher than 43.5 μJ and 14 kW at 40 kHz.

REFERENCES

1 T.T. Basiev, V.V. Osiko, A.M. Prokhorov, E.M. Dianov, Top. Appl. Phys. **89**, 351 (2003)
2 T.T. Basiev, R.C. Powell, *Solid State Raman Lasers* in *Handbook of Laser Technology and Applications*, B1.7, 469 (Institute of Physics Publishing, London, 2003)
3 H.M. Pask, Prog. Quantum Electron. **27**, 3 (2003)
4 R.G. Zevrev, T.T. Basiev, A.M. Prokhorov, Opt. Mater. **11**, 335 (1999)
5 T.T. Basiev, A.A. Sobol, P.G. Zverev, L.I. Iveleva, V.V. Osiko, R.C. Powell, Opt. Mater. **11**, 307 (1999)
6 P. Cerný, P.G. Zverev, H. Jelínková, T.T. Basiev, Opt. Commun. **177**, 397 (2000)
7 J.T. Murray, W.L. Austin, R.C. Powell, Advanced Solid-State Lasers, ed. by W.R. Bosenberg, M.J. Fejer, Vol. 19 of OSA, *Trends in Optics and Photonics Series* (Optical Society of America, Washington D.C., 1998), pp. 129–135
8 J.T. Murray, W.L. Austin, R.C. Powell, Advanced Solid-State Lasers, ed. by M.J. Fejer, H. Injeyan, U. Keller, Vol. 26 of OSA, *Trends in Optics and Photonics Series* (Optical Society of America, Washington D.C., 1999), pp. 575–578
9 C. He, T.H. Chyba, Opt. Commun. **135**, 273 (1997)
10 J.T. Murray, W.L. Austin, R.C. Powell, Opt. Mater. **11**, 353 (1999)
11 T.T. Basiev, S.V. Vassiliev, M.E. Doroshenko, V.V. Osiko, V.M. Puzikov, M.B. Kosmyna, Opt. Lett. **31**, 65 (2006)
12 T.T. Basiev, S.V. Vassiliev, M.E. Doroshenko, V.V. Osiko, *Laser Oscillation and Self-Raman Frequency Conversion in* Nd:$PbMoO_4$ *and* Nd:$SrMoO_4$ *Crystals under Laser Diode Pumping*, Technical Digest, Advanced Solid State Photonics, Jan. 29, 2006, Lake Tahoo, OSA, TuB21 (2006)
13 G. Eckhardt, D.P. Bortfeld, M. Geller, Appl. Phys. Lett. **3**, 137 (1963)
14 A.S. Eremenko, S.N. Karpukhin, A.I. Stepanov, Sov. J. Quantum Electron. **10**, 113 (1980)
15 E.O. Ammann, C.D. Decker, J. Appl. Phys. **48**, 1973 (1977)
16 A.S. Grabtachikov, A.N. Kuzmin, V.A. Lisinetskii, V.A. Orlovich, G.I. Ryabtsev, A.A. Demidovich, Appl. Phys. Lett. **75**, 3742 (1999)
17 J. Findeisen, H.J. Eichler, A.A. Kaminskii, IEEE J. Quantum Electron. **QE-35**, 173 (1999)
18 T.T. Basiev, A.A. Sobol, P.G. Zverev, L.I. Iveleva, V.V. Osiko, R.C. Powell, *Laser material for stimulated Raman scattering*, patent of Russian Fedration, 2178938 C1 1, pending 25.04.2000
19 T.T. Basiev, P.G. Zverev, A.A. Sobol, V.V. Skornyakov, L.I. Iveleva, N.M. Polozkov, V.V. Osiko, Sov. J. Quantum Electron. **30**, 55 (2000)
20 P.G. Zverev, T.T. Basiev, M.E. Doroshenko, V.V. Osiko, *Barium Tungstate Raman laser – A new Coherent Source for Sodium Star Experiments*, Trends in Optics and Photonics 34, Advanced Solid State Lasers, ed. by H. Injeyan, U. Keller, C. Marshall, (OSA, Washington D.C., 2000), pp. 348–354
21 P.G. Zverev, T.T. Basiev, L.I. Ivleva, V.V. Osiko, N.M. Polozkov, I.S. Voronina, *Raman Laser on Strontium Tungstate Crystal*, Trends in Optics and Photonics, Vol. 68 (OSA, Washington D.C., 2002), pp. 70–73
22 P. Cerný, H. Jelínková, T.T. Basiev, P.G. Zverev, IEEE J. Quantum Electron. **QE-38**, 1471 (2002)

23 A.A. Lagatsky, A. Abdolvand, N.V. Kuleshov, Opt. Lett. **25**, 616 (2000)
24 K. Andryunas, Y. Vishakas, V. Kabelka, I.V. Mochalov, A.A. Pavlyuk, G.T. Petrovskii, V. Syrus, JETP Lett. **42**, 333 (1985)
25 K. Andryunas, Y. Vishakas, V. Kabelka, I.V. Mochalov, A.A. Pavlyuk, N.V. Ionina, V. Syrus, Patent of USSR #1227074
26 A.M. Ivanyuk, M.A. Ter-Pogosyan, P.A. Shakhverdov, V.D. Belyaev, V.L. Ermolaev, H.P. Tikhonova, Opt. Spectrosc. **59**, 950 (1985)
27 Y.K. Vishakas, I.V. Mochalov, A.V. Mikhailov, R.F. Klevtsova, A.V. Lyubimov, Lietuvos Fizikos Rinkinys **28**, 224 (1988)
28 I.V. Mochalov, Opt. Eng. **36**, 1660 (1997)
29 A.M. Ivanyuk, V.A. Sandulenko, M.A. Ter-Pogosyan, P.A. Shakhverdov, V.G. Chervinskii, A.V. Lukin, V.L. Ermolaev, Opt. Spectrosc. **62**, 961 (1987)
30 V.A. Berenberg, S.N. Karpukhin, I.V. Mochalov, Sov. J. Quantum Electron. **14**, 1849 (1987)
31 J. Findeisen, H.J. Eichler, P. Peuser, Opt. Commun. **181**, 129 (2000)
32 W. Chen, Y. Inagawa, T. Omatsu, M. Tateda, N. Takeuchi, Y. Usuki, Opt. Commun. **194**, 401 (2001)
33 A.A. Kaminskii, K. Ueda, H.J. Eichler, Y. Kuwano, H. Kouta, S.N. Bagaev, T.H. Chyba, J.C. Barnes, G.M.A. Gad, T. Murai, J. Lu, Opt. Commun. **194**, 201 (2001)
34 Y.F. Chen, M.L. Ku, L.Y. Tsai, Y.C. Chen, Opt. Lett. **29**, 2279 (2004)
35 Y.F. Chen, Opt. Lett. **29**, 1251 (2004)
36 Y.F. Chen, Opt. Lett. **29**, 1915 (2004)
37 T.T. Basiev, S.V. Vassiliev, V.A. Konjushkin, V.V. Osiko, A.I. Zagumennyi, Y.D. Zavartsev, S.A. Kutovoi, I.A. Shcherbakov, Laser Phys. Lett. **1**, 237 (2004)
38 Y.F. Chen, Appl. Phys. B **78**, 685 (2004)
39 Y.F. Chen, Opt. Lett. **29**, 2632 (2004)
40 Y.P. Lan, Y.F. Chen, S.C. Wang, Appl. Phys. B **71**, 27 (2000)
41 P.G. Zverev, A.Y. Karasik, A.A. Sobol, D.S. Chunaev, T.T. Basiev, A.I. Zagumennyi, Y.D. Zavartsev, S.A. Kutovoi, V.V. Osiko, I.A. Shcherbakov, Stimulated Raman scattering of picosecond pulses in $GdVO_4$ and YVO_4 crystals, Advanced Solid State Photonics Conference, Technical digest, Feb. 1–4 (2004), Santa Fe, USA, WB9, OSA TOPS ASSL, TuB10, pp. 25–27

Diode-pumped multi-frequency Q-switched laser with intracavity cascade Raman emission

Y. T. Chang, Y. P. Huang, K. W. Su, and Y. F. Chen*

Department of Electrophysics, National Chiao Tung University, Hsinchu, Taiwan
yfchen@cc.nctu.edu.tw

Abstract: A diode-pumped actively Q-switched mixed Nd:$Y_{0.3}Gd_{0.7}VO_4$ laser with an intracavity KTP crystal is developed to produce cascade SRS emission up to the fourth order. With an incident pump power of 14 W and a repetition rate of 50 kHz, the average output powers at the first, second , third and fourth Stokes modes are approximately 0.05 W, 0.61 W, 0.25 W, and 0.11 W, respectively. The maximum peak power is greater than 2 kW.

OCIS codes: (140.3540) Lasers, Q-switched (140.3550) Lasers, Raman.

References and links

1. R. A. Fields, M. Birnbaum, and C. L. Fincher, "Highly efficient Nd:YVO_4 diode-laser end-pumped laser," Appl. Phys. Lett. **51**, 1885-1886 (1987).
2. A. Sennaroglu, "Efficient continuous-wave operation of a diode-pumped Nd:YVO_4 laser at 1342 nm," Opt. Commun. 164, 191-197 (1999).
3. Y. F. Chen, "Design criteria for concentration optimization in scaling diode end-pumped lasers to high powers: influence of thermal fracture," IEEE J. Quantum Electron. **35**, 234-239 (1999).
4. A. Y. Yao, W. Hou, Y. P. Kong, L. Guo, L. A. Wu, R. N. Li, D. F. Cui, Z. Y. Xu, Y. Bi, and Y. Zhou, " Double-end-pumped 11-W Nd:YVO_4 cw laser at 1342 nm," J. Opt. Soc. Am. B **22**, 2129-2133 (2005).
5. T. Jensen, V. G. Ostroumov, J. P. Meyn, G. Huber, A. I. Zagumennyi, and I. A. Shcherbarkov, "Spectroscopic characterization and laser performance of diode-laser-pumped Nd:$GdVO_4$," Appl. Phys. B **58**, 373-379 (1994).
6. H. J. Zhang, X. L. Meng, L. Zhu, H. Z. Zhang, P. Wang, J. Dawes, C. Q. Wang, and Y. T. Chow, "Investigation on the growth and laser properties of Nd:$GdVO_4$ single crystal," Cryst. Res. Technol. **33**, 801-806 (1998).
7. T. Ogawa, Y. Urata, S. Wada, K. Onodera, H. Machida, H. Sagae, M. Higuchi, and K. Kodaira, "Efficient laser performance of Nd:$GdVO_4$ crystals grown by the floating zone method," Opt. Lett. **28**, 2333-2335 (2003).
8. V. Lupei, N. Pavel, Y. Sato, and T. Taira, "Highly efficient 1063-nm continuous-wave laser emission in Nd:$GdVO_4$," Opt. Lett. **28**, 2366-2368 (2003).
9. L. J. Qin, X. L. Meng, L. Zhu, J. H. Liu, B. C. Xu, H. Z. Xu, F. Y. Jiang, C. L. Du, X. Q. Wang, and Z. S. Shao, "Influence of the different Gd/Y ratio on the properties of Nd:$Y_xGd_{1-x}VO_4$ mixed crystals," Chem. Phys. Lett. 380, 273-278 (2003).
10. J. Liu, X. Meng, Z. Shao, M. Jiang, B. Ozygus, A. Ding, and H. Weber, "Pulse energy enhancement in passive Q-switching operation with a class of Nd:$Gd_xY_{1-x}VO_4$ crystals," Appl. Phys. Lett. **83**, 1289-1291 (2003).
11. Y. F. Chen, M. L. Ku, L. Y. Tsai, and Y. C. Chen, "Diode-pumped passively Q-switched picosecond Nd:$Gd_xY_{1-x}VO_4$ self-stimulated Raman laser," Opt. Lett. **29**, 2279-2281 (2004).
12. J. L He, Y. X. Fan, J. Du, Y. G. Wang, S. Liu, H. T. Wang, L. H. Zhang, and Y. Hang, "4-ps passively mode-locked Nd:$Gd_{0.5}Y_{0.5}VO_4$ laser with a semiconductor saturable-absorber mirror," Opt. Lett. **29**, 2803-2805 (2004).
13. S. P. Ng, D. Y. Tang, A. Q. Liu, L. J. Qin, and X. L. Meng, "Short pulse passively Q-switched NdGdYVO_4 laser using a GaAs mirror, " Opt. Commun. **259**, 256-260 (2006).
14. H. H. Yu, H. J. Zhang, Z. P. Wang, J. Y. Wang, Y. G. Yu, Z. S. Shao, M. H. Jiang, and X. Y. Zhang, "Continuous wave and passively Q-switched laser performance of Nd-doped mixed crystal Nd:$Lu_{0.5}Gd_{0.5}VO_4$," Appl. Phys. Lett. **90**, 231110 (2007).
15. A. A. Kaminskii, "Modern developments in the physics of crystalline laser materials," Phys. Status Solidi (A) **200**, 215-296 (2003).
16. T. T. Basiev and R. C. Powell, "Special issue on solid state Raman lasers-Introduction," Opt. Mater. **11**, 301-306 (1999).
17. H. M. Pask, "The design and operation of solid-state Raman lasers," Prog. Quantum Electron. **27**, 3-56 (2003).
18. Y. F. Chen, "Stimulated Raman scattering in a potassium titanyl phosphate crystal: simultaneous self-sum frequency mixing and self-frequency doubling," Opt. Lett. **30**, 400-402 (2005).

19. S. Pearce, C. L. M. Ireland, and P. E. Dyer, "Solid-state Raman laser generating <1ns, multi-kilohertz pulses at 1096 nm," Opt. Commun. **260**, 680-686 (2006).
20. V. Pasiskevicius, C. Canalias, and F. Laurell, "Highly efficient stimulated Raman scattering of picosecond pulses in $KTiOPO_4$," Appl. Phys. Lett. **88**, 041110 (2006).
21. G. A. Massey, T. M. Loehr, L. J. Willis, and J. C. Johnson, ""Raman and Electro-optic Properties of Potassium Titanate Phosphate," Appl. Opt. **19**, 4136-4137 (1980).
22. K. Kawase, M. Mizuno, S. Sohma, H. Takahashi, T. Taniuchi, Y. Urata, S. Wada, H. Tashiro, and H. Ito, "Difference-frequency terahertz-wave generation from 4-dimethylamino-N-methyl-4-stilbazolium-tosylate by use of an electronically tuned Ti:sapphire laser," Opt. Lett. **24**, 1065-1067 (1999).
23. K. Kawase, T. Hatanaka, H. Takahashi, K. Nakamura, T. Taniuchi, and H. Ito, "Tunable terahertz-wave generation from DAST crystal by dual signal-wave parametric oscillation of periodically poled lithium niobate," Opt. Lett. **25**, 1714-1716 (2000).
24. K. Suizu, K. Miyamoto, T. Yamashita, and H. Ito, "High-power terahertz-wave generation using DAST crystal and detection using mid-infrared powermeter," Opt. Lett. **32**, 2885-2887 (2007).
25. J. J. Zayhowski and A. Mooradian, "Single-frequency microchip Nd lasers," Opt. Lett. **14**, 24-26 (1989).
26. G. J. Dixon, L. S. Lingvay, and R. H. Jarman, "Properties of close coupled monolithic, lithium neodymium, tetraphosphate lasers," Proc. SPIE **1104**, 107 (1989).
27. Y. F. Chen, T. M. Huang, C. F. Kao, C. L. Wang, and S. C. Huang, "Optimization in scaling fiber-coupled laser-diode end-pumped lasers to higher power: influence of thermal effect," IEEE J. Quantum Electron. **33**, 1424-1429 (1997).
28. Y. F. Chen, "High-power diode-pumped Q-switched intracavity frequency-doubled Nd:YVO4 laser with a sandwich-type resonator," Opt. Lett. **24**, 1032-1034 (1999).

1. Introduction

Neodymium-doped single vanadate crystals including Nd:YVO_4 and Nd:$GdVO_4$ have been identified as excellent laser materials for diode-pumped solid-state lasers because of their large absorption and large emission cross sections [1-8]. In the Q-switching operation, however, the large emission cross sections usually limit their energy storage capacities. To overcome this hindrance, mixed Nd:$Y_xGd_{1-x}VO_4$ crystals were recently developed with Y ions replacing some of the Gd ions in Nd:$GdVO_4$ single crystal [9-12]. It has been experimentally confirmed that such mixed crystals are substantially superior to single crystals for Q-switching and mode-locking performance because of their broader fluorescence linewidth [12-14].

Raman lasers which are based on intracavity stimulated Raman scattering (SRS) in Raman active crystals have a very promising potential for various applications such as pollution detection, remote sensing, and medical system [15-17]. Recently, potassium titanyl phosphate (KTP) and rubidium titanyl phosphate (RTP) which are widely recognized as prominent nonlinear optical crystals involving nonlinear optical susceptibility $\chi^{(2)}$ have been experimentally confirmed to be practical SRS converter devices [18-20]. The low value of the KTP-related Stokes shift (270 cm^{-1}) [21] permits generation of multi-frequency radiation with cascade SRS. Nowadays, simultaneous multi-frequency lasing lines with high peak powers in the room temperature is of practical importance for the terahertz (THz) generation with the nonlinear optical difference frequency method [22-24].

In this paper, we present the first demonstration of a diode-pumped actively Q-switched mixed Nd:$Y_{0.3}Gd_{0.7}VO_4$ laser with an intracavity KTP crystal to produce cascade SRS emission up to the fourth order. With an incident pump power of 14 W, the actively Q-switched intracavity Raman laser, operating at 50 kHz, produces an average output power up to 0.92 W with a pulse energy of 18.4 μJ. The maximum peak power is generally higher than 2 kW.

2. Experimental setup

The schematic diagram for the experimental setup of a diode-pumped actively Q-switched Nd:$Y_xGd_{1-x}VO_4$ laser with a KTP crystal as an intracavity SRS medium is illustrated in Fig. 1. Spontaneous Raman spectral data on KTP crystal reveal that the strongest Raman scattering was observed near 270 cm^{-1} [21]. With a fundamental pump wavelength of 1064 nm, the first four Stokes lines for the most intense Raman peak can be calculated to be 1096, 1129, 1166, and

1204 nm, respectively. The flat front mirror has antireflection coating (R<0.2%) at the diode wavelength on the entrance face, high-reflection coating (R>99.5%) at the lasing and SRS wavelengths, and high-transmission coating (T>90%) at the diode wavelength on the other surface. The flat output coupler had the reflectivities R=99.6% at 1064 nm, R=99.1% at 1096 nm, R=86.3% at 1129 nm, R=48.0% at 1166 nm, and R=27.5% at 1204 nm. Note that the present output coupler was selected, but not optimized, from the available mirrors in our laboratory. Nevertheless, experimental results revealed that cascade SRS operation including the first four Stokes components could be obtained.

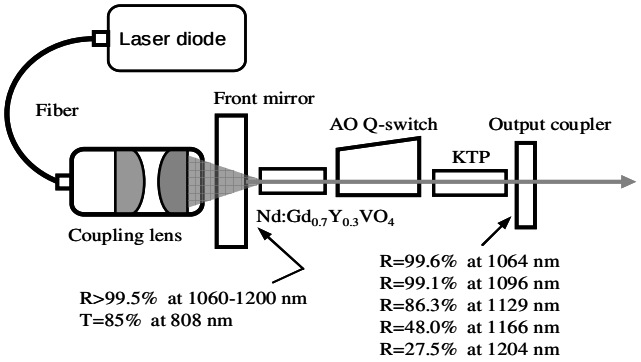

Fig. 1. Experimental setup for a diode-pumped actively Q-switched Nd:$Y_{0.3}Gd_{0.7}VO_4$ laser with a KTP crystal as an intracavity SRS medium.

The pump source was an 808-nm fiber-coupled laser diode (Coherent Inc.) with a core diameter of 0.8 mm, a numerical aperture of 0.16, and a maximum output power of 16 W. A focusing lens with a 12.5-mm focal length and 85% coupling efficiency was used to reimage the pump beam into the laser crystal. The average radius of the pump beam was near 0.35 mm. The active laser medium was a 0.2-at.% Nd:$Y_{0.3}Gd_{0.7}VO_4$ crystal with a length of 10 mm. The Raman medium was a 20-mm-long KTP crystal with a cutting angle along the *x* axis ($\theta=90^o$ and $\phi=0^o$). Both sides of the Nd: $Y_{0.3}Gd_{0.7}VO_4$ and KTP crystals were coated for antireflection at 1000–1200 nm (R< 0.2%). In addition, they were wrapped with indium foil and mounted in a water-cooled copper block. The water temperature was maintained at 20 ^{o}C. The 30-mm-long acousto-optic Q-switch device (NEOS Model 33027-15-2-1) had antireflection coating at 1064 nm on both faces and was driven at a 27.12-MHz center frequency with 15.0 W of rf power.

The present cavity is a flat–flat resonator that was stabilized by the thermally induced lens in the laser crystal. This concept was found nearly simultaneously by Zayhowski and Mooradian [25] and by Dixon *et al* [26]. A linear flat–flat cavity is an attractive design because it reduces complexity and makes the system compact and rugged. However, the end-pump-induced thermal lens is not a perfect lens, but is rather a lens with aberration. It has been found that the thermally induced diffraction loss is a rapidly increasing function of the mode-to-pump ratio at a given pump power. When the incident pump power is greater than 5 W, the optimum mode-to-pump ratio is found to be in the range of 0.8-1.0 [27]. Since the laser rod is very close to the front mirror, the laser mode size in the gain medium can be given by [28]

$$\omega_l = \sqrt{\frac{\lambda}{\pi}} \frac{(L f_{th})^{1/4}}{(1 - L/f_{th})^{1/4}} \tag{1}$$

where f_{th} is the effective focal length of the thermal lens,

$$L = L_{cav} + l\,(1/n - 1) + l_{\mathrm{KTP}}\,(1/n_{\mathrm{KTP}} - 1) + l_{\mathrm{Q}}\,(1/n_{\mathrm{Q}} - 1) \tag{2}$$

is the effective cavity length, L_{cav} is the cavity length, l is the length of the gain medium, n is the refractive index of the gain medium, l_{KTP} is the length of the KTP crystal, n_{KTP} is the KTP refractive index for the output laser beam, l_Q is the length of the Q-switched crystal, and n_Q is the refractive index of the Q-switched crystal for the output laser beam. The effective focal length for an end-pumped laser rod can be approximately expressed as

$$f_{th} = C\,\omega_p^2 / P_{in} \tag{3}$$

where ω_p is the pump size in the unit of mm, P_{in} is the incident pump power in the unit of watt (W), and C is a proportional constant in the unit of W/mm. The effective focal length at a given pump power can be experimentally estimated from the longest cavity length with which a flat-flat cavity can sustain stable. Therefore, we perform the laser experiments to obtain the critical cavity lengths for different pump powers at a fixed pump size. We used Eq. (3) to fit the experimental results and found the constant C to be approximately 1.7×10^4 W/mm.

The dependence of the mode-to-pump size ratio on the pump power for the present cavity was calculated by using Eqs. (1)-(3) and the following parameters: C=1.7×10^4 W/mm, ω_p =0.35 mm, l_Q=30 mm, n_Q=1.5, l=10 mm, n=2.16, n_{KTP}=1.75, and l_{KTP}=20 mm. The calculated results for several cavity lengths were shown in Fig. 2. It is clear that the mode-to-pump size ratio is around 0.8 at L_{cav}=130 mm for the pump powers in the range of 5~15 W, leading to a good compromise between overlapping efficiency and thermal effect. As a consequence, we arranged the cavity length to be 130 mm.

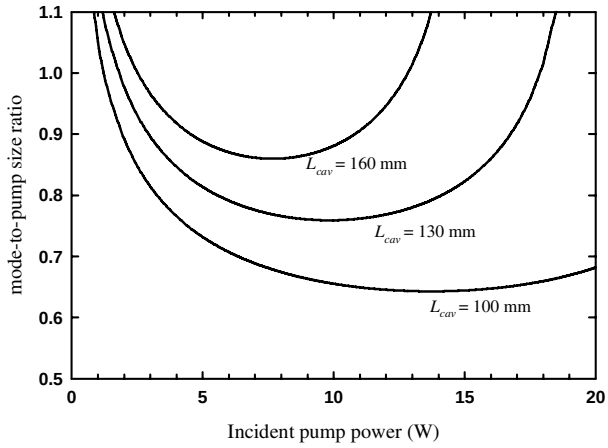

Fig. 2. Dependence of the mode-to-pump size ratio on the incident pump power for several cavity lengths.

3. Experimental results and discussions

Figure 3 depicts the average output powers with respect to the incident pump power at the 50-kHz Q-switching operation for the setup shown in Fig. 1. The threshold powers for the first Stokes mode is 4.5 W. The first Stokes output at 1096 nm increases with the pump power until the second Stokes threshold of 6.2 W is reached, and it is then clamped at a level of 50 mW. When the pump power is increased to approximately 8.2 W, the third Stokes radiation at 1166 nm start to be emitted and the second Stokes emission is almost saturated at a power of 0.6 W. The slope efficiency of the second Stokes at 1129 nm with respect to the pump power from 6.2 W to 8.2 W is approximately 30%. At pump power higher than the fourth Stokes

threshold of 10.5 W, the total output power is nearly clamped at 0.92 W. The maximum output powers at 1096 nm, 1129 nm, 1166 nm, and 1204 nm are approximately 0.05 W, 0.61 W, 0.25 W, and 0.11 W, respectively. Note that the present output coupler was not optimized for the overall conversion efficiency. Therefore, it is possible to obtain a higher output power with the optimum output coupler. On the other hand, the optimum conversion efficiency for the specific Stokes component can be obtained by optimizing the output coupler with high reflection for the lower order Stokes modes and high transmission for the next order Stokes mode. Furthermore, no damage to the KTP crystal was observed over several hours of operation, and the laser performance was reproducible on a day-to-day basis.

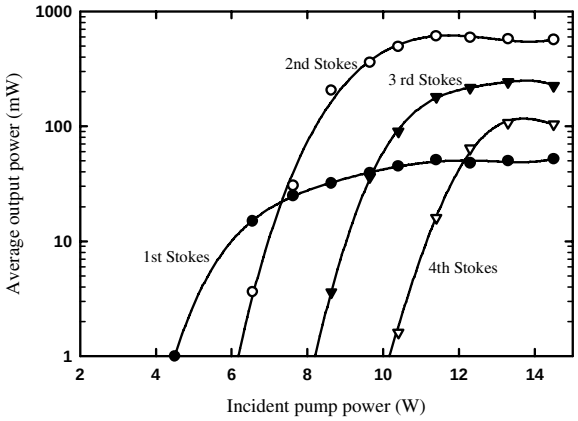

Fig. 3. Dependence of the average output power on the incident pump power for Q-switching operation at 50 kHz.

An optical spectrum analyzer (Advantest Q8381A) was used to measure the spectral information of the laser output. The present spectrum analyzer employing a diffraction lattice monochromator can be used for high-speed measurement of pulse light with a resolution of 0.1 nm. Figure 4 shows the emission spectrum measured at the output of the Raman laser for the pump power of 14.0 W. It can be seen that the optical spectra include the main output of the different order Stokes lines as well as the residual outputs of the fundamental wave at 1064 nm. The frequency shift between the Stokes and the laser lines is in good agreement with the asymmetric bending mode of a distorted TiO_6 octahedron 270 cm^{-1} [21].

The temporal behavior of the output pulse was recorded by a LeCroy digital oscilloscope (Wavepro 7100, 1-GHz bandwidth, 10 G samples/sec) with two InGaAs p-i-n photodiodes for measuring the output pulses at fundamental and SRS emissions, respectively. The temporal characteristics of the fundamental pulse and Raman pulses are depicted in Figs. 5(a)-5(d) for four different pump powers of 5.0 W, 7.0 W, 9.0 W and 11.0 W. It can be seen that when the intracavity power density at the fundamental wavelength reaches the SRS threshold, the fundamental pulse is rapidly converted the Stokes output. Although the channel numbers of the oscilloscope are not sufficient to separate the temporal profiles of each Stokes orders, the experimental results in Figs. 5(a)-5(d) apparently reveal that various order Stokes pulses are generated step by step with increasing the pump power. Furthermore, the Q-switched pulse envelope displays clear modulated pulses. The separation of the modulated pulses was found to be 0.86 ns, which matched exactly with the cavity roundtrip time. Therefore, the modulated pulses can be confirmed to come from the longitudinal-mode beating. The estimated energy of the highest pulse inside envelope was found to be close to 18.4 μJ and the maximum peak power was greater than 2 kW.

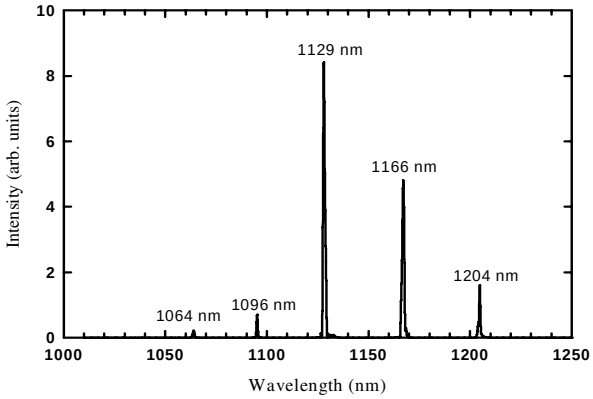

Fig. 4. Emission spectrum measured at the output of the Raman laser for the pump power of 14 W.

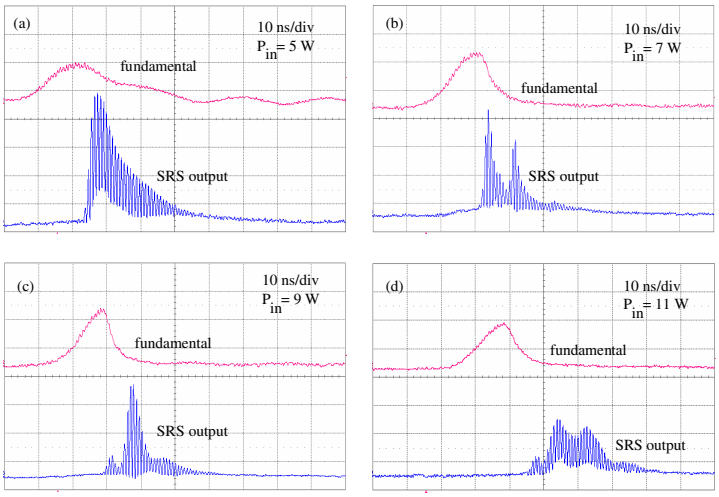

Fig. 5. Temporal characteristics of the fundamental pulse and Raman pulses (a) 5 W, (b) 7 W, (c) 9 W, (d) 14 W.

4. Conclusion

In summary, we have developed a diode-pumped actively Q-switched mixed Nd:$Y_{0.3}Gd_{0.7}VO_4$ laser with an intracavity KTP crystal to produce cascade SRS emission up to the fourth order. With an incident pump power of 14 W and a repetition rate of 50 kHz, the average output powers at 1096 nm, 1129 nm, 1166 nm, and 1204 nm are approximately 0.05 W, 0.61 W, 0.25 W, and 0.11 W, respectively. The maximum peak power is found to be higher than 2 kW.

Acknowledgments

The authors also thank the National Science Council for their financial support of this research under Contract No. NSC-95-2112-M-009-041-MY2.

AlGaInAs intracavity selective absorber for an efficient high-power Nd:YAG laser operation at 1.44 μm

Y. P. Huang, Y. T. Chang, K. W. Su, Y. F. Chen,* and K. F. Huang

Department of Electrophysics, National Chiao Tung University, Hsinchu, Taiwan
**Corresponding author: yfchen@cc.nctu.edu.tw*

Received April 14, 2008; accepted May 16, 2008;
posted May 27, 2008 (Doc. ID 94981); published June 23, 2008

We develop an AlGaInAs material as a promising intracavity selective absorber for an efficient high-power Nd:YAG laser at 1.44 μm. With the ISA to suppress operation at 1.06 μm, the output coupler at 1.44 μm can be straightforwardly designed and optimized. At a pump power of 16 W an output power of 2.5 W at 1.44 μm, with a slope efficiency of 23%, was achieved. © 2008 Optical Society of America

OCIS codes: 140.0140, 140.3480, 140.3380, 140.3530.

The fluorescence spectra of Nd-doped laser crystals have revealed many transitions in the $^4F_{3/2}$ to $^4I_{9/2}$, $^4I_{11/2}$, and $^4I_{13/2}$ manifolds [1]. Based on these multiple transitions most Nd-doped laser crystals can be operated in the laser wavelengths between 0.91 and 1.38 μm. In Nd:YAG crystals the long-wavelength end of the $^4F_{3/2} \rightarrow {}^4I_{13/2}$ transition is remarkably up to 1.44 μm at which the absorption coefficient of water is comparable with that at 2.1 μm [2]. As a consequence, the Nd:YAG laser at 1.44 μm is of particular interest not only in the field of surgery but also for many technical applications such as lidar and communications [3–5].

The well-known attempts at line selection in Nd-doped lasers rely on appropriately coated cavity mirrors with a sufficiently large loss difference to suppress the competing transition channels [6]. Since the stimulated emission cross section of the 1.44 μm transition is approximately 20 times smaller than that of the 1.06 μm line, the operation of a Nd:YAG laser at 1.44 μm requires a rather tough coating. Even though the coated cavity mirrors with a sufficient reflection contrast can lead to the 1.44 μm emission at low and middle pump powers, the power scaling tends to be hindered by the lasing of the 1.06 μm transition at high pump powers. A method for overcoming this obstacle is to utilize the three-mirror folded resonator with an additional mirror to increase the loss difference between the lasing and competing channels. An alternative approach is the use of an intracavity selective absorber (ISA) in a simple linear cavity to absorb the competing emissions without introducing substantial losses at the lasing wavelength [7]. Therefore, the development of an ISA is practically beneficial to the power scaling of the weak transition in Nd-doped lasers.

In this Letter we demonstrate the development of an AlGaInAs material as a promising ISA for an efficient high-power Nd:YAG laser at 1.44 μm. With the ISA to suppress operation at 1.06 μm, the output coupling at 1.44 μm can be flexibly optimized; as a consequence, an output power of 2.5 W at 1.44 μm, with a slope efficiency of 23%, was achieved. We further verify that even if the cavity mirrors have a high-reflection coating at 1.06 μm, the developed ISA can still completely suppress the 1.06 μm oscillation and make a Nd:YAG laser cavity with an appropriate coupling to operate at 1.44 μm.

The present ISA was composed of AlGaInAs quantum wells (QWs) with the barrier structure grown on a Fe-doped InP transparent substrate by metalorganic chemical-vapor deposition. Note that the conventional S-doped InP substrate cannot be used because of its significant absorption in the 1.0–2.0 μm spectral region, whereas the Fe-doped InP substrate is transparent in this spectral region. The absorption region of the ISA consists of 10 groups of two 10 nm QWs with the absorption wavelength around 1.32 μm, spaced at 190 nm intervals by AlGaInAs barrier layers with the absorption wavelength around 1.06 μm, as shown in Fig. 1. An InP window layer was deposited on the gain structure to avoid surface recombination and oxidation. The backside of the substrate was mechanically polished after growth. Both sides of the gain chip were antireflection (AR)-coated to reduce backreflections. The total residual reflectivity of the AR-coated sample is less than 5%. Figure 2 shows the transmittance spectrum for the AR-coated ISA device. It can be seen that the strong absorption of the barrier layers leads to an extremely low transmittance near 1.06 μm. The total absorption efficiency of the barrier layers at 1.06 μm

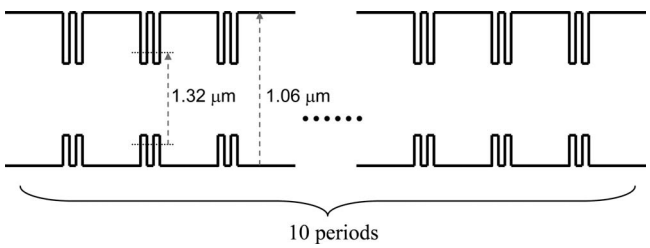

Fig. 1. Structure of the present ISA: the absorption region including 10 groups of two 10 nm QWs with the absorption wavelength around 1.32 μm, spaced at 190 nm intervals by AlGaInAs barrier layers with the absorption wavelength around 1.06 μm.

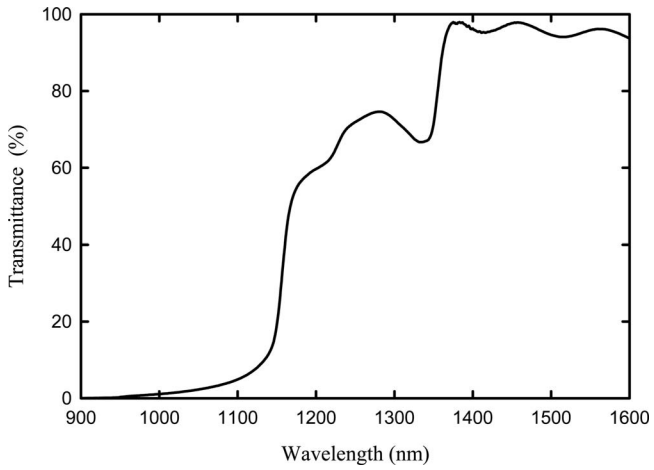

Fig. 2. Transmittance spectrum for the developed ISA device.

was found to be higher than 96%. On the other hand, the absorption efficiency of the AlGaInAs QWs near 1.32 μm was approximately 35%. Although the AlGaInAs material with a similar structure has been employed as a gain medium or a saturable absorber [8–12], it is designed as an ISA in solid-state lasers for the first time, to the best of our knowledge.

A schematic of the laser experiment is shown in Fig. 3. The active medium was 1.0 at. % Nd:YAG crystal with a length of 10 mm. The entrance surface of the laser crystal was coated for high reflection at 1.06 μm ($R>99.5\%$), 1.32 μm ($R>99.5\%$), and 1.44 μm ($R>99.5\%$) and for high transmission at 0.81 μm ($T>85\%$). Note that the high reflection at 1.06 and 1.32 μm on the entrance surface was for the purpose of exploring the suppression ability of the developed ISA. The other surface of the laser crystal was coated for AR in the spectral range of 1.06–1.44 μm ($R<0.2\%$). The laser crystal was wrapped with indium foil and mounted in a water-cooled copper block. The pump source was a 20 W 808 nm fiber-coupled laser diode with a core diameter of 600 μm and a numerical aperture of 0.16. A focusing lens with a 5 mm focal length and 85% coupling efficiency was used to reimage the pump beam into the laser crystal. The pump spot radius was approximately 200 μm. The cavity length was approximately 15 mm. The spectral information of the laser was monitored by an optical spectrum analyzer (Advantest Q8381A).

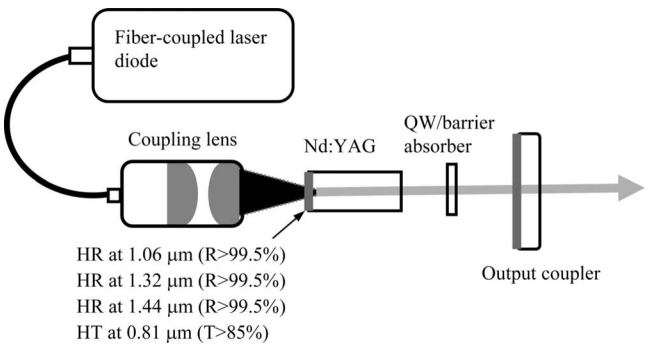

Fig. 3. Experimental schematic of the laser experiment.

Three different flat output couplers were used to test the function of the developed ISA. The first output coupler (OC1) was used to estimate the insertion loss of the ISA; its reflectivities at 1.06, 1.32, and 1.44 μm are 5%, 50%, and 99%, respectively. The loss difference of the OC1 for various transitions ensured that the oscillations at 1.06 and 1.32 μm were completely suppressed and the laser operated at 1.44 μm. Figure 4 shows the average output powers, with and without the ISA inserted into the cavity with the OC1, versus the incident pump power. The reduction in the slope efficiency due to the ISA can be seen to be rather small. With the Findlay–Clay analysis the insertion loss of the ISA is found to be approximately 0.2%. Note that the output efficiency with the OC1 is rather low because the output coupling is not optimal for the operation at 1.44 μm.

The second output coupler (OC2) was used to test the suppression ability of the ISA; its reflectivities at 1.06, 1.32, and 1.44 μm are 50%, 70%, and 95%, respectively. Experimental results reveal that the laser cavity with the OC2 and without the ISA is completely lasing at 1064 nm. With the insertion of the ISA, the laser cavity with the OC2 can be purely lasing at 1444 nm. Figure 5 shows the input–output characteristics for the output powers with and without the ISA inserted into the cavity with the OC2. It can be seen that the ISA can make the laser cavity to change the lasing wavelength from 1.06 to 1.44 μm. An output power of 2.5 W at 1.44 μm, with a slope efficiency of 23%, was achieved with the ISA inserted into the cavity with the OC2. At a pump power of 10 W the present output power is up to 1.7 W, which is superior to the previous data of 10 W obtained with a 2% output coupler [2,5]. The superiority comes from the advantage that an output coupler with a higher transmission can be used to optimize the output power because of the strong suppression at 1.06 μm transition by the ISA.

Finally, the third output coupler (OC3) was used to further investigate the maximum suppression ability of the ISA. The reflectivities of the OC3 at 1.32 and 1.44 μm are nearly the same as those of the OC2;

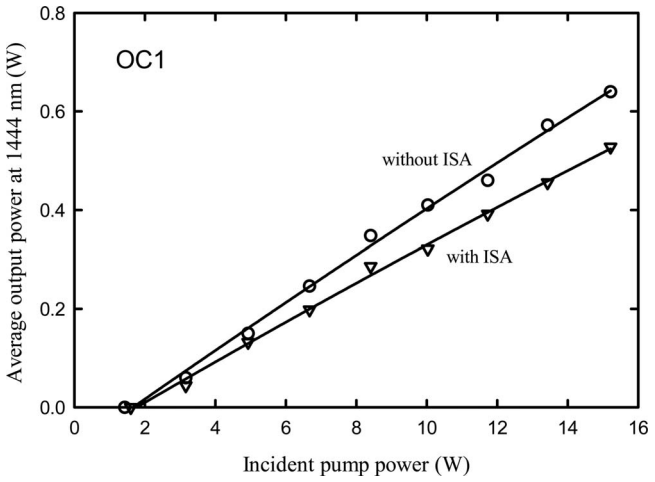

Fig. 4. Average output powers, with and without the ISA inserted into the cavity with the OC1, versus the incident pump power.

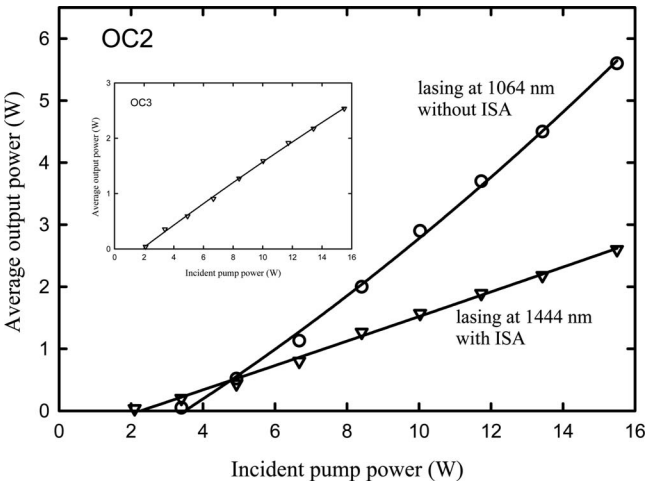

Fig. 5. Average output powers, with and without the ISA inserted into the cavity with the OC2, versus the incident pump power. Inset: average output power with ISA inserted into the cavity with the OC3.

however, the reflectivity of the OC3 at 1.06 μm is up to 99.5%. Experimental results reveal that the ISA can still suppress the 1.06 μm emission and lead to a Nd:YAG laser operating at 1.44 μm. More importantly, the output performance with the OC3 is almost the same as that obtained with the OC2, as seen in the inset of Fig. 5. In other words, the optimum output coupler at 1.44 μm can be straightforwardly designed by means of the ISA to suppress operation at 1.06 μm.

In summary, an AlGaInAs QW–barrier structure grown on a Fe-doped InP transparent substrate was developed to be an ISA for an efficient high-power Nd:YAG laser at 1.44 mm. Experimental results confirm that the developed ISA can still fully suppress the 1.06 μm oscillation even if the cavity mirrors have a high-reflection coating at 1.06 μm. With the ISA to suppress operation at 1.06 μm, the output coupler at 1.44 μm can be straightforwardly optimized. At a pump power of 16 W, an output power of 2.5 W at 1.44 μm, with a slope efficiency of 23%, was achieved.

The authors gratefully acknowledge various AlGaInAs/InP chips from TrueLight Corporation. The authors also thank the National Science Council for their financial support of this research under contract NSC-93-2112-M-009-034.

References

1. S. Singh, R. G. Smith, and L. G. Van Uitert, Phys. Rev. B **10**, 2566 (1974).
2. H. M. Kretschmann, F. Heine, V. G. Ostroumov, and G. Huber, Opt. Lett. **22**, 466 (1997).
3. N. Hodgson, W. L. Nighan, Jr. , D. J. Golding, and D. Eisel, Opt. Lett. **19**, 1328 (1994).
4. S. K. Wong, P. Mathieu, and P. Pace, Appl. Phys. Lett. **57**, 650 (1990).
5. A. Agnesi, S. Dell'Acqua, C. Pennacchio, G. Reali, and P. G. Gobbi, Appl. Opt. **37**, 3984 (1998).
6. J. Marling, IEEE J. Quantum Electron. **14**, 56 (1978).
7. I. V. Klimov, I. A. Shcherbakov, and V. B. Tsvetkov, Proc. SPIE **3829**, 165 (1999).
8. C. E. Zah, R. Bhat, B. N. Pathak, F. Favire, W. Lin, M. C. Wang, N. C. Andreadakis, D. M. Hwang, M. A. Koza, T. P. Lee, Z. Wang, D. Darby, D. Flanders, and J. J. Hsieh, IEEE J. Quantum Electron. **30**, 511 (1994).
9. N. Nishiyama, C. Caneau, B. Hall, G. Guryanov, M. H. Hu, X. S. Liu, M.-J. Li, R. Bhat, and C. E. Zah, IEEE J. Sel. Top. Quantum Electron. **11**, 990 (2005).
10. O. Hanaizumi, K. T. Jeong, S. Y. Kashiwada, I. Syuaib, K. Kawase, and S. Kawakami, Opt. Lett. **21**, 269 (1996).
11. K. W. Su, S. C. Huang, A. Li, S. C. Liu, Y. F. Chen, and K. F. Huang, Opt. Lett. **31**, 2009 (2006).
12. S. C. Huang, S. C. Liu, A. Li, K. W. Su, Y. F. Chen, and K. F. Huang, Opt. Lett. **32**, 1480 (2007).

Efficient high-peak-power diode-pumped actively *Q*-switched Nd:YAG/YVO_4 intracavity Raman laser

Kuan-Wei Su,* Ya-Ting Chang, and Yung-Fu Chen

Department of Electrophysics, National Chiao Tung University, 1001 Ta Hsueh Road, Hsinchu 300, Taiwan

*Corresponding author: sukuanwei@mail.nctu.edu.tw

Received 29 May 2008; revised 25 September 2008; accepted 21 October 2008; posted 23 October 2008 (Doc. ID 96803); published 10 December 2008

An undoped YVO_4 crystal is employed to achieve efficient stimulated Raman scattering conversion in a diode-pumped actively *Q*-switched Nd:YAG laser. With an incident pump power of 16.2 W, an 1176 nm first Stokes average output power of 3.0 W was generated at a pulse repetition rate of 50 kHz, corresponding to an optical-to-optical conversion efficiency of 18.3%. Moreover, the maximum optical-to-optical conversion efficiency of 21.3% was found at 20 kHz. The maximum pulse energy is higher than 83 μJ at both 20 and 30 kHz. With an incident pump power of 7.6 W, the underestimated peak power of 43.5 kW was demonstrated at 20 kHz with mode-locked modulation. © 2008 Optical Society of America

OCIS codes: 140.3480, 140.3540, 140.3550, 290.5910.

1. Introduction

Neodymium-doped yttrium aluminum garnet and yttrium vanadate (Nd:YAG and Nd: YVO_4) are the most widely used materials for solid-state laser gain medium [1,2]. The Nd: YVO_4 crystal has a strong broadband absorption and an effective stimulated emission cross section that is five times larger than Nd:YAG [1]. These properties imply that a Nd: YVO_4 laser usually has higher efficiency and a broader operating temperature than a Nd:YAG laser. In the field of Raman lasers, the availability of a self-Raman process also made the study of diode-pumped passively *Q*-switched (PQS) and actively *Q*-switched (AQS) Nd: YVO_4 Raman lasers attractive [3,4]. However, the Nd:YAG crystal has other advantages such as better thermal property and a much longer fluorescence lifetime. In particular, the long lifetime can raise the output pulse energy of a fundamental AQS laser and should be able to raise the output pulse energy of an AQS Raman laser at the Stokes wavelength. This means that the conversion efficiency of intracavity stimulated Raman scattering (SRS) might be increased in an AQS Nd:YAG solid-state laser.

With the development of the crystals as Raman shifters, intracavity Raman lasers are realized as an efficient and practical scheme for extending the lasing spectrum [2,5–8]. $Ba(NO_3)_2$ [9], $LiIO_3$ [10], $KGd(WO_4)_2$ [11], $PbWO_4$ [12], and $BaWO_4$ [5,13–17] are well-known materials for SRS. Furthermore, YVO_4 and $GdVO_4$ were found to be efficient $\chi^{(3)}$ materials for Raman lasers [18]. We have exhibited the AQS Nd: YVO_4 Raman laser with an undoped YVO_4 crystal that was demonstrated as a potential Raman shifter [19]. However, *Q*-switched Nd:YAG intracavity Raman lasers based on YVO_4 crystals have not been reported to our knowledge.

Here we report the high-pulse-energy and high-peak-power intracavity YVO_4 SRS generation in a compact diode-pumped AQS Nd:YAG laser. At an incident pump power of 16.2 W, the 1176 nm first Stokes average output power of 3.0 W is efficiently generated at a pulse repetition frequency (PRF) of 50 kHz. The maximum output pulse energy is higher than 83 μJ, and the overall conversion efficiency was as much as 21.3 – 18.3%. The output pulses display a

0003-6935/08/356675-05$15.00/0

mode-locking phenomenon that results in a maximum peak power of 43.5 kW.

2. Experimental Setup

Figure 1 depicts the experimental configuration for the diode-pumped AQS Nd: YAG/YVO_4 Raman laser. The cavity mirrors with a special dichroic coating for efficient conversion at the first Stokes component form a plano–concave configuration. The input mirror is a 500 mm radius-of-curvature concave mirror with an antireflection coating of 808 nm on the entrance face ($R < 0.2\%$), a high-reflection coating of 1050 – 1200 nm ($R > 99.8\%$), and a high-transmission coating of 808 nm on the other surface ($T > 90\%$). The output coupler is a flat mirror with a high-reflection coating of 1064 nm ($R > 99.8\%$) and a partial-reflection coating of 1176 nm ($R = 51\%$). Note that the output coupler reflectivity is not optimized and has limited availability.

The pump source was an 808 nm fiber-coupled laser diode with a core diameter of 800 μm, a numerical aperture of 0.16, and a maximum output power of 25 W. A focusing lens system with 85% coupling efficiency was used to reimage the pump beam into the laser crystal. The waist radius of the pump beam was approximately 400 μm. The laser medium was an 0.8 at.% Nd^{3+}: YAG crystal with a length of 10 mm. Both sides of this laser crystal were coated for antireflection (AR) at 1.06 μm ($R < 0.2\%$). The Raman crystal was an a-cut undoped YVO_4 crystal with a length of 9.6 mm. These two crystals were both wrapped with indium foil and mounted in water-cooled copper blocks individually. The water temperature was maintained at 20 °C. The 30 mm long acousto-optic Q-switch (NEOS Technologies) had antireflection coatings at 1064 nm on both faces and was driven at a 27.12 MHz center frequency with 15 W of RF power. The overall laser cavity length was around 9 cm. A thermal detector (Coherent LM-10 HTD) was used to measure the average power of the fundamental and Stokes output.

3. Experimental Results and Discussion

The AQS Nd:YAG laser performance at 1064 nm was first studied to evaluate the conversion efficiency of intracavity SRS. For this investigation, an output coupler with partial reflection at 1064 nm was used instead of the above-mentioned Raman cavity output coupler. The optimum reflectivity of the output coupler was found to be approximately 80%. The pump threshold for 1064 nm oscillation was below 2.5 W and was insensitive to the PRF. With an incident pump power of 16.2 W, the average output powers at 1064 nm were 5.8 – 6.3 W for PRFs in the range of 20 – 50 kHz. In addition, the partially polarized laser beam with a polarization ratio of 3 : 1 should be excited by the acousto-optic Q-switch and nonlinear Raman crystal. However, when the intracavity Raman laser was used, the relatively random polarization compared with the Nd: YVO_4/YVO_4 Raman laser [19] could benefit the robustness of the Raman crystal. Therefore, our experimental results revealed that the same Raman crystals can sustain higher peak power per unit area in Nd:YAG lasers. In other words, the damage threshold was improved. The experimental result for the optical spectrum of a Raman laser was monitored by an optical spectrum analyzer (Advantest Q8381A), including a diffraction grating monochromator with a resolution of 0.1 nm. The first Stokes wavelength of 1176 nm was converted from the fundamental wavelength at 1064 nm by a Raman shift at 890 cm^{-1} from a YVO_4 crystal [18,19]. There is no second Stokes wavelength observed for all the pumping power.

Figure 2 illustrates the average output power at 1176 nm with respect to the incident pump power for PRFs of 20, 30, and 50 kHz. For the Raman operation with a fixed PRF and a fixed cavity length, a critical pump power or a maximum operating pump power exists. The thermal lensing causes the cavity to be unstable after the critical pump power. Reducing the PRF leads to a lower threshold for stimulated Raman output, but it leads to a smaller critical pump power and a smaller maximum output power because of the increased thermal loading of the end-pumped Q-switched Nd-doped laser [20]. However, the meaning behind the critical pump power may not be all the same as normal AQS

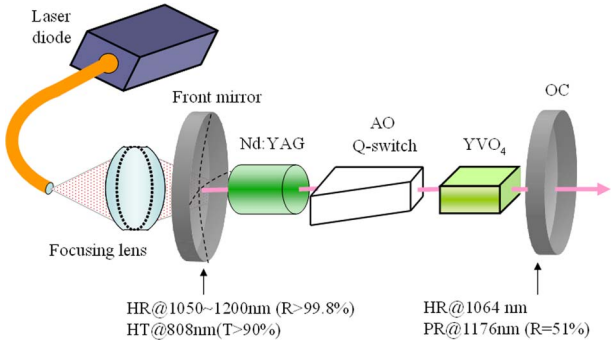

Fig. 1. (Color online) Scheme of a diode-pumped AQS Nd: YAG/YVO_4 Raman laser.

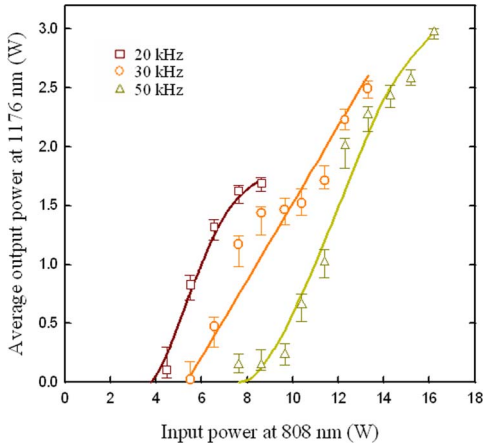

Fig. 2. (Color online) Average output power at the Stokes wavelength of 1176 nm with respect to the incident pump power at different pulse repetition rates of 20, 30, and 50 kHz.

Nd-doped lasers. Compared with the fundamental operation at 1064 nm, the much lower optical-to-optical conversion efficiency for the Raman operation could cause much higher thermal loading on the gain medium. The additional thermal lensing effect from SRS on a Raman crystal should also be considered. Then, the SRS conversion efficiency could be sensitive to the cavity stability, which will induce the drop in critical pump power. The advanced studies on thermal effects are still under way. Moreover, the self-focusing-induced damage on the YVO_4 crystal never occurred at a low PRF while the pump power is being overdriven.

Nevertheless, the efficient average output powers at 1176 nm were separately 1.6, 2.5, and 3.0 W at PRFs of 20, 30, and 50 kHz with incident pump power of 7.6, 13.3, and 16.2 W. As a consequence, the maximum SRS conversion efficiency of 62 – 47% with respect to the output power that is available from the fundamental laser of 1064 nm was demonstrated at the PRF of 20 – 50 kHz. Then, the maximum optical-to-optical conversion efficiency from an 808 nm pump was as high as 21.3 – 18.3% at the PRF of 20 – 50 kHz. The overall conversion efficiency is the second highest one for Raman lasers until now to our knowledge [2,21]. The efficiency would improve if we could use a *c*-cut YVO_4 crystal [22] with proper antireflection coating and an optimized output coupler. From the average output power and the PRF, pulse energy E_p at 1176 nm with respect to the incident pump power was depicted in Fig. 3. The maximum pulse energies E_{max} at PRFs of 20 and 30 kHz were both higher than 83 μJ. The E_{max} of this Nd: YAG/YVO_4 Raman laser was almost two times the E_{max} of the Nd: YVO_4/YVO_4 Raman laser in almost the same AQS scheme [19].

The temporal behaviors were recorded with a LeCroy digital oscilloscope (Wavepro 7100, 10 GSamples/s, 1 GHz bandwidth) with two fast InGaAs p-i-n photodiodes. An interference filter that allows transmission only at 1064 nm was used to extract a weak fundamental signal. Figure 4 shows the pulse shape for the fundamental and Raman components. With a pulse energy of 81.2 μJ at 1176 nm, the pulse width of the pulse envelope in Fig. 4 is 2.2 ns, and the peak power of the pulse seen as a Gaussian shape without oscillation should be 36.9 kW. However, the observed mode-locked phenomenon causes the Raman pulse to assume a deeply modulated shape, and peak power P_{peak} cannot be approximated as the E_p divided by the envelope width [19]. We had to use the temporal shape of a single pulse in arbitrary units, $\psi(t)$, to determine the correct P_{peak}. Note that the screen shots and numerical data of $\psi(t)$ were recorded in the oscilloscope at the same time so that we could use the numerical data for calculation, which can be expressed as $P_{peak} = C \cdot \psi_{max}(t)$, where the $\psi_{max}(t)$ indicates the peak value of $\psi(t)$. Factor C is determined by the fact that $E_p = C \cdot \int_T \psi(t)dt$, where T indicates the temporal range of the single pulse. Consequently, the peak power of the Raman pulse in Fig. 4 is 43.5 kW. It can also be observed that the pulse shape and modulated oscillation depth were varied with increased pump power. For example, Fig. 5 depicts the typical evolvement of pulse shapes that are dependent on pump power at 50 kHz. Note that the vertical axes of the pulses were separate arbitrary units With a pump power of 8.6 W, which is near the threshold of SRS, the envelope width of 7.1 ns and deep mode-locked oscillation are shown in Fig. 5(a). Although the pump power was increased to 12.3 W, the envelope width was narrowed to a minimum of 3.1 ns with a P_{peak} of 13.1 kW as shown in Fig. 5(b). Meanwhile, the mode-locked oscillation depth decreased when the pump power was increased from the threshold to the 12.3 W. Then the pulse envelope broadened slightly after the pump power of 12.3 W, but the mode-locking effect was enhanced. With a pump power of 14.8 W, the pulse was observed with an almost saturated P_{peak} of 15.5 kW as shown in Fig. 5(c). Finally, the pulse-to-pulse amplitude fluctuation of the Raman output was monitored to be approximately less than $\pm 10\%$.

The temporal behavior and real P_{peak} appear to be available. In fact, with further observation, the

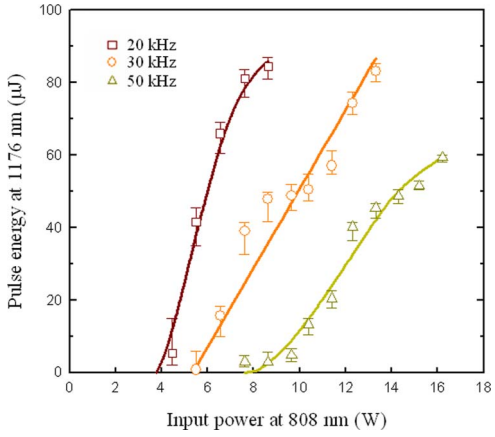

Fig. 3. (Color online) Pulse energy at 1176 nm with respect to the incident pump power at different pulse repetition rates of 20, 30, and 50 kHz.

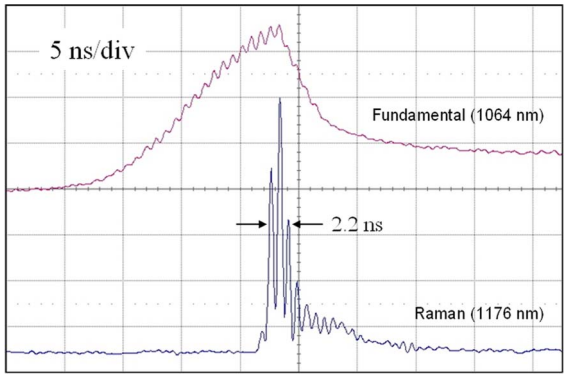

Fig. 4. (Color online) Oscilloscope trace with a mode-locking effect for fundamental and Raman pulses. This figure was recorded with an incident pump power of 7.6 W at a pulse repetition rate of 20 kHz.

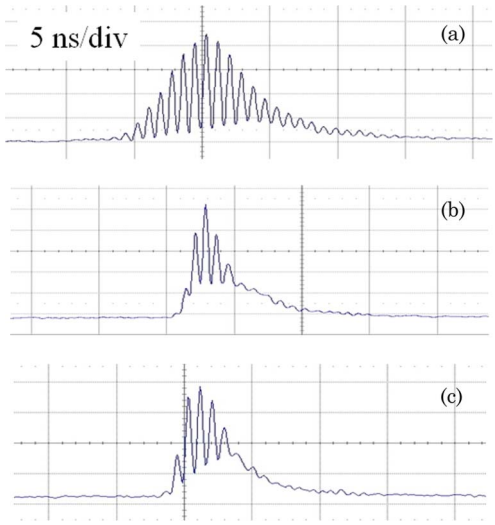

Fig. 5. (Color online) Evolvement of pulse shapes dependent on pump power at a pulse repetition rate of 50 kHz. With incident pump power of 8.6, 12.3, and 14.8 W , the peak power is (a) 560 W, (b) 13.1 kW, (c) 15.5. kW.

FWHM of each mode-locked pulse inside the envelope was 500 – 600 ps. Narrow mode-locked pulses might be restricted by the 1 GHz bandwidth of the oscilloscope and photodetectors. The restriction is easy to overlook during the experiment. In other words, the P_{peak} could be much higher than what we calculated in our research and in Ref. [19]. However, a conventional autocorrelator for short-pulse measurement of a stable cw mode-locked laser cannot provide reliable measurement results for Q-switched mode-locked lasers. We estimate that the real-time oscilloscope and photodetectors with an 8 – 10 GHz bandwidth are required for sure tracing of the time domain. Nevertheless, the high-speed optoelectronic equipment is still being fine tuned and is not yet available for general use. It will be interesting to study the mechanism and behavior of the compact mode-locked AQS intracavity Raman lasers by use of undoped YVO_4 crystals. Compared with the results from the Nd: YVO_4/YVO_4 Raman laser in almost the same AQS scheme, the Nd: YAG/YVO_4 Raman laser raised the maximum output pulse energy from 43 to 83 μJ and the peak power from 14 to 43.5 kW [19].

4. Conclusions

In summary, an efficient diode-pumped actively Q-switched Nd: YAG/YVO_4 intracavity Raman laser has been demonstrated. Compared with a similar Raman laser with another gain medium, Nd: YVO_4, the damage threshold and conversion efficiency were improved simultaneously. An 1176 nm average output power of 3.0 W was generated at a pulse repetition rate of 50 kHz. In addition, the maximum SRS conversion efficiency and overall optical-to-optical conversion efficiency from an 808 nm pump were as high as 62 – 47% and 21.3 – 18.3% at a PRF of 20 – 50 kHz. The maximum pulse energy was higher than 83 μJ at both 20 and 30 kHz. The output pulses displayed a mode-locking phenomenon that leads to high peak power. With an incident pump power of 7.6 W, the underestimated peak power of 43.5 kW was demonstrated at 20 kHz.

References

1. W. Koechner and M. Bass, *Solid-State Lasers*, Advanced Texts in Physics (Springer-Verlag, 2003), Chap. 2.
2. J. A. Piper and H. M. Pask, "Crystalline Raman lasers," IEEE J. Sel. Top. Quantum Electron. **13**, 692–704 (2007).
3. Y. F. Chen, "Efficient subnanosecond diode-pumped passively Q-switched Nd: YVO_4 self-stimulated Raman laser," Opt. Lett. **29**, 1251–1253 (2004).
4. Y. F. Chen, "High-power diode-pumped actively Q-switched Nd: YVO_4 self-Raman laser: influence of dopant concentration," Opt. Lett. **29**, 1915–1917 (2004).
5. T. T. Basiev, A. A. Sobol, P. G. Zverev, L. I. Ivleva, V. V. Osiko, and R. C. Powell, "Raman spectroscopy of crystals for stimulated Raman scattering," Opt. Mater. **11**, 307–314 (1999).
6. P. G. Zverev, T. T. Basiev, and A. M. Prokhorov, "Stimulated Raman scattering of laser radiation in Raman crystals," Opt. Mater. **11**, 335–352 (1999).
7. H. M. Pask, "The design and operation of solid-state Raman lasers," Prog. Quantum Electron. **27**, 3–56 (2003).
8. P. Dekker, H. M. Pask, and J. A. Piper, "All-solid-state 704 mW continuous-wave yellow source based on an intracavity, frequency-doubled crystalline Raman laser," Opt. Lett. **32**, 1114–1116 (2007).
9. A. S. Eremenko, S. N. Karpukhin, and A. I. Stepanov, "Stimulated Raman scattering of the second harmonic of a neodymium laser in nitrate crystals," Sov. J. Quantum Electron. **10**, 113–114 (1980).
10. E. O. Ammann and C. D. Decker, "0.9-W Raman oscillator," J. Appl. Phys. **48**, 1973–1975 (1977).
11. A. S. Grabtchikov, A. N. Kuzmin, V. A. Lisinetskii, V. A. Orlovich, G. I. Ryabtsev, and A. A. Demidovich, "All solid-state diode-pumped Raman laser with self-frequency conversion," Appl. Phys. Lett. **75**, 3742–3744 (1999).
12. J. Findeisen, H. J. Eichler, and A. A. Kaminskii, "Efficient picosecond $PbWO_4$ and two-wavelength $KGd(WO_1)_2$ Raman lasers in the IR and visible," IEEE J. Quantum Electron. **35**, 173–178 (1999).
13. P. Cerný, P. G. Zverev, H. Jelínková, and T. T. Basiev, "Efficient Raman shifting of picosecond pulses using $BaWO_4$ crystal," Opt. Commun. **177**, 397–404 (2000).
14. T. T. Basiev, A. A. Sobol, P. G. Zverev, L. I. Ivleva, and V. V. Osiko, "Laser material for stimulated Raman scattering," Russian Fedration Patent 2178938 C1 1 (25 April 2000).
15. P. G. Zverev, T. T. Basiev, M. E. Doroshenko, and V. V. Osiko, "Barium tungstate Raman laser—a new coherent source for sodium star experiments," in *Advanced Solid State Lasers*, H. Injeyan, U. Keller, and C. Marshall, eds., Vol. 34 of OSA Trends in Optics and Photonics Series (Optical Society of America, 2000), pp. 348–354.
16. P. G. Zverev, T. T. Basiev, L. I. Ivleva, V. V. Osiko, N. M. Polozkov, and I. S. Voronina, "Raman laser on strontium tungstate crystal," in *Vol. 68 of OSA Trends in Optics and Photonics Series* (Optical Society of America, 2002), pp. 70–73.
17. P. Cerný, H. Jelínková, T. T. Basiev, and P. G. Zverev, "Highly efficient picosecond Raman generators based on the $BaWO_4$ crystal in the near infrared, visible, and ultraviolet," IEEE J. Quantum Electron. **38**, 1471–1478 (2002).
18. A. A. Kaminskii, K. Ueda, H. J. Eichler, Y. Kuwano, H. Kouta, S. N. Bagaev, T. H. Chyba, J. C. Barnes, G. M. A. Gad, T. Murai, and J. Lu, "Tetragonal vanadates YVO_4 and $GdVO_4$—new

efficient $\chi^{(3)}$-materials for Raman lasers," Opt. Commun. **194**, 201–206 (2001).
19. K. W. Su, Y. T. Chang, and Y. F. Chen, "Power scale-up of the diode-pumped actively *Q*-switched Nd: YVO_4 Raman laser with an undoped YVO_4 crystal as a Raman shifter," Appl. Phys. B **88**, 47–50 (2007).
20. Y. P. Lan, Y. F. Chen, and S. C. Wang, "Repetition-rate dependence of thermal loading in diode-end-pumped *Q*-switched lasers: influence of energy-transfer upconversion," Appl. Phys. B **71**, 27–31 (2000).
21. X. H. Chen, X. Y. Zhang, Q. P. Wang, P. Li, S. T. Li, Z. H. Cong, G. H. Jia, and C. Y. Tu, "Highly efficient diode-pumped actively *Q*-switched Nd: YAG – $SrWO_4$ intracavity Raman laser," Opt. Lett. **33**, 705–707 (2008).
22. P. G. Zverev, A. Y. Karasik, A. A. Sobol, D. S. Chunaev, T. T. Basiev, A. I. Zagumennyi, Y. D. Zavartsev, S. A. Kutovoi, V. V. Osiko, and I. A. Shcherbakov, "Stimulated Raman scattering of picosecond pulses in $GdVO_4$ and YVO_4 crystals," in *Advanced Solid State Photonics* (Optical Society of America. 2004), papers WB9, TuB10.

Comparison of thermal lensing effects between single-end and double-end diffusion-bonded Nd:YVO_4 crystals for $^4F_{3/2}\rightarrow{}^4I_{11/2}$ and $^4F_{3/2}\rightarrow{}^4I_{13/2}$ transitions

Y. T. Chang, Y. P. Huang, K. W. Su*, and Y. F. Chen

Department of Electrophysics, National Chiao Tung University, Hsinchu, Taiwan
**Corresponding author: sukuanwei@mail.nctu.edu.tw*

Abstract: The effective focal lengths of thermal lens in diode-end-pumped continuous-wave Nd:YVO_4 lasers for the $^4F_{3/2}\rightarrow{}^4I_{11/2}$ and $^4F_{3/2}\rightarrow{}^4I_{13/2}$ transitions were determined. The experimental results revealed that the thermal lensing effect for the $^4F_{3/2}\rightarrow{}^4I_{11/2}$ transition can be sufficiently improved by employing a single-end diffusion-bonded Nd:YVO_4 crystal replacing a conventional Nd:YVO_4 crystal. However, using a double-end diffusion-bonded Nd:YVO_4 crystal was a great improvement over a single-end diffusion-bonded Nd:YVO_4 crystal for the $^4F_{3/2}\rightarrow{}^4I_{13/2}$ transition with stronger thermal lensing effect.

OCIS codes: (140.3480) Lasers, diode-pumped; (140.6810) Thermal effects.

References and links

1. T. Y. Fan and R. L. Byer, "Diode laser-pumped solid-state lasers," IEEE J. Quantum Electron. **24**, 895-912 (1988).
2. A. K. Cousins, "Temperature and thermal stress scaling in finite-length end-pumped laser rods," IEEE J. Quantum Electron. **28**, 1057-1069 (1992).
3. W. Koechner, *Solid-State Laser Engineering*, 6th ed. (Springer, New York, 2006), Chap. 7.
4. Y. F. Chen, "Design criteria for concentration optimization in scaling diode end-pumped lasers to high powers: influence of thermal fracture," IEEE J. Quantum Electron. **35**, 234-239 (1999).
5. Y. F. Chen, T. M. Huang, C. F. Kao, C. L. Wang, and S. C. Wang, "Optimization in scaling fiber-coupled laser-diode end-pumped lasers to higher power: influence of thermal effect," IEEE J. Quantum Electron. **33**, 1424-1429 (1997).
6. Y. F. Chen, C. F. Kao, T. M. Huang, C. L. Wang, and S. C. Wang, "Influence of thermal effect on output power optimization in fiber-coupled laser-diode end-pumped lasers," IEEE J. Sel. Top. Quantum Electron. **3**, 29-34 (1997).
7. W. A. Clarkson, "Thermal effects and their mitigation in end-pumped solid-state lasers," J. Phys. D **34**, 2381-2395 (2001).
8. S. C. Tidwell, J. F. Seamans, M. S. Bowers, and A. K. Cousins, "Scaling CW diode-end-pumped Nd:YAG lasers to high average powers," IEEE J. Quantum Electron. **28**, 997-1009 (1992).
9. B. Neuenschwander, R. Weber, and H. P. Weber, "Determination of the thermal lens in solid-state lasers with stable cavities," IEEE J. Quantum Electron. **31**, 1082-1087 (1995).
10. B. Ozygus, and Q. Zhang, "Thermal lens determination of end-pumped solid-state lasers using primary degeneration modes," Appl. Phys. Lett. **71**, 2590-2592 (1997).
11. F. Song, C. Zhang, X. Ding, J. J. Xu, and G. Y. Zhang, "Determination of thermal focal length and pumping radius in gain medium in laser-diode-pumped Nd:YVO_4 lasers," Appl. Phys. Lett. **81**, 2145-2147 (2002).
12. S. Chénais, S. Forget, F. Druon, F. Balembois, and P. Georges, "Direct and absolute temperature mapping and heat transfer measurements in diode-end-pumped Yb:YAG," Appl. Phys. B **79**, 221-224 (2004).
13. S. Z. Fan, X. Y. Zhang, Q. P. Wang, S. T. Li, S. H. Ding, and F. F. Su, "More precise determination of thermal lens focal length for end-pumped solid-state lasers," Opt. Commun. **266**, 620-626 (2006).
14. F. Hanson, "Improved laser performance at 946 and 473 nm from a composite Nd:$Y_3Al_5O_{12}$ rod," Appl. Phys. Lett. **66**, 3549-3551 (1995).
15. R. Weber, B. Neuenschwander, M. M. Donald, M. B. Roos, and H. P. Weber, "Cooling schemes for longitudinally diode laser-pumped Nd:YAG rods," IEEE J. Quantum Electron. **34**, 1046-1053 (1998).

16. M. Tsunekane, N. Taguchi, T. Kasamatsu, and H. Inaba, "Analytical and experimental studies on the characteristics of composite solid-state laser rods in diode-end-pumped geometry," IEEE J. Sel. Top. Quantum Electron. **3**, 9-18 (1997).
17. M. Tsunekane, N. Taguchi, and H. Inaba, "Efficient 946-nm laser operation of a composite Nd:YAG rod with undoped ends," Appl. Opt. **37**, 5713-5719 (1998).
18. M. Tsunekane, N. Taguchi, and H. Inaba, "Improvement of thermal effects in a diode-end-pumped, composite Tm:YAG rod with undoped ends," Appl. Opt. **38**, 1788-1791 (1999).
19. M. P. MacDonald, Th. Graf, J. E. Balmer, and H. P. Weber, "Reducing thermal lensing in diode-pumped laser rods," Opt. Commun. **178**, 383-393 (2000).
20. J. Šulc, H. Jelínková, V. Kubeček, K. Nejezchleb, and K. Blažek, "Comparison of different composite Nd:YAG rods thermal properties under diode pumping," Proc. SPIE **4630**, 128-134 (2002).
21. D. Kracht, R. Wilhelm, M. Frede, K. Dupré, and L. Ackermann, "407 W end-pumped multi-segmented Nd:YAG laser," Opt. Express **13**, 10140-10144 (2005), http://www.opticsinfobase.org/oe/abstract.cfm?URI=oe-13-25-10140.
22. Z. Zhuo, T. Li, X Li, and H. Yang, "Investigation of Nd:YVO_4/YVO_4 composite crystal and its laser performance pumped by a fiber coupled diode laser," Opt. Commun. **274**, 176-181 (2007).
23. Y. F. Chen, "Pump-to-mode size ratio dependence of thermal loading in diode-end-pumped solid-state lasers," J. Opt. Soc. Am. B **17**, 1835-1840 (2000).
24. M. E. Innocenzi, H. T. Yura, C. L. Fincher, and R. A. Fields, "Thermal modeling of continuous-wave end-pumped solid-state lasers," Appl. Phys. Lett. **56**, 1831-1833 (1990).
25. W. Koechner, "Thermal lensing in a Nd:YAG laser rod," Appl. Opt. **9**, 2548-2553 (1970).

1. Introduction

Diode-pumped solid-state laser has been adopted widely due to its compactness, high efficiency, and reliability [1]. Comparing with a diode-side-pumped configuration, the smaller laser beam waist, higher density of pump power, and inhomogeneous heating make thermal lensing effect become a serious problem in a diode-end-pumped configuration. The localized absorption of pump power in a laser crystal leads heat converted from pump power to accumulate near the pumped facet of laser crystal. The nonuniform temperature distribution of laser crystal is represented by a parabolic-logarithmic function [2]. The temperature-dependent variation of refractive index and the end bulging effect make laser crystal act as a thermal lens [3]. Owing to the nonuniform temperature distribution the temperature gradients accrue stress that could bring thermal fracture under high pump power operation [3]. There exists a fracture-limited pump power for laser crystal that makes scaling to a higher average power be restricted [4]. For a diode-end-pumped solid-state laser, the laser performance including laser stability, maximum achievable average power, efficiency, and degradation of laser beam quality is significantly influenced by thermal lensing effect [5-7]. Therefore, promotion of laser performance can be accomplished by efficient reduction of thermal lensing effect. End-pumped solid state laser cavity can be designed to optimize the laser performance by determining the focal length of thermal lens. Several methods for determining the focal length of thermal lens in diode-end-pumped laser crystal have been presented [8-13]. In the past few years, employing a composite crystal with nonabsorbing undoped end has been regarded as a promising method for cooling the laser crystal to improve the laser performance of diode-pumped solid state laser [14-22]. With the reduction of temperature and stress, a more uniform longitudinal temperature distribution can be generated to bring out a higher fracture-limited pump power and a higher average power.

Nd:YVO_4 crystal has been seen as an excellent laser material for diode-pumped solid-state laser due to its broad absorption bandwidth and large laser emission cross section at the $^4F_{3/2}\rightarrow{}^4I_{11/2}$ (1064 nm) and $^4F_{3/2}\rightarrow{}^4I_{13/2}$ (1342 nm) transitions. In this work, we measured the focal lengths of thermal lens for one conventional and two types of composite Nd:YVO_4 crystal, and for the 1064- and 1342-nm transitions. One composite Nd:YVO_4 crystal is bounded with an undoped end at its pumped facet, and the other composite crystal is bounded with undoped ends at its two facets. The composite crystals were fabricated by the method of diffusion-bonding with high quality on the interface. The simple setup of continuous-wave (CW) laser was utilized to measure the focal length of thermal lens under easy operation. While the cavity length was increased to the critical cavity length, the thermal lensing effect led the laser cavity to become unstable. By finding the critical cavity length, the effective

focal length of thermal lens can be worked out. We observed that the stronger thermal lensing effect in Nd:YVO_4 crystal for the 1342-nm transition than that for the 1064-nm transition due to the higher thermal loading accompanying the lower conversion efficiency. The power performance, focal lengths of thermal lens and thermal lensing effects for the three types of Nd:YVO_4 crystal for the 1064 and 1342 nm transitions will be discussed in this work.

2. Experimental setup

The experimental setup shown in Fig. 1 for measuring effective focal lengths of thermal lens in a diode-end-pumped laser crystal is the setup of normal CW Nd:YVO_4 laser. The output coupler connected with a stepper motor can be moved in the longitudinal direction to change the cavity length. The cavity length can be changed from 2.5 to 50 cm by controlling the stepper motor. The laser crystal was pumped by an 808-nm fiber-coupled laser diode with a core diameter of 0.8 mm, a numerical aperture of 0.16, and the maximum output power was 22 W. The pump beam was reimaged into the laser crystal and the radius was about 0.4 mm. The laser crystal was wrapped in indium foil and mounted on water-cooled copper blocks. The water temperature was maintained at 17°C. The entrance face of the 500-mm radius-of-curvature concave front mirror was coated for antireflection at the pump wavelength of 808nm (R<0.2%) and the other face was coated for high-transmission at 808 nm (T>90%) as well as high-reflection (R>99.8%) at the lasing wavelength. In this work, we consider the thermal lensing effect for the diode-end-pumped CW Nd:YVO_4 lasers operated at 1064 and 1342 nm. The individual coatings of front mirrors and output couplers were required for achievement of different lasing wavelengths. The two flat output couplers had the reflectance of 88% at 1064 and 92% at 1342 nm used for CW 1064 and 1342 nm lasers, respectively.

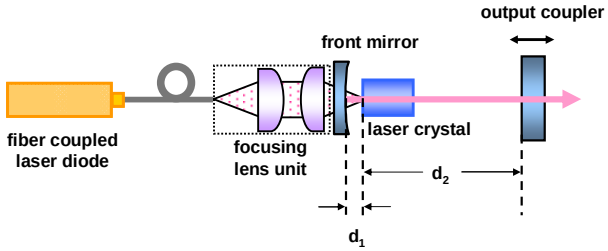

Fig. 1. Experimental setup of a diode-end-pumped Nd:YVO_4 CW laser for measuring the effective focal length of thermal lens in the laser crystal.

Figure 2 shows the three types of a-cut Nd:YVO_4 laser crystal employed in this work. Fig. 2(a) shows a 3 mm × 3 mm × 9 mm, 0.27-at.% Nd:YVO_4 crystal. Fig. 2(b) shows a 4 mm × 4 mm × 12 mm diffusion-bonded crystal called YVO_4-Nd:YVO_4 with single 2.7-mm-long undoped YVO_4 end at the pumped facet of 0.3-at.% active Nd:YVO_4 crystal. Fig. 2(c) shows a 4 mm × 4 mm × 14 mm diffusion-bonded crystal called YVO_4-Nd:YVO_4-YVO_4 with double 2.1-mm-long undoped YVO_4 end bonded to the both facets of 0.3-at.% active Nd:YVO_4 crystal. The Nd concentration was measured by the company supplying the crystals. Both sides of the three crystals were coated for antireflection at 1064 and 1342 nm (R<0.2%).

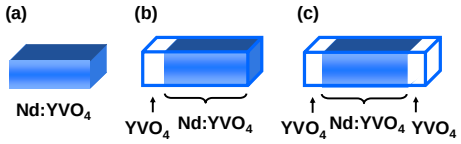

Fig. 2. The three types of laser crystal with different structures. (a) Conventional Nd:YVO_4 crystal. (b) Diffusion-bonded Nd:YVO_4 crystal with single-end at its pumped facet (YVO_4-Nd:YVO_4). (c) Diffusion-bonded Nd:YVO_4 crystal with double-end (YVO_4-Nd:YVO_4-YVO_4).

3. Experimental results and discussions

The laser performance of diode-end-pumped solid-state laser was strongly affected by thermal lensing effect. Figure 3 and Fig. 4 depict experimentally measured average CW power of 1064 and 1342 nm with respect to the cavity length for the three types of Nd:YVO_4 crystal under individual pump power, respectively. The sign of P_{in} in the Fig. 3 and Fig. 4 means the input pump power. The average CW power was optimized at the cavity length of 2.5 cm with pump power of 8.32 and 7.61 W for 1064 and 1342 nm, respectively. In order to make sure that the transverse mode was the TEM_{00} mode without high-order mode, the optimization was done near the pump threshold. Note that while the cavity length was increased and the power was decreased rapidly, optimizing average power was not allowed. It is because the extraordinary high-order mode may compensate the power decay from thermal lensing effect.

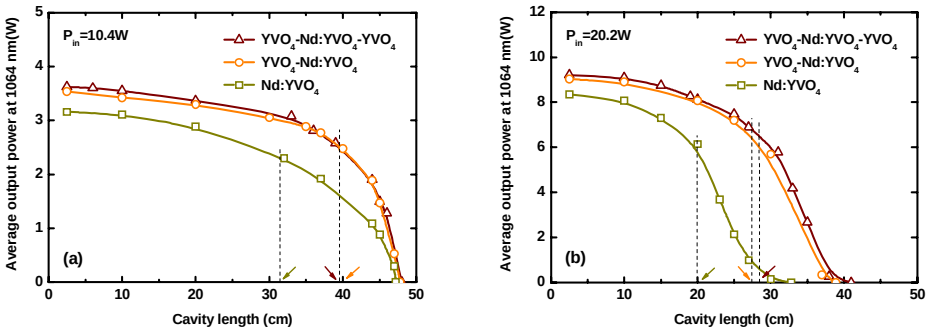

Fig. 3. Experimentally measured average CW output power of 1064 nm with respect to the cavity length for the three types of Nd:YVO_4 laser crystal with an input pump power (a) Pin=10.4W (b) Pin=20.2W. The arrows indicate the locations of critical cavity length.

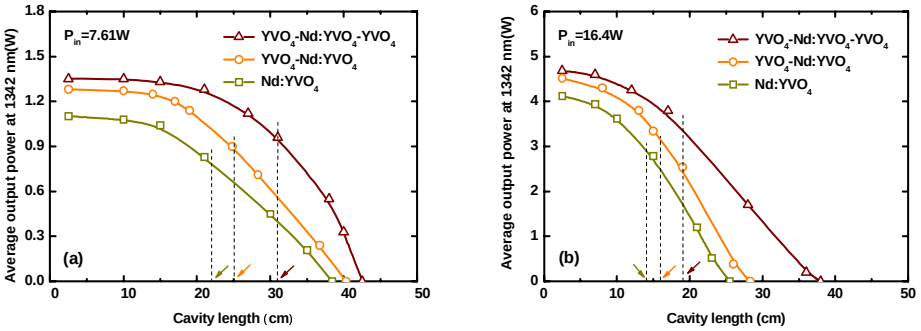

Fig. 4. Experimentally measured average CW output power of 1342 nm with respect to the cavity length for the three types of Nd:YVO_4 laser crystal with an input pump power (a) Pin=7.61W (b) Pin=16.4W. The arrows indicate the locations of critical cavity length.

While the cavity length was increased to a critical cavity length, the strong thermal lensing effect caused the laser cavity to become unstable. The relationships between average CW output power and cavity length are shown as Fig. 3 and Fig. 4. The maximum power at short cavity of the conventional crystal was much lower than that of the other two composite crystals mainly due to the difference in dopant concentration. The critical cavity length is determined based on unified criterion that the output power is dropped to the 70% of maximum power at the stable (short) cavity. The corresponding focal length of thermal lens f_{th} is expressed by [23]

$$\frac{1}{f_{th}} = \frac{1}{d_2 + l\left(\frac{1}{n} - 1\right)} - \frac{1}{r - d_1} \tag{1}$$

where d_1 and d_2 are the distances from the pumped facet of laser crystal to the front mirror and output coupler, respectively, l is the length of the laser crystal, n is the refractive index of the laser crystal, r is the radius of curvature of the front mirror. d_1 was around 2.4, 1.1, and 1.6 mm for conventional Nd:YVO_4, composite YVO_4-Nd:YVO_4, and YVO_4-Nd:YVO_4-YVO_4, respectively, and was fixed during the experiments. We substitute the critical cavity lengths in terms of d_1 and d_2 into the Eq. (1) to get the effective focal lengths of thermal lens f_{th}. Even though this easy experimental method can not give an absolutely accurate f_{th}, the relative precision is sufficient to make comparison of thermal properties. The experimentally obtained f_{th} are plotted as symbols in Fig. 5. According to the theoretical thermal modeling of CW end-pumped solid-state laser presented by Innocenzi *et al.*, the effective focal length can be approximately expressed by [24]

$$f_{th} = \frac{\pi K \omega_p^{\ 2}}{\xi P_{in}(dn/dT)}\left[\frac{1}{1-\exp(-\alpha l_a)}\right] = \frac{C\omega_p^{\ 2}}{P_{in}} \tag{2}$$

where K is the thermal conductivity, ω_p is the pump-beam radius in the active medium in the unit of mm, ξ is the fractional thermal loading, P_{in} is the pump power in the unit of watt (W), (dn/dT) is the thermal-optical coefficient of n, α is the absorption coefficient, l_a is the length of the active medium, C is a proportional constant in the unit of W/mm. Because the thermal conductivity of YVO_4 in the b- and c-axis of 5.1 and 5.23 W/mK are very close, respectively, it can be seen as a radial symmetry thermal model [4]. The Innocenzi model for rod-type crystal is available here. The Eq. (2) is used to fit the experimental data and the theoretical fitted curves with the approximate corresponding constants C are depicted in Fig. 5.

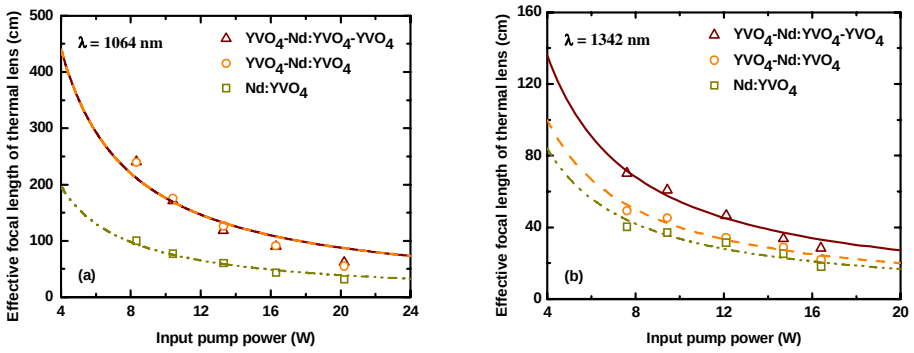

Fig. 5. The relationship between the effective focal length of thermal lens and the input pump power for three types of Nd:YVO_4 crystal operated at (a) 1064 (b) 1342 nm. The symbols represent experimental data and the curves are theoretical fitted results.

The constants C of the conventional Nd:YVO_4, composite YVO_4-Nd:YVO_4, and YVO_4-Nd:YVO_4-YVO_4 for the 1064-nm transition are 4.9×10^4, 11×10^4, and 11×10^4 W/mm, respectively. The constants C of the conventional Nd:YVO_4, composite YVO_4-Nd:YVO_4, and YVO_4-Nd:YVO_4-YVO_4 for the 1342-nm transition are 2.1×10^4, 2.5×10^4, and 3.4×10^4 W/mm, respectively. The bigger constant C which represents the longer focal length of thermal lens means the weaker thermal lensing effect. The increase of the pump power enhanced the thermal lensing effect. With the equal pump power, the focal length of thermal lens for CW 1342-nm laser was shorter than that for CW 1064-nm laser due to the higher thermal loading.

The higher thermal loading accompanying the lower conversion efficiency was mainly attributed to the higher quantum defect for the longer laser wavelength.

According to the above-mentioned constants C, it is proven that both the focal lengths of thermal lens in the YVO_4-Nd:YVO_4 and YVO_4-Nd:YVO_4-YVO_4 were increased by nearly 2.2-times that in the conventional Nd:YVO_4 for the 1064-nm transition. The focal lengths of thermal lens in the YVO_4-Nd:YVO_4 and YVO_4-Nd:YVO_4-YVO_4 were increased by nearly 1.2 and 1.6-times that in the conventional Nd:YVO_4 for the 1342-nm transition, respectively. Even though the ability of thermal diffusivity in a laser crystal with bigger cross section was inferior [16, 25], the focal lengths of thermal lens in the two composite Nd:YVO_4 crystals were longer than that in the conventional Nd:YVO_4 crystal. In addition, we discuss the influence of different dopant concentration and the length of active medium on the thermal lens. The absorption coefficient α for a typical laser diode with the center wavelength of 808 nm is expressed by [4]

$$\alpha = 2 \cdot N_d \ \ (\mathrm{mm}^{-1}) \tag{3}$$

where N_d is the Nd dopant concentration in the unit of %. The values of αl were 4.86, 5.58, and 5.88 for the conventional Nd:YVO_4, the composite YVO_4-Nd:YVO_4, and YVO_4-Nd:YVO_4-YVO_4, respectively. According to the Eq. (2), the bigger value of αl represents the shorter focal length of thermal lens. But the differences in the value of $[1-\exp(-\alpha l)]^{-1}$ between the three crystals was below 0.5 % and could be ignored. Further, the influence of different cross section on the thermal diffusivity was small for edge cooling system. Even we consider the influence, the conventional crystal with small cross section would have better thermal diffusivity and the conclusion does not be changed. Therefore, it is seen that the improvement of thermal lensing effect contributed by employing the two diffusion-bonded Nd:YVO_4 crystals greatly overcame the disadvantage of the bigger cross section.

The experimental results revealed that the thermal lensing effect in the YVO_4-Nd:YVO_4 was nearly equal to that in the YVO_4-Nd:YVO_4-YVO_4 for the highest efficient 1064-nm transition. Therefore only single undoped end at the pumped facet of laser crystal was sufficient for improving the thermal lensing effect to increase the effective focal length of thermal lens to nearly 2.2 times that of the conventional Nd:YVO_4 crystal for CW 1064-nm laser. However, the improvement in thermal lensing effect of the YVO_4-Nd:YVO_4-YVO_4 noticeably outperformed that of the YVO_4-Nd:YVO_4 for the 1342-nm transition. As a result of the stronger thermal lensing effect for the 1342-nm transition, the double undoped ends bonded to the both facets of active medium were essential for assisting thermal diffusing to increase the effective focal length of thermal lens to nearly 1.6 times that of the conventional Nd:YVO_4 crystal.

4. Conclusion

The comparison of thermal lensing effects between diffusion-bonded YVO_4-Nd:YVO_4 and YVO_4-Nd:YVO_4-YVO_4 crystals with single- and double-end, respectively, was demonstrated by measuring the effective focal lengths of thermal lens. The both types of diffusion-bonded crystal could improve the thermal lensing effects of conventional Nd:YVO_4 crystal. The YVO_4-Nd:YVO_4 was capable of accomplishing the improvement in thermal lensing effect of YVO_4-Nd:YVO_4-YVO_4 for the 1064-nm transition. However, the improvement of YVO_4-Nd:YVO_4-YVO_4 remarkably towered over that of YVO_4-Nd:YVO_4 for the 1342-nm transition with stronger thermal lensing effect. Therefore YVO_4-Nd:YVO_4 and YVO_4-Nd:YVO_4-YVO_4 crystals can serve as promising substitutes for a conventional Nd:YVO_4 crystal to reduce thermal lensing effect and scale to a higher average power of diode-end-pumped CW Nd:YVO_4 lasers operated at 1064 and 1342 nm, respectively.

Acknowledgments

The authors thank the National Science Council for their financial support of this research under Contract No. NSC-95-2112-M-009-041-MY2.

Subnanosecond mJ eye-safe laser with an intracavity optical parametric oscillator in a shared resonator

Y. P. Huang[1], H. L. Chang[1], Y. J. Huang[1], Y. T. Chang[1], K. W. Su[1], W. C. Yen[2], and Y. F. Chen[1]*

[1]*Department of Electrophysics, National Chiao Tung University, Hsinchu, Taiwan*
[2]*Chung-Shan Institute of Science & Technology, Lung-Tan, Tao-Yuan, Taiwan*
**Corresponding author: yfchen@cc.nctu.edu.tw*

Abstract: We theoretically verify that the threshold of an intracavity optical parametric oscillator pumped by a passively Q-switched laser is entirely controlled by the bleach of the saturable absorber not by the signal output reflectivity. We use a series of different output couplers to optimize the output performance. With a signal output reflectivity of 15%, we experimentally achieve an efficient subnanosecond eye-safe laser with 3.3 mJ pulse energy and 1.5 MW peak power.

OCIS codes: (140.3540) Lasers, Q-switched; (190.4410) Nonlinear optics, parametric processes; (140.3480) Lasers, diode-pumped.

References and links

1. E. Gregor, D. E. Nieuwsma, and R. D. Stultz, "20 Hz eyesafe laser rangefinder for air defense," Proc. SPIE, **1207**, 124-134 (1990).
2. L. R. Marshall, A. D. Hays, and J. Kasinski, "Highly efficient optical parametric oscillators," Proc. SPIE **1419**, 141–152 (1991).
3. J. E. Nettleton, B. W. Schilling, D. N. Barr, and J. S. Lei, "Monoblock laser for a low-cost, eyesafe, microlaser range finder," Appl. Opt. **39**, 2428-2432 (2000).
4. T. Debuisschert, J. Raffy, J. P. Pocholle, and M. Papuchon, "Intracavity optical parametric oscillator: Study of the dynamics in pulsed regime," J. Opt. Soc. Am. **B 13**, 1569–1587 (1996).
5. Z. Liu, Q. Wang, X. Zhang, Z. Liu, J. Chang, H. Wang, S. Fan, W. Sun, G. Jin, X. Tao, S. Zhang, and H. Zhang, "Efficient acoustic-optically Q-switched intracavity Nd:YAG/ $KTiOAsO_4$ parametric oscillator," Appl. Phys. **B 92**, 37-41 (2008).
6. H. T. Huang, J. L. He, X. L. Dong, C. H. Zuo, B. T. Zhang, G. Qiu, and Z. K. Liu, "High-repetition-rate eye-safe intracavity KTA OPO driven by a diode-end-pumped Q-switched Nd:YVO_4 laser," Appl. Phys. **B 90**, 43-45 (2008).
7. Y. F. Chen, S. W. Chen, S. W. Tsai, and Y. P. Lan, "High repetition-rate eye-safe optical parametric oscillator intracavity pumped by a diode-pumped Q-switched Nd:YVO_4 laser," Appl. Phys. **B 76**, 263–266 (2003).
8. J. Miao, J. Peng, B. Wang, H. Tan, and H. Bian, "Compact low threshold Cr:YAG passively Q-switched intracavity optical parametric oscillator," Opt. Commun. **281**, 2265–2270 (2008).
9. Y. F. Chen, S. W. Chen, Y. C. Chen, Y. P. Lan, and S. W. Tsai, "Compact efficient intracavity optical parametric oscillator with a passively Q-switched Nd:YVO4/Cr^{4+}:YAG laser in a hemispherical cavity," Appl. Phys. **B 77**, 493-495 (2003).
10. Y. F. Chen, S. W. Chen, L. Y. Tsai, Y. C. Chen, and C. H. Chien,"Efficient subnanosecond intracavity optical parametric oscillator pumped with a passively Q-switched Nd:$GdVO_4$ laser," Appl. Phys. **B 79**, 823–825 (2004).
11. R. Dabu, C. Fenic, and A. Stratan, "Intracavity pumped nanosecond optical parametric oscillator emitting in the eye-safe range," Appl. Opt. **40**, 4334-4340 (2001).
12. Y. Yashkir and H. M. van Driel, "Passively Q-switched 1.57-μm intracavity optical parametric oscillator," Appl. Opt. **38**, 2554-2559 (1999).
13. A. Agnesi, S. Dell'Acqua, and G. Reali, "Diode-pumped quasi-cw intracavity optical parametric oscillator at 1.57 μm with efficient pulse shortening," Appl. Phys. B **70**, 751-753 (2000).
14. W. Zendzian, J. K. Jabczyński, and J. Kwiatkowski, "Intracavity optical parametric oscillator at 1572-nm wavelength pumped by passively Q-switched diode-pumped Nd:YAG laser," Appl. Phys. **B 76**, 355-358 (2003).

15. B. W. Schilling, S. R. Chinn, A. D. Hays, L. Goldberg, and C. W. Trussell, "End-pumped 1.5 μm monoblock laser for broad temperature operation," Appl. Opt. **45**, 6607-6615 (2006).
16. Y. F. Chen and L. Y. Tsai, "Comparison between shared and coupled resonators for passively Q-switched Nd:GdVO4 intracavity optical parametric oscillators," Appl. Phys. **B 82**, 403–406 (2006).
17. Y. F. Chen, K. W. Su, Y. T. Chang, and W. C. Yen, "Compact efficient eye-safe intracavity optical parametric oscillator with a shared cavity configuration," Appl. Opt. **46**, 3597-3601 (2007).
18. R. J. Beach, "Theory and optimization of lens ducts," Appl. Opt. **35**, 2005-2015 (1996).
19. R. Fu, G. Wang, Z. Wang, E. Ba, G. Mu, and X. Hu, "Design of efficient lens ducts," Appl. Opt. **37**, 4000-4003 (1998).
20. J. J. Degnan, "Optimization of passively Q-switched lasers," IEEE J. Quantum Electron., **vol. 31**, pp. 1890–1901, 1995.
21. S. J. Brosnan and R. L. Byer, "Optical parametric oscillator threshold and linewidth studies," IEEE J. Quantum Electron., **vol. 15**, pp. 415–431, 1979.

1. Introduction

Human exposure is usually inevitable in many applications such as laser radar, remote sensing, rangefinder, target designation, and laser countermeasures; consequently, protection again injury of the eye is one of the most important issues [1-3]. Since water absorption in eye tissue and the intraocular fluid prevents light in the spectral range of 1.4-1.8 μm from reaching the retina, there is a considerable interest in compact laser sources with wavelengths in this eye-safe regime. One of the most promising approaches for high-peak-power eye-safe laser sources is based on intracavity optical parametric oscillators (OPO) [4-15]. The advent of high damage threshold nonlinear crystals and diode-pumped Nd-doped lasers leads to a renaissance of interest in intracavity OPO's. In recent years, a number of efficient eye-safe intracavity OPOs pumped by actively [5-7] or passively [8-10] Q-switched Nd-doped lasers have been demonstrated to produce pulse energies of tens of μJ with pulse peak powers of 1-100 kW. Nevertheless, eye-safe laser systems with pulse energies in the mJ range and peak powers greater than MW are indispensable for the many long-distance applications [11-15].

The intracavity OPOs are mostly constructed with the coupled cavity configuration in which the resonators for the signal and fundamental wave fields are separate. Recently, it was found [16,17] that the shared cavity configuration in which the pump and signal beams share the same resonator provides a substantially superior amplitude stability, in comparison with the coupled cavity configuration. Even so, the maximum peak power in a shared cavity is usually several times lower than that in a coupled cavity under the circumstance of the same output coupler. Therefore, it is a practical interest to explore an intracavity OPO in a shared resonator in quest of optimal pulse energies and peak powers.

Here, for what is believed to be the first time, a subnanosecond mJ eye-safe laser is experimentally demonstrated with an intracavity OPO pumped in a shared resonator. We first confirm that the threshold of an intracavity OPO pumped by a passively Q-switched laser is essentially determined by the bleach of the saturable absorber not by the signal output reflectivity. As a result, a series of different output couplers are used to ascertain the design criteria for the output optimization. With a signal output reflectivity of 15%, we realize an efficient subnanosecond eye-safe laser with 3.3 mJ pulse energy and 1.5 MW peak power.

2. Experimental setup

Figure 1 shows the experimental setup for an intracavity OPO pumped by a high-power quasi-continuous-wave (QCW) diode-pumped passively Q-switched Nd:YAG laser in a shared resonator. The fundamental laser cavity was formed by a coated Nd:YAG crystal and an output coupler. The OPO cavity entirely overlapped with the fundamental laser cavity. The pump source is a high-power QCW diode stack (Quantel Laser Diodes) that consists of three 10-mm-long diode bars generating 130 W per bar, for a total of 390 W at the central wavelength of 808 nm. The diode stack is designed with 0.4 mm spacing between the diode bars so the overall area of emission is approximately 10 mm (slow axis) × 0.8 mm (fast axis). The full divergence angles in the fast and slow axes are approximately 35^{o} and 10^{o}, respectively. A lens duct was exploited to couple the pump light from the diode stack into the

laser crystal. The lens duct has the benefits of simple structure, high coupling efficiency, and unaffected by slight misalignment. The geometric parameters of a lens duct include r, L, H_1, H_2, and H_3, where r is the radius of the input surface, L is the length of the duct, H_1 is the width of the input surface, H_2 is the width of the output surface, and H_3 is the thickness of the duct [18, 19]. Here a lens duct with the parameters of r = 10 mm, L = 32 mm, H_1 = 12 mm, H_2 = 2.7 mm, and H_3 = 2.7 mm was manufactured and used in the experiment. The coupling efficiency of this lens duct is found to be approximately 85%.

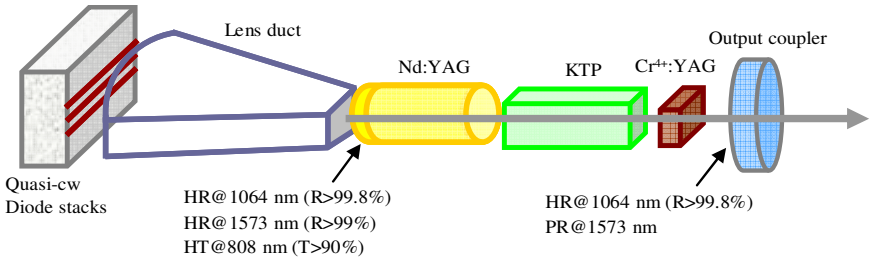

Fig. 1. Experimental setup for an intracavity OPO pumped by a high-power QCW diode-pumped passively Q-switched Nd:YAG laser in a shared resonator.

The gain medium was a 1.0 at. % Nd:YAG crystal with a diameter of 5 mm and a length of 10 mm. The incident surface of the laser crystal was coated to be highly reflective at 1064 nm and 1573 nm (R>99.8%) and highly transmitted at the pump wavelength of 808 nm (T>90%). The other surface of the laser crystal was coated to be antireflective at 1064 nm and 1573 nm (R<0.2%). The nonlinear material for the intracavity OPO was an x-cut KTP crystal with a size of 4×4×20 mm^3. The saturable absorber for the passive Q-switching was a Cr^{4+}:YAG crystal with a thickness of 3 mm and an initial transmission of 60% at 1064 nm. Both surfaces of the KTP and Cr^{4+}:YAG crystals were coated for antireflection at 1573 nm and 1064 nm. All crystals were wrapped with indium foil and mounted in conductively cooled copper blocks. The output coupler had a dichroic coating that was highly reflective at 1064 nm (R > 99.8%) and partially reflective at 1573 nm. Several output couplers with different reflectivities (10% ≤ Rs ≤ 70%) at 1573 nm were used in the experiment to investigate the output optimization. The total cavity length was approximately 5.5 cm. The pulse temporal behavior at 1063 nm and 1571 nm was recorded by a LeCroy digital oscilloscope (Wavepro 7100; 10 G samples/sec; 1 GHz bandwidth) with a fast InGaAs photodiode. The spectral information was monitored by an optical spectrum analyzer (Advantest Q8381A) that employs a diffraction grating monochromator to for measure high-speed light pulses with the resolution of 0.1 nm. In all investigations, the diode stack was driven to emit optical pulses 250 μs long, at a repetition rate less than 40 Hz, with a maximum duty cycle of 1%.

3. Theoretical analysis

The advantage of the intracavity OPO mainly consists in the exploit of high photon density of the fundamental wave. First of all, we analyze the maximum value of the intracavity photon density for the fundamental wave in a passively Q-switched laser. Next, we verify that the intracavity photon density of the present laser cavity can generally exceed the threshold of a singly resonant intracavity OPO by far, even though the reflectivity of the output mirror at the signal wavelength is nearly zero. In a passively Q-switched laser with a fast Q-switching condition, the maximum value of the intracavity photon density of the fundamental wave can be expressed as [20]

$$\phi_{f,\max} = \frac{l_{gm}}{l_{cav}}\left\{ n_i - n_t\left[1+\ln\left(\frac{n_i}{n_t}\right)\right]\right\} \tag{1}$$

where $n_i = \frac{1}{2\sigma l_{gm}}\left[\ln\left(1/T_o^2\right)+\ln(1/R)+L\right]$; $n_t = \frac{1}{2\sigma l_{gm}}\left[\beta\ln\left(1/T_o^2\right)+\ln(1/R)+L\right]$; $\beta = \frac{\sigma_{es}}{\sigma_{gs}}$; n_i is the initial population density in the gain medium; σ is the stimulated emission cross section of the gain medium; l_{gm} is the length of the gain medium; l_{cav} is the cavity length; T_o is the initial transmission of the saturable absorber; σ_{gs} and σ_{es} are the ground-state and excited-state absorption cross sections in the saturable absorber, respectively; R is the reflectivity of the output mirror at the fundamental wavelength; and L is the nonsaturable intracavity round-trip loss. With the properties of the Nd:YAG and Cr^{4+}:YAG crystals and the typical cavity parameters: $\sigma = 2.8\times10^{-19}$ cm^2 , $\sigma_{gs} = 8.7\times10^{-19}$ cm^2, $\sigma_{es} = 2.2\times10^{-19}$ cm^2, $l_{cav} = 5.5$ cm, $R = 99.8\%$, $T_o = 0.6$, and $L = 0.01$, it can be found that $\phi_{f,\max}$ can be up to 1.56×10^{17} cm^{-3}.

With Brosnan and Byer's equation [21], the threshold photon density for the double-pass pumped, single resonant OPO is derived to be given by

$$\phi_{f,th}(R_s) = \frac{1.12}{G\, g_s\,(1+\gamma)^2}\left[33\frac{l_{cav}}{c\,\tau_p}+\ln\left(\frac{1}{\sqrt{R_s}}\right)+L_s+\ln 4\right]^2 \tag{2}$$

with the gain coefficient

$$G = \frac{2\hbar\omega_3\,\omega_1\,\omega_2\; d_{eff}^2\; l_{nl}^2}{n_3\, n_1\, n_2\, \varepsilon_0\, c^2} \tag{3}$$

where g_s is the mode coupling coefficient, γ is the ratio of backward to forward pump amplitude in the cavity; ω_1, ω_2 and ω_3 are the signal, idler and pump frequencies, respectively;, n_2 and n_3 are the refractive indices at the signal, idler and pump wavelengths, respectively; τ_p is the FWHM of the pump pulse; d_{eff} is the effective non-linear coefficient; ε_0 is the vacuum permittivity; c is the speed of light; l_{nl} is the length of the nonlinear crystal; L_s is the round-trip signal wave intensity loss in the cavity; and R_s is the output reflectivity at the signal wavelength.

Figure 2 depicts the calculated results for the dependence of the threshold photon density $\phi_{f,th}(R_s)$ on the output reflectivity R_s with the properties of the KTP crystal and the typical cavity parameters: $\omega_1 = 1.198\times10^{15}$ sec^{-1}, $\omega_2 = 5.712\times10^{14}$ sec^{-1}, $\hbar\omega_3 = 1.865\times10^{-19}$ J, $d_{eff} = 3.64$ pm/V, $l_{nl} = 20$ cm, $n_1 = 1.737$ $n_2 = 1.771$, $n_3 = 1.748$, $\varepsilon_0 = 8.854$ pF/m, $L_s = 0.01$, $\gamma = 0.9$, $g_s = 0.9$, $\tau_p = 10$ ns and c = 3×10^8 m/s. It can be seen that the threshold photon density $\phi_{f,th}$ increases from 6×10^{15} cm^{-3} to 6×10^{16} cm^{-3} for the reflectivity R_s varying from 99.9% to 0.1%. As analyzed earlier, the obtainable intracavity photon density of the fundamental wave generally exceeds 10^{17} cm^{-3}. Therefore, the intracavity OPO for any value of R_s can be promisingly generated in the shared cavity, as long as the pump energy can excite the fundamental wave to bleach the saturable absorber and to overcome the lasing threshold.

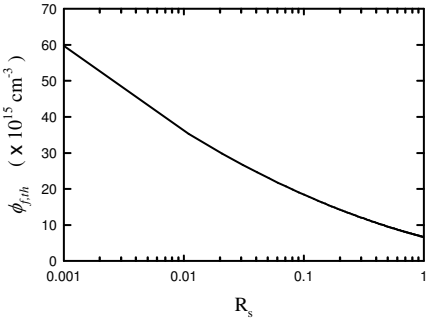

Fig. 2. Calculated results for the dependence of the threshold photon density on the output reflectivity R_s.

4. Experimental results and discussions

Figure 3 shows the experimental results for the threshold pump energy versus the OPO output reflectivity. Experimental results confirm that the threshold pump energy is determined by the bleach of the saturable absorber not by the signal output reflectivity. Consequently, a wide range of the signal output reflectivity can be used to optimize the output performance. Figure 4 depicts the experimental results for the pulse energy of the signal output versus the signal output reflectivity. The optimal output reflectivity for the output pulse energy can be found to be within R_s =40–50%. With the optimum output coupler, the conversion efficiency from the diode input energy to the signal output energy is approximately 7%, which is slightly superior to the efficiency of 4–6% obtained in a coupled cavity [15].

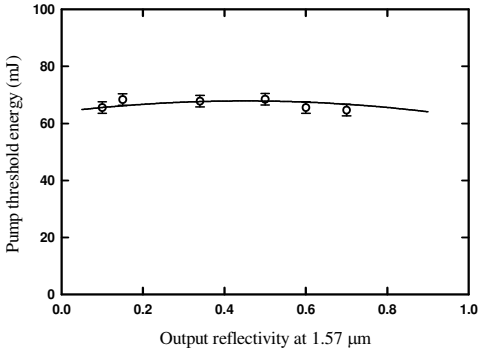

Fig. 3. Experimental results for the threshold pump energy versus the OPO output reflectivity.

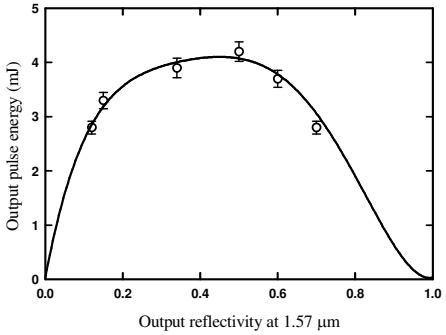

Fig. 4. Experimental results for the pulse energy of the signal output versus the OPO output reflectivity.

Figures 5(a)-(c) show the experimental results for the temporal shapes of the fundamental and the signal pulses obtained with three different output couplers. It can be seen that the pulse durations of the signal output are 4.4 ns, 2.1 ns, and 0.85 ns for R_s=60%, 50%, and 15%, respectively. The pulse width obtained with R_s = 15% is 2.4 times shorter than that obtained with R_s = 50%; however, the pulse energy is only 20% less than the maximum value. In other words, the peak power reached with R_s = 15% can be nearly two times higher than that obtained with R_s = 50%. To be more accurate, the output peak was calculated with the experimental pulse energy and the numerical integration of the measured temporal pulse profile. Figure 6 depicts the experimental results for the peak power of the signal output versus the OPO output reflectivity. The optimal output reflectivity for the output peak power can be found to be within R_s =10–20%. With the optimum output coupler, the maximum peak power can be up to 1.5 MW.

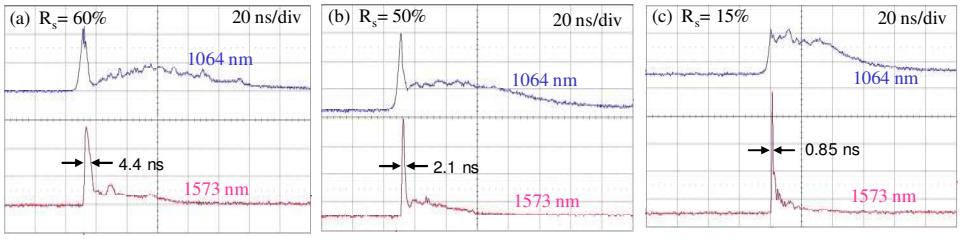

Fig. 5. Experimental results for the temporal shapes of the fundamental and the signal pulses.

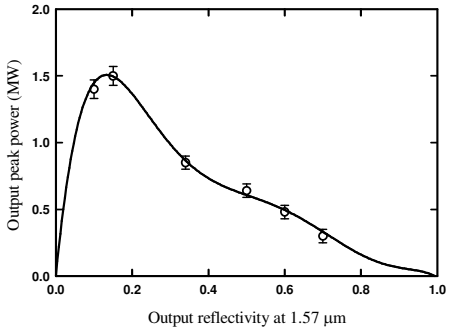

Fig. 6. experimental results for the peak power of the signal output versus the OPO output reflectivity.

5. Summary

In summary, we have theoretically and experimentally explored the output performance of an intracavity OPO in a shared cavity configuration. The threshold of an intracavity OPO pumped by a passively Q-switched Nd:YAG laser has been verified to be utterly controlled by the bleach of the saturable absorber not by the signal output reflectivity. Based on thorough experimental studies, we found that an efficient subnanosecond eye-safe laser with 3.3 mJ pulse energy and 1.5 MW peak power could be achieved with a signal output reflectivity of 15%.

Acknowledgments

The authors also thank the National Science Council for their financial support of this research under Contract No. NSC-97-2112-M-009-016-MY3.

Compact efficient Q-switched eye-safe laser at 1525 nm with a double-end diffusion-bonded Nd:YVO_4 crystal as a self-Raman medium

Y. T. Chang, K. W. Su*, H. L. Chang, and Y. F. Chen*

Department of Electrophysics, National Chiao Tung University, Hsinchu, Taiwan
**Corresponding author: sukuanwei@mail.nctu.edu.tw, yfchen@cc.nctu.edu.tw*

Abstract: We report on an efficient Q-switched eye-safe laser at 1525 nm with a double-end diffusion-bonded Nd:YVO_4 crystal as a self-Raman gain medium. A diffusion-bonded crystal not only reduces the thermal effects but also increase the interaction length for the stimulated Raman scattering. With an input pump power of 17.2 W, average power of 2.23 W at the first-Stokes wavelength of 1525 nm is generated at a pulse repetition rate of 40 kHz, corresponding to a conversion efficiency of 13%.

OCIS codes: (140.3550) Lasers, Raman; (140.3380) Laser Materials; (140.3480) Lasers, diode-pumped.

References and links

1. L. R. Marshall and A. Kaz, "Eye-safe output from noncritically phase-matched parametric oscillators," J. Opt. Soc. Am. B, **10**, 1730-1736 (1993).
2. G. H. Xiao, M. Bass, and M. Acharekar, "Passively Q-switched solid-state lasers with intracavity optical parametric oscillators," IEEE J. Quantum Electron. **34**, 2241-2245 (1998).
3. Y. F. Chen, S. W. Chen, S. W. Tsai, and Y. P. Lan, "High-repetition-rate eye-safe optical parametric oscillator intracavity pumped by a diode-pumped Q-switched Nd:YVO_4 laser, Appl. Phys. B **76**, 263-266 (2003).
4. Y. F. Chen, Y. C. Chen, S. W. Chen and Y. P. Lan, "High-power efficient diode-pumped passively Q-switched Nd:YVO_4/KTP/Cr^{4+}:YAG eye-safe laser," Opt. Commun. **234**, 337-342 (2004).
5. R. Fluck, R. Häring, R. Paschotta, E. Gini, H. Melchior, and U. Keller, "Eyesafe pulsed microchip laser using semiconductor saturable absorber mirrors," Appl. Phys. Lett. **72**, 3273-3275 (1998).
6. I. Sokólska, E. Heumann, S. Kück, and T. Łukasiewicz, "Laser oscillation of Er^{3+}:YVO_4 and Er^{3+}, Yb^{3+}:YVO_4 crystals in the spectral range around 1.6 μm," Appl. Phys. B **71**, 893-896 (2000).
7. A. Sennaroglu, "Broadly tunable Cr^{4+}-doped solid-state lasers," Prog. Quantum Electron. **26**, 287-352 (2002).
8. N. Takei, S. Suzuki, and F. Kannari, "20-Hz operation of an eye-safe cascade Raman laser with a $Ba(NO_3)_2$ crystal," Appl. Phys. B **74**, 521-527 (2002).
9. Y. F. Chen, "Compact efficient all-solid-state eye-safe laser with self-frequency Raman conversion in a Nd:YVO_4 crystal," Opt. Lett. **29**, 2172-2174 (2004).
10. Y. F. Chen, "Efficient 1521-nm Nd:$GdVO_4$ Raman laser," Opt. Lett. **29**, 2632-2634 (2004).
11. A. Brenier, G. Jia, and C. Tu, "Raman lasers at 1.171 and 1.517 μm with self-frequency conversion in $SrWO_4$:Nd^+ crystal," J. Phys.: Condens. Matter **16**, 9103-9108 (2004).
12. J. H. Huang, J. P. Lin, R. B. Su, J. H. Li, H. Zheng, C. H. Xu, F. Shi, Z. Z. Lin, J. Zhuang, W. R. Zeng, and W. X. Lin, "Short pulse eye-safe laser with a stimulated Raman scattering self-conversion based on a Nd:KGW crystal," Opt. Lett. **32**, 1096-1098 (2007).
13. Y. X. Fan, Y. Liu, Y. H. Duan, Q. Wang, L. Fan, H. T. Wang, G. H. Jia, and C. Y. Tu, "High-efficiency eye-safe intracavity Raman laser at 1531 nm with $SrWO_4$ crystal," Appl. Phys. B **93**, 327-330 (2008).
14. Z. P. Wang, D. W. Hu, X. Fang, H. J. Zhang, X. G. Xu, J. Y. Wang, and Z. H. Shao, "Eye-safe Raman laser at 1.5 μm based on $BaWO_4$ crystal," Chin. Phys. Lett. **25**, 122-124 (2008).
15. G. M. A. Gad, H. J. Eichler, and A. A. Kaminskii, "Highly efficient 1.3-μm second-Stokes $PbWO_4$ Raman laser," Opt. Lett. **28**, 426-428 (2003).
16. H. M. Pask, "The design and operation of solid-state Raman lasers," Prog. Quantum Electron. **27**, 3-56 (2003).
17. P. Černý, H. Jelínková, P. G. Zverev, and T. T. Basiev "Solid state laser with raman frequency conversion," Prog. Quantum Electron. **28**, 113-143 (2004).

18. J. A. Piper and H. M. Pask, "Crysatalline Raman Lasers," IEEE J. Sel. Top. Quantum Electron. **13**, 692-704 (2007).
19. A. A. Kaminskii, K. Ueda, H. J. Eichler, Y. Kuwano, H. Kouta, S. N. Bagaev, T. H. Chyba, J. C. Barnes, G. M. A. Gad, T. Murai, and J. Lu, "Tetragonal vanadates YVO_4 and $GdVO_4$ – new efficient $\chi^{(3)}$-materials for Raman lasers," Opt. Commun. **194**, 201-206 (2001).
20. S. H. Ding, X. Y. Zhang, Q. P. Wang, F. F. Su, P. Jia, S. T. Li, S. Z. Fan, J. Chang, S. S. Zhang, and Z. J. Liu, "Theoretical and experimental study on the self-Raman laser with Nd:YVO_4 crystal," IEEE J. Quantum Electron. **42**, 927-933 (2006).
21. Y. F. Chen, "High-power diode-pumped actively Q-switched Nd:YVO_4 self-Raman laser: influence of dopant concentration," Opt. Lett. **29**, 1915-1917 (2004).
22. F. F. Su, X. Y. Zhang, Q. P. Wang, S. H. Ding, P. Jia, S. T. Li, S. Z. Fan, C. Zhang, and B. Liu "Diode pumped actively Q-switched Nd:YVO4 self-Raman laser," J. Phys. D: Appl. Phys. **39**, 2090-2093 (2006).
23. F. Hanson, "Improved laser performance at 946 and 473 nm from a composite Nd:$Y_3Al_5O_{12}$ rod," Appl. Phys. Lett. **66**, 3549-3551 (1995).
24. R. Weber, B. Neuenschwander, M. M. Donald, M. B. Roos, and H. P. Weber, "Cooling schemes for longitudinally diode laser-pumped Nd:YAG rods," IEEE J. Quantum Electron. **34**, 1046-1053 (1998).
25. M. Tsunekane, N. Taguchi, T. Kasamatsu, and H. Inaba, "Analytical and experimental studies on the characteristics of composite solid-state laser rods in diode-end-pumped geometry," IEEE J. Sel. Top. Quantum Electron. **3**, 9-18 (1997).
26. M. Tsunekane, N. Taguchi, and H. Inaba, "Improvement of thermal effects in a diode-end-pumped, composite Tm:YAG rod with undoped ends," Appl. Opt. **38**, 1788-1791 (1999).
27. M. P. MacDonald, Th. Graf, J. E. Balmer, and H. P. Weber, "Reducing thermal lensing in diode-pumped laser rods," Opt. Commun. **178**, 383-393 (2000).
28. J. Šulc, H. Jelínková, V. Kubeček, K. Nejezchleb, and K. Blažek, "Comparison of different composite Nd:YAG rods thermal properties under diode pumping," Proc. SPIE **4630**, 128-134 (2002).
29. Z. Zhuo, T. Li, X Li, and H. Yang, "Investigation of Nd:YVO_4/YVO_4 composite crystal and its laser performance pumped by a fiber coupled diode laser," Opt. Commun. **274**, 176-181 (2007).
30. Y. T. Chang, Y. P. Huang, K. W. Su, and Y. F. Chen, "Comparison of thermal lensing effects between single-end and double-end diffusion-bonded NdYVO4 crystals for $^4F_{3/2} \rightarrow {}^4I_{11/2}$ and $^4F_{3/2} \rightarrow {}^4I_{13/2}$ transitions," Opt. Express, **16**, 21155-21160 (2008), http://www.opticsinfobase.org/oe/abstract.cfm?URI=oe-16-25-21155.

1. Introduction

Since water absorption in eye tissue and the intraocular fluid prevents light in the spectral range of 1.4-1.8 μm from reaching the retina, there is a considerable interest in compact laser sources with wavelengths in this eye-safe regime. The methods of generating eye-safe laser include optical parametric oscillators [1-4], Er^{3+}, Cr^{4+}, and Yb^{3+} doped solid-state laser [5-7], and stimulated Raman scattering (SRS) [8-15]. SRS has been convinced to be a promising method for wavelength conversion in solid-state lasers [16-18]. The discovery of new Raman materials gives birth to the laser sources at new wavelengths. In the recent years, eye-safe lasers from SRS frequency conversion have been successfully demonstrated in several Raman materials such as $Ba(NO_3)_2$, Nd:YVO_4, Nd:$GdVO_4$, Nd:$SrWO_4$, Nd:$KGWO_4$, $BaWO_4$, and $PbWO_4$ [8-15]. The laser crystal simultaneously serving as a Raman crystal can provide the advantage of compactness and simplicity for an intracavity SRS laser [19,20]. The laser emission at wavelengths of 1176 and 1525 nm based on self-SRS action in 1064- and 1342-nm actively Q-switched Nd:YVO_4 laser have been reported, respectively [9, 21-22]. However, the overall performance is hindered by the thermal effects because the Raman gain coefficient decreases substantially with increasing temperature above room temperature [21]. Therefore, to improve the thermal effects in the gain medium is critically important for developing self-Raman solid-state lasers.

In the past few years, the thermal effects have been verified to be efficiently improved by using the so-called composite crystal as a gain medium. The composite crystal is fabricated by the diffusion bonding of a doped crystal to an undoped crystal with the same cross section [23-29]. To the best of our knowledge, the composite crystal has not been applied to the self-Raman laser systems. In this work, we employ a double-end diffusion-bonded Nd:YVO_4 crystal to investigate the output performance of the self-Raman laser at 1525 nm. With an input pump power of 17.2 W, the maximum average power at 1525 nm is 2.23 W at a pulse repetition rate of 40 kHz, corresponding to conversion efficiency of 13%. The maximum

average output power with the composite crystal is found to be nearly 40% higher than that with a conventional Nd:YVO_4 crystal at the same pulse repetition rate.

2. Experimental setup

The experimental setup of a diode-pumped actively Q-switched eye-safe Raman laser employing a composite Nd:YVO_4 crystal is shown in Fig. 1. The laser crystal is an *a*-cut 4 mm × 4 mm × 20 mm double-end diffusion-bonded Nd:YVO_4 crystal bounded with one 2-mm-long undoped YVO_4 end at the pumped facet of 0.3-at.% Nd^{3+}-doped Nd:YVO_4 crystal and one 8-mm-long undoped YVO_4 end at the other facet. The laser crystal is supplied by Witcore Co., Ltd. With the 1342-nm fundamental pump wavelength, the wavelength of the first-Stokes component for the YVO_4 Stokes shift at 890-cm^{-1} can be calculated to be around 1525 nm. The front and output coupler are designed for the first-Stokes generation. Both sides of the laser crystal are coated for antireflection at 1330-1530 nm (R<0.2%). In addition, the laser crystal is wrapped with indium foil and mounted in a water-cooled copper block. The water temperature was maintained at 22°C. The front mirror is a 500-mm radius-of-curvature concave mirror with antireflection coating at 808 nm on the entrance face (R<0.2%), high-transmission (HT) coating at 808 nm (T>90%), and high-reflection (HR) coating at 1342 and 1525 nm on the other face (R>99.8%). The output coupler is a flat mirror with high-reflection coating at 1342 nm and partial-reflection (PR) coating at 1525 nm (R=65%). The pump source is an 808-nm fiber-coupled laser diode with a core diameter of 600 μm, a numerical aperture of 0.16, and a maximum power of 17.2 W. The pump beam is reimaged at the laser active medium and the waist radius is nearly 250 μm. The 30-mm-long acousto-optic Q-switcher (NEOS Technologies) had antireflectance coatings at 1342 nm on both faces and was driven at a 27.12-MHz center frequency with 15.0 W of rf power. The overall laser cavity length is 75 mm.

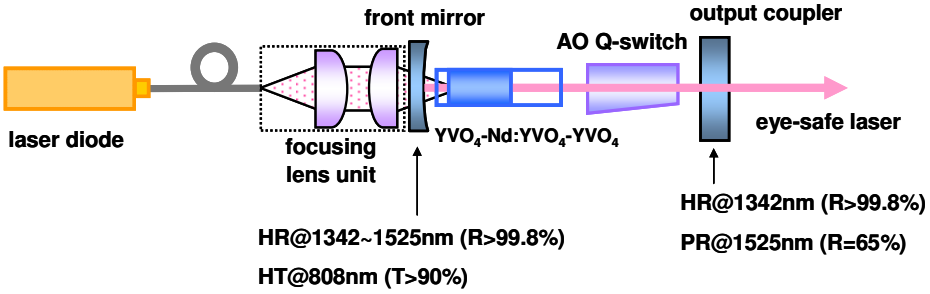

Fig. 1. Experimental setup of a diode-end-pumped actively Q-switched Nd:YVO_4 Raman laser.

3. Experimental results and discussions

We firstly used a simple laser setup for CW operation at 1342 nm to investigate the improvement of the thermal lensing effect in a double-end diffusion-bonded Nd:YVO_4 crystal [30]. For this investigation an output coupler with partial reflection at 1342 nm was used instead of the above-mentioned Raman cavity output coupler. The optimum reflectivity of the output coupler was found to be approximately 92–94%. The effective focal lengths of the thermal lens were estimated based on the fact that the laser system would start unstable for a cavity length longer than the critical length related to the thermal lensing. Even though the absolute accuracy is not easily achieved, this method is confirmed to provide the high relative accuracy for the effective focal lengths of the thermal lens [30]. Figure 2 shows the experimental data and fitted lines of thermal lensing power in a conventional crystal and a double-end diffusion-bonded crystal with the same dopant concentration. It can be seen that the effective focal length in a double-end diffusion-bonded crystal is nearly 1.6 times that in a conventional Nd:YVO_4 crystal. As a result, the thermal effects can be substantiated to be significantly reduced in a double-end diffusion-bonded crystal.

When the Raman cavity output coupler was used in the laser cavity, the pumping threshold for the Raman laser output was found to be 2–3 W for the pulse repetition rates within 20-40 kHz. The beam quality factor was found to be better than 1.5 over the entire operating region. The spectrum of laser output is measured by an optical spectrum analyzer (Advantest Q8381A) employing a diffraction lattice monochromator with a resolution of 0.1 nm. As shown in Fig. 3, the optical spectrum for the actively Q-switched self-Raman output displayed that the fundamental laser emission was at 1342 nm and the Stokes component was at 1525 nm. The frequency shift between Stokes and laser lines is in good agreement with the optical vibration modes of tetrahedral VO_4^{-3} ionic groups (890 cm^{-1}) [19].

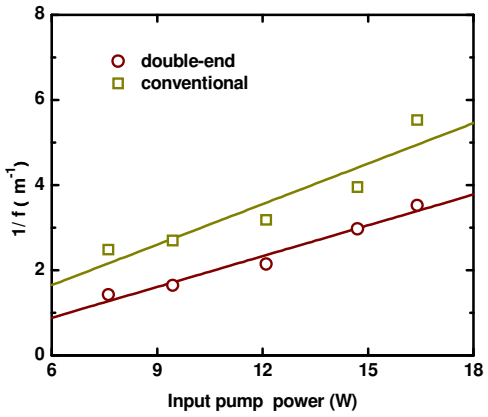

Fig. 2. Dependences of thermal lensing power on input pump power for conventional and double-end diffusion-bonded Nd:YVO_4 CW laser at 1342 nm.

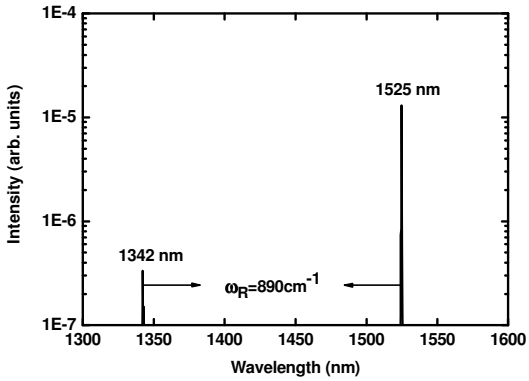

Fig. 3. Optical spectrum of the diode-pumped actively Q-switch Nd:YVO_4 self-Raman laser.

Figure 4 shows the experimental results of the average output power at 1525 nm with respect to the input pump power for the present self-Raman laser at pulse repetition rates of 20 and 40 kHz. For comparison, the previous results obtained by Chen [9] with a conventional 0.2%-doped Nd:YVO_4 crystal at a repetition rate of 20 kHz is also depicted in the same figure. Note that there were no experimental data for a conventional 0.2%-doped Nd:YVO_4 crystal at a pulse repetition rate of 40 kHz because of the high lasing threshold. It can be seen that the Raman lasing threshold for a double-end diffusion-bonded Nd:YVO_4 crystal is approximately 2.0 W that is substantially lower than the lasing threshold of 8.5 W for a conventional Nd:YVO_4 crystal at the repetition rate of 20 kHz. Moreover, the lasing threshold at a pulse

repetition rate of 40 kHz for present self-Raman laser is below 3.0 W. A rather low lasing threshold for high pulse repetition rates comes from the fact that the undoped part of the composite crystal increases the interaction length and then enhances the Raman gain.

It has been experimentally evidenced that the maximum output power for a conventional self-Raman laser is limited by the critical pump power that induces a large temperature gradient in the gain medium to lead to the Raman gain lower than the cavity losses [21]. Consequently, the output power begins to saturate when the pump power exceeds the critical pump power. As shown in Fig. 4, the critical pump power for the self-Raman laser with a double-end diffusion-bonded Nd:YVO_4 crystal can exceed 17.2 W that is limited by the available pump power and is considerably greater than the critical pump power of 13.5 W with a conventional Nd:YVO_4 crystal. As a result, the self-Raman laser with a double-end diffusion-bonded Nd:YVO_4 crystal can generate the maximum average output power up to 1.72 W that is approximately 43% higher than the result with a conventional 0.2 %-doped Nd:YVO_4 crystal [9]. At a repetition rate of 40 kHz, the maximum power at 1525 nm is even up to 2.23 W with an input pump power of 17.2 W, corresponding to a conversion efficiency of 13%. To the best of our knowledge, this is the highest average power for diode-pumped eye-safe self-Raman laser.

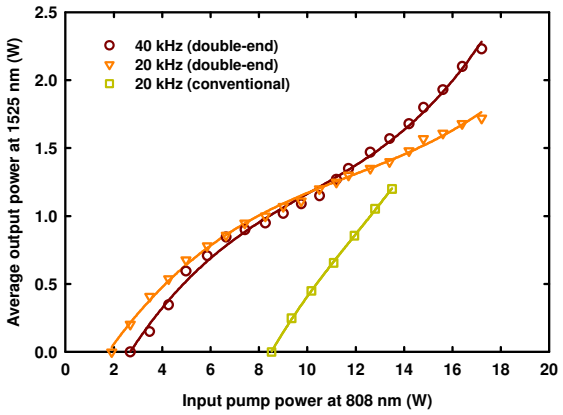

Fig. 4. The average output power at 1525 nm with respect to the input pump power at pulse repetition rates of 20 and 40 kHz shown as the down-triangle and circle symbols respectively for the double-end diffusion-bonded Nd:YVO_4 crystal and that at 20 kHz shown as the square symbol for a conventional Nd:YVO_4 crystal reported by Chen [9].

The temporal traces for the fundamental and Raman pulses are recorded by a LeCroy digital oscilloscope (Wavepro 7100, 10 Gsamples/s, 1-GHz bandwidth) with two fast p-i-n photodiodes. At a repetition rate of 40 kHz the pulse energy is up to 56 μJ with an input pump power of 17.2 W and the pulse width is measured to be approximately 3.2 ns, as shown in Fig. 5. The corresponding peak power is higher than 17 kW. At the pulse repetition rate of 20 kHz, the maximum pulse energy is up to 86 μJ. Figure 6 shows the pulse width at a pulse repetition rate of 20 kHz with a pump power of 17.2 W. It can be seen that although a second tiny Raman pulse usually follows the main first peak, its contribution is rather limited. Consequently the peak power can be generally higher than 22 kW. Since the fundamental energy is remained after first Raman pulse, the sub-pulse of fundamental wave is formed shown as Fig. 5 and Fig. 6. At a pulse repetition rate of 20 kHz, the remaining energy is sufficient to reach Raman gain and a second tiny Raman pulse is produced shown as Fig. 6. The sub-pulse would not be generated if the reflectivity of output coupler was lowered.

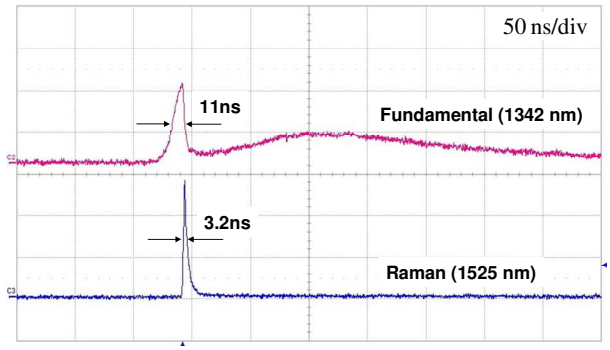

Fig. 5. Temporal characteristics of the fundamental and Raman pulses at a pulse repetition rate of 40 kHz with a pump power of 17.2 W.

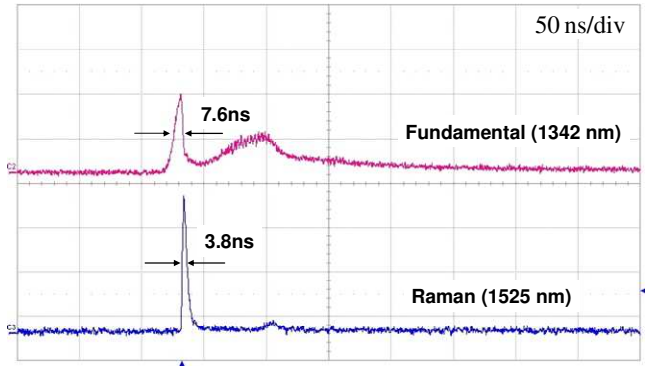

Fig. 6. Temporal characteristics of the fundamental and Raman pulses at a pulse repetition rate of 20 kHz with a pump power of 17.2 W.

4. Conclusion

A compact efficient high-power diode-pumped actively Q-switched self-Raman laser at 1525 nm is demonstrated by employing a double-end diffusion-bonded Nd:YVO_4 crystal. Experimental results reveal that the composite crystal can reduce the thermal effects to reach a higher critical pump power. More importantly, the undoped part plays a critical role in lowering the lasing threshold at high pulse repletion rates because of the increase of the Raman interaction length. The maximum average output power of 2.23 W at first-Stokes wavelength of 1525 nm is generated at a pulse repetition rate of 40 kHz, and the pulse width of Raman pulse is about 3.2 ns with an input pump power of 17.2 W. The corresponding conversion efficiency and peak power are approximately 13% and 17.4 kW, respectively.

Acknowledgments

The authors thank the National Science Council for their financial support of this research under Contract No. NSC-95-2112-M-009-041-MY2.

High-efficiency Q-switched dual-wavelength emission at 1176 and 559 nm with intracavity Raman and sum-frequency generation

Y. T. Chang, H. L. Chang, K. W. Su*, and Y. F. Chen*

Department of Electrophysics, National Chiao Tung University, Hsinchu, Taiwan
**sukuanwei@mail.nctu.edu.tw, yfchen@cc.nctu.edu.tw*

Abstract: An efficient Q-switched dual-wavelength laser with self-frequency Raman conversion in composite Nd:YVO_4 and intracavity sum-frequency generation in BBO is reported. With an input pump power of 17.5 W, average power of 0.53 W at the first-Stokes 1176 nm and average power of 1.67 W at the sum-frequency mixed 559 nm are simultaneously generated at a pulse repetition rate of 100 kHz, corresponding to a total conversion efficiency of 12.5%.

OCIS codes: (140.3550) Lasers, Raman; (140.7300) Visible lasers; (140.3480) Lasers, diode-pumped; (190.2620) Harmonic generation and mixing.

References and links

1. J. A. Piper, and H. M. Pask, "Crysatalline Raman Lasers," IEEE J. Sel. Top. Quantum Electron. **13**(3), 692–704 (2007).
2. H. M. Pask, P. Dekker, R. P. Mildren, D. J. Spence, and J. A. Piper, "Wavelength-versatile visible and UV sources based on crystalline Raman lasers," Prog. Quantum Electron. **32**(3-4), 121–158 (2008).
3. S. T. Li, X. Y. Zhang, Q. P. Wang, X. L. Zhang, Z. H. Cong, H. J. Zhang, and J. Y. Wang, "Diode-side-pumped intracavity frequency-doubled Nd:YAG/$BaWO_4$ Raman laser generating average output power of 3.14 W at 590 nm," Opt. Lett. **32**(20), 2951–2953 (2007).
4. A. J. Lee, H. M. Pask, P. Dekker, and J. A. Piper, "High efficiency, multi-Watt CW yellow emission from an intracavity-doubled self-Raman laser using Nd:$GdVO_4$," Opt. Express **16**(26), 21958–21963 (2008).
5. W. Telford, M. Murga, T. Hawley, R. Hawley, B. Packard, A. Komoriya, F. Haas, and C. Hubert, "DPSS yellow-green 561-nm lasers for improved fluorochrome detection by flow cytometry," Cytometry A **68A**(1), 36–44 (2005).
6. C. He, and T. H. Chyba, "Solid-state barium nitrate Raman laser in the visible region," Opt. Commun. **135**(4-6), 273–278 (1997).
7. A. A. Kaminskii, C. L. McCray, H. R. Lee, S. W. Lee, D. A. Temple, T. H. Chyba, W. D. Marsh, J. C. Barnes, A. N. Annanenkov, V. D. Legun, H. J. Eichler, G. M. A. Gad, and K. Ueda, "High efficiency nanosecond Raman lasers based on tetragonal $PbWO_4$ crystals," Opt. Commun. **183**(1-4), 277–287 (2000).
8. F. Q. Jia, Q. Zheng, Q. H. Xue, Y. K. Bu, and L. S. Qian, "Yellow light generation by frequency doubling of a diode-pumped Nd:YAG laser," Opt. Commun. **259**(1), 212–215 (2006).
9. E. Räikkönen, O. Kimmelma, M. Kaivola, and S. C. Buchter, "Passively Q-switched Nd:YAG/KTA laser at 561 nm," Opt. Commun. **281**(15-16), 4088–4091 (2008).
10. S. Hilbich, W. Seelert, V. Ostroumov, and C. Kannengiesser, R. v. Elm, J. Mueller, E. Weiss, H. Zhou, and J. Chilla, "New wavelengths in the yellow orange range between 545 nm to 580 nm generated by an intracavity frequency-doubled Optically Pumped Semiconductor Laser," Proc. SPIE **6451**, 64510C (2007).
11. H. M. Pask, R. P. Mildren, and J. A. Piper, "Optical field dynamics in a wavelength-versatile, all-solid-state intracavity cascaded pulsed Raman laser," Appl. Phys. B **93**(2-3), 507–513 (2008).
12. A. A. Kaminskii, K. Ueda, H. J. Eichler, Y. Kuwano, H. Kouta, S. N. Bagaev, T. H. Chyba, J. C. Barnes, G. M. A. Gad, T. Murai, and J. Lu, "Tetragonal vanadates YVO_4 and $GdVO_4$ – new efficient $\chi^{(3)}$-materials for Raman lasers," Opt. Commun. **194**(1-3), 201–206 (2001).
13. A. A. Kaminskii, "Laser crystals and ceramics: recent advances," Laser & Photon. Rev. **1**(2), 93–177 (2007).
14. A. A. Kaminskii, S. N. Bagayev, H. J. Eichler, H. Rhee, K. Ueda, K. Takaichi, K. Oka, H. Shibata, Y. Hatanaka, and Y. Matsumoto, "Steady-state picosecond stimulated Raman scattering in two host-crystals for Ln^{3+} and Ln^{2+} lasants," Laser Phys. Lett. **3**(8), 385–391 (2006).
15. Y. F. Chen, "High-power diode-pumped actively Q-switched Nd:YVO_4 self-Raman laser: influence of dopant concentration," Opt. Lett. **29**(16), 1915–1917 (2004).
16. Y. F. Chen, "Compact efficient all-solid-state eye-safe laser with self-frequency Raman conversion in a Nd:YVO_4 crystal," Opt. Lett. **29**(18), 2172–2174 (2004).
17. F. F. Su, X. Y. Zhang, Q. P. Wang, S. H. Ding, P. Jia, S. T. Li, S. Z. Fan, C. Zhang, and B. Liu, "Diode pumped actively Q-switched Nd:YVO_4 self-Raman laser," J. Phys. D Appl. Phys. **39**(10), 2090–2093 (2006).

18. Y. F. Chen, "Compact efficient self-frequency Raman conversion in diode-pumped passively Q-switched Nd:$GdVO_4$ laser," Appl. Phys. B **78**(6), 685–687 (2004).
19. Y. F. Chen, "Efficient 1521-nm Nd:$GdVO_4$ Raman laser," Opt. Lett. **29**(22), 2632–2634 (2004).
20. A. A. Kaminskii, M. Bettinelli, J. Dong, D. Jaque, and K. Ueda, "Nanosecond Nd^{3+}:$LuVO_4$ self-Raman laser," Laser Phys. Lett. **6**(5), 374–379 (2009).
21. Y. T. Chang, K. W. Su, H. L. Chang, and Y. F. Chen, "Compact efficient Q-switched eye-safe laser at 1525 nm with a double-end diffusion-bonded Nd:YVO_4 crystal as a self-Raman medium," Opt. Express **17**(6), 4330–4335 (2009).

1. Introduction

Stimulated Raman scattering (SRS) has been recognized as a promising and practical approach of wavelength conversion for infrared solid-sate laser [1]. In the recent years, new laser sources in the spectral range of visible and UV light have been successfully generated by combining SRS with second-Harmonic-generation (SHG) or sum-frequency-generation (SFG) [2]. More interestingly and importantly, yellow lights are useful for biomedicine, ophthalmology and dermatology. To date, the highest yellow average power of 3.14 W at 590 nm for a pulse repetition rate of 10 kHz was obtained by doubling diode-side-pumped Nd:YAG/$BaWO_4$ Raman laser [3]. In continuous-wave (CW) operation, the highest yellow average power of 2.51 W at 586.5 W was generated from intracavity frequency-doubling of a diode-end-pumped Nd:$GdVO_4$ self-Raman laser [4]. Recently, the yellow-green laser near 560 nm has been shown to give excellent excitation of phycoerythrins and low molecular weight fluorochromes [5]. The methods of generating yellow-green solid-state laser sources include external-cavity Raman laser pumped by frequency-doubled Nd^{3+} lasers, SHG in low-gain Nd^{3+} lasers, frequency-doubled optically pumped semiconductor laser, and SFG or SHG in infrared Raman lasers. Firstly, He et al. reported on a 532 nm-pumped multi-wavelength lasers comprising 25-mJ yellow-green emission at 563 nm based on cascade Raman generation in a $Ba(NO_3)_2$ crystal [6]. Kaminskii et al. reported on a greater than 1-mJ $PbWO_4$ Raman laser at 559 nm pumped by Q-switched frequency-doubled Nd:YAG laser at 532 nm [7]. Then, Jia et al. reported on a 1.67-W CW laser at 556 nm generated by frequency-doubling 1112-nm diode-pumped Nd:YAG laser [8]. Räikkönen et al. reported on a 55-mW yellow-green emission at 561 nm from frequency-doubling of a 1123-nm diode-pumped passively Q-switched Nd:YAG laser [9]. Hilbich et al. reported on diode-pumped frequency-doubled optically pumped semiconductor lasers comprising two higher than 100-mW CW yellow-green emissions at 554 and 565 nm [10]. In addition, selectable-wavelength Q-switched Nd:YAG/KGW Raman laser with intracavity SFG and SHG in angle-tuned BBO (β-BaB_2O_4) generated average power of 0.77 W at 559 nm presented by Pask et al. [11].

Recently, Nd:YVO_4 and Nd:$GdVO_4$ crystals have been identified as excellent laser gain media as well as SRS gain media for diode-pumped all-solid-state lasers [12,13]. Quite recently, the $\chi^{(3)}$-nonlinear generation effects in tetragonal $LuVO_4$ vanadates has been discovered [13,14]. The realization of Nd:YVO_4, Nd:$GdVO_4$, and Nd:$LuVO_4$ self-Raman lasers have been demonstrated [15–20]. In this work we employ a self-Raman Nd:YVO_4 laser to develop an efficient yellow-green laser at 559 nm based on intracavity sum-frequency-mixing of the 1064-nm fundamental wave and the 1176-nm first-Stokes component. With an input pump power of 17.5 W, the maximum average power at 559 nm is 1.67 W and the residual average power at 1176 nm is 0.53 W at a pulse repetition rate of 100 kHz, corresponding to conversion efficiency of 9.5% and 3%, respectively. To the best of our knowledge, it is the highest power at 559 nm obtained with intracavity SFG in a self-Raman laser.

2. Experimental setup

The experimental setup of a diode-end-pumped actively Q-switched Nd:YVO_4 self-Raman laser with intracavity SFG is shown in Fig. 1. The pump source is an 808-nm fiber-coupler laser diode with a core diameter of 600 μm, a numerical aperture of 0.16 and a maximum power of 18 W. The pump beam is focused at the active medium, and the waist radius is approximately 250 μm. An *a*-cut 20-mm-long composite 0.3-at.% Nd^{3+}-doped Nd:YVO_4

crystal bounded with a 2-mm-long and an 8-mm-long undoped YVO_4 ends at its pumped facet and the other facet, respectively, is simultaneously used as a laser crystal and a self-Raman medium. With a fundamental pump wavelength of 1064 nm, the wavelength of the first-Stokes emission in accordance with the YVO_4 Stokes shift at 890 cm^{-1} is calculated to be around 1176 nm [12]. Both sides of the laser crystal is coated for antireflection at 1000-1200 nm (R<0.2%). The laser cavity is designed for the sum-frequency mixing of the fundamental wave and the first-Stokes laser. The 10-mm-long type-**I** BBO crystal with a phase-matching cutting angle ($\theta = 22.1°$ and $\psi = 0°$) is used as a sum-frequency mixer. Besides, the composite Nd:YVO_4 and BBO crystals are both wrapped with indium foil and mounted in water-cooled copper blocks. The water temperature is maintained at 20°C. The front mirror M1 is a 500-mm radius-of-curvature concave mirror with antireflection coating at 808 nm on the entrance face (R<0.2%), high-transmission coating at 808 nm (T>90%), and high-reflection coating at 1000-1200 nm on the other face (R>99.8%). The 30-mm-long acousto-optic Q-switcher (NEOS Technologies) had antireflectance coatings at 1064 nm on both faces and was driven at a 27.12-MHz center frequency with 15.0 W of rf power. The flat intracavity mirror M2 has high-transmission coating at 1064 nm and 1176 nm (T>95%) as well as high-reflection coating at 559 nm (R>99.7%). The output coupler M3 is a flat mirror with high-reflection coating at 1064 nm (R>99.8%), partial-reflection coating at 1176 nm (R = 98.1%), and high-transmission coating at 559 nm (T>85%). The overall laser cavity length is around 113 mm.

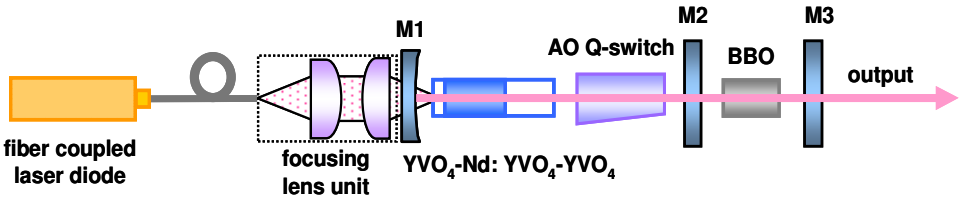

Fig. 1. Experimental setup of a diode-end-pumped actively Q-switched Nd:YVO_4/BBO laser with intracavity self-Raman frequency conversion and sum-frequency generation.

3. Experimental results and discussions

Since it has been verified that the enhancement of Raman gain is attributed from the significant reduced thermal effects and the increase of the Raman interaction length in a double-end diffusion-bonded Nd:YVO_4 crystal [21], we use a double-end diffusion-bonded Nd:YVO_4 crystal as a self-Raman gain medium in this work. The two two-mirror cavities are set up. The first two-mirror cavity with a output coupler having partial-reflection coating at 1064 nm (R = 85%) is used to set up a Q-switched Nd:YVO_4 laser at 1064 nm. With an input pump power of 17.5 W, average power of 8.7 W at 1064 nm is obtained at a pulse repetition rate of 100 kHz. The second two-mirror cavity with a output coupler having high-reflection coating at the 1064 nm and partial reflection coating at the first-Stokes component of 1176 nm (R = 56%) is used for the Q-switched Nd:YVO_4 self-Raman laser at 1176 nm. The laser cavity length is 7 cm and the pumping threshold for the Raman laser is 2.7 W to 3.5 W at the pulse repetition rates of 80 kHz to 120 kHz. With an input pump power of 12.1 W, the average output power of 3 W and the peak power of 7.6 kW at 1176 nm are achieved at a pulse repetition rate of 100 kHz, corresponding to a high conversion efficiency of 24.8%. The average power at 1176 nm and conversion efficiency are 2 times and 1.8 times that of the Nd:YVO_4 self-Raman laser with a conventional Nd:YVO_4 crystal without undoped endcaps, respectively [15].

After confirming the performance of the Q-switched Raman laser at 1176 nm, the laser cavity is designed for sum-frequency mixing of the fundamental wave and the first-Stokes component. The BBO crystal, the intracavity mirror M2, and the output coupler M3 are inserted in the laser cavity. The cavity alignment and the tilt of BBO crystal must be regulated to optimize the laser performance. As a result of the high-reflection coating at SFG

wavelength on mirror M2, the present linear three-mirror-cavity takes the advantages of reduced loss of SFG emission transmitting through the front mirror M1 as well as reduced absorption of SFG emission in the Nd:YVO_4 which lowers the thermal load in the Nd:YVO_4 compared to the linear two-mirror-cavity [4]. Additionally, the present laser configuration is more compact than the three-mirror folded cavity. Note that the present output coupler M3 is non-optimal for SFG emission. Therefore, a higher output power at SFG wavelength can be obtained with the optimum output coupler having high-reflection coating at 1176 nm. The spectrum of laser output is measured by an optical spectrum analyzer (Advantest Q8381A) employing a diffraction lattice monochromator with a resolution of 0.1 nm. The experimental optical spectrum of the laser output is shown in Fig. 2, and it can be seen that the main laser output is the yellow-green laser at 559 nm from sum-frequency-mixing of 1176 and 1064 nm. The pumping threshold for oscillation at 559 nm is around 4.3 W to 6 W for the pulse repetition rates of 80 kHz to 120 kHz. The residual laser output is the first-Stokes laser at 1176 nm. The intensity of the fundamental wave at 1064 nm is weak and hard to measure due to the high-reflection coating at 1064 nm on the output coupler.

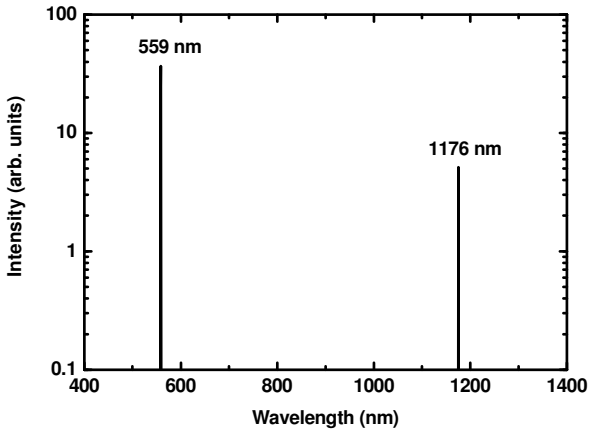

Fig. 2. Optical spectrum of the diode-end-pumped actively Q-switched Nd:YVO_4/BBO laser.

Figure 3 shows the total average power as well as individual average power at Stokes wavelength of 1176 nm and SFG wavelength of 559 nm with respect to the input pump power at a pulse repetition rate of 100 kHz. The M^2 beam quality factor is found to be less than 2.0 for all pump powers. The average power at 1176 nm is saturated at around 0.55 W with an input pump power above 12 W. With an input pump power of 12.9 W, the average power of 0.56 W at 1176 nm is obtained, corresponding to a conversion efficiency of 4.3%. However, increasing input pump power to higher than 12 W is beneficial for enhancing SFG average power. While the input pump power is increased to 17.5 W, the average power at 559 nm is up to 1.67 W corresponding to a conversion efficiency of 9.5%. The higher average output at 559 nm and the lower average output power at 1176 nm would be obtained if an output coupler with high-reflection coating at both 1064 and 1176 nm (R>99.8%) was used.

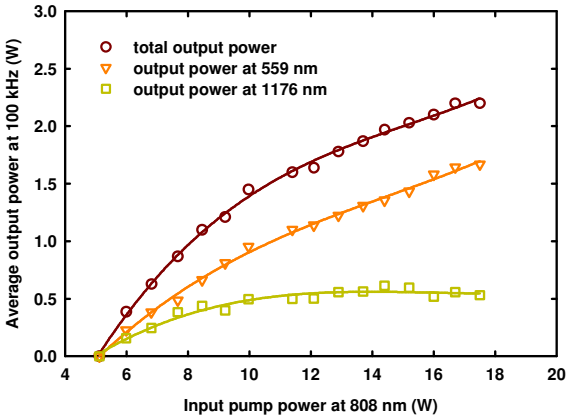

Fig. 3. The total average output power as well as individual average output power at 559 and 1176 nm with respect to the input pump power at a pulse repetition rate of 100 kHz.

The temporal traces for the laser emission comprising the fundamental, Raman, and SFG pulses are recorded by a LeCroy digital oscilloscope (Wavepro 7100, 10 Gsamples/s, 1-GHz bandwidth) with two fast p-i-n photodiodes. The oscilloscope trace of output pulse trains is shown in Fig. 4. It can be seen that the pulse-to-pulse amplitude fluctuation is within ± 15%. Note that the vertical scales for the pulses at 1064, 1176, and 559 nm are separate arbitrary units. The pulse widths of 1176 and 559 nm are measured to be shorter than 55 and 10 ns over the entire operation, respectively. As shown in Fig. 5, the pulse widths of 1176 and 559 nm pulses are approximately 32 and 5.4 ns with an input pump power of 17.5 W at a pulse repetition rate of 100 kHz, respectively. As shown in Fig. 5, the Raman pulse is generated after SFG pulse. It is because that when the intracavity power density of the fundamental pulse reaches the SRS threshold, the Raman and fundamental pulses are simultaneously rapidly converted to SFG pulse. Therefore, there exists a longer time shift of fundamental and Raman pulses than Raman laser without SFG. In summary, an efficient dual-wavelength Q-switched laser at 559 and 1176 nm based on self-Raman and intracavity SFG is demonstrated by using a double-end diffusion-bonded Nd:YVO_4 crystal and a BBO crystal. At a pulse repetition rate of 100 kHz, the main average output power of 1.67 W at 559 nm and the residual average output power of 0.53 W at 1176 nm is generated with an input pump power of 17.5 W, corresponding to conversion efficiency of 9.5% and 3% and peak power of 3.1 and 0.17 kW, respectively. The total conversion efficiency of SRS and SFG is 12.5%.

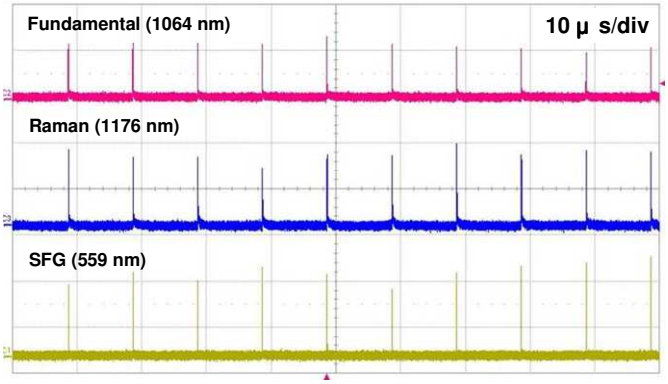

Fig. 4. Typical oscilloscope traces of pulse trains at 1064, 1176, and 559 nm.

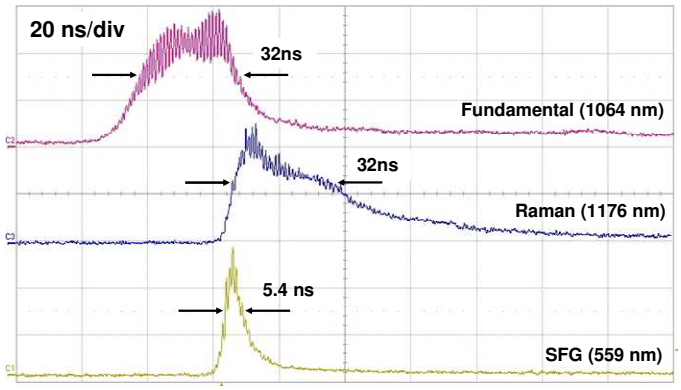

Fig. 5. Typical oscilloscope traces for output pulses at 1064, 1176, and 559 nm.

4. Conclusion

In conclusion, an efficient yellow-green laser at 559 nm with intracavity SFG in a diode-pumped Q-switched Nd:YVO_4 self-Raman laser is demonstrated. We utilize a double-bonded diffusion-bonded Nd:YVO_4 crystal as a self-Raman gain medium to improve thermal lensing effect and enhance the Raman gain. With input pump power of 17.5 W, the maximum average power at 559 nm is 1.67 W and the average power at 1176 nm is 0.53 W at a pulse repetition rate of 100 kHz, corresponding to conversion efficiency of 9.5% and 3%, respectively. The peak power of 559 nm pulse amounts to 3.1 kW.

Acknowledgments

The authors thank the National Science Council for their financial support of this research under Contract No. NSC-97-2112-M-009-016-MY3.

High-peak-power diode-pumped actively Q-switched Nd:YAG intracavity Raman laser with an undoped YVO_4 crystal

K. W. Su, Y. T. Chang, and Y. F. Chen

Department of Electrophysics, National Chiao Tung University, Hsinchu, Taiwan

ABSTRACT

The efficient stimulated Raman scattering conversion in a diode-pumped actively Q-switched Nd:YAG laser was achieved with an undoped YVO_4 crystal as a Raman shifter. With an incident pump power of 16.2 W, 1176-nm first Stokes average output power of 2.97 W was generated at a pulse repetition rate of 50 kHz. The maximum pulse energy is higher than 83 μJ at both 20 kHz and 30 kHz. With mode-locked modulation, the effective pulse width far above threshold is usually below 5 ns. With an incident pump power of 7.62 W, the peak-power of 43.5 kW was demonstrated at 20 kHz.

Keywords: Raman laser; diode-pumped laser; actively Q-switched

Correspondence:

Dr. Kuan-Wei Su

Department of Electrophysics

National Chiao Tung University,

1001 Ta Hsueh Road, Hsinchu

TAIWAN, 30010

E-mail: sukuanwei@mail.nctu.edu.tw

Fax: +886-3-5725230

Solid State Lasers XVII: Technology and Devices
edited by W. Andrew Clarkson, Norman Hodgson, Ramesh K. Shori
Proc. of SPIE Vol. 6871, 68712J, (2008) · 0277-786X/08/$18 · doi: 10.1117/12.762821

1. Introduction

Neodymium-doped yttrium aluminum garnet and yttrium vanadate (Nd:YAG and Nd:YVO_4) are the most widely used materials of solid-state laser gain medium [1,2]. The Nd:YVO_4 crystal has a strong broadband absorption and an effective stimulated emission cross section which is five times larger than Nd:YAG [1]. These properties imply that a Nd:YVO_4 laser usually has the higher efficiency and broader operating temperature than a Nd:YAG laser. In the field of Raman laser, the availability of self-Raman process also made the study of diode-pumped passively Q-switched (PQS) and actively Q-switched (AQS) Nd:YVO_4 Raman lasers attractive [3,4]. However, the Nd:YAG crystal has other advantages such as better thermal property and much longer fluorescence life time. Especially the long life time can raise the output pulse energy of a fundamental AQS laser, and should be able to raise the output pulse energy of a AQS Raman laser at the Stokes wavelength. This means that the conversion efficiency of the intracavity stimulated Raman scattering (SRS) might be increased in an AQS Nd:YAG solid-state laser.

With the development of the crystals as Raman shifters, intracavity Raman lasers are realized as an efficient and practical scheme for extending lasing spectrum [2,5-8]. $Ba(NO_3)_2$ [9], $LiIO_3$ [10], $KGd(WO_4)_2$ [11], $PbWO_4$ [12], and $BaWO_4$ [13-19] are well known materials for SRS. Further more, YVO_4 and $GdVO_4$ were found to be the efficient $\chi^{(3)}$-materials for Raman laser [20]. Recently, we have exhibited the AQS Nd:YVO_4 Raman laser with an undoped YVO_4 crystal which was demonstrated as a potential Raman shifter [21]. However, Q-switched Nd:YAG intracavity Raman lasers based on YVO_4 crystals have not been reported to our knowledge.

In this letter, we report the high-pulse-energy and high-peak-power intracavity YVO_4 SRS generation in a compact diode-pumped AQS Nd:YAG laser. At an incident pump power of 16.2 W, 1176-nm first Stokes average output power of 2.97 W is efficiently generated at a pulse repetition frequency (PRF) of 50 kHz. The maximum output pulse energy is higher than 83 μJ. Then, the overall conversion efficiency were up to 21.3-18.3%. The output pulses display a mode-locking phenomenon that leads the narrow effective pulse width and the maximum peak power to be 43.5 kW.

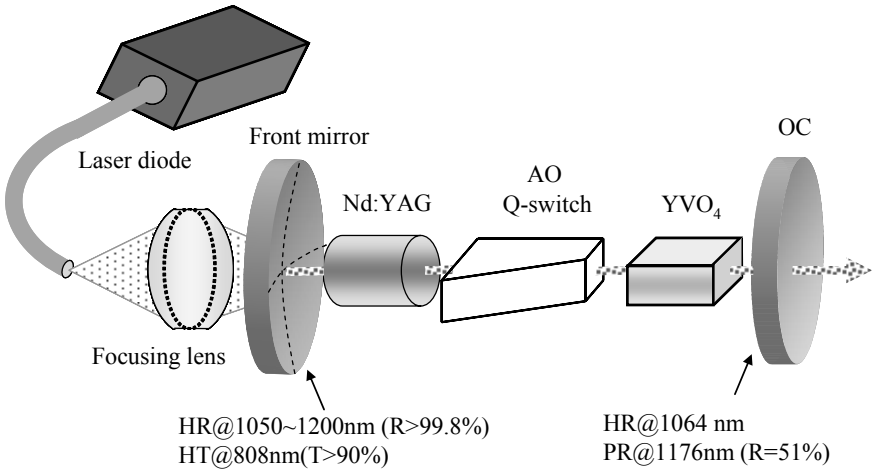

Fig. 1. Scheme of a diode-pumped actively Q-switched Nd:YAG/YVO_4 Raman laser.

2. Experimental setup

Figure 1 depicts the experimental configuration for the diode-pumped AQS Nd:YAG/YVO_4 Raman laser. The cavity mirrors which have special dichroic coating for efficient conversion at the first Stokes component form a plano-concave configuration. The input mirror is a 500-mm radius-of-curvature concave mirror with antireflection coating at 808 nm on the entrance face (R<0.2%), high-reflection coating at 1050-1200 nm (R>99.8%) and

high-transmission coating at 808 nm on the other surface (T>90%). The output coupler is a flat mirror with high-reflection coating at 1064 nm (R>99.8%) and partial-reflection coating at 1176 nm (R=51%). Note that the output coupler reflectivity is not optimized and it is limited in availability.

The pump source was an 808-nm fiber-coupled laser diode with a core diameter of 800 μm, a numerical aperture of 0.16 and a maximum output power of 25 W. A focusing lens system with a 85% coupling efficiency was used to re-image the pump beam into the laser crystal. The waist radius of the pump beam was approximately 400 μm. The laser medium was a 0.8-at.% Nd^{3+}:YAG crystal with a length of 10 mm. Both sides of this laser crystal were coated for antireflection (AR) at 1.06 μm (R<0.2%). The Raman crystal was an a-cut undoped YVO_4 crystal with a length of 9.6 mm. These two crystals were both wrapped with indium foil and mounted in water-cooled copper blocks individually. The water temperature was maintained at 20 ℃. The 30-mm-long acousto-optic Q-switch (NEOS Technologies) had antireflection coatings at 1064 nm on both faces and was driven at a 27.12 MHz center frequency with 15 W of RF power. The overall laser cavity length was around 9 cm and depended on pumping power.

3. Experimental results and discussion

The AQS Nd:YAG laser performance at 1064 nm was firstly studied for evaluating the conversion efficiency of the intracavity SRS. For this investigation, an output coupler with partial reflection at 1064 nm was used instead of the above-mentioned Raman cavity output coupler. The optimum reflectivity of the output coupler was found to be approximately 80%. Figure 2 shows the average output power at the fundamental wavelength of 1064 nm with respect to the incident pump power at different pulse repetition rate from 20 kHz to 50 kHz. The threshold for 1064-nm oscillation was below 2.5 W and insensitive to the PRF. With an incident pump power of 8.63, 13.3, and 16.2 W, the average output powers at 1064 nm were 2.6-2.9, 4.7-5.0, and 5.8-6.3 W for PRFs in the range of 20-50 kHz.

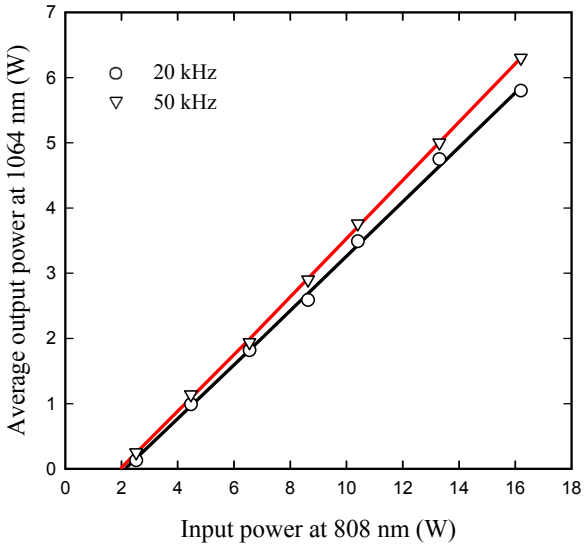

Fig. 2. The average output power at the fundamental wavelength of 1064 nm with respect to the incident pump power at different pulse repetition rate from 20 kHz to 50 kHz.

Besides, the partially polarized laser beam with a polarization ratio of 3:1 should be excited by the acousto-optic Q-switch and nonlinear Raman crystal. However, when the intracavity Raman laser was used, the relatively random polarization compared to Nd:YVO_4/YVO_4 Raman laser may benefit the robustness of the Raman crystal. Therefore,

our experimental results revealed that the same Raman crystals can sustain higher peak power per unit area in Nd:YAG laser.

The experimental result for optical spectrum of the Raman laser was monitored by an optical spectrum analyzer (Advantest Q8381A, including a diffraction grating monochromator) with a resolution of 0.1 nm. The Raman scattering spectrum of an YVO_4 crystal is showed in Fig. 3. The first Stokes wavelength of 1176 nm was converted from the fundamental wavelength at 1064 nm by Raman shift at 890 cm^{-1} came from the YVO_4 crystal [20,21]. There is no second Stokes wavelength observed for all pumping power.

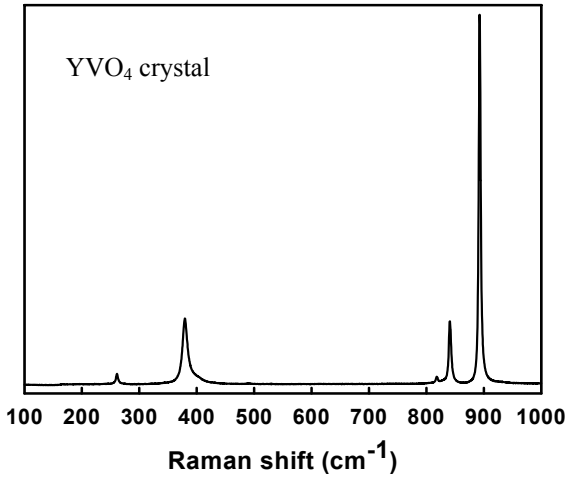

Fig. 3 (a). The Raman scattering spectrum of an YVO_4 crystal, which is almost the same as it of Nd:YVO_4 crystal.

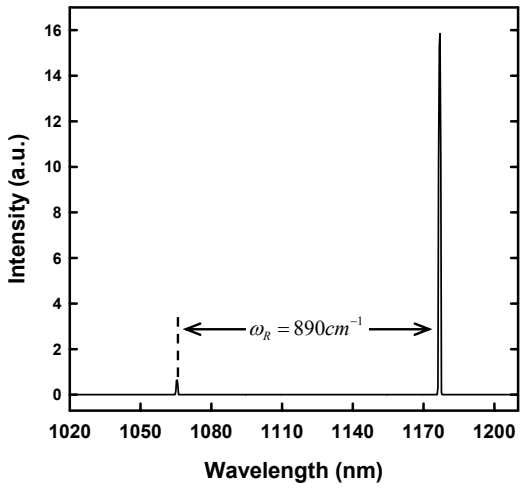

Fig. 3 (b). Optical spectrum of the actively Q-switched Raman output. The fundamental and Raman component are at 1064.5 nm and 1175.9 nm.

Figure 4 illustrates the average output power and output pulse energy at 1176 nm with respect to the incident pump power for PRF of 20, 30, and 50 kHz. Reducing the PRF leads to a lower threshold for stimulated Raman output, but it leads to a smaller maximum output power due to the increasing thermal loading of the end-pumped Q-switched Nd-doped laser [22]. Moreover, the self-focusing-induced damage on YVO_4 crystal usually occurred especially at low PRF while the pump power is been over driving. Nevertheless, the efficient average output powers at 1176 nm were separately 1.62, 2.49, and 2.97 W at PRFs of 20, 30, and 50 kHz with the incident pump power of 7.62, 13.3, and 16.2 W. As a consequence, the maximum SRS conversion efficiency of 62-47% with respect to the output power available from the fundamental laser of 1064 nm was demonstrated at the PRF of 20-50 kHz. Then, the maximum optical-to-optical conversion efficiency from 808-nm pump were as high as 21.3-18.3% at the PRF of 20-50 kHz. The overall conversion efficiency is the highest one for Raman lasers until now to our knowledge [2]. The efficiency could be improved if we can use a c-cut YVO_4 crystal [23] with properly antireflection coating and an optimized output coupler. The maximum pulse energies, E_{max}, at PRFs of 20, 30 and 50 kHz were 84.5, 83.1 and 59.4 μJ. The E_{max} were higher than 83 μJ at PRFs below 30 kHz. Therefore, the E_{max} of this Nd:YAG/YVO_4 Raman laser was almost two times the E_{max} of the Nd:YVO_4/YVO_4 Raman laser in almost the same AQS scheme [21].

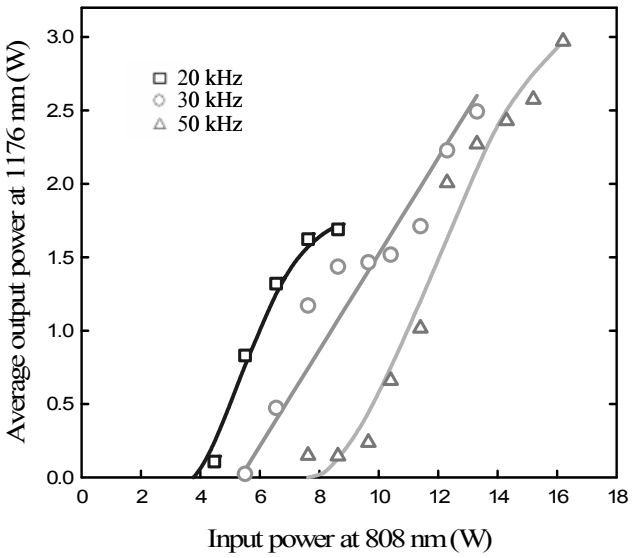

Fig. 4. The average output power at the Stokes wavelength of 1176 nm with respect to the incident pump power at different pulse repetition rate from 20 kHz to 50 kHz.

The temporal behaviors were recorded by a LeCroy digital oscilloscope (Wavepro 7100, 10 GS/s, 1-GHz bandwidth) with two fast p-i-n photodiode and an interference filter allowing transmission only at 1064 nm. Figure 5 and 6 show the typical pulse train and pulse shape for the fundamental and Raman components. The pulse-to-pulse amplitude fluctuation was not more than ±10% in optimized cavity. With the pulse energy of 81.2 μJ at 1176 nm, the pulse width of the pulse envelop in Fig. 6. is 2.2 ns. Because the mode-locked phenomenon cause the Raman pulse a deeply modulated shape, the peak power can not be approximated as the pulse energy divided by envelope's pulse width. After numerical computing, the peak power of the Raman pulse in Fig. 6. is 43.5 kW corresponding to an effective pulse width, W_{eff}, of 1.87 ns. Here we defined the W_{eff} as the pulse energy divided by peak power [21]. Consequently, the W_{eff} for Raman pulses far above threshold are distributed among 3.6-1.8, 5.0-3.5, and 5.0-3.0 ns at the PRFs of 20, 30, and 50 kHz. For example, Fig. 7. depicts the typical evolvement of pulse shapes dependent on pump power at 50 kHz. With a pump power of 8.63 W which was near threshold of SRS, broad envelope and deep mode-locked modulation was observed with a W_{eff} of 5.17 ns showed in Fig. 7 (a). While pump power was increased to 12.3 W, the W_{eff} was narrowed to 3.07 ns showed in Fig. 7 (b). Then, W_{eff} was become broader due to growing pulse tail. With a pump power of 14.8 W, the pulse was observed with a W_{eff} of 3.33 ns showed in Fig. 7 (c). Comparing to results of the

Nd:YVO_4/YVO_4 Raman laser in almost the same AQS scheme, this Nd:YAG/YVO_4 Raman laser raised maximum ouput pulse energy and peak power from 43 μJ to 83 μJ and 14 kW to 43.5 kW [21].

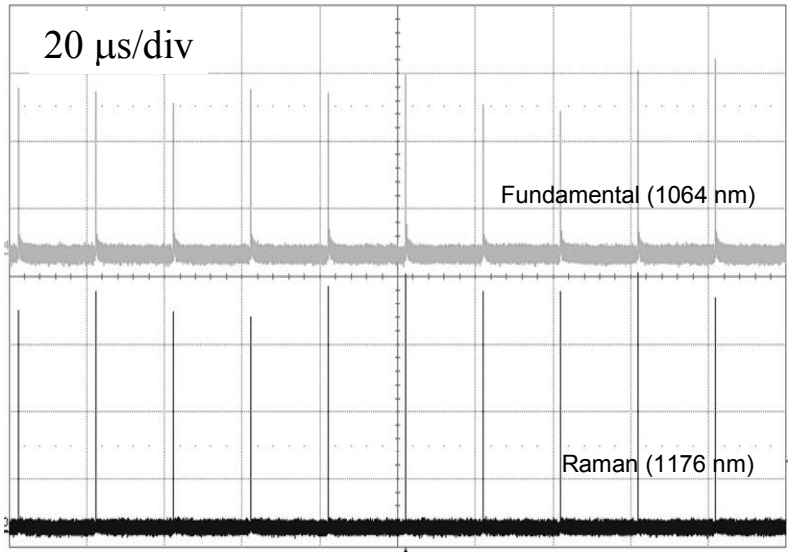

Fig. 5. Typical oscilloscope trace of a train for fundamental and Raman pulses.

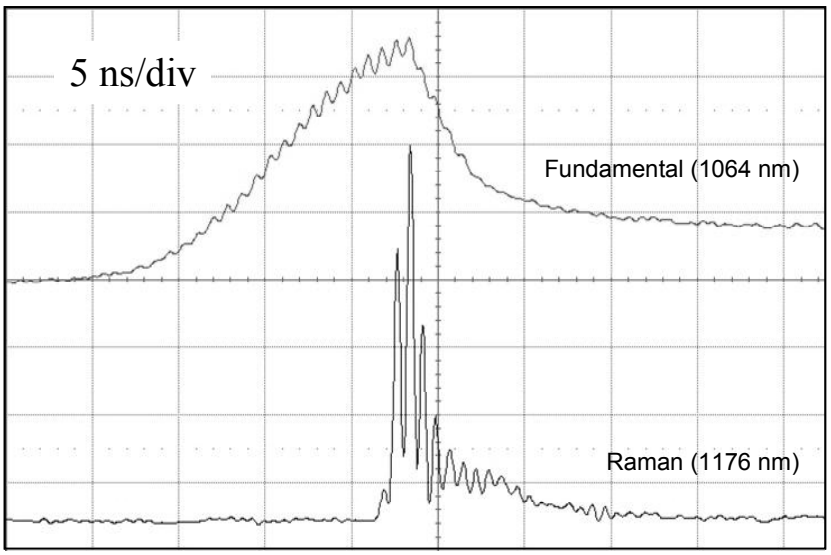

Fig. 6. Oscilloscope trace with mode-locking effect for fundamental and Raman pulses at a pulse repetition rate of 20 kHz.

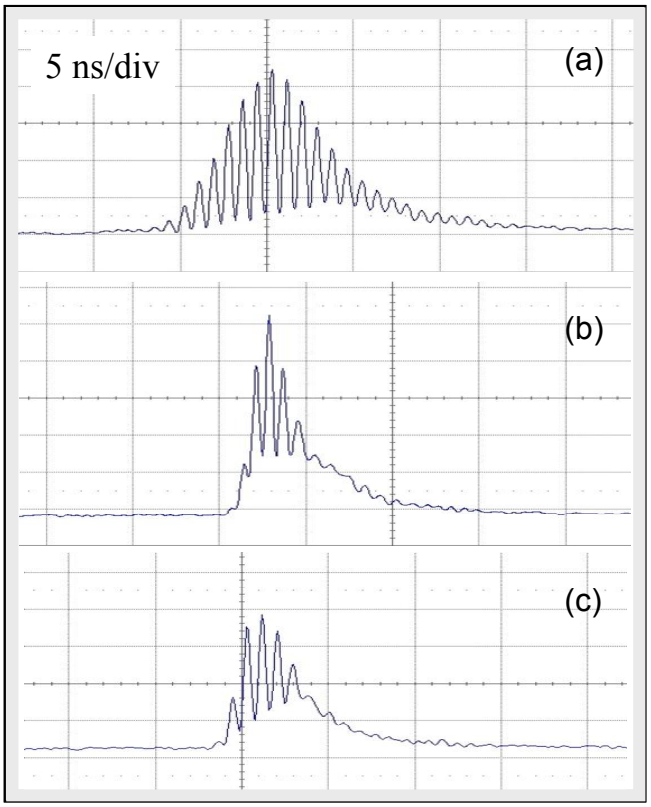

Fig. 7. With input power of 8.6 W, 12.3 W, and 14.8 W at a pulse repetition rate of 50 kHz, the effective pulse width (pulse energy divided by real peak power) of (a), (b), and (c) is 5.17 ns, 3.07 ns, and 3.33 ns. The vertical scales are in alternative units.

4. Conclusions

In summary, an efficient diode-pumped actively Q-switched Nd:YAG/YVO_4 intracavity Raman laser has been demonstrated. 1176-nm average output power of 2.97 W has been generated at a pulse repetition rate of 50 kHz. Further, the maximum optical-to-optical conversion efficiency from 808-nm pump were as high as 21.3-18.3% at the PRF of 20-50 kHz. The maximum pulse energy was higher than 83 μJ at both 20 kHz and 30 kHz. The output pulses displayed a mode-locking phenomenon that leads to narrow effective pulse width compared with envelope's pulse width. With an incident pump power of 7.62 W, the peak-power of 43.5 kW was demonstrated at 20 kHz.

REFERENCES

[1] W. Kochner and M. Bass, chapter 2 in *Solid-State Lasers*, Springer-Verlag (2003)

[2] J.A. Piper and H.M. Pask, "Crystalline Raman Lasers," IEEE J. Selected Topics in Quantum Electron. 13, 3, 692-704 (2007)

[3] Y.F. Chen, "Efficient subnanosecond diode-pumped passively Q-switched Nd : YVO_4 self-stimulated Raman laser", Opt. Lett. 29, 11, 1251 (2004)

[4] Y.F. Chen, "High-power diode-pumped actively Q-switched Nd : YVO4 self-Raman laser: influence of dopant concentration", Opt. Lett. 29, 16, 1915 (2004)

[5] T.T. Basiev, A.A. Sobol, P.G. Zverev, L.I. Iveleva, V.V. Osiko, R.C. Powell, "Raman spectroscopy of crystals for stimulated Raman scattering," Opt. Mater. 11, 4, 307-314 (1999)

[6] P.G. Zverev, T.T. Basiev, and A.M. Prokhorov, "Stimulated Raman scattering of laser radiation in Raman crystals", Opt. Mater. 11, 335 (1999)

[7] H.M. Pask, "The design and operation of solid-state Raman lasers", Prog. Quantum Electron. 27, 3 (2003)

[8] Peter Dekker, Helen M. Pask, David J. Spence and James A. Piper, "All-solid-state 704 mW continuous-wave yellow source based on an intracavity, frequency-doubled crystalline Raman laser," Opt. Lett. 32, 9, 1114-1116 (2007)

[9] A.S. Eremenko, S.N. Karpukhin, and A.I. Stepanov, "Stimulated Raman scattering of the second harmonic of a neodymium laser in nitrate crystals", Sov. J. Quantum Electron. 10, 113 (1980)

[10] E.O. Ammann and C.D. Decker, "0.9-W Raman oscillator", J. Appl. Phys. 48, 1973 (1977)

[11] A.S. Grabtachikov, A.N. Kuzmin, V.A. Lisinetskii, V.A. Orlovich, G.I. Ryabtsev, and A. A. Demidovich, "All solid-state diode-pumped Raman laser with self-frequency conversion", Appl. Phys. Lett. 75, 3742 (1999)

[12] J. Findeisen, H.J. Eichler, and A.A. Kaminskii, "Efficient picosecond $PbWO_4$ and two-wavelength $KGd(WO_4)_2$ Raman lasers in the IR and visible", IEEE J. Quantum Electron. 35, 173 (1999)

[13] T.T. Basiev, A.A. Sobol, P.G. Zverev, L.I. Iveleva, V.V. Osiko, R.C. Powell, "Raman spectroscopy of crystals for stimulated Raman scattering," Opt. Mater. 11, 4, 307-314 (1999)

[14] P. Cerný, P.G. Zverev, H. Jelínková, T.T. Basiev, "Efficient Raman shifting of picosecond pulses using $BaWO_4$ crystal," Opt. Commun. 177, 397-404 (2000)

[15] T.T. Basiev, A.A. Sobol, P.G. Zverev, L.I. Ivleva, V.V. Osiko, "Laser material for stimulated Raman scattering," Patent of Russian Fedration, 2178938 C1 1, pending 25.04.2000

[16] P.G. Zverev, T.T. Basiev, M.E. Doroshenko, V.V. Osiko, "Barium tungstate Raman laser – a new coherent source for sodium star experiments," Trends in Optics and Photonics 34, Advanced Solid State Lasers, H. Injeyan, U. Keller, and C. Marshall, eds.(OSA Washington D.C.) 348-354 (2000)

[17] P.G. Zverev, T.T. Basiev, L.I. Ivleva, V.V. Osiko, N.M. Polozkov, I.S. Voronina, "Raman laser on strontium tungstate crystal," Trends in Optics and Photonics 68, (OSA Washington D.C.) 70-73 (2002)

[18] P. Cerný, H. Jelínková, T.T. Basiev, and P.G. Zverev, "Highly efficient picosecond Raman generators based on the BaWO4 crystal in the near infrared, visible, and ultraviolet," IEEE J. Quantum Electron. 38, 11, 1471-1478 (2002)

[19] Y. F. Chen, K. W. Su, H. J. Zhang, J. Y. Wang, M. H. Jiang, "Efficient diode-pumped actively Q-switched Nd:YAG/BaWO4 intracavity Raman laser," Opt. Lett. 30 (24), 3335 (2005)

[20] A.A. Kaminskii, K. Ueda, H.J. Eichler, Y. Kuwano, H. Kouta, S.N. Bagaev, T.H. Chyba, J.C. Barnes, G.M. A. Gad, T. Murai, and J. Lu, "Tetragonal vanadates YVO_4 and $GdVO_4$ – new efficient $\chi^{(3)}$-materials for Raman lasers", Opt. Commun. 194, 201 (2001)

[21] K.W. Su, Y.T. Chang, and Y.F. Chen, "Power scale-up of the diode-pumped actively Q-switched Nd:YVO_4 Raman laser with an undoped YVO_4 crystal as a Raman shifter," Appl. Phys. B 88, 47-50(2007)

[22] K. Andryunas, Y. Vishakas, V. Kabelka, I.V. Mochalov, A.A. Pavlyuk, G.T. Petrovskii, V. Syrus, JETP Lett. 42, 333 (1985)

[23] P.G. Zverev, A.Y. Karasik, A.A. Sobol, D.S. Chunaev, T.T. Basiev, A.I. Zagumennyi, Y.D. Zavartsev, S.A. Kutovoi, V.V. Osiko, I.A. Shcherbakov, "Stimulated Raman scattering of picosecond pulses in $GdVO_4$ and YVO_4 crystals," Advanced Solid State Photonics Conference, Technical digest, Feb. 1-4, 2004, Santa Fe, USA, WB9. OSA TOPS ASSL, TuB10, 25-27